Stochastic and non-linear processes in nano-electro-mechanical systems

Olivier Maillet

Communauté
UNIVERSITÉ Grenoble Alpes

THÈSE

Pour obtenir le grade de

DOCTEUR DE LA COMMUNAUTE UNIVERSITE GRENOBLE ALPES

Spécialité : **Physique de la Matière Condensée et du Rayonnement**

Arrêté ministériel : 25 mai 2016

Présentée par

Olivier MAILLET

Thèse dirigée par **Eddy COLLIN, CNRS Institut Néel**

préparée au sein du **CNRS Institut Néel**
dans **l'École Doctorale de Physique**

Processus stochastiques et non-linéaires dans les systèmes nano-électro-mécaniques

Thèse soutenue publiquement le **26 mars 2018**,
devant le jury composé de :

Monsieur Adrian BACHTOLD
Professeur, ICFO Barcelone, Rapporteur
Monsieur Andrew ARMOUR
Professeur associé, Université de Nottingham, Rapporteur
Madame Eva WEIG
Professeur, Université de Constance, Examinatrice
Monsieur Pierre-François COHADON
Professeur associé, Ecole Normale Supérieure de Paris, Examinateur
Madame Signe SEIDELIN
Professeur associé, Université Grenoble Alpes, Examinatrice
Monsieur Olivier BOURGEOIS
Directeur de recherche, CNRS Institut Néel, Président

Acknowledgements

Avant de céder aux sirènes d'un *globish* laxiste, je voudrais remercier un certain nombre de personnes qui ont contribué à l'excellent déroulement de ces quatre années.

Commençons donc par le plus facile : Eddy mérite les plus amples remerciements, lui qui a été moteur en toutes choses. J'ai tout particulièrement apprécié le fait de trouver un interlocuteur zen, patient et dépourvu de condescendance (une qualité plutôt rare par les temps qui courent), ainsi qu'un scientifique de haut vol à l'ouverture d'esprit remarquable. Au-delà, j'ai beaucoup appris de nos looongues pauses café mêlant physique shadok (plus ce sera compliqué, plus cela aura de chances de marcher !), dettes abyssales envers la machine et destruction de feutres. On aura aussi massacré des zombies en surcharge pondérale (incarnations de referees obtus ?), bu quelques pintes aux quatre coins du globe, et déchiffré nombre de codes mathematica "fluctuv82" avec en toile de fond, "J'ai trouvé la solution en nageant hier soir !". Une façon idéale de faire de la recherche, en somme.

Il me faut ensuite mentionner les collègues de l'équipe UBT : du côté des permanents, Henri Godfrin, infatigable conteur, et Andrew Fefferman, qui a été un interlocuteur de choix lorsque j'effectuais mes mesures de dissipation. Quant aux *autres*, eh bien...j'ai une pensée particulière pour Martial "Fokker-Bank" Defoort, qui m'a guidé pas à pas lorsque je n'étais qu'un bleu prétentieux et ignorant. En outre, je ne puis passer sous silence les concerts de salon *avec des ballons* et l'accueil californien, entre autres. Viennent ensuite Rasul Gazizulin et Xin "Go to the hell!" Zhou, avec qui j'ai plus ou moins directement travaillé, pour l'enrichissement culturel indéniable consistant à savoir jurer indifféremment en russe ou en chinois à une heure avancée de la nuit. Enfin, merci et bon courage à ceux qui y sont encore, Annina, David, Dylan, Sumit, et ceux qui y étaient : Ketty, Ana, Yuriy, Ahmad mais aussi Kunal dont l'aide concentrée sur une semaine et un coup de téléphone en particulier m'auront été très précieux.

Au cours de ces quatre années, j'ai notamment pu apprendre à *bidouiller* un peu mais aussi à apprécier le travail en salle blanche, ce qui aujourd'hui encore ne cesse de m'étonner. Ces progrès sont à mettre au crédit du personnel technique de l'Institut Néel : à l'électronique, Christophe Guttin, Olivier Exshaw, Guillaume Brès et Jean-Luc Mocellin m'ont sorti d'affaire plus d'une fois, et Christophe Hoarau et Daniel Lepoittevin ont été d'agréables compagnons d'enseignement. Je remercie également l'ensemble de l'équipe de Nanofab pour toute l'aide fournie, en particulier Thierry "le magicien" Crozes et Jeff Motte pour les trésors de patience déployés lors de ma formation à la litho électronique. A la cryogénie, je remercie Sébastien Triqueneaux, Guillaume Donnier-Valentin, Anne Gérardin et Olivier Tissot. En outre, j'ai largement bénéficié de discussions, scientifiques ou non, avec des chercheurs d'horizons divers : citons parmi d'autres l'ensemble de l'équipe TPS/pôle capteurs et tout particulièrement Olivier Bourgeois, mais aussi Olivier Arcizet, Benjamin Pigeau, Ben-

jamin Besga, Clemens Winkelmann, Philippe Roche, Elsa Lhotel, Franck Balestro, Panayothis Spathis, Florence Lévy-Bertrand, Etienne Wolf, Nicolas Roch, Klaus Hasselbach, Pierre Verlot, Jukka Pekola qui m'a accordé le temps nécessaire pour finir mon manuscrit tout en commençant le post-doc et Mark Dykman pour un échange rapide mais ô combien crucial. Je remercie également les membres de mon jury : Olivier Bourgeois qui a accepté d'en être le président, Adrian Bachtold et Andrew Armour pour avoir accepté de relire ce manuscrit un tantinet *épais*, ainsi que Eva Weig, Pierre-François Cohadon et Signe Seidelin pour une séance de questions très stimulante.

J'ai eu la possibilité d'enseigner pendant deux ans à Phelma. Pour cela, je tiens à remercier Jean-Christophe Toussaint, Julien Poëtte, Nicolas Ruty, Aurélien Kuhn et David Riassetto, pour n'avoir jamais été avares en conseils et m'avoir permis de relativiser quant à la difficulté de la tâche.

Mais ce n'est pas tout ! Le chemin de croix avait à peine commencé que le sort m'avait fait croiser la route de deux compagnons d'infortune toute relative, eux aussi à l'aube de leur voyage scientifique, mais qui avaient en plus l'avantage d'être très proches géographiquement de ma caverne sous pompage, ce qui avouons-le est pratique lorsqu'il s'agit par exemple d'organiser une rando calamiteuse en Chartreuse : Adib (*beauté de la science !*) et Clothilde, vous avez été géniaux, que ce soit au labo, en montagne, à Bordeaux ou dans quelque rade Grenoblois. Il me tarde de parcourir l'Iran avec vous.

Bien sûr, en termes de proximité géographique, je ne peux oublier Karim et Ketty (encore !), qui m'ont accueilli royalement lors de mon passage express pour la soutenance et avec qui j'ai découvert Prague, Marine et Yann pour une escapade celtique bienvenue, Mathias pour les badinages à rallonge devant ma salle de manip', mais aussi et sans aucun ordre particulier Gogo, Artaud, Sylvain, Emilie, Valentin, Clément, Begüm, Jessy, Tiphaine, Céline, Elie, Laura, Alexis, Rémy, Victor, Vadim, et tous les autres, pour les séances de nanars, les barbecues, les séminaires non-permanents, les cafés, etc. Je n'oublie pas non plus le noyau dur des Grenoblois de la vieille époque, avec une mention spéciale à Eymeric et Loïc pour nos péripéties musicales et Elie avec qui nous avons probablement fait exploser les recettes de tous les cinémas de la ville. Si mon séjour prolongé à Grenoble fut à ce point agréable, c'est en grande partie grâce à vous tous. Sachez qu'un canapé sera toujours à disposition s'il vous vient l'idée saugrenue de vous aventurer au nord du monde.

Enfin, merci à ma famille, qui m'a suivi à distance toutes ces années et m'a toujours soutenu dans ce que j'entreprenais, et enfin à Laure sans qui rien ne serait pareil.

Contents

Chapter 1

General Introduction

Contents

1.1 Nano-electro-mechanical systems: sensors and versatile platforms for basic research

Fundamental experimental research, by definition, relies on the most sensitive detectors: this ranges from subatomic physics, where ongoing discoveries of new particles make use of state-of-the-art calorimeters, to general relativity, where one major milestone was the recent observation of gravitational waves predicted almost a century ago thanks to ultrasensitive interferometers [1], not to mention superconducting circuits for quantum-limited detection of extremely small electromagnetic signals [2], to name a few. These tremendous achievements go hand in hand with endless detector improvements, which further grow into research topics on their own, as in the case of optomechanics which expanded along with gravitational wave detectors [3, 4]. Among these instruments, **Micro-Electro-Mechanical Systems** (**MEMS**) are probes of choice: they are transducers of electrical signals into mechanical ones (and vice-versa) with very low masses, due to their small volume (at least one of their dimensions is in the µm range), which permits extreme sensitivities. They are now most conveniently used as biosensors or as accelerometers in cars or cellphones, but along these technological aspects they also present a fundamental interest for the physicist, as their small dimensions make them sensitive to forces that manifest only on small length-scales, such as the Casimir force originating from quantum vacuum fluctuations [5], or possible deviations to Newtonian gravity [6]. Even more appealing is the possibility offered by tremendous progresses in nanofabrication over the last decades, which have put **Nano-Electro-Mechanical Systems** (**NEMS**, having at least one sub-micronic dimension) within reach at the end of the 1990's [7, 8]. Since then, nanomechanics has extended its range to smaller and smaller systems that are now atomically thin, like

e.g. graphene and carbon nanotubes [9]. While industrial applications for such objects are still not widespread, they do push further sensitivity limits that allow to probe even smaller lengthscales previously out of reach for MEMS: an example is a 150 nm long carbon nanotube used as a mass spectrometer which enabled the detection of adsorption events of naphtalene molecules with a yoctogram resolution [10], that is, at the proton level (see Fig. 1.1 upper left corner).

Not only NEMS are suitable sensors, they have also proven ideal, versatile **model systems** for fundamental studies. At the most basic level, a vibrating NEMS simply is a macroscopic mechanical degree of freedom, and possesses modes of vibrations that depend on the structure's geometry. Each one of these modes is at first order a harmonic oscillator, but it can be pushed further to display a more subtle behaviour: a resonator undergoing a strong mechanical excitation can display a non-linear behaviour [11], adding a great deal of complexity. Thus, because of their relative simplicity of use, they are suitable to study in the non-linear regime e.g. bifurcation phenomena or chaotic dynamics [12, 13]. As mechanical modes are coupled to their environment, they experience also position fluctuations, which are of interest when a non-linear interaction mixes them with a deterministic motion. As such, they are interesting testbeds for statistical physics, in and out of equilibrium [14, 15]. The fluctuations, that is, Brownian motion, are also representative of a mode's thermal occupancy, that can be for instance removed to cool this oscillator down to its ground state of motion. This quest was first pursued by the close field of opto-mechanics, where mechanical motion is detected and controlled by light fields, and where light confined in a cavity with a movable mirror can be used to cool down the mirror's mechanical motion (in the sense of having its thermal occupancy lowered) [3, 16, 17]. The experimental tour de force consisting in reaching the quantum regime, as far as electrical means are concerned, was demonstrated a few years ago in Ref. [18] (see Fig. 1.1 upper right corner) with passive cooling of a GHz resonator in a dilution refrigerator, and in Ref. [19] with microwave sideband cooling of a thin membrane capacitively coupled to a quantum-limited detector (see Fig. 1.1 lower left corner). These impressive achievements are first steps towards systematic studies of the elusive quantum coherence of macroscopic mechanical degrees of freedom, addressed theoretically for MEMS and NEMS in e.g. Refs. [20, 21], in relation with fundamental theories on decoherence of position states or wave function collapse associated with a quantum measurement. Those very fundamental purposes force to ask ourselves what is truly quantum in a measurement [22]. In that regard, recent works highlight the formal analogies that can be made between coherently driven quantum two-level systems and classical coupled nanomechanical modes [23, 24], showing that the answer is less trivial than it may seem at first glance (see Fig. 1.1 lower right corner).

The race towards efficient and reliable quantum opto- and electro-mechanical systems obviously requires a good mastering of the resonator's environment, hence a good understanding of it: these macroscopic model systems are coupled to micro-

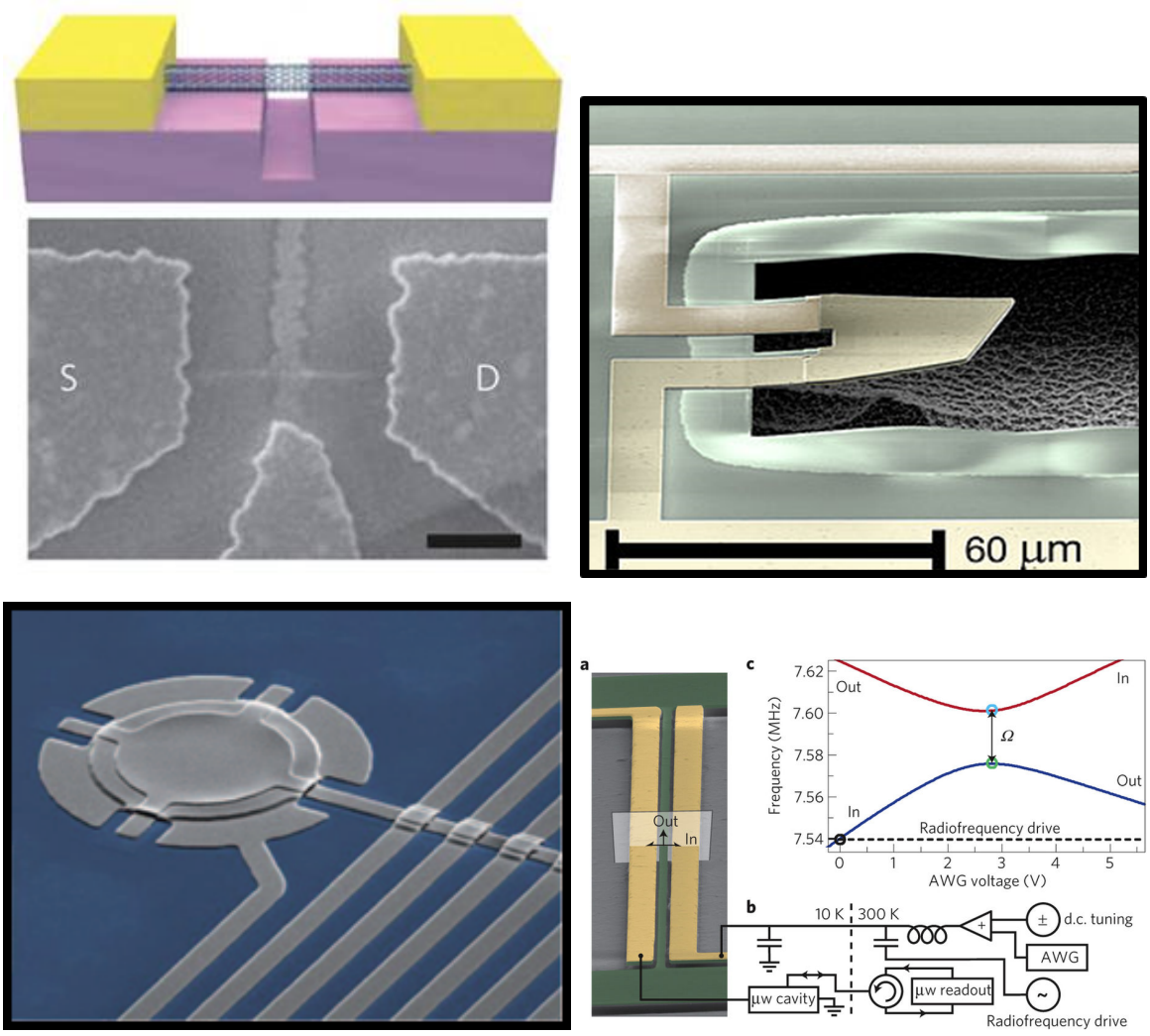

Figure 1.1: upper left: suspended carbon nanotube used in Ref. [10] where a yoctogram resolution is reached in mass sensing, through measurements of naphtalene molecules adsorption on the nanotube and xenon binding energy. Upper right: piezoelectric GHz device cooled down passively to a base temperature of 50 mK [18]. A compression/dilatation mode is measured in its quantum ground state and coherently controlled at the single phonon level through capacitive coupling to a phase superconducting quantum bit circuit. Lower left: MHz "drum" membrane capacitively coupled to a superconducting LC circuit [19] acting as a microwave cavity. One mode is selectively cooled down in its quantum ground state by driving the cavity with a tone detuned to lower frequencies (on the "red-detuned sideband"), where the detuning is equal to the mechanical frequency. Then energy is pumped out of the mechanical mode thanks to an equivalent opto-mechanical coupling: the circuit capacitance is modulated by thermomechanical motion. Lower right: silicon nitride nanobeam with two flexural modes of different families coupled through capacitive actuation, forming an effective classical two-level system, where usual NMR and quantum information-like operations (e.g. Rabi pulses or Hahn echo) can be reproduced [24].

scopic degrees of freedom towards which mechanical energy flows in an irreversible way, limiting in the first place mechanical coherence. But low temperatures allow to selectively turn off uncontrolled degrees of freedom, leaving only a few possibilities that can be addressed readily, be it the damping by a surrounding fluid or intrinsic low energy excitations arising from defects in the constitutive materials of the NEMS. In itself, it turns out to go beyond the focus on NEMS: the issue of two-level systems in amorphous materials is a long-standing problem [25] that is still lacking of a compelling evidence as to whether they even exist or not in all glass-like materials. In that regard, a NEMS, with reduced dimensions, is a suitable condensed matter probe to bring new insights into the field [26, 27, 28].

1.2 Context and structure of this thesis

This thesis deals with both model systems aspects and microscopic ones. Several subfields of physics are invoked, and yet, one common feature is noticeable: in all the results reported, **fluctuations or disorder** play a role, which in the end affects mechanical damping or (classical) phase coherence. It can be a noisy signal in time, on the position or frequency, that affects the mechanical phase coherence, or it can be spatial disorder of e.g. the materials of which the NEMS is made of. To leave out possible additional difficulty, we use what is arguably the most simple vibrating structures: nanometre-scale (in their cross-dimensions) **beams**, resonating in the MHz range, which have basic properties very well described by continuum mechanics and do not require heavy simulation tools. That allows us to reach a rather high degree of analytic, quantitative modelling of our results, making discussions sharper mathematically. As such, even though the present thesis is by no means a theoretical work, we shall put a strong emphasis on quantitative modelling when it is possible.

The nano-metre scale aspect is relevant for two reasons: first, it makes the vibrating object very sensitive to non-linearities [29], and second, it allows to study the role of reduced dimensionality on dissipation mechanisms, as it is still poorly understood up to now. Besides, the results reported in this manuscript are obtained at low temperatures, ranging from 30 K at most to 10 mK, with a good accuracy above typically 30 mK. However they do not restrict to low temperature physics in their nature. Most of the time, a low temperature is convenient mainly because it guarantees a high level of environment control and reproducibility. Besides, some signatures, such as the Knudsen layer reported in Chapter 5 or the TLS-induced damping described in Chapter 6 would not manifest clearly at room or even liquid nitrogen temperatures. Finally, we point out that while some of our experiments can call for further developments in the quantum regime, and though the damping issue has a direct impact on the feasibility of quantum-limited experiments, our apparatus is **classical**, and our treatment of the various problems will mostly remain at the classical level, with the exception of

Chapter 6, where we must on occasion invoke quantum tunneling of two-level systems to explain the microscopic origin of damping in our structures.

The manuscript is organized as follows: the first Chapter aims at setting the experimental and theoretical grounds useful for the rest of the manuscript. It reports our calibration procedures in a high-impedance environment and some techniques, e.g. clean room fabrication, low temperature settings or the NEMS actuation and detection technique. As such, it is rather detailed for the interested reader but does not introduce new results. Therefore the experienced reader can skip it at first reading.

The first part of the results obtained in this thesis deals with the model system aspect, at a purely macroscopic scale. In Chapter 3, we provide an in-depth study of the frequency noise originating from position fluctuations, that are translated as frequency noise through intrinsic geometric non-linearities. Though it has been reported qualitatively over the last few years [30, 14], it had not yet been completely elucidated, and we show that its full explanation is rather involved, producing an analytic model based on Ref. [31] which reproduces our data. Besides, it can be a major limitation as for the performance of some devices like e.g. carbon nanotubes [32]. This is mainly what is reported in Ref. [33], with a greater attention paid here to theoretical aspects based on the analysis of Ref. [31]. We show also preliminary results obtained in the case of a strongly driven NEMS, where position fluctuations themselves get altered and their dynamics is slowed down by the back-action of the strong drive.

The mechanism studied in Chapter 3 does not involve further energy exchanges, and yet it broadens our resonance lines. As such it can be understood in the framework of decoherence, here seen from a purely classical perspective. In Chapter 4, we build on the analogy by comparing time and frequency domain measurements of the mechanical response in the non-linear regime and under the influence of external, gate-controlled frequency noise, extracting energy relaxation and phase coherence times in analogy with Nuclear Magnetic Resonance. It reports and goes a little beyond the work done in Ref. [34].

The second part of this thesis focuses more on the microscopic degrees of freedom to which our macroscopic mechanical mode couples. In Chapter 5, we investigate first extrinsic sources of mechanical damping due to a surrounding cryogenic Helium gas, by deliberately injecting gas in the cell. The aim is twofold: while attempting to measure intrinsic damping, we must first remove other external sources. But it is also a preamble to more involved studies of quantum fluids such as superfluid ^{3}He. We report on the first measurements by a nano-mechanical probe of the controversial Knudsen layer, which were published in Ref. [35], and discuss the mechanisms behind its existence, as reported in Ref. [36].

Once this external source is well characterized, we focus on intrinsic sources of damping in Chapter 6, by measuring it down to millikelvin temperatures. We interpret our results within a framework adapted from the long existing so-called Standard Tunneling Model (STM) [25, 37], to the case of a nanomechanical beam with reduced

dimensions and suppressed phononic channels, building on different approaches to damping proposed by Refs. [38] and [39]. In addition, we develop a sensitive technique to measure intrinsic frequency noise in bistable resonators, as reported in Ref. [40]. We use it at 4 K and at dilution temperatures, highlighting the link between intrinsic frequency fluctuations and damping due to low-energy excitations.

Chapter 2

Experimental and theoretical tools

Contents

2.1 Introduction

The first Chapter of this thesis is essentially technical: it aims at providing the basic resources that are useful to understand the results presented further. In the first section, nanofabrication techniques are described. Then, experimental techniques such as cryogenics, the magnetomotive scheme or lock-in amplifier measurements, that are common to many experiments are reported. Finally, a comprehensive calibration of our devices is detailed: it involves common basic and simple theoretical tools such as beam mechanics, electronics and thermal diffusion models. Some extensions to non-linear theories are considered, as they are ubiquitous in our studies. These calibrations enable us to obtain quantities in real units, such as forces in newtons and displacements in meters, which is not a trivial task when it comes to vibrating nanostructures.

In the following, we put the emphasis on having measurements and theory as close as possible, with none or minimum free parameters when needed. We believe that it provides a solid basis to explain quantitatively more subtle results that are presented further. As this calibration procedure has been already described earlier in Refs. [41, 42] for cantilever structures, some details are overlooked, especially when no difference exists whether we use a cantilever or a doubly-clamped beam, or when they concern only cantilevers. As a proof of robustness of our calibration, we show measurements of parametrically amplified motion, which require that every calibration step be validated to be reproduced accurately by theory.

On a more technical note, while experimental frequencies f are in hertz (Hz) units, in the text we use angular frequencies $\omega = 2\pi f$, in rad.s^{-1}, as they appear more naturally in theoretical descriptions, but values are given in Hz units.

2.2 Fabrication of suspended vibrating nanostructures

All devices presented in this work have been designed and developed in the nanofabrication facility (Nanofab) at Néel Institute. They only rely on mature and reproducible top-down fabrication techniques. We give here an overview of the general process, as further developments are only specific to single experiments.

The basic process only requires one lithography step on a 1 cm^2 silicon substrate covered with a 100 nm thick silicon nitride film with a Young's modulus $E_{\mathrm{SiN}} = 250 \pm 150$ GPa and a chosen stored stress value. The latter is obtained through differential contraction between the silicon substrate and the grown nitride thin film. Typical internal tensile stress values for NEMS involved in this work are 100 MPa, 0.9 GPa, 1.1 GPa with a typical error bar $\pm$ 0.05MPa.

Sample design

While the nanomechanical strucure is itself small, one needs to design an environment that allows to address its motion with electrical means. Thus, as seen in Fig. 2.1, the NEMS is connected to electrodes that are large enough so that 1) their electrical resistance is negligble and 2) one can microbond electrical wires on it. Two electrodes are designed on each side of the NEMS (one side is connected to the ground), so one can perform four wire measurements. Clamps, as well as tracks connecting the NEMS to the electrodes, must be wide enough (at least 20 µm) so that they do not collapse during the etching step (see below).

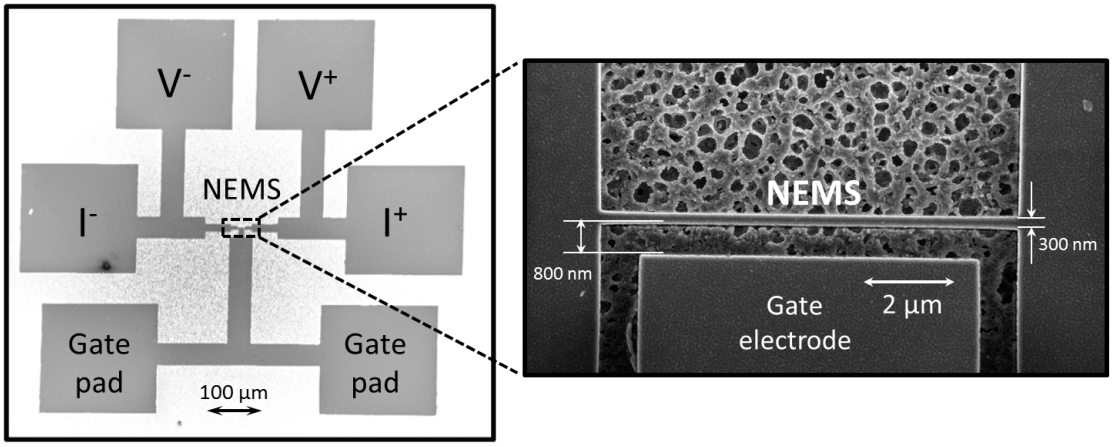

Figure 2.1: left: global picture of a typical nanofabricated sample measured in this thesis. Each pad is annoted according to the bonding scheme. Right: zoom on the central part, with a Scanning Electron Microscope picture of the NEMS. The beam is here 10 µm long, with a gate electrode designed in its vicinity (see Section 2.8.3). Note the spongy silicon bottom, which is a consequence of XeF_2 etching.

Electron beam lithography

To allow selective etching of the structure a mask needs to be deposited. This mask will define the structure around which the wafer will be etched, while functionalizing the device for electrical control.

To do so, after cleaning the wafer with acetone or isopropanol (IPA) we first deposit a thin layer (about 100 nm) of polymethyl methacrilate (PMMA 4%) resist on top of the wafer. To obtain a uniform layer, the coated wafer is spinned at 6000 rows per minutes speed for 30 second, then baked at 180 °C for 5 minutes. Note that the resist thickness to be used depends on the metal thickness to be evaporated. It must be thick enough to clearly discriminate insulated parts from non-insulated, but not too thick so that e-beam insulation diffuse over the whole resist depth.

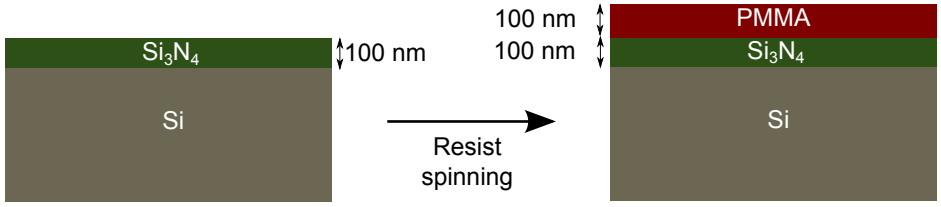

Figure 2.2: the initial wafer, made of bulk silicon with a thin film of stressed, amorphous silicon nitride, is coated with a PMMA resist, made uniform by spinning and baking.

After resist deposition, the resist coated wafer is patterned through electron beam lithography performed with a Scanning Electron Microscope (SEM): the resist is selectively insulated with a beam of electrons accelerated at 20 keV, which then diffuse into the resist. With this voltage value patterning can reach a resolution down to 30 nm for light electron doses and small SEM apertures. Typical doses used in this work are about 250 $\mu C/cm^2$, which is enough to guarantee such a resolution. The insulated resist is then put in a mixture of methyl-isobutyl-ketone (MIBK) and IPA for 35 s, then in IPA for 1 min. This removes the insulated parts.

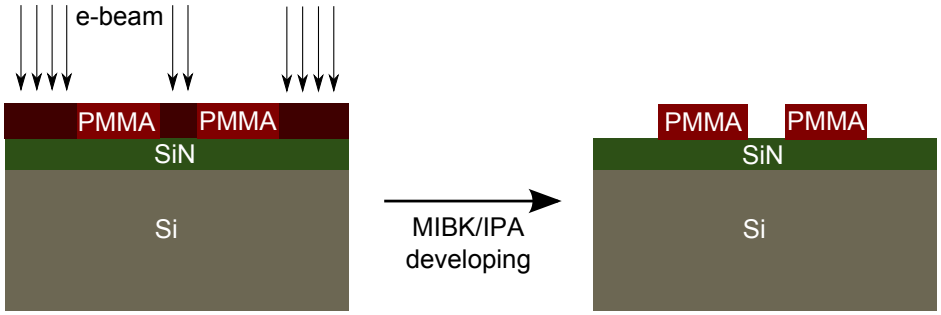

Figure 2.3: schematics of the electron beam lithography step, with darker red representing the insulated parts of the resist, removed after developing in MIBK/IPA.

Metallic layer evaporation and resist removal

The mask is obtained by evaporating a metal (in this work, aluminium) in a vacuum chamber. The evaporation is triggered by e-gun bombarding of a metallic crucible. The evaporated metal sticking on the nitride film is organized in crystalline grains of typical size 20 nm at a deposition speed of 0.1 nm/s in a typical vacuum of 10^{-6} Torr, but this can be tuned with an appropriate choice of deposition speed: a faster evaporation will result in bigger grains, hence bigger grain boundaries. To be as sensitive as possible to the nitride properties, we evaporate a layer of typical thickness 30 nm, which is significantly thinner than the nitride layer and at the same time thick

enough to ensure that the metallic layer is continuous (conducting) over the whole sample area.

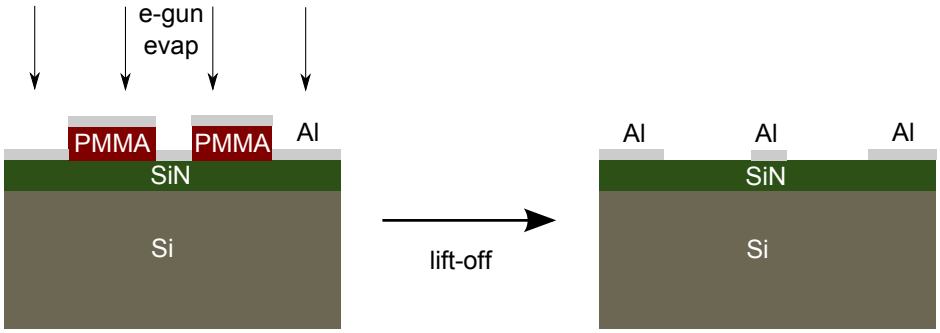

Figure 2.4: schematics of the evaporation and lift-off steps.

The result is displayed in Fig. 2.4. While the aluminium sticks on the SiN where lithography was performed, the other parts, sustained on resist, will be stripped off with the resist. To do so, the wafer is left in N-methyl-2-pyrrolidone (NMP) at 80 °C for at least an hour, and is occasionally shaked with weak ultrasound waves. In addition, after this, the wafer can be put in acetone to enhance the removing. After cleaning with ethanol and deionized water, the result is now a wafer covered by a mask on the parts where the nanostructures will be processed.

Etching steps

Once the functional parts are delimited, they must be released from the silicon bulk to be able to vibrate. First the SiN layer is attacked throughout a 2 min 30 sec Reactive Ion Etching (RIE) step with a sulfure hexafluoride plasma (SF_6). While being very selective (it does not attack aluminium), it is also very anisotropic, which allows to dig as vertically as possible. However, it is not very effective for silicon under-etching, which is limiting if we pattern long nanobeams or if we want huge gaps between the nanobeam and the bottom.

Our solution to etch the silicon part with better efficiency is to use a Xenon fluoride (XeF_2) gas. This allows us to selectively etch silicon over considerable thicknesses, as schematically depicted in Fig. 2.5 (right panel). The etching is very isotropic, thus releasing the beams. However, this also results in a so-called undercut, that is an etching of the silicun underneath the clamping electrodes. This limits our possibilities, as undercuts bigger than typically 20 µm might make the structure collapse. This is also the biggest gap between the beam and the bottom allowed by the straightforward use of this technique. Note that to etch deeper, more sophisticated processes must be developed, as in Chapter 5.

A puzzling feature observed on most of the fabricated samples is that the metallic layer gets sometimes "polluted" with fluor, which corrupted the electrical and mechan-

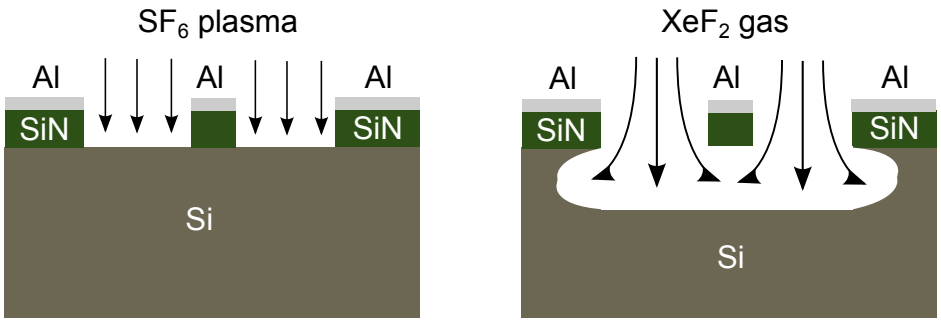

Figure 2.5: left: reactive Ion Etching of the structure, selectively removing the exposed nitride layer. Right: Xenon Fluoride etching of the exposed silicon layer.

ical properties of the nanobeams when occuring. We therefore remove the metallic layer with melanine-formadehyde (MF-26) after etching, and re-evaporate the metal following the standard procedure, but without any mask (full field evaporation).

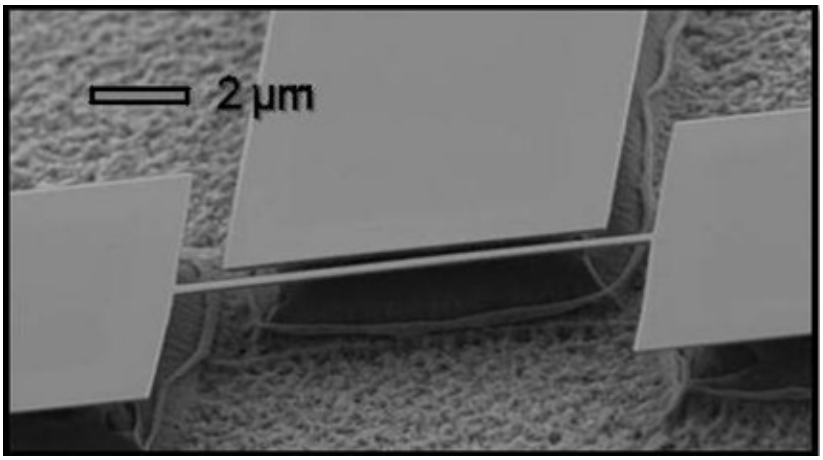

Figure 2.6: tilted SEM picture of a nanofabricated NEMS of dimensions 15 µm long × 130 nm thick × 300 nm wide. The SiN thickness is 100 nm, with a 30 nm Aluminium on top.

A typical NEMS obtained after the procedure described above is shown in Fig. 2.6. Note the distance between the suspended beam and the bottom. The significant undercut as well as the spongy nature of the bottom are consequences of the XeF_2 etching. The whole process is very reproducible, with well-controlled dimensions: the typical error on the SiN film dimensions is at most 5 nm, while the e-gun evaporation leads to at most a few nanometers error on the evaporated aluminum thickness monitored through the e-gun machine.

2.3 Cryogenics and thermometry

2.3.1 Measurements at liquid helium temperatures

A significant part of the results reported in this manuscript have been obtained at moderately low temperature on a standard liquid ^{4}He bath cryostat. Multiple reasons explain this choice, compared to room temperature measurements:

- From a practical point of view, high magnetic fields can be generated with small coils made of conventional superconductors, which is helpful if we use the magnetomotive scheme (see Section 2.6.2).
- The electrical environment is less noisy, resulting in much cleaner measurements. In addition, since measurements are performed well below the Debye temperature, we are not sensitive (or limited) by phonon-phonon scattering processes that are responsible for additional damping [43]. In particular, we resolve the low energy excitations which couple dissipatively to the mechanics (see Chapter 6).
- We have cryogenic vacuum for free, with residual pressures below 10^{-6} mbar. This greatly reduces the gas damping for the NEMS, while ensuring negligible outgasing.
- Thermal contraction/expansion is much smaller, almost inexistant. Therefore dimensions and internal stresses of our devices are well defined.

The sample cell is mounted on a stick, with its upper part fixed to a room temperature flange, and its lower part fixed to a solenoid coil, used as a magnet for our experiments. The room temperature flange integrates connectors for thermometers and coil wiring, two injection and two detection lines, and one gate electrode line.

The sample holder is a bulk copper piece, designed so that a plastic circuit board (PCB) can be screwed on it. The wafer is glued to this PCB with General Electric (GE) varnish, then electrically connected to it through microbonding wires from the PCB copper tracks to the designed pads (see Fig. 2.2). A carbon resistor is mounted at the back of the copper piece for thermometry in the Kelvin range, as well as a 100 Ω resistor used as a sample holder heater. A picture of the actual sample holder is shown in Fig. 2.7.

The sample holder is joined together with the upper part of a stainless steel cell, on which connectors allow to pass currents from the top of the stick through coaxial cables. This upper part of the cell is soldered to a pumping line. The lower part is large enough to nest the sample holder while fitting the inner diameter of the coil. Before cooling the experiment, the two cell parts are joined and sealed with indium wire, and the closed cell is pumped down to 10^{-4} mbar. Lower pressures, below 10^{-6} mbar,

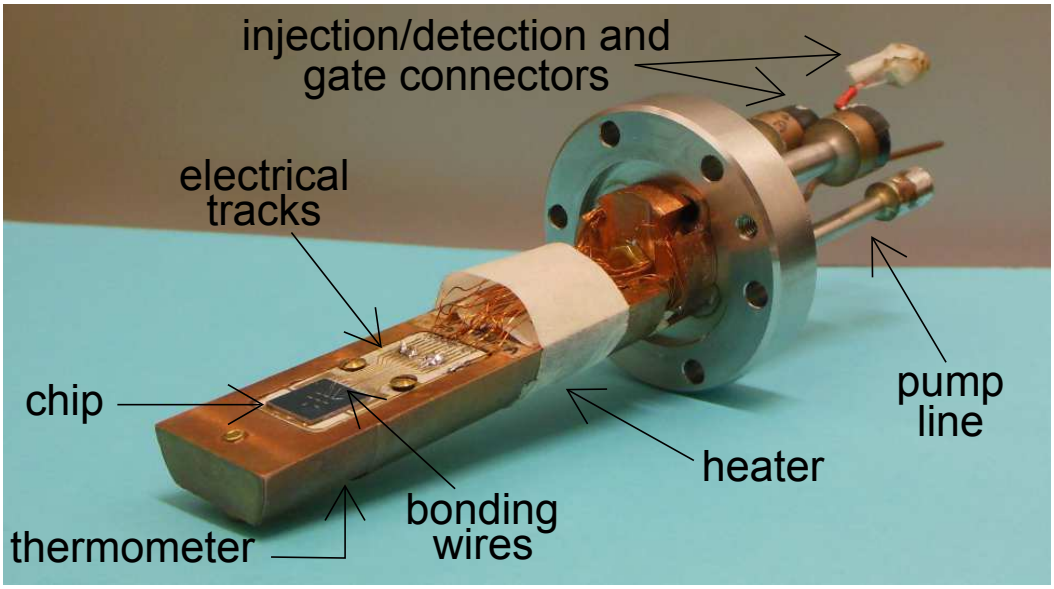

Figure 2.7: picture of the sample holder, a copper rod connected to the upper flange of the cell. A typical chip, containing several samples, is glued on the finger.

are reached through cryo-pumping during the cooling process, with the remaining gas being adsorbed on the cell's walls. The temperature is measured by a platinum resistor mounted on the stick down to 77 K by 4-wire measurements, while the carbon resistor mounted on the sample holder measures temperatures down to 1 K using a home-made (PID) balanced bridge technique. The same technique can be used to regulate the sample holder temperature up to 30 K.

The cryostat itself simply consists of two concentric stainless steel cans separated by a vacuum partition. The outer reservoir is filled with liquid nitrogen at 77 K, which precools the inner bath. The latter is then filled with liquid helium to cool down the experimental cell to 4 K. From then on, the liquid nitrogen bath protects the helium part from thermal radiation at 300 K, which reduces the helium evaporation rate. The typical working temperature is that of liquid helium, 4.2 K. However, one can heat the sample to higher temperatures as mentioned above, or cool the whole bath by pumping on helium vapour in the bath. By doing so, one shifts the vapour-liquid equilibrium at the surface down to lower temperatures, following the transition curve in the P-T diagram. Temperatures down to 1.4 K can be obtained with this method, which allows one to go below the superfluid transition occuring at 2.17 K and thus study dissipation or dispersion phenomena linked to ^{4}He superfluidity (see Chapter 5). However, due to the dramatic increase in helium heat capacity around the transition temperature, almost half of the helium bath is evaporated in the process, which limits the duration of a continuous experiment below 2.17 K to about a day.

2.3.2 Measurements at dilution temperatures

A brief overview of dilution refrigeration

While obtaining cryogenic temperatures above 1 K is rather straightforward at Néel Institute, it is much more demanding to reach temperatures in the mK range. This can be achieved with a dilution refrigerator, which takes advantage of the mixture properties of ^{3}He and ^{4}He to reach temperatures down to $5 - 10$ mK. Detailed descriptions and discussions can be found in reference books, e.g. Refs. [44] and [45]. Here we will simply give an overview, with a schematic drawing shown in Fig. 2.8, left panel, along with a picture of the cryostat we used (right panel).

While our laboratory has a long standing tradition in the development of dilution cryogenics, our experiments have been carried out on a commercial machine. The BlueFors cryostat used in this thesis uses a pulse tube cooler to cool and maintain the environment around the dilution stage at 3 K. Thus, as opposed to the usual, "wet" cryostat no liquid helium is required to keep the experiment cold. First, to limit heat leaks, the environment (called "calorimeter" or "vacuum jacket") is pumped down to below 10^{-3} mbar, while the dilution unit is protected by a series of thermal screens screwed to the upper parts of the dilution cryostat to minimize heat radiation.

Once the cryostat is pre-cooled down to 3 K, the mixture is condensed by a compressor at 2 bar, then goes into the dilution circuit. Below 870 mK, the mixture separates into two phases: one is concentrated in ^{3}He, while the other is ^{3}He diluted in ^{4}He. Below 200 mK the concentrated phase is almost pure ^{3}He, while the dilute phase has a fixed ^{3}He concentration of 6.4 %. This separation occurs in the **mixing chamber** (MxC), which is the coldest part of the dilution unit. As ^{4}He is heavier, the dilute phase lies beneath the concentrated phase. A pumping line connected to the distiller enables to circulate the mixture. The distiller itself is connected to the mixing chamber through a line that opens in the dilute phase of the mixing chamber.

With the still under pumping and at a higher temperature, an osmotic pressure gradient is created along the pumping line, which makes ^{3}He atoms go from the bottom of the mixing chamber up to the still, where mainly ^{3}He is evaporated, due to a higher saturated vapour pressure than ^{4}He. To maintain the concentration in the dilute phase at the mixing chamber level, ^{3}He has to move from the concentrated to the dilute phase. This process relies on the different quantum properties of the two phases and is at the very core of the dilution refrigeration process. Indeed, liquid ^{3}He is a Fermi liquid, with each atom having an effective mass renormalized by its interactions with the other atoms. In the dilute phase, superfluid ^{4}He acts as a vacuum background for diluted ^{3}He atoms, which are then much less interacting in this phase: their effective mass is closer to the bare mass. Therefore, ^{3}He somehow "prefers" to be in the dilute phase and the transfer from one phase to the other is endothermic, hence the cooling.

At the still level, ^{3}He will be pumped outside the still and will go back to the mixing chamber via an injection line. The cooling power $\dot{Q}$ is proportional to the ^{3}**He**

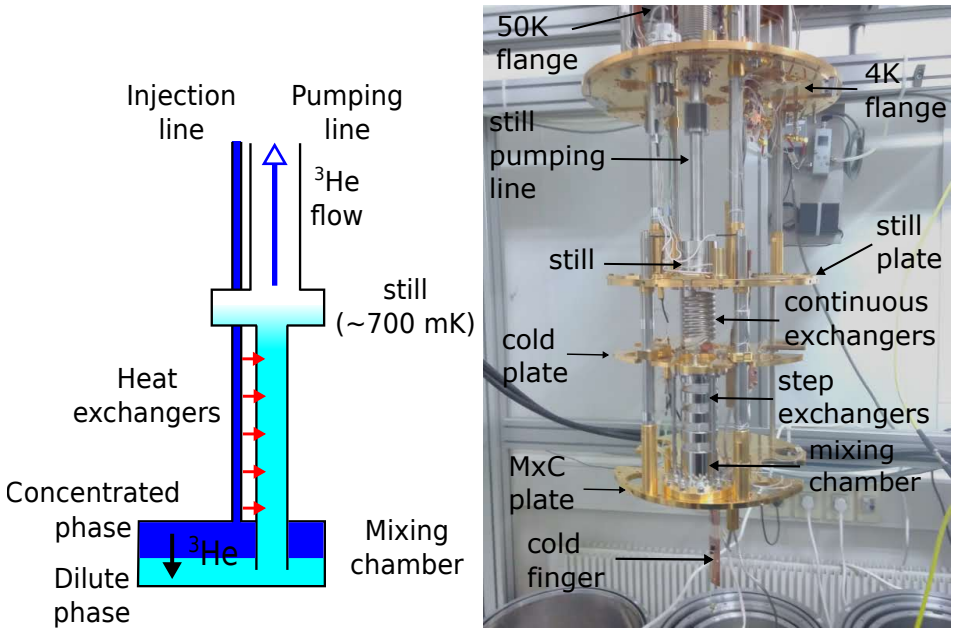

Figure 2.8: left: schematic basic operating principle of a dilution unit. Right: overview of the Bluefors dilution unit used for our experiments.

flow rate in the pumping line, $\dot{n}_3$, which is about a few hundreds of µmol/s, and to the enthalpy difference between the two phases present in the MxC. It writes, as a function of the temperature at the phase interface T_{mix} [44]:

$$\dot{Q} \approx 83\dot{n}_3 T_{mix}^2. \tag{2.1}$$

It then depends on the heating power applied to the still, which regulates the flow through the evaporation temperature in the range 500 mK − 1 K. To keep the dilution unit functional over time, the circuit is operating in closed cycle. Once pumped out of the still, the evaporated mixture goes outside the refrigerator, through the pumping system and a liquid nitrogen trap to prevent impurities to block the injection line, and is then re-injected in the cryostat. In the injection line, the mixture recondenses through an impedance while undergoing a Joule-Thompson expansion, and is thus cooled down to 1 K, this cycling playing the role of the usual 1 K pot used in wet cryostats. It is thermalized while going back to the mixing chamber through heat exchangers that thermally connect the condensing line to the pumping line all the way between the mixing chamber and the still.

With the dilution unit operating, our refrigerator can reach 7 mK within 48 hours. Note that it is possible to heat the mixing chamber stage with a resistance, with heating powers in the mW range. Temperatures up to 1 K are reached, and higher temperatures are possible if one turns off the turbomolecular pump on the pumping

line, as the flow through the pumping line increases a lot with the still temperature increasing.

Experimental setup

While having a 4 K environment for the NEMS is easily achievable, ensuring a good thermalization of the device especially below 100 mK is a difficult task. Moreover, since no exchange gas or cryogenic liquids can thermalize external leads, these must be well clamped to refrigerator parts, while also being either superconducting or very good electrical and heat conductors. This is particularly important as far as the coil used for the magnetomotive scheme is concerned: for experimental purposes, currents up to 15 A are needed in the coil, so it is vital to minimize the resulting heat loads. Note also that ramping current in the coil will result in eddy currents heating the cold finger, hence heating the mixing chamber. A reasonable ramp speed chosen is 10 mA/sec: for this range eddy currents do not heat much the mixing chamber stage, which goes quickly back to its base temperature. The magnet coil is made of niobium titanium and generates a magnetic field of 58 mT/A, uniform at the cm scale. The actual coil setup, mounted on the still thermal screen, is shown in Fig. 2.9. Since this screen does not touch the mixing chamber plate, and since the PCB does not touch the coil, the mixing chamber stage is as thermally decoupled as possible from external heat loads.

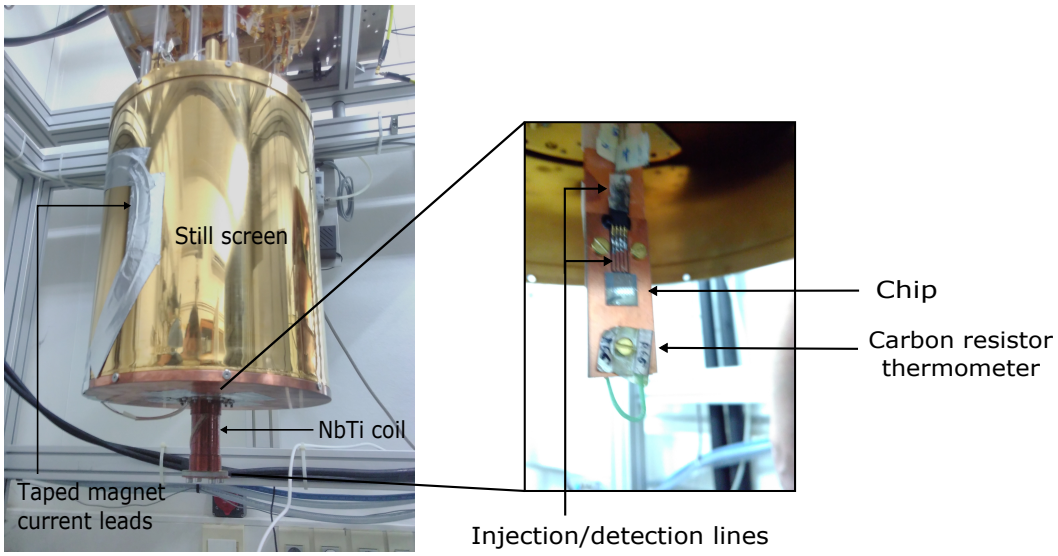

Figure 2.9: coil setup, with the still screen on and a zoom on the cold finger inserted into the coil.

As seen in Fig. 2.9, the NEMS substrate is glued on a PCB with silver paste, which ensures better heat conduction than GE varnish. A carbon resistor is also screwed at

the bottom of the PCB, which offers a thermometry point as close as possible to the NEMS. The PCB is then tightly screwed on a cold finger made of copper, which is itself tightly screwed to the mixing chamber plate for good thermal anchoring, and thin enough to fit the coil inner diameter while leaving some space. As in the 4 K NEMS setup, SMA coaxial cables are going through the entire cryostat down to the cold finger, with thermal anchors at each stage of the refrigerator. These cables are superconducting below 8 K, which limits significantly heat loads carried by our NEMS driving currents on the mixing chamber plate.

The current leads used to energize the magnet are made of copper until 50 K, where high T_c lines are used down to the 4 K plate. The total wiring displays resistances of about 0.1 mΩ while the fridge is running. This residual resistance is most likely dominated by the leads resistance on the upper part of the cryostat, which is above 50 K. Thus, the heat load due to the coil current is negligible (in the most unfavorable case a few mW distributed over the still screen and mostly the 50 K zone), and does not affect directly the mixing chamber. While passing current through the coil, no significant heating or voltage increase in the coil circuit was observed throughout experimental runs.

Thermometry

On each one of the upper stages (50 K plate, 4 K plate, still, and cold plate) a resistor measures the temperature. Since these thermometers are not primary (i.e. they do not have a universal and/or explicit dependence in temperature) they must be calibrated using another (already calibrated) thermometer. Currents as small as a few nA are used, so they do not constitute a significant heat load. These resistors are measured with a home-made resistance bridge (TRMC2) through properly filtered lines. Temperatures as low as 10 mK are thus measurable.

On the mixing chamber, four resistances are connected, made either of Ruthenium Oxide or carbon. A carbon one is directly attached to the cold finger, and is well calibrated down to 10 mK where it saturates. This resistance is monitored by the TRMC2 to regulate the mixing chamber temperature through the heater. Note that it presents a small magnetoresistance, as reported in Ref. [46], which can lead to discrepancies of at most 3 mK with another calibrated thermometer.

In addition to resistive thermometry, a noise thermometer, namely a SQUID MFFT setup from the company Magnicon, measures the temperature on the mixing chamber. While it is not directly attached to the cold finger, it is almost a primary thermometer: it measures the current noise created by the electrical environment, and the integrated noise spectrum is proportional to the temperature (Nyqvist formula). The only non-universal parameter is the noise measurement bandwidth, which does not depend on temperature. Therefore, this thermometer only needs one calibration point, for instance at 1 K where other thermometers can display a reliable temperature. Once

this calibration is done, the SQUID thermometer can measure temperatures down to at least 300 μK [47].

2.4 Modal decomposition and vibration eigenmodes

Our patterned structures are rectangular **beams**, i.e. perhaps the most simple object described in the framework of continuum mechanics. An in-depth description can be found in reference books [48, 43]. Here we will focus on the main features that are relevant to our studies.

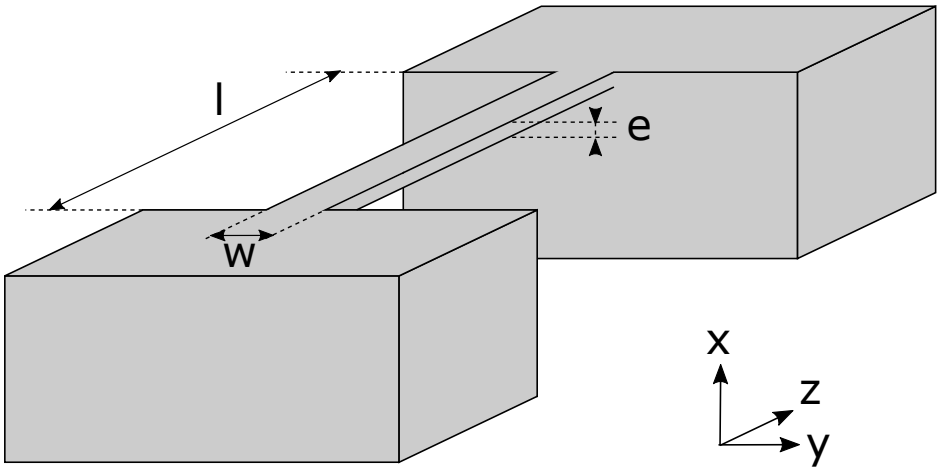

Figure 2.10: schematic clamped-clamped (or doubly-clamped) beam, with oriented axes.

Let us consider, a rectangular beam of length l, width w and thickness e with high aspect ratio, i.e. $l \gg e, w$, as shown in Fig. 2.10. We introduce its cross-section $A = w \times e$, mass density ρ (hence a total mass $M = \rho A l$), bending rigidity (Young's modulus) E, second moment of area along the displacement axis $I = we^3/12$ and in-built stress σ. Applying the least action principle to the displacement field $u(z,t)$ of the beam, one can derive the well-known Euler-Bernoulli equation [48]

$$EI\frac{\partial^4 u(z,t)}{\partial z^4} + \rho A\frac{\partial^2 u(z,t)}{\partial t^2} - \sigma A\frac{\partial^2 u(z,t)}{\partial z^2} = 0. \tag{2.2}$$

For the clamped-clamped geometry, it is clear that the displacement must be zero at each clamp. We are left with the following boundary conditions:

$$u\left(z = \pm\frac{l}{2}, t\right) = 0. \tag{2.3}$$

There is no general analytic solution to Eq.(2.2), yet we can separate the displacement

field into a simple product:

$$u(z,t) = \Psi(z)x(t). \tag{2.4}$$

The time-independent part $\Psi(z)$ is the displacement profile, while $x(t)$ represents the oscillation of the mechanical wave at a frequency ω: $x(t) = x_0 e^{i\omega t}$. By making such a separation, we use the convention that the local maximum of the profile that is nearest to the center of the beam is scaled to 1. One can distinguish two limiting cases where an analytic solution exists, depending on whether tensile stress or bending rigidity dominates in the beam.

Bending limit

In the bending (or **low-stress**) limit, the potential energy term due to stress is small compared to the one arising from the bending moment. In the vanishing stress limit, Euler-Bernoulli equation can be simplified:

$$EI\frac{\partial^4 u(z,t)}{\partial z^4} + \rho A\frac{\partial^2 u(z,t)}{\partial t^2} = 0. \tag{2.5}$$

Moreover, an additional boundary condition to (2.3) must be introduced, that of **an ideal clamp**: for pure flexure, the beam does not bend at the clamp level, which means that:

$$\left.\frac{\partial u(z,t)}{\partial z}\right|_{z=\pm\frac{l}{2}} = 0. \tag{2.6}$$

From the structure of this equation, one can introduce the following ansatz for the mode profile:

$$\Psi(z) = a_1\cosh(\lambda z) + a_2\sinh(\lambda z) + a_3\cos(\lambda z) + a_4\sin(\lambda z). \tag{2.7}$$

This ansatz can be, by construction, a solution of Euler-Bernoulli equation for particular values of wave vectors λ set by boundary conditions. Applying boundary conditions (2.3) to the ansatz displacement field, we obtain the condition on λ, which is a transcendental equation:

$$\cos(\lambda_n l)\cosh(\lambda_n l) = 1. \tag{2.8}$$

This equation has an infinite but discrete ensemble of solutions, hence the n index.

These solutions correspond to wave vectors for which the incoming and reflected mechanical wave are dephased by 2π, i.e. constructively interfere, building a standing wave: the corresponding wave vectors define the so-called **vibration eigenmodes**.

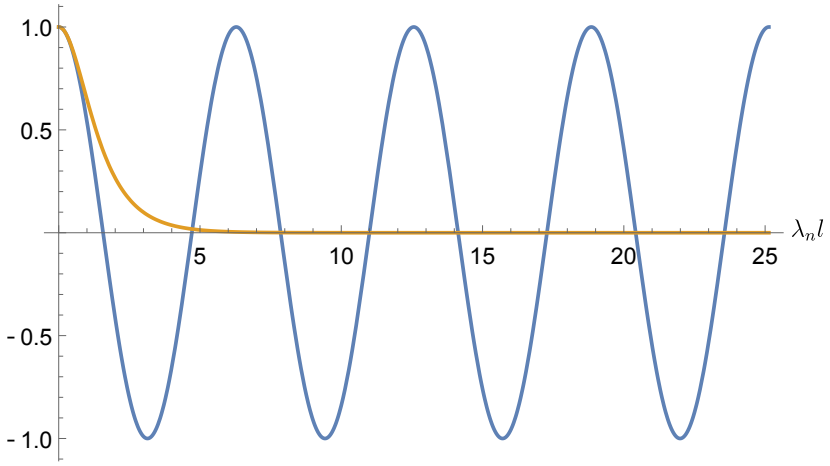

Figure 2.11: functions $\cos(\lambda_n l)$ (blue) and $1/\cosh(\lambda_n l)$ (yellow). Eigenmodes correspond to the intersection points.

While solutions to Eq. (2.8) are non analytic, a graphic representation as in Fig. (2.11) shows that in good approximation, the wave vectors are defined rather simply:

$$\lambda_n l \approx \left(n + \frac{1}{2}\right)\pi, \tag{2.9}$$

when $n \gg 1$, and $\lambda_n l = 4.73, 7.85, 11.00, 14.14$ for $n = 1$ to 4 [43]. The next step is to find the dispersion relation $\omega(\lambda)$ giving the eigenfrequencies of vibration. In principle, this can be obtained by injecting the ansatz (2.7) in Eq.(2.2):

$$\omega_n = \sqrt{\frac{EI}{\rho A}}\lambda_n^2 \approx \sqrt{\frac{EI}{\rho A}}\left(n + \frac{1}{2}\right)^2\left(\frac{\pi}{l}\right)^2. \tag{2.10}$$

String limit

In the **high stress** limit where the potential energy due to a tensile axial load is much bigger than the one due to the bending moment, the beam equation becomes that of a vibrating string:

$$\rho A\frac{\partial^2 u(z,t)}{\partial t^2} - \sigma A\frac{\partial^2 u(z,t)}{\partial z^2} = 0. \tag{2.11}$$

In this limit the sinh and cosh terms in the ansatz lead to imaginary, unphysical wave

vectors. We are left with the following profile:

$$\Psi(z) = a_1 \cos(\lambda z) + a_2 \sin(\lambda z). \tag{2.12}$$

Applying the boundary conditions (2.3), one finds the relation:

$$\cos\left(\frac{\lambda_n l}{2}\right) \sin\left(\frac{\lambda_n l}{2}\right) = 0. \tag{2.13}$$

This leads to a family of eigenwave vectors:

$$\lambda_n l = (n+1)\,\pi. \tag{2.14}$$

Injecting the ansatz (2.12) in Eq.(2.11), one finds the natural frequencies of vibration:

$$\omega_n = \sqrt{\frac{\sigma}{\rho}}\lambda_n = \frac{(n+1)\pi}{l}\sqrt{\frac{\sigma}{\rho}}. \tag{2.15}$$

The obtained frequencies are equally spaced, and do not depend on the resonator's transverse dimensions. Most of the NEMS used in our experiments are made out of highly pre-stressed silicon nitride, with a stored in-built stress of approximately 1 GPa. For these high-stress devices, the relation (2.15) is found to be always valid within $\pm$ 5 %, which justifies the string limit approach in most cases. Other beams used are less pre-stressed, but they are still close to this limit within some correction involving their Young's modulus [49]. An example of typical profiles obtained for real high-stress beams is shown in Fig. 2.12. Of course one can never be perfectly in the string limit for a doubly clamped geometry, since it implies that there would be a discontinuity in the displacement field derivative at the level of the clamp, which is unphysical. Rather, the profile is smoothed near the clamp, and one can show that the length of the zone where the string limit fails to apply near the boundaries vanishes as a power law of the parameter $EI/(\sigma A l^2)$.

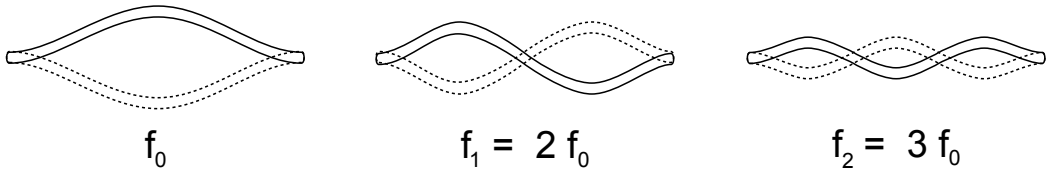

Figure 2.12: three first flexural modes of a doubly-clamped beam close to the string limit.

Note that in this section, we did not take into account the bi-layer nature of the beam. However, aluminium and silicon nitride present similar mass densities, such that the bilayer effect only introduces small corrections owing to the fact that the stress is mostly present in the nitride layer and that the Young's modulus for aluminum is about a third of that of SiN. This correction is addressed in [50] and lead to an effective description with slightly renormalized mechanical parameters.

2.5 Time dependence: the 1D, linear, damped harmonic oscillator

So far we have not explicited the time dependence of the displacement field. In fact, once the spatial dependence is addressed and the mode's eigenfrequency is known, the dynamics of the abscissa $x_n(t)$ can be re-written as that of the simplest spring-mass system:

$$m_n \frac{\mathrm{d}^2 x_n(t)}{\mathrm{d}t^2} + m_n \omega_n^2 x_n(t) = F(t), \tag{2.16}$$

with $m_n = M \int \Psi_n(z)^2 \mathrm{d}z$ the mode mass, where the integral is made over the whole beam length. Note that in the string limit, $m_n = M/2$, and one also defines the mode spring constant: $k_n = m_n \omega_n^2$. Compared to the initial displacement field, we have obtained a simpler equation, for a **collective variable** $x_n(t)$ that describes the beam's motion with renormalized parameters (mass, frequency) that contain all the information on the excited mode, that is, its shape under deformation. This simplification is rather convenient if the actuation/detection technique is non-local, which is the case for the capacitive or magnetomotive techniques presented in the following.

Let us now assume that the flexural mode n is excited by a sine wave. In this case, an excitation right at the resonance frequency causes the motion to diverge, which is unphysical. In fact, the modelling presented so far does not take into account the **friction mechanisms** that any real oscillator always experiences. These mechanisms act as damping forces, that counteract the motion set by the driving force. We will address some of these mechanisms later. Here, we simply mention that they can be all gathered in a single phenomenological constant which is called the **damping rate** of the mode Γ_n. We assume in this section that the damping force is linear, that is, the damping rate does not depend on the displacement. The total damping force associated to the collective variable $x_n(t)$ writes then:

$$F_d(t) = -m_n \Gamma_n \frac{\mathrm{d}x_n(t)}{\mathrm{d}t}. \tag{2.17}$$

This term accounts for the power dissipated by the mechanical motion into the sur-

roundings. The actual dynamics equation is then:

$$m_n \frac{\mathrm{d}^2 x_n(t)}{\mathrm{d}t^2} + m_n \Gamma_n \frac{\mathrm{d}x_n(t)}{\mathrm{d}t} + m_n \omega_n^2 x_n(t) = F(t). \tag{2.18}$$

If initially, the mechanical amplitude $x_n(t=0)$ is nonzero and no force is applied for $t > 0$, one can solve Eq. (2.18) and show that:

$$x_n(t) = x_n(t=0) e^{-\Gamma_n t/2} \cos(\omega_r t). \tag{2.19}$$

This means that the oscillator amplitude will decay to its rest position, releasing mechanical energy to its environment, over a typical timescale $2/\Gamma_n$. While relaxing to equilibrium, it will oscillate at a frequency $\omega_r = \omega_n \sqrt{1 - 1/(2Q_n)^2}$, with $Q_n = \omega_n/\Gamma_n$ the **quality factor** of the mechanical oscillator. This Q factor is the number of oscillations performed during the typical decay time. For an underdamped oscillator, i.e. $Q_n \gg 1$, the pseudo oscillation frequency will be in very good approximation the natural eigenmode frequency.

Under harmonic forcing $F(t) = F_0 \cos(\omega t + \phi_0)$ with a phase reference ϕ_0, a generic solution to Eq. (2.16) is:

$$x_n(t) = x_n^c(\omega) \cos(\omega t) + x_n^s(\omega) \sin(\omega t), \tag{2.20}$$

with:

$$\begin{cases} x_n^c(\omega) &= \dfrac{F_0}{m_n} \times \dfrac{(\omega_n^2 - \omega^2)\cos(\phi_0) + \Gamma_n \omega \sin(\phi_0)}{(\omega_n^2 - \omega^2)^2 + \Gamma_n^2 \omega^2}, \\ x_n^s(\omega) &= \dfrac{F_0}{m_n} \times \dfrac{\Gamma_n \omega \cos(\phi_0) - (\omega_n^2 - \omega^2)\sin(\phi_0)}{(\omega_n^2 - \omega^2)^2 + \Gamma_n^2 \omega^2}. \end{cases} \tag{2.21}$$

x_n^c and x_n^s are the so-called **quadratures** of the mechanical motion. They are a linear combination of a component **in phase** with the excitation and its orthogonal component **in quadrature**, i.e. dephased by $\pi/2$ from the excitation. The quadrature component is nonzero, as the damping rate creates a finite time delay over which the response is fully established, hence a dephasing. Tuning the phase reference to $\phi_0 = +\pi/2$, the two components, called $X_n(\omega)$ (in-phase) and $Y_n(\omega)$ (in quadrature), describing a point in the complex plane for a given excitation frequency ω, appear straightforwardly:

$$\begin{cases} X_n(\omega) &= \dfrac{F_0}{m_n} \times \dfrac{\Gamma_n \omega}{(\omega_n^2 - \omega^2)^2 + \Gamma_n^2 \omega^2}, \\ Y_n(\omega) &= \dfrac{F_0}{m_n} \times \dfrac{\omega^2 - \omega_n^2}{(\omega_n^2 - \omega^2)^2 + \Gamma_n^2 \omega^2}. \end{cases} \tag{2.22}$$

The component $X_n(\omega)$ is also called the absorption part of the mechanical response, while $Y_n(\omega)$ is the dispersion part. Indeed, if the excitation frequency is at the resonance frequency, the applied force will be maximally converted into a displacement. For excitations at higher frequencies, the system's response will be established with an increased delay, i.e. dephasing, until it cannot follow the excitation: it then becomes transparent to the excitation. At resonance:

$$\begin{cases} X_n(\omega_n) &= \dfrac{F_0 Q_n}{k_n}, \\ Y_n(\omega_n) &= 0, \end{cases} \tag{2.23}$$

with $Q_n = \omega_n / \Gamma_n$ the quality factor of the mechanical mode and $k_n = m_n \omega_n^2$ the effective mode spring constant.

A useful approximation can be considered when the resonator is in the high Q limit, i.e. $Q_n \gg 1$. The drive frequency is then such that $(\omega - \omega_n)/\omega_n \ll 1$, and $\omega + \omega_n \approx 2\omega_n$. In that limit Eq. (2.22) becomes:

$$\begin{cases} X_n(\omega) &= \dfrac{F_0}{2 m_n \omega_n} \times \dfrac{\Gamma_n/2}{(\omega_n - \omega)^2 + \Gamma_n^2/4}, \\ Y_n(\omega) &= \dfrac{F_0}{2 m_n \omega_n} \times \dfrac{\omega - \omega_n}{(\omega_n - \omega)^2 + \Gamma_n^2/4}. \end{cases} \tag{2.24}$$

The absorption curve then has a Lorentzian line shape. As all our measurements are performed in the high Q regime, we use Lorentzian fits to extract relevant parameters. In particular, the damping rate is directly the full width at half maximum (FWHM) of the X_n curve.

2.6 Electromechanical transduction

2.6.1 Electrical setup

In absence of a magnetic field, the nanomechanical beam simply acts as a resistance R_N in series integrated in the experimental setup. This resistance is dominated by the aluminium layer on the beam itself, due to the submicronic confinement on 2

dimensions. In practice, contacts also display very small resistances, on the Ω range, so we consider them as almost ideal. The typical resistances at 4 K range from about 50 Ω for small beams (5 µm long) to about 1 kΩ for the longest ones (300 µm). To prevent too huge currents from flowing through the device, especially in the case of low impedance beams, a bias resistance $R_b = 1$ kΩ is inserted in the injection line in series with the NEMS. It is also suitable for measurement purposes (see paragraph 2.6.3), since the NEMS is then kept in a high impedance environment on the injection side. This arrangement is made at the expense of having a 50 Ω adaptation, thus leading to transmission losses in our setup. Nonetheless, these losses can be calibrated (see Section 2.8).

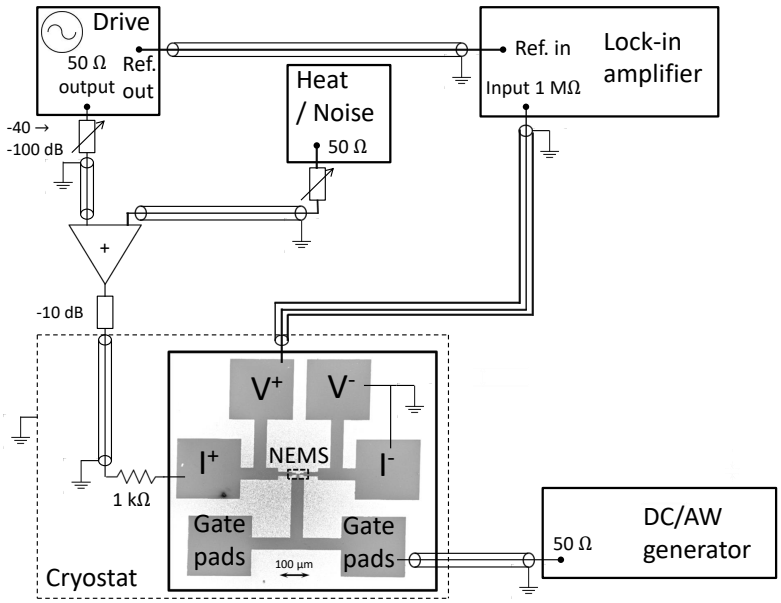

Figure 2.13: generic schematic picture of the wiring. Depending on the experiments, arrangements are made, which will be detailed in the appropriate chapters.

An AC input voltage is delivered by an arbitrary function generator Tektronix AFG3252 suited for near-radiofrequency signal generation (up to 240 MHz). In the most general configuration, schematized in Fig. 2.13, this generator is synchronized with a lock-in amplifier Stanford Research SR844 which can operate at frequencies up to 200 MHz. A HP 33120 A arbitrary wave generator with a 10 MHz bandwith is used to generate noise or heating signals when needed. These will be discussed in due time in the manuscript.

2.6.2 Magnetomotive actuation and detection of the motion

All the measurements presented in this manuscript have been made using the so-called magnetomotive transduction scheme. For fundamental research purposes, it

has been widely used for decades in the superfluid ^{3}He community to actuate and detect viscometers, thermometers, or bolometers [51, 52], and has been introduced, for NEMS structures, in 1999 by A. N. Cleland and M. L. Roukes [53]. Since then, many progresses have been made in measuring nanometer scale motions, but this technique remains used mainly for its simplicity.

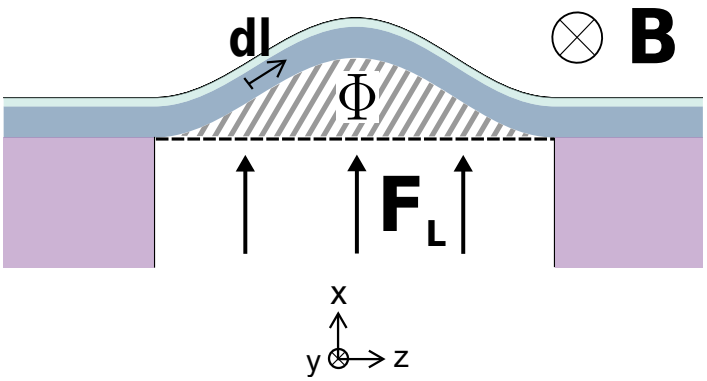

Figure 2.14: schematic representation of the magnetomotive actuation and detection principle, for the first flexural mode.

While the current $I(t)$ flows through the suspended beam (**z** direction), a static magnetic field $\mathbf{B} = B\mathbf{y}$, uniform at the scale of the sample, is applied perpendicularly to the device. This results in a Laplace force exciting the out-of-plane motion of the NEMS. Assuming that the current is sinusoidal at a frequency close to that of a mechanical mode n, such a force applied to an infinitesimal oriented portion $\mathbf{dl}(z)$ at abscissa z of the beam writes:

$$\mathbf{dF}_L(z,t) = I(t)\mathbf{dl}(z) \times \mathbf{B}. \tag{2.25}$$

For all the structures measured in this thesis the maximum displacement of the beam from its rest position is at most 0.2 % of its length. It is then safe to simplify the above expression for a given mode n:

$$\mathbf{dF}_L(z,t) \approx I(t)B\Psi_n(z)\mathrm{d}z\,\mathbf{x}. \tag{2.26}$$

Integrating over the whole length l of the beam, we obtain the total Laplace force applied on the mode, in the **x** direction:

$$F_{L,n}(t) = \xi_n I(t) l B. \tag{2.27}$$

Here ξ_n is a so-called mode shape factor, which accounts for the fact that the force

is not uniform along the **z** axis. This shape factor is then the only mode-dependent parameter in the problem, and an effective 1D force can be written, renormalized by ξ_n:

$$\xi_n = \int_{-l/2}^{l/2} \Psi_n(z)\mathrm{d}z. \tag{2.28}$$

For doubly-clamped beams in the string limit, $\Psi_n(z) = \sin(\lambda_n z)$, with λ_n the eigenmode wave vectors in the string limit from Eq. (2.14), therefore $\xi_n = 2/\left[(n+1)\pi\right]$ for n odd with our notations. As this renormalization is done on the applied force, it should be done also for the displacement, which is distributed along the beam. Indeed, the local motion writes: $u_n(z,t) = \Psi_n(z)x(t)$. Integrating over the whole beam, we can use a collective variable $x(t)$ describing the displacement of the beam, and which is the maximum amplitude of the beam's deflection. For instance, for the fundamental flexural mode, $x(t)$ will be the displacement of the central abscissa of the beam.

As induction creates the force applied on the beam, it is also used to detect the resulting motion. Indeed, as the beam is moving, an effective area is swept between the instantaneous position and the position at rest. For an oscillating excitation, this area will be varying in time. The magnetic flux crossing a differential effective area d^2A will be:

$$\mathrm{d}^2\Phi(t) = \mathbf{B}.\mathrm{d}^2A(t)\mathbf{y}. \tag{2.29}$$

Again, the double differential area can be simplified in the small deflection limit, for mode n:

$$\mathrm{d}^2A_n(t) \approx \Psi_n(z)\mathrm{d}z\mathrm{d}x(t). \tag{2.30}$$

After integration over the whole length, the one-time differential magnetic flux will be:

$$\mathrm{d}\Phi_n(t) = \xi_n lB\mathrm{d}x(t). \tag{2.31}$$

As a time-dependent motion will respond to a time-dependent excitation, this magnetic flux is also time-dependent, and according to Faraday's law, this variation generates an electromotive force $e(t)$ in addition to the Ohmic response of the NEMS:

$$e(t) = -\frac{\mathrm{d}\Phi_n}{\mathrm{d}t} = -\xi_n lB\frac{\mathrm{d}x}{\mathrm{d}t}. \tag{2.32}$$

The experimental technique introduced here thus detects the velocity of the beam. Assuming that the drive excitation is sinusoidal, with angular frequency ω, the resulting velocity will be also an oscillation at ω: $v(\omega) = i\omega x(\omega)$ in frequency domain. Then,

the detected voltage drop $e(\omega)$ will be simply proportional to the complex amplitude $x(\omega)$ of the sine displacement, within a phase factor of $\pi/2$, which mathematically translates the fact that displacement and velocity are in quadrature:

$$e(\omega) = i\omega\xi_n lBx(\omega). \tag{2.33}$$

With a properly set phase reference for lock-in detection such that we look in the quadrature components X_n, Y_n directions defined in Eq. (2.23)one measures (in the high-Q limit):

$$V_{out}(\omega) \approx \omega_n\xi_n lB\left[X_n(\omega) - iY_n(\omega)\right]. \tag{2.34}$$

This explains the choice of reference phase ϕ_0 made when producing Eq. 2.22.

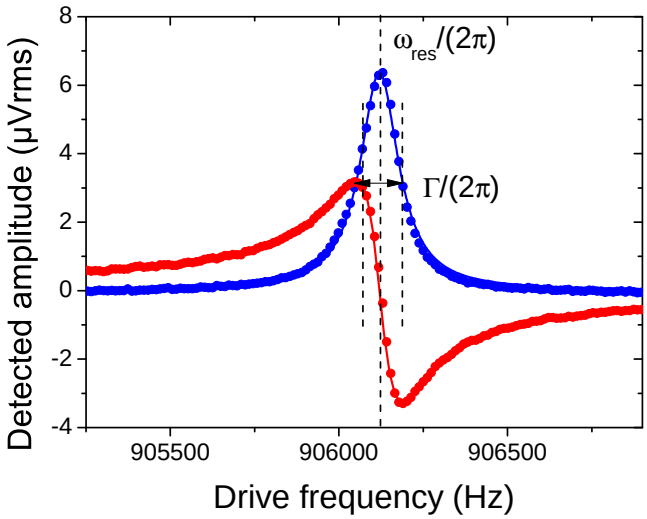

Figure 2.15: electro-mechanical in-phase (blue dots) and in-quadrature (red dots) responses to a sinusoidal magnetomotive excitation swept in frequency around the resonance, as detected at the lock-in amplifier level. Solid lines are fits from Eq. (2.22) in Volt units.

An example is shown in Fig. 2.15. From the fit one extracts the mode's frequency, its height of vibration and its damping rate. Note that only the in-phase component is then needed. In particular, at the resonance frequency, the quadrature component must be zero. Note also that the cost of measuring velocity instead of the motion is a minus sign on the quadrature, with inverted definitions for in-phase and quadrature components. On a more practical level, the above description does not take into account attenuation in the measurement setup so far. This will be addressed later, in the calibration section.

This technique, on the whole, is very convenient mainly for two reasons:

- As opposed to e.g. a capacitive transduction scheme, the magnetomotive scheme is very linear, i.e. the applied force is independent of the displacement, and uniform at the NEMS scale, since magnetic field gradients are negligible on the cm scale here.

- The actuation and detection profile match by construction since they are based on the two facets of the same principle and use the same element (a magnetic field), and the applied force/detected displacement are both simple integrated quantities.

Besides, the scheme suffers from a few drawbacks, which definitely rule it out of competition if very sensitive measurements are required:

- By construction, additional electrical losses are generated due to Lenz law of induction. This will be addressed in the next section.

- It is only possible to excite and detect modes with an even spatial profile, as those with odd profiles will provide a zero net contribution to the integrated applied force or detected voltage: $\xi_n = 0$ for n even (in our notations).

- Its sensitivity is rather poor, and decreases quadratically with the applied field and beam length. A good lower limit **in the driven regime** is in the fraction of nm range **for averaged signals**, for all NEMS, and in practice, addressing the real Brownian motion at 4 K, of spatial extension $\sqrt{k_B T/k} \sim 10$ pm at best (i.e. for long beams) is impossible: it lies well below the limits fixed by the apparatus electrical noise, even at 4 K with a cryogenic amplifier, including the bias resistance Johnson-Nyqvist noise. For such measurements optical techniques are by far more adapted [4, 54].

As far as this manuscript is concerned, the required sensitivity is not tremendous. When needed, Brownian motion is artificially created by a white noise source (see Chapter 3). All the measurements realized during this thesis are performed through magnetomotive actuation and detection, and capacitive schemes are only used as an additional channel to achieve frequency tuning or parametric control of the mechanical resonator.

2.6.3 External loading by the electrical environment

We showed that in presence of a magnetic field B, an electromotive force due to the NEMS motion, opposed to the Laplace force, is generated in addition to the usual Ohmic response described in Section 2.8.1. This e.m.f. has a parallel RLC circuit characteristic, so here we can model the measured nanomechanical mode from the electrical point of view as a parallel RLC circuit loaded by an external complex impedance

(See Fig. 2.16). A direct correspondence, described in Ref. [53], is made between the equivalent electrical parameters (R_m, C_m, L_m) and the mechanical ones (intrinsic resonance frequency ω_m and linewidth Γ_m, mode mass m_n and length $\xi_n l$), together with the magnetic field. The equivalent electrical parameters satisfy:

$$\begin{cases} \omega_m = \dfrac{1}{\sqrt{L_m C_m}}, \\ \Gamma_m = \dfrac{1}{R_m C_m}. \end{cases} \tag{2.35}$$

The total impedance seen by the lock-in amplifier, i.e. the one of the RLC circuit loaded in parallel with $Z_{ext} = R_{ext} + iX_{ext}$ can be thoroughly obtained:

$$Z_{load}(\omega) = \frac{i\omega/C_m}{i\omega\left(\Gamma_m + \dfrac{R_{ext}}{|Z_{ext}|^2 C_m}\right) + \omega_m^2 - \omega^2 + \dfrac{X_{ext}}{|Z_{ext}|^2 C_m}\omega}. \tag{2.36}$$

As for the electrical environment, we can use the modelling of Section 2.6.1, represented with Norton convention in Fig. 2.16.

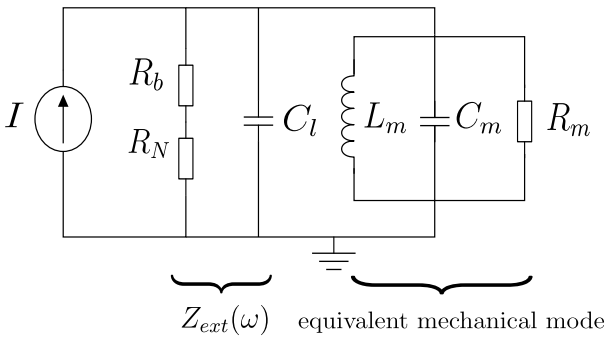

Figure 2.16: equivalent electrical circuit in Norton representation, with C_l the capacitive part of the loading impedance.

Note that in Fig. 2.16, C_l may not be the total capacitance of the line, as Z_{ext} is merely an impedance **seen** by the NEMS. Then, the capacitances located before the bias resistance do not significantly contribute to the loading impedance in this frequency range. Besides, it also includes the geometric capacitance created by the gate-NEMS configuration in case we are using the gate. From the model presented in Fig. 2.16, the loading impedance is:

$$Z_{ext}(\omega) = \frac{R_b + R_N}{1 + i(R_b + R_N)C_l\omega}. \tag{2.37}$$

Writing the equivalence between the observed e.m.f and the loaded electrical circuit, we obtain:

$$\begin{cases} \dfrac{\xi_n^2 l^2 B^2}{m_n} = \dfrac{1}{C_m}, \\ \omega_{res} = \omega_m \sqrt{1 + \dfrac{X_{ext}}{|Z_{ext}|^2} \dfrac{\xi_n^2 l^2 B^2}{m_n \omega}} = \omega_m \sqrt{1 - \dfrac{C_l \xi_n^2 l^2 B^2}{m_n}}, \\ \Gamma = \Gamma_m + \dfrac{R_{ext}}{|Z_{ext}|^2} \dfrac{\xi_n^2 l^2 B^2}{m_n} = \Gamma_m + \dfrac{\xi_n^2 l^2 B^2}{(R_b + R_N) m_n}. \end{cases} \tag{2.38}$$

The measured properties are thus renormalized by the magnetic field together with electrical and geometric properties. In the frequency ranges investigated, the measured relative change in frequency does not exceed 10^{-5}. However, the correction to the damping rate is not necessarily negligible. In particular, longer beams are more affected by this loading correction while the extrapolated intrinsic damping rate decreases with length. For the longest measured beams in the present work, the loading contribution to the damping rate can reach 200 Hz for intrinsic rates of about 1Hz, as seen on Fig. 2.17. Meanwhile the capacitive contribution is often negligible, with loading capacitances on the 10 pF range at most. On the other hand for a given beam the mode dependence of the additional damping decreases as $1/n^2$, with n being the mode number. Higher modes of a beam are then much less affected by this loss mechanism.

Physically, this can be explained from two equivalent points of view. One is the illustration of the Lenz law of induction: the induced e.m.f. at the terminals of the conducting NEMS leads to a current proportional to the driving current and flowing in the opposite direction. This translates into a reaction Laplace force opposed to the driving one and proportional to the velocity, hence the additional damping contribution scaling as B^2. On the other hand, the measured resonance properties are that of a coupled system: the mechanical mode hybridizes with its electrical environment, through a coupling which strength is set by the magnetic field. Thus, the more it is coupled to the electrical system, the more electro-mechanical energy is dissipated. Meanwhile the coupling strength also depends on the impedance seen by the NEMS: if this loading external impedance is high, the NEMS is less coupled to the electrical circuit i.e. less easily detectable, but experiences less extra damping.

As a result, a trade-off situation must be found between having a high quality resonator (hence a high environment impedance) and good resolution (hence a NEMS long enough, which results in more electrical damping). On the detection side the lock-in amplifier input impedance is set to 1 MΩ which can be regarded as an infinite value for all NEMS investigated here. With a bias resistance of 1kΩ, added to that of the metallic layer of the NEMS, we ensure that at least short NEMS are very weakly loaded even for high fields.

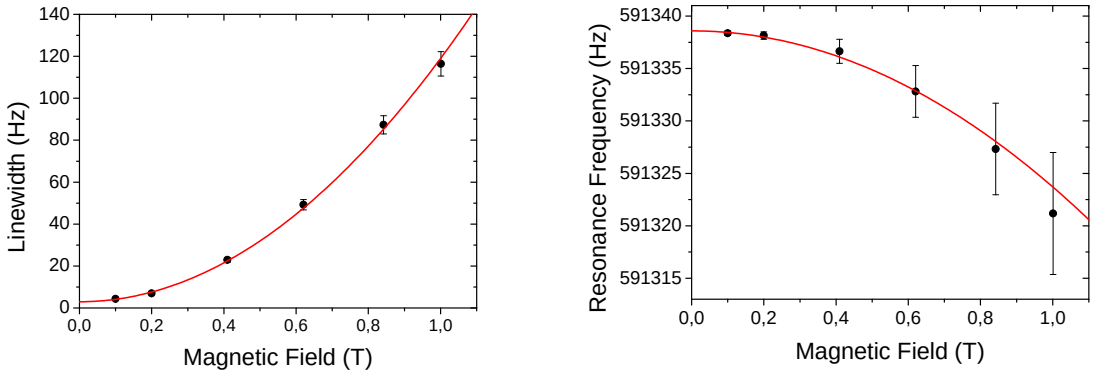

Figure 2.17: effect of the loading impedance on the measured resonance properties for a long (300 µm) nanobeam. Left: effect on the damping rate. The solid line is a quadratic law following Eq. (2.38). The zero field value is the extrapolated intrinsic damping rate, left as a free parameter. Here we obtain $\Gamma_m = 2.96 \pm 0.5$ Hz. The parameters used for the NEMS resistance (1.1 kΩ) and mass (2.5×10^{-14} kg) are obtained by different procedures, which leaves no other free parameter. Right: effect on the resonance frequency. Note the small dynamic range. The solid line is a fit from Eq. (2.38) with $C_l = 30$ pF.

2.7 Thermal properties of the system

In presence of electrical signals passing through resistive metals, or direct heating of the sample holder, the thermal environment of the NEMS will be affected, which in turn will modify the NEMS materials' properties. Since all the mechanical parameters (resonance, dissipation, amplitude) depend on the materials, it can be useful to estimate quantitatively thermal effects on the mechanics. Moreover, for calibration purposes (see Section 2.8.2), one needs at least a qualitative prediction of what happens to the mechanics for a given heating of the system.

2.7.1 Temperature dependence of measured mechanical properties

With a simple microscopic picture it is natural to think that materials properties will be affected by a temperature change: atoms' motion will grow bigger with temperature, which in turn will change the potential energy seen by each of them in the materials, hence the stiffness. From a macroscopic perspective, materials will experience a change in Young's modulus as well as thermal expansion/contraction. While thermal expansions are small at cryogenic temperatures, there is nonetheless a non-negligible contribution in metal-coated doubly-clamped beams due to the expansion mismatch between the two layers. Thus, for a homogeneous temperature field T a differential strain $\varepsilon(T, z) = \delta l(T, z)/l$ exists, and this in turn creates internal stress $\delta\sigma$ according to Hooke's law for elastic media:

$$\delta\sigma(T,z) = E(T)\varepsilon(T,z), \tag{2.39}$$

if we restrict the discussion to 1D with the **z** axis. The potential energy associated to an oscillating motion writes:

$$E_p = \frac{1}{2}x_n^2(t)\int_{-l/2}^{l/2}\left[\left(\frac{\partial^2\Psi_n(z)}{\partial z^2}\right)^2 E(T)I - \frac{\partial^2\Psi_n(z)}{\partial z^2}\Psi_n(z)\sigma(T)A\right]\mathrm{d}z, \tag{2.40}$$

where we emphasize the temperature dependence of Young's modulus and internal tensile stress $\sigma(T) = \sigma(T_0) + \delta\sigma(T)$. Assuming the drive current is not heating much the device (which in normal operating conditions is reasonable), we can consider that the device is always at thermal equilibrium and forget for the moment the time and space dependences of the temperature field. The integral in Eq. (2.40) is in fact a spring constant, and assuming small, low-order polynomial expansions in temperature for Young's modulus, in-built stress and differential strain, the potential energy can be written:

$$E_p = \frac{1}{2}\left[k_n(T_0) + \delta k_n(T - T_0)\right]x_n^2(t), \tag{2.41}$$

with T_0 a reference temperature (e.g. 4.2 K). This change in spring constant with temperature is measured through the resonance frequency. An example is displayed in Fig. (2.18), left panel. The shift in frequency is well captured with a polynomial dependence (see caption). The cubic dependence originates from the differential strain and possibly the in-built stress, as it is absent for cantilevers measurements [41], where differential strain does not affect the neutral line. The weak, linear dependence, also observed for cantilever [41] is then most likely due to a small, linear variation of the Young's modulus with temperature.

On the other hand, taking into account a small variation of the friction coefficient with temperature in the considered range the instantaneous mechanical power dissipated writes:

$$P_d = -\frac{1}{2}M\dot{x}_n^2(t)\int_{-l/2}^{l/2}\left[\Gamma_n(T_0) + (T - T_0)\left.\frac{\mathrm{d}\Gamma_n}{\mathrm{d}T}\right|_{T=T_0}\right]\Psi_n^2(z)\mathrm{d}z. \tag{2.42}$$

A typical measurement of the linewidth up to 23 K is shown in Fig. 2.18, right panel. The dependence in temperature is linear, with a weak slope $\mathrm{d}\Gamma_n/\mathrm{d}T$. Its value is rather reproducible from one sample to the other, between 1 % and 2 %. In addition, it has been observed that the extrapolated zero value scales with the metal thickness evaporated [55, 50, 56] for the same sample, which seems to show that metallic coatings are the dominant source of damping for temperatures above 1 K in our structures.

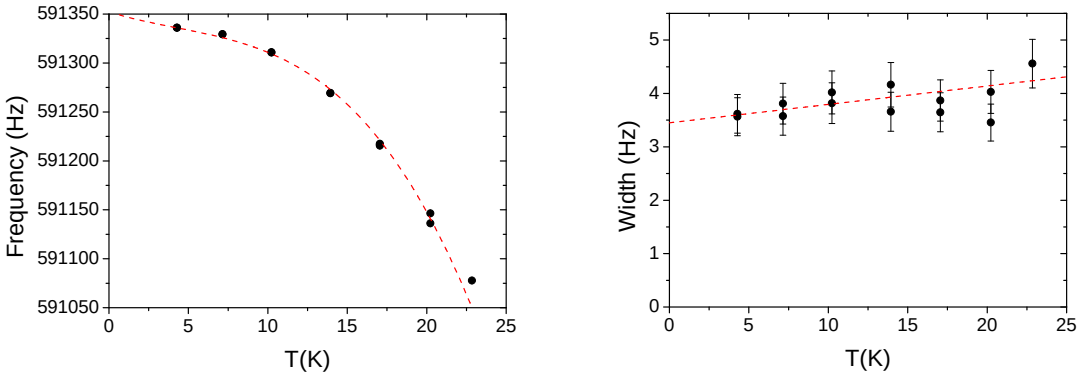

Figure 2.18: left: measured resonance frequency of a 300 µm NEMS as a function of the cell temperature. A fit (dashed line) of the form $a(T-T_0)+b(T-T_0)^3$ is used as a guide for the eyes (see text). Right: Measured damping rate of the same device as a function of temperature, with a linear fit as a guide for the eyes (note the weak slope).

In Ref. [39], a macroscopic model describing losses in nanomechanical resonators based on continuum mechanics showed that the bending energy is responsible for losses. This explains, at least partially, why the Q factor of stressed SiN resonators have rather high values [57]: the added in-built stress does not contribute to the dissipated energy while increasing the stored energy (since it is the dominant contribution to the stiffness). However, the actual microscopic friction mechanisms remain elusive. In our case, thermoelastic damping [11] and clamping losses [58] should be negligible for such materials and frequencies, at such temperatures. Then, one candidate could be friction occuring at grain boundaries, with a temperature dependence arising from thermal contraction or expansion. Below typically 1 K, new mechanisms start to be dominant, which will be addressed in Chapter 6.

2.7.2 Thermal balance in presence of a driving current

In this section we shall derive a simple thermal model describing the effect of external Joule heating on the thermal profile $T(z,t)$ of the beam, in the range 1 K-30 K. This will be useful for calibration purposes (see Section 2.8.2). The major contribution for thermal conductivity in the aluminium layer will arise from conduction electrons. In the Kelvin range the Wiedemann-Franz law linking the electrical resistivity ρ_e and the thermal conductivity κ_e is accurate. Thus $\kappa_e = \pi^2 k_B^2 T/(3e^2\rho_e)$, and we can neglect the contribution from phonons in the aluminium. Conduction electrons will be also the dominant contribution to specific heat: $C_{V,e} = \gamma_e T$ up to 10 K.

In the nitride layer, the phonon bath is responsible for a specific heat $C_{V,ph} \propto T^n$, where n depends both on materials disorder and sample dimensionality. The latter is to be compared with the dominant phonon wavelength $\lambda_{\mathrm{dom}} = hc/(2.82k_BT)$, with c the sound speed. Meanwhile, thermal conductivity cannot be properly defined, as it is

proportional to the phonon mean free path, which is much bigger (around 1 cm) than the beam's cross-dimensions at cryogenic temperatures. Rather, we use the **thermal conductance** K_{ph}, which depends on the layer's cross-dimensions, defined as:

$$K_{ph} = \beta_{cas} \Lambda_{ph} T^3. \tag{2.43}$$

Here $\Lambda_{ph} = 1.12\sqrt{e_{\mathrm{SiN}} w}$ is the effective mean free path in the diffusive (Casimir) regime of thermal phonon transport: in this limit thermal phonons are inelastically scattered at the NEMS boundaries. Meanwhile, β_{cas} is a constant extracted from kinetic theory, which depends on dimensions, and is found experimentally in similar devices [59] to be:

$$\beta_{cas} = 3.2 \times 10^3 \left(\frac{2\pi^2 k_B^4}{5\hbar^3 c^3} \right)^{2/3} \frac{e_{\mathrm{SiN}} w}{l}. \tag{2.44}$$

Below 15 K thermal conductance due to phonons in the nitride layer does not exceed a fraction of the one due to electrons in the metallic layer. However, as the ratio between the two $K_{ph} S_e/(\kappa_e l) \propto T^2$, this quickly becomes wrong above approximately $10 - 15$ K. Therefore, for simplicity we first assume in our modelling that heating will not bring the device to too high temperatures so that we can keep only the electronic contribution in the model.

We assume that intially, the beam is thermalized at a base temperature T_0, be it the cryogenic temperature 4.21 K or the one obtained by heating the sample holder. Due to the huge aspect ratio, we can reduce the situation to a 1D heat diffusion model in the aluminium layer. After switching on a heating electrical current, contacts are assumed to be big enough so as to remain thermalized at the base temperature, but due to the small section S_e of the resonator's metallic layer, any electrical current $I(t)$ flowing through the latter will result by Joule effect in a heat load per unit volume $\dot{q}(t) = \rho_e I^2(t)/S_e^2$. S_e denotes here the cross-section of the aluminium layer, which is the only conducting part of the beam. The evolution of the temperature profile along the beam (**z** axis) is determined through a heat diffusion equation:

$$\mu_e C_V \left[T(z,t)\right] \frac{\partial T(z,t)}{\partial t} = \frac{\partial}{\partial z} \left(\kappa \left[T(z,t)\right] \frac{\partial T(z,t)}{\partial z} \right) + \dot{q}(t), \tag{2.45}$$

where $\mu_e = 2.7$ g/cm^3 is the mass density of the aluminium layer. The boundary conditions express the symmetry of the heat load distribution and the thermalization of the device, at the clamps, to the reservoir formed by the contacts, which are at temperature T_0:

$$\begin{cases} T(z = \pm l/2, t) & = & T_0, \\ \kappa\left[T(z=0,t)\right] \dfrac{\partial T(z=0,t)}{\partial z} & = & 0. \end{cases} \tag{2.46}$$

2.7.3 Temperature profile along the Joule-heated nanobeam

We write the heating current as $I(t) = I_h \cos(\omega_h t)$, so the heating power per unit volume will be:

$$\dot{q}(t) = \frac{\rho_e I_h^2 \left[1 + \cos(2\omega_h t)\right]}{2S_e^2}. \tag{2.47}$$

Eq. (2.45) is solved in details for a different NEMS geometry in Ref. [41], we give here a solution adapting the procedure for our geometry. The AC part of the solution oscillating at $2\omega_h$ scales in amplitude with a thermal skin depth vanishing as $1/\sqrt{\omega_h}$. As the lock-in detection averages over a time $\gg \omega_h^{-1}$, We can safely neglect it in the problem, which amounts to saying that the NEMS is only sensitive to the average temperature at a given abscissa z. We are left with the DC temperature profile:

$$T_{\mathrm{DC}}(z, I_h) = \sqrt{\frac{3e^2\rho_e^2 I_h^2}{2\pi^2 k_B^2 S_e^2}\left(\frac{l^2}{4} - z^2\right) + T_0^2}. \tag{2.48}$$

The profile is maximum at the center of the beam, which is consistent with the fact that it is the most isolated part from the thermal reservoirs, i.e. the contacts, while the current is uniform along the beam. Thus the steady-state temperature will be further from equilibrium at the center, while the clamps will more easily leak to the contacts and therefore thermalize to base temperature.

Let us define $\Delta T_{\mathrm{DC}}(z, I_h) = T_{\mathrm{DC}}(z, I_h) - T_0$ the difference between the heated beam temperature at an abscissa z and the base temperature (i.e. temperature at the clamps), and $\Delta T_{\max} = \Delta T_{\mathrm{DC}}(0, I_h)$ the temperature at the centre of the beam, i.e. the maximum temperature:

$$\Delta T_{\max}(I_h) = \sqrt{\frac{3e^2\rho_e^2 I_h^2 l^2}{8\pi^2 k_B^2 S_e^2} + T_0^2} - T_0. \tag{2.49}$$

This heating results in a shift of the spring constant which is an average over the temperature gradient along the beam:

$$\omega_n(I_h) = \omega_n(0) + a\Delta T_{\max}(I_h)\frac{\int\left(\frac{\partial^2\Psi_n(z)}{\partial z^2}\right)^2\frac{\Delta T_{\rm DC}(z,I_h)}{\Delta T_{\max}}\mathrm{d}z}{\int\left(\frac{\partial^2\Psi_n(z)}{\partial z^2}\right)^2\mathrm{d}z} + b\Delta T^3_{\max}(I_h)\frac{\int\frac{\partial^2\Psi_n(z)}{\partial z^2}\Psi_n(z)\left(\frac{\Delta T_{\rm DC}(z,I_h)}{\Delta T_{\max}}\right)^3\mathrm{d}z}{\int\frac{\partial^2\Psi_n(z)}{\partial z^2}\Psi_n(z)\mathrm{d}z}. \quad (2.50)$$

This expression shows that the frequency shift due to a heating current depends only on the geometry (through the temperature profile calculated with the thermal model and the mode shape) and on the coefficients found for a uniform heating a and b. The fractions in Eq.(2.50) are not analytic but can be evaluated numerically. Over the range of heating currents considered, they yield constant values of respectively 0.92 for the bending contribution and 0.79 for the stress contribution in the doubly-clamped geometry. In addition, the NEMS resistance $R_N = \rho_e l/S_e$ is found to be independent of temperature between 1 and 30 K, within 1 %. Therefore our thermal model has, apart from coefficients R_N, a and b which are measured independently, no free parameters.

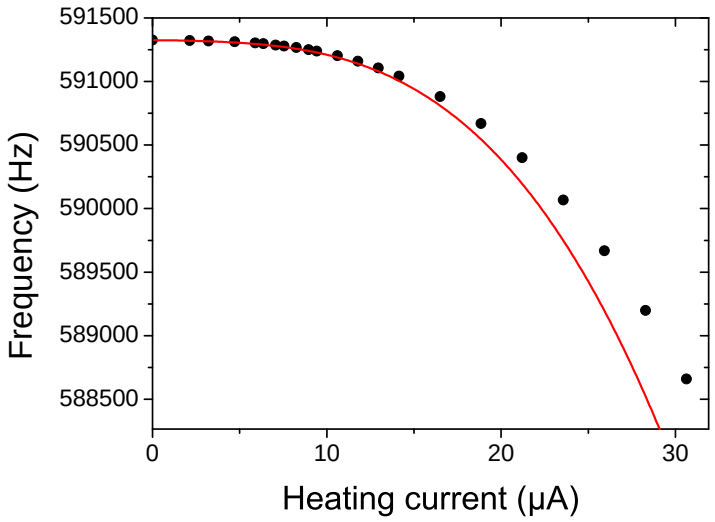

Figure 2.19: shift of a 300 μm long NEMS resonance frequency as a function of the 50 kHz heating current amplitude. The solid line is the application of Eq.(2.50), with a and b parameters determined above (see Fig. 2.18), left panel.

An example is shown in Fig. 2.19 with an almost DC heating current (50 kHz). The data are well reproduced by theory up to moderate heating currents, choosing a and b as in the example of Fig. 2.18 which is taken from the same device and measurement campaign. For strong heating, which corresponds to temperatures of 15 K or more at

the center of the beam, a discrepancy appears. This corresponds to the appearance of another heat conduction channel, namely phonons in the nitride part of the beam, similar to silicon based devices [60]. It explains why the frequency is less strongly shifted, as the real temperature is lower than the one predicted by our model: indeed, the additional phonon conduction enhances the beam thermalization to the reservoirs, therefore reducing the temperature increase due to Joule heating.

2.8 In-situ calibration of the system

The magnetomotive technique introduced in paragraph 2.6.2 should in principle allow to determine the applied forces and the displacements in real units, since all parameters are known. However, this accuracy is strongly limited by the apparatus. The injection and detection cables, which are about a few meters long each, are responsible for low-pass filtering due to their capacitance and can exhibit parasitic resonances for high frequencies $\gtrsim$ 10 MHz. The NEMS resistance itself is not necessarily 50 Ω, its environment is high impedance for measurement purposes (see Section 2.6.3), while the coaxial cables impedance is 50 Ω, leading to impedance mismatches for an AC drive. A thorough definition of each imperfection is unrealistic, but it is possible nonetheless to obtain in-situ calibration factors for both injection and detection lines, called $G_I(\omega)$ and $G_D(\omega)$ in the following. The technique is described extensively in Ref. [41], and here we will focus on the essential features.

2.8.1 Characterization of the global transmission in frequency

The transmission is simply measured at the lock-in detection through the Ohmic response of the NEMS to a current flowing in its metallic layer. The injection and detection lines are coaxial cables with a capacitance dristributed all over their length (a few meters for both). The estimated lineic capacitance is 100 pF/m. To keep the modelling simple, we describe it as a discrete capacitance C, of about a few 100 pF, but which we keep as a fit parameter, since electrical connections are likely to vary a lot in length depending on the experiment requirements. The canonical electrical circuit associated to a basic experiment, i.e. driving and detecting a NEMS around resonance, is displayed in Fig. 2.13, and its transfer function is:

$$G(\omega) = \frac{V_{out}(\omega)}{V_{in}(\omega)} = \frac{1}{1 + R_b/R_N + jR_bC\omega}. \tag{2.51}$$

The complete circuit is then a low-pass filter with a cut-off frequency which differ, from one experiment to another on the same setup, by the NEMS resistance R_N and the line capacitance C. R_N is measured at room temperature through the 4-wire technique

and $R_b = 1\ \mathrm{k}\Omega$ is known, so we are left with only one fit parameter C for the measured transmission.

The transmission characterization is then done at 4.2 K. The resistivity of the aluminium layer on top of the NEMS should drop, and this evolution can be quantitatively fit. Indeed, since R_b and C are temperature-independent, only the DC gain of the transmission line will be affected :

$$G(\omega \to 0) = \frac{R_N}{R_b + R_N}. \tag{2.52}$$

An example of transmission line characterization is shown in Fig. 2.20, with a NEMS

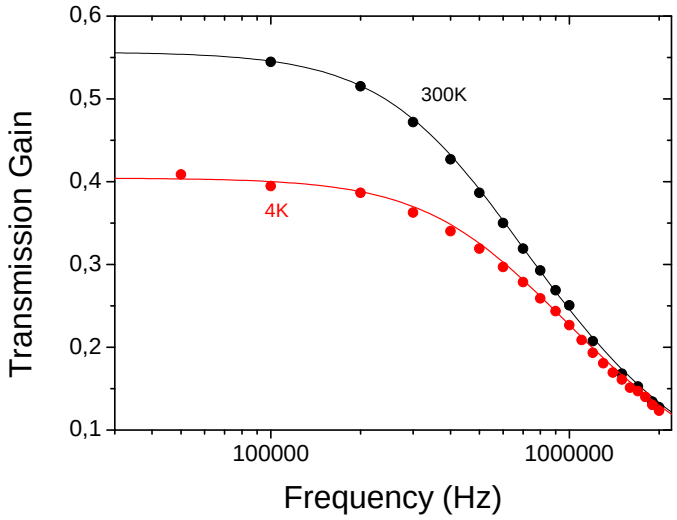

Figure 2.20: total transmission amplitude gain $|G(\omega)|$ of the transmission line with a 150 µm long NEMS inserted, at room temperature (black dots) and helium temperature (red dots). Solid lines are fits to a simple RC circuit model through Eq. (2.51).

resistance measured at room temperature with 4-wire technique $R_N = 1.3\ \mathrm{k}\Omega$. At room temperature, the only free parameter is then the total line capacitance $C = 530$ pF. Down to liquid helium temperatures, we fit a NEMS resistance $R_N = 730\ \Omega$ at 4.2 K. This gives a Room temperature Resistivity Ratio (RRR) between 300 K and 4.2 K of 1.78. Typical RRR measured in this work vary between 1.1 and 2.5, which is consistent with previous works. Note that the metallic layer becomes superconducting below $1.2 - 1.4$ K (the critical temperature of aluminum tends to increase as the thickness is decreased).

2.8.2 Characterization of the injection and detection lines

To obtain the injection coefficient $|G_I(\omega)|$ independently from the global transmission, we use the following technique: while the usual drive current is applied around the resonance frequency, a strong heating current I_h will be added at a frequency ω_h off-resonance. For this we use a homemade additioner, of bandwidth 100 MHz and gain 1. By Joule effect, a heat load will flow through the beam, resulting in a temperature increase. The thermal model at stake is analyzed in Section 2.7. Here we will simply use the fact that heating the structure will shift its resonance frequency towards low frequencies.

- For $\omega_h \to 0$ (DC heating), we assume that there is no loss: $G_I(\omega_h \to 0) = 1$. The actual current flowing through the beam is then the calculated current $I_h = V_{in,h}/(R_b + R_N)$. The measured shift of the resonance frequency $\delta\omega_0[I_h(0)]$ due to Joule heating will then serve as a reference curve (see Fig. 2.19).
- For $\omega_h \neq 0$, $|G_I(\omega_h)| \neq 1$ as a consequence of losses and/or reflections in the line, so the actual current flowing through the device is not the calculated one. This current will nonetheless heat the device, so we can have access to its actual value, by simply rescaling the calculated heating current $I_h(\omega_h)$. The scaling factor will be by construction the injection factor $|G_I(\omega_h)|$ such that the resonance shift curve $\delta\omega_0[|G_I(\omega_h)|I_h(\omega_h)]$ will collapse on the reference curve $\delta\omega_0[I_h(0)]$.

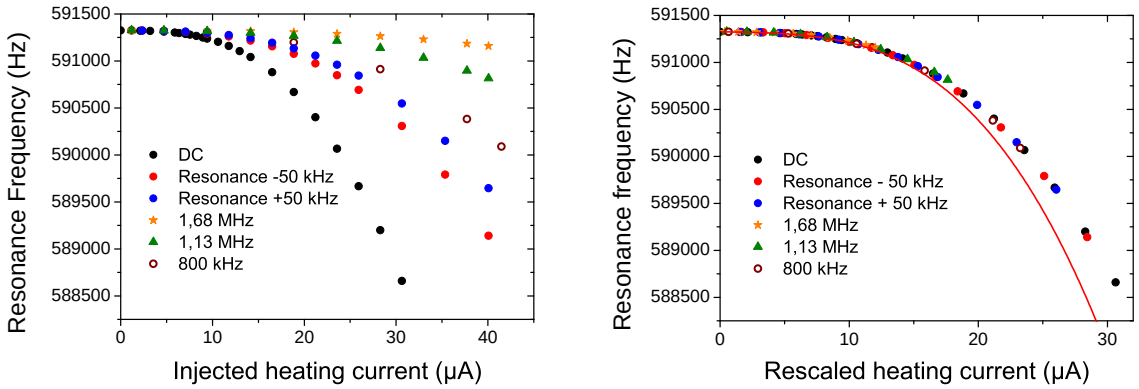

Figure 2.21: left: shift of the resonance frequency as a function of the injected heating current applied at different frequencies (see legend), without applying a rescaling factor. Right: shift of the resonance frequency as a function of the same heating currents, with a rescaling factor. For each heating current frequency, a different rescaling factor is applied, so that all the data collapse on the DC heating curve. The line is the same as in Fig. 2.19.

An example of this procedure is shown in Fig. 2.21. To each dataset corresponding to one heating current frequency, a scaling factor is applied on the current injected, to obtain the actual current flowing through the beam.

The main advantage of this technique is to rely only on genuine (and local) properties of the device, that unequivocally depend on the amount of heating current passing in the metallic layer. Moreover, while we derived a thermal model that accounts fairly well for the observations in presence of a moderate heating current, it is not crucial, as the calibration procedure is **relative** to the DC transmission, which is 1 by definition. Thus, the accuracy on the measured injection loss coefficient value is very good, within ± 5 %.

However this technique has got one drawback for doubly-clamped beams. This class of structure experiences a rather strong nonlinear behaviour (see Section 2.9 below), so possible nonlinear mixing effects (such as the self-coupling scheme described in [61]) can arise if ω_h is too close to the resonance frequency. To prevent this situation to happen the characterization around resonance frequency is made with detunings from ω_0 of about ± 10 kHz at least, while $G_I(\omega_0)$ is deduced by interpolation. In addition, since thermal properties are field-independent, we repeat the procedure for several magnetic fields to rule out non-linear mixing effects that would depend on the magnetic field, since they are of mechanical origin. The actual force exerted on the beam then writes:

$$F_{L,n}(\omega) = \xi_n l B \frac{|G_I(\omega)| V_0}{R_b + R_N}. \tag{2.53}$$

Knowing the injection factor $|G_I(\omega)|$, we can now express the actual force exerted on the beam in real units. And since we know the global factor as well, we also have a direct access to the detection coeffictient $|G_D(\omega)|$:

$$|G_D(\omega)| = \frac{|G(\omega)|}{|G_I(\omega)|}. \tag{2.54}$$

Knowing the detection coefficient, we can now obtain the displacement of the beam in **real units**:

$$x(\omega) = \frac{V_{out}(\omega)}{i\omega \xi_n l B |G_D(\omega)|}. \tag{2.55}$$

Thus, our calibration procedure should in principle leave no ambiguity on the applied forces or measured displacements. However, a cross-talk effect is often observed in practice between the injection and the detection line. While this is taken into account by construction for the injection line calibration, this limits our ability to determine with precision the detection line coefficient, and discrepancies up to a 40 % deviation to the expected value have been observed on occasion. Note also that while the RC circuit modelling is rather accurate for (sub-)MHz beams, it breaks down around 10 MHz as the electrical signal wavelength in the circuit becomes comparable with the

total cable length (a few meters): it leads to the formation of standing wave patterns, i.e. parasitic electrical resonances in the transmission because of the reflected signal due to impedance mismatch.

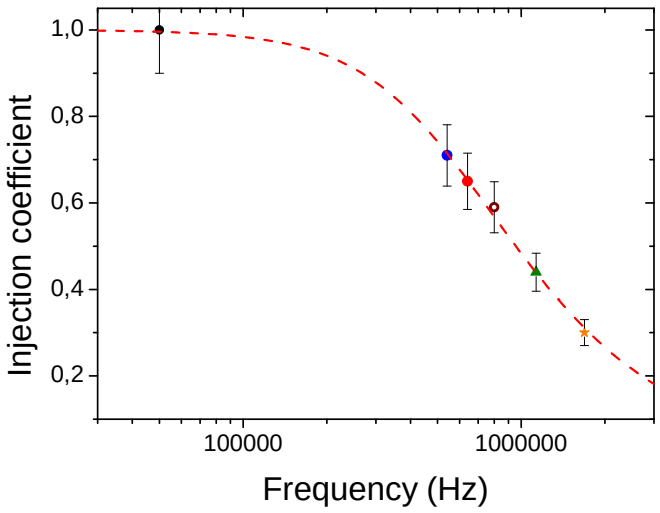

Figure 2.22: Injection losses as a function of frequency with a 300 µm long NEMS resonating at 591 kHz, with a resistance in the metallic layer $R_N = 1.1$ kΩ. The data are obtained from the scaling factors used to produce Fig. 2.21, with corresponding colors and shapes for data points. The dashed line is a fit from a RC circuit modelling, with a capacitance fit parameter $C = 550$ pF.

Nonetheless, we have another way to determine the detection coefficient accurately, assuming that all parameters are known otherwise. At resonance, the relation (2.23) links the applied force (calibrated, with known injection coefficient) and the displacement (which should be obtained through the detection coefficient), through the resonance linewidth, which is measured. Then, the linewidth can be recalculated with a detection coefficient left as a single free parameter:

$$\Gamma_{\text{calc}} = \frac{F_0}{m_n \omega_n X_n(\omega_n)} = \frac{F_0}{m_n} \left| \frac{\xi_n l B G_D(\omega)}{V_{out}(\omega)} \right|. \tag{2.56}$$

Then, the actual detection loss coefficient is the one such that the recalculated linewidth matches the measured one. This self-consistent check enables to quantifying potential cross-talks in the detection line.

2.8.3 Capacitive tuning with a gate electrode

With our fabrication technique it is straightforward to design a sample with a metal-coated electrode placed in the vicinity of the resonator, with a gap between them that

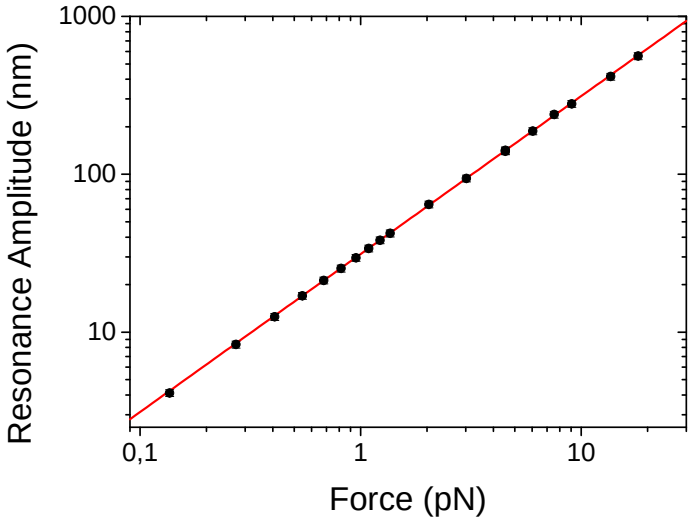

Figure 2.23: Typical linear response curve of a 300 µm NEMS. The red solid line is the application of Eq. (2.23), with a measured $Q = 12800$ and spring constant $k = 0.41$ N/m. Points at high amplitudes (≥ 50 nm) are taken in the nonlinear regime (see Section 2.9).

can reach values as low as 100 nm routinely. This so-called **gate electrode** forms with the beam a geometric capacitance with the vacuum gap in between acting as a dielectric medium. It can be used to tune properties of the mechanical resonator such as its resonance frequency or its nonlinear coefficients [62]. It can also be used as a transduction scheme based on dielectric forces [63], while one can think of it as a way to parametrically pump a mode [64] or couple two modes [24]. Here we present some of these aspects which will be useful for our work. The same calibration technique used before for the injection line applies to the capacitive line, so we do not describe it here. All further references to gate voltages concern the actual ones at the level of the electrode.

We name C_g the geometric capacitance created by the NEMS-gate electrode configuration. Applying a DC bias voltage V_0 on the gate electrode, the charging potential energy for the capacitance is:

$$E_C = \frac{1}{2} C_g V_0^2. \tag{2.57}$$

As the beam moves, electrostatic field lines are modified, in a non-uniform way, such that it creates a capacitance gradient. As a result, an electrostatic force is exerted on the beam:

$$\mathbf{F}_C = \frac{1}{2} V_0^2 \nabla C_g. \tag{2.58}$$

One can show that for flexural out-of-plane motion, in our geometry, the gradient in y and z direction is small [64], hence leading to very small forces applied to the beam in these directions. In the limit of small displacements, we can expand the capacitance gradient in the x direction at first order in displacement, which yields for the electrostatic force:

$$F_C^x = \frac{1}{2}V_0^2\left(\frac{\partial C_g(0)}{\partial x} + \frac{\partial^2 C_g(0)}{\partial x^2}x + \mathcal{O}(x^2)\right) \tag{2.59}$$

The first term is a static force which magnitude is in practice very small, and it does not affect substantially the NEMS dynamical behaviour. The high order terms lead to renormalizations of the NEMS nonlinearities, as they can be recasted as effective nonlinear terms in the dynamics equation [62]. Here we drop them in the modelling, but they can be used for instance with cantilevers, where they offer the possibility to tune with great precision e.g. the non-linear behaviour (as the intrinsic one is small in this case) [65].

The first order term can be recasted in the dynamics equation as a static modification $\delta k(V_0)$ of the bare spring constant k_0:

$$\delta k(V_0) = -\frac{1}{2}\frac{\partial^2 C_g(0)}{\partial x^2}V_0^2. \tag{2.60}$$

For small changes of the spring constant, the resonance frequency is then:

$$\omega_{res}(V_0) = \omega_0\sqrt{1 + \frac{\delta k(V_0)}{k_0}} \approx \omega_0 - \frac{1}{4m_0\omega_0}\frac{\partial^2 C_g(0)}{\partial x^2}V_0^2. \tag{2.61}$$

The parameter $\partial^2 C_g(0)/\partial x^2$ therefore characterizes the coupling strength between the gate electrode and the mechanical motion, and we can measure it through the resonance shift as a function of the gate voltage. One must take into account that trapped charges can exist on the gate electrode, leading to small offset voltages (see Fig. 2.24).

2.9 Basic nonlinear behaviour of nanomechanical systems

2.9.1 Geometric nonlinearity

When oscillating, any real beam undergoes a deformation. As such, because of the finite length of the beam and the boundary conditions for the oscillating motion (the displacement field must be zero at the clamps), some additional stretching will appear,

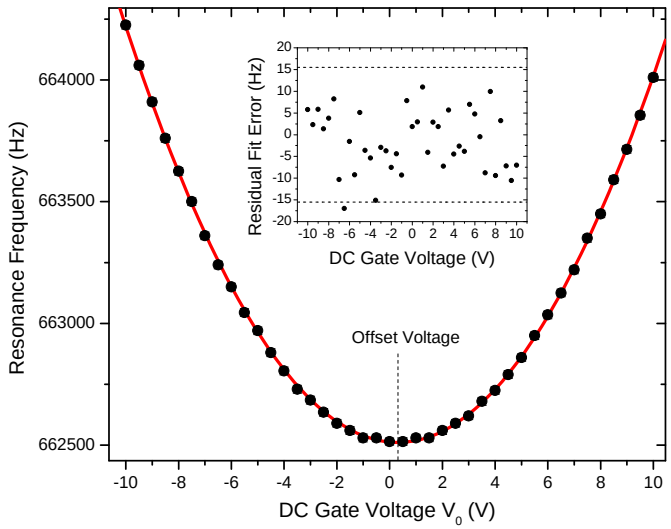

Figure 2.24: Main: shift of a 300 µm NEMS resonance frequency as a function of the bias voltage applied on the gate electrode. The red solid curve is a fit from Eq. (2.61), from which we obtain a coupling strength $\partial^2 C(0)/\partial x^2 = 4.3 \times 10^{-5}$ F/m^2. Note the voltage offset $V_{\text{off}} = 315$ mV added to consistently fit the whole data range. Inset: Residual error on the fit. All the error is contained into 10 % of the NEMS damping rate (see dashed lines).

hence an additional axial load (stress). This can be quantified from the curvature radius of the deformation $u(z,t)$, which is to be compared to the beam's length l.

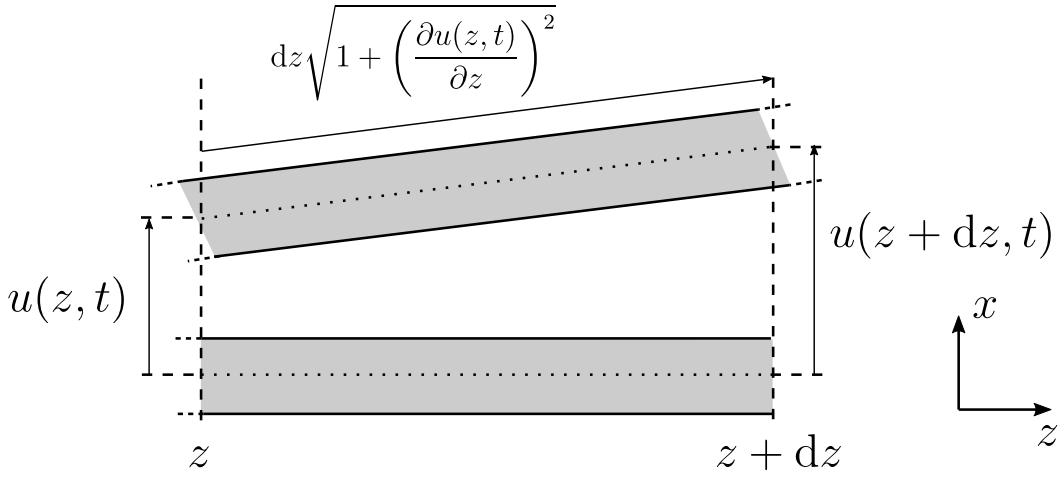

Figure 2.25: Behaviour of a local portion of the beam under deformation. The dotted line is the neutral axis, whose points only displace in the x direction [43].

Fig. 2.25 illustrates the elongation effect when considering a small portion of the beam: if one neglects shear effects, the neutral axis should be displaced only in the

x direction [43]. As the clamps impose a non-uniform displacement to the neutral axis, the latter stretches on each small portion, and for not too large deformations (compared to the portion length) its length is easily calculated at first order (see Fig. 2.25). If the deformation is small compared to the beam's length, the total length writes [29]:

$$l + \delta l = \int_l \sqrt{1 + \left(\frac{\partial u(z,t)}{\partial z}\right)^2} \mathrm{d}z \approx l + \frac{1}{2}\int_l \left(\frac{\partial u(z,t)}{\partial z}\right)^2 \mathrm{d}z. \tag{2.62}$$

This additional length creates additional stress according to Hooke's law. It can be recasted in Euler-Bernoulli equation (2.2), replacing the usual stress term:

$$EI\frac{\partial^4 u(z,t)}{\partial z^4} + \rho A\frac{\partial^2 u(z,t)}{\partial t^2} - A\left(\sigma + \frac{E}{2l}\int_l \left(\frac{\partial u(z',t)}{\partial z'}\right)^2 \mathrm{d}z'\right)\frac{\partial^2 u(z,t)}{\partial z^2} = 0. \tag{2.63}$$

Using the decomposition of the displacement field $u(z,t) = \Psi(z)x(t)$, we can obtain the dynamics equation for the displacement, which is that of an anharmonic oscillator with a non-linear restoring force acting on the beam:

$$F_{nl} = m\gamma x^3, \tag{2.64}$$

where γ is the non-linear interaction constant [29, 66]:

$$\gamma = \frac{E}{2l^2\rho}\left(\int_l \left(\frac{\partial \Psi(z)}{\partial z}\right)^2 \mathrm{d}z\right)^2. \tag{2.65}$$

Note that here the nonlinear constant is positive, meaning that the geometric nonlinearity is stiffening the resonator. For cantilevers the same effect would be softening, due to the contraction of the cantilever during its deflection [67]. However, in this case the situation is more subtle than for doubly clamped beams, and to date experimental results are not satisfactorily explained by the simplest 1D theories [68].

The nonlinear coefficient expression (2.65) can be well simplified in the case of a doubly-clamped beam in the high-stress limit, where $\Psi_n(z) = \sin[(n+1)\pi z/l]$:

$$\gamma = \frac{(n+1)^4 E\pi^4}{8l^4\rho}. \tag{2.66}$$

2.9.2 The Duffing oscillator

In good approximation, the main effect of geometric nonlinearities, from a single mode perspective, can be encompassed in the so-called **Duffing model**. A more exhaustive analysis is proposed in Ref. [69], that takes into account non-linearities for damping

and inertial terms. Here we focus on the main geometric effect, which appears through a non-linear restoring force cubic in displacement:

$$m\ddot{x} + m\Gamma\dot{x} + m\omega_0^2 x + m\gamma x^3 = F(t). \tag{2.67}$$

Here γ is the non-linear coefficient. Solving directly Eq. (2.67) is no easy task. The cubic term will generate, from a monochromatic forcing $F(t) = F_0\cos(\omega t)$, a multifrequency response: a sum of a static term, the ω response, and harmonics at $\pm\ 3\omega$...to capture this, we write a generic displacement ansatz in the Fourier basis, following Landau and Lifshitz [70]:

$$x(t) = \sum_{n=0}^{+\infty} \left[x_n^c(\omega)\cos(n\omega t) - x_n^s(\omega)\sin(n\omega t)\right]. \tag{2.68}$$

Injecting this ansatz in Eq.(2.67) and projecting the result onto the Fourier basis components, one can in principle fully solve the equation. This task is tedious, and one can show that in the high-Q limit, at leading order, only the term $n = 1$ is relevant, the other amplitudes decreasing as $1/Q^n$. This is an adiabatic approximation, meaning that the Duffing non-linearity essentially does not allow at first order any energy flow from the fundamental response to higher-order harmonics. Within this approximation, in the frequency domain, the oscillation amplitude can be written in a self-consistent way:

$$x(\omega) = \frac{F_0}{2m\omega_0\big(\omega_0 - \omega + \beta|x(\omega)|^2 + i\Gamma/2\big)}. \tag{2.69}$$

In other words, the Duffing non-linearity introduces a correction to the mechanical linear susceptibility, which scales as $|x|^2$. Experimentally, the Duffing term will result in distorted lineshapes, as shown in Fig. 2.26.

We choose to name $\beta = 3\gamma/(8\omega_0)$ the Duffing coefficient, as it is immediately accessible experimentally. Indeed, in the high-Q limit (always valid in the present work), the renormalized resonance frequency writes:

$$\omega_{res} = \omega_0 + \beta|x_{max}|^2. \tag{2.70}$$

It is then easy to extract a non-linear coefficient β by measuring the resonance shift with an increasing driving force, hence an increasing resonance amplitude. An example is given in Fig. 2.27. A quadratic fit from the Duffing model agrees well with the experiment, which allows us to extract a β coefficient with a good accuracy. Note, however, that at this stage of the calibration, the discrepancy between a theoretical value of β and the measured value can reach 20 %. This can be due to accumulated small errors

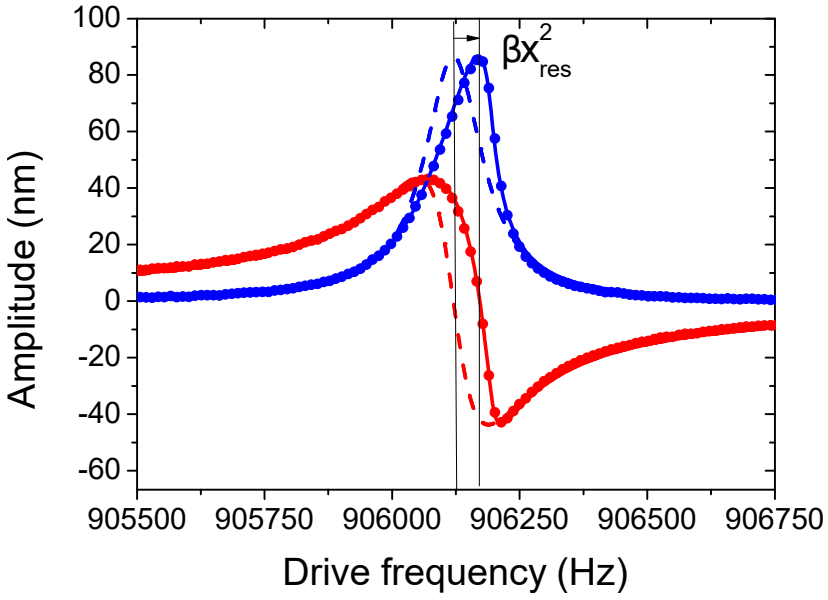

Figure 2.26: Typical response in the non-linear regime, with the same device as Fig. 2.15. The measured line shape is distorted, with a resonance frequency shift described by Eq. (2.70) and $\beta = 8.5$ mHz/nm^2. Solid lines follow Eq. (2.69). The dashed lines are fits for the same amplitude with the non-linear interaction term of Eq. (2.69) removed, as a guide for the eye.

in the calibration procedure, as well as the uncertainty on materials properties such as Young modulus or internal tensile pre-stress. As far as experimental results are concerned, we will use the measured value to quantitatively address nonlinear phenomena in the following.

Knowing the β coefficient, we can now fit the distorted lines without free parameter. Indeed, for maximum amplitudes below a critical threshold x_c, Eq. (2.67) possesses only one analytic solution in real space. A typical application is shown in Fig. 2.26. Moreover, one cannot directly extract a damping coefficient through the linewidth. However, Eq. (2.23) is still valid if one substitutes ω_n with the Duffing-shifted resonance ω_{res}. Then, one can extract the actual damping even in the non-linear regime, through the recalculated nonlinear linewidth.

Above a certain maximum threshold amplitude x_c corresponding to an applied force F_c such that $x_c^2 = \frac{\sqrt{3}\Gamma}{2\beta}$, the self-consistent equation (2.69) possesses 3 solutions in real space. We will always refer to them in an implicit way, as their expressions are tedious to manipulate even though they are analytic. Physically, this threshold corresponds to a Duffing frequency shift that becomes comparable with the damping rate. This multi-valued zone adds a great deal of physical complexity, and can be useful as a model system to study non-trivial nonlinear dynamics, such as the bifurcation phenomenon [13, 12, 71]. Some of these aspects will be addressed in Chapters 3 and 6.

If we study in detail the stability of these three possible states, we see that two of

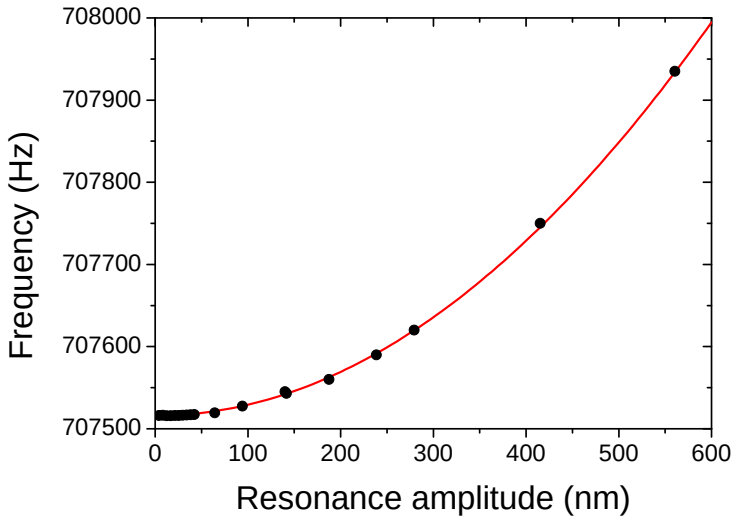

Figure 2.27: Typical shift of the resonance frequency due to the Duffing interaction (same device as the previous figure). The red solid line is a fit from Eq. (2.70), with an extrapolated zero-displacement frequency 707516 ± 5 Hz and a Duffing coefficient $\beta = 1.33$ mHz/nm^2.

them correspond to stable orbits in the phase space (the so-called attractors), while the third one is an unstable state. In the coexistence zone, for a given driving frequency, the system can jump by thermal activation from one stable state to the other. The critical point F_c beyond which a coexistence region appears is called the **spinodal point**. If one measures the response at a given force F_0 beyond the spinodal point, sweeping the frequency upwards or downwards will not give the same results, as the system is initially prepared in the most energetically favorable state, which is not the same whether one sweeps upwards or downwards. Thus, experimentally, a hysteretic behaviour is observed, as shown in Fig. 2.28.

This hysteresis is delimited by two frequencies $\omega_{bif,\uparrow}$ and $\omega_{bif,\downarrow}$. At the hysteresis opening ($F_0 = F_c$), we have $\omega_{bif,\uparrow} = \omega_{bif,\downarrow}$, but $\omega_{bif} \neq \omega_{res}$. The underlying phenomenology around these peculiar points will be detailed in Chapters 3 and 6. Here, we just mention that at these frequencies sharp jumps are observed in the response. This corresponds to one metastable state merging with the unstable one, thus becoming unstable, as shown in Fig. 2.29. Hence only one state becomes possible at these frequencies and outside the hysteresis zone: the merging maps the transition from three motional solutions to only one, and can be viewed as an example of **saddle-node bifurcation**, where two stable states correspond to potential wells, separated by a potential barrier (the saddle).

The properties of the bifurcation process and the spinodal point will be exploited further in Chapters 3 and 6.

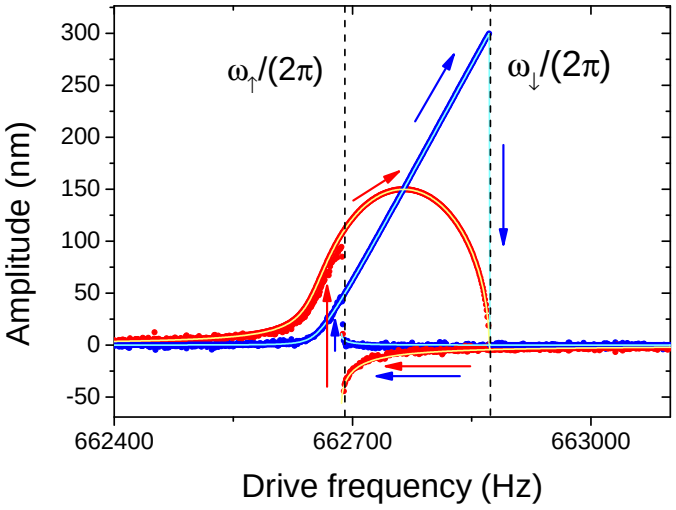

Figure 2.28: example of bistable response for a 300 µm string. The hysteretic region is located between the two bifurcation frequencies $\omega_{\uparrow,\downarrow}$. Solid lines are fits from the solutions of Eq. (2.69), with a Duffing coefficient $\beta = 2.75$ mHz/nm^2.

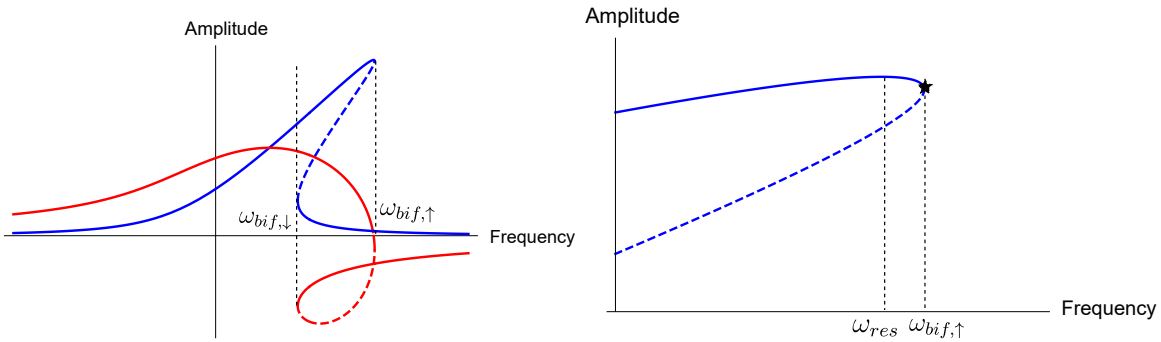

Figure 2.29: left: bistable response, where the dashed line represents the unstable state. Right: zoom in the bifurcation region where the upper branch metastable state and the unstable state merge.

2.9.3 Dispersive mode coupling

It is straightforward to realize that the mechanism responsible for the Duffing nonlinearity will also break the eigenmodes orthogonality, since the geometric nonlinearity is a **global** tensioning effect. As such, it couples different eigenmodes, dispersively at first order, i.e. there is no energy flow from one mode to another. If we assume that two modes m, n are excited, they are coupled through a biquadratic potential:

$$V_{m,n} = \frac{3}{4}\gamma_{m,n} x_m^2 x_n^2, \tag{2.71}$$

with $\gamma_{m,n}$ being proportional to the overlap of two different modes profiles. It has a similar expression to the non-linear constant, which owes to their common origin:

$$\gamma_{m,n} = \frac{E}{l^4\rho}\left(\frac{I_{n,n}I_{m,m}}{2} + I_{m,n}^2\right), \tag{2.72}$$

where $I_{m,n} = \int \Psi'_n(z)\Psi'_m(z)\mathrm{d}z$. The most natural configuration to witness this coupling will be that a mode m will undergo a strong excitation (a **pump** tone) at its resonance frequency ω_m while the mode n will be weakly excited, acting as a **probe**. Indeed, the resulting non-linear restoring force $F_{n,m}$ exerted on the probe mode can be derived from the coupling potential energy (2.71):

$$F_{m,n} = -\frac{\partial V_{m,n}}{\partial x_n} = -\frac{3}{2}\gamma_{m,n}x_m^2 x_n. \tag{2.73}$$

With an adiabatic treatment similar to that of Section 2.9.2, one can discard fast oscillating terms appearing in the dynamics equation with this non-linear force. We are then left with the following mode n mechanical response:

$$x_n(\omega) = \frac{F_0}{2m_n\omega_n\left[(\omega_n - \omega + \beta_{m,n}|x_{m,res}|^2)^2 + i\Gamma_n/2\right]}, \tag{2.74}$$

with $\beta_{m,n} = 3\gamma_{m,n}/(4\omega_n)$. Note that while $\gamma_{m,n} = \gamma_{n,m}$, this does not hold for the β factors, which depend also on the probe mode's frequency. Assuming that the pump amplitude stays constant, the effect on the probe mode is just a shift of its resonance frequency depending quadratically on the pump resonant amplitude [72, 73, 67] :

$$\omega_{n,res} = \omega_n + \beta_{m,n}|x_{m,res}|^2. \tag{2.75}$$

One can then quite easily measure the coupling strength given by the factor $\beta_{m,n}$. An example is shown on Fig. 2.30. As for the Duffing coefficient, our measured mode coupling factors are usually in good agreement with theoretical expressions, again within 20 % for the same reasons as in paragraph 2.9.2. While being another proof of robustness of our calibration procedure, these mode coupling constants measurements are also useful when it comes to quantitatively address the phenomena described in Chapter 3.

2.9.4 The parametric amplification scheme

We have seen in section 2.8.3 that a gate electrode enables additional control of the nanomechanical beam through e.g. resonance frequency tuning. If now the ap-

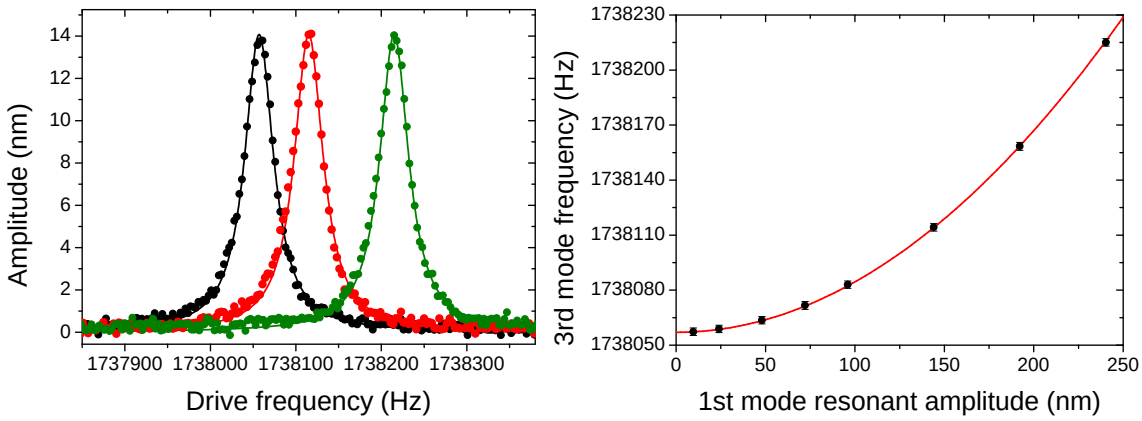

Figure 2.30: left: third mode in-phase resonance lines of a 300 µm NEMS while the first mode is resonantly excited, with a resonant amplitude $x_{1,res} = 10$ nm (black), 144 nm (red), 240 nm (green). Solid lines are Lorentzian fits, all having the same height and width. Right: shift of the resonance frequency as a function of the 1^{st} mode resonant amplitude. The red solid line is a quadratic fit, yielding a mode coupling coefficient $\beta_{1,3} = 2.75$ mHz/nm^2.

plied voltage V_g on the gate is modulated in amplitude at a frequency ω', such that $V_g = V_0 + V_m \cos(\omega' t + \phi_g)$, the result will be a periodic modulation of the NEMS spring constant i.e. of the linear restoring force. Indeed Eq. (2.60) becomes:

$$\delta k(t) = -\frac{1}{2}\frac{\partial^2 C(0)}{\partial x^2}\left[V_0^2 + \frac{V_m^2}{2} + 2V_0 V_m \cos(\omega' t + \phi_g) + \frac{V_m^2}{2}\cos(2\omega' t + 2\phi_g)\right]. \quad (2.76)$$

If one chooses to modulate at $\omega' = 2\omega$ where ω is the magnetomotive excitation frequency, the last term in Eq. (2.76) will yield fast oscillating terms in the dynamics and can be dropped. The first two DC terms correspond to the situation described in the previous paragraph, where the AC amplitude is a correction to the usual DC frequency shift. Of utmost interest is the middle term. It corresponds to a modulation around twice the resonance frequency, analogous to a child's swing motion which is sustained by the child's legs moving at half the swing period. It is then possible, for certain conditions in phase, to amplify or reduce the motion in certain directions in the phase space. This is the so-called **parametric amplification** scheme, since a parameter (mass, spring, damping) is modulated to enhance the dynamics. Note that the scheme can be implemented for modulation frequencies $\omega' = 2\omega/n$, yet the 2ω modulation avoids additional resonant forces that would be superposed with the magnetomotive scheme. Dropping the non-resonant term, with $k = k_0 - 1/2 \times \partial^2 C/\partial x^2 (V_0^2 + V_m^2/2)$, the dynamics equation becomes:

$$m\ddot{x} + m\Gamma\dot{x} + [k + \delta k_0 \cos(2\omega t + \phi_g)]\, x = F_0 \cos(\omega t + \phi_0), \quad (2.77)$$

where $\delta k_0 = -\partial^2 C/\partial x^2 V_m V_0$. To solve this non-linear equation in x one can use again

the ansatz (2.68). An exhaustive solving is proposed in [64]. Here we focus on the resonant terms, which are dominant in the dynamics. At resonance, the amplitude is renormalized by a factor which depends on the phase of the modulation signal ϕ_g and its amplitude, which we write in a normalized form $\mathrm{h} = \frac{\delta k_0}{2k} Q$:

$$x(\omega_{res}) = \frac{F_0 Q}{k} \sqrt{\frac{\sin^2\left(\frac{\pi}{4} + \frac{2\phi_0 - \phi_g}{2}\right)}{1+\mathrm{h}^2} + \frac{\cos^2\left(\frac{\pi}{4} + \frac{2\phi_0 - \phi_g}{2}\right)}{1-\mathrm{h}^2}}. \tag{2.78}$$

We can see that the appropriate choice of phase parameter $\phi = \phi_0 - \phi_g/2$ allows one to either amplify or squeeze the resonant amplitude. Maximum squeezing (+) or amplification (-) occur for $\phi = \pm\pi/4$, with the two quadratures writing:

$$\begin{cases} X(\omega) &= \dfrac{F_0}{m} \cdot \dfrac{\omega\Gamma\,(1 \mp \mathrm{h})}{(\omega_{res}^2 - \omega^2)^2 + \omega^2\Gamma^2(1-\mathrm{h}^2)}, \\ Y(\omega) &= \dfrac{F_0}{m} \cdot \dfrac{\omega_{res}^2 - \omega^2}{(\omega_{res}^2 - \omega^2)^2 + \omega^2\Gamma^2(1-\mathrm{h}^2)}. \end{cases} \tag{2.79}$$

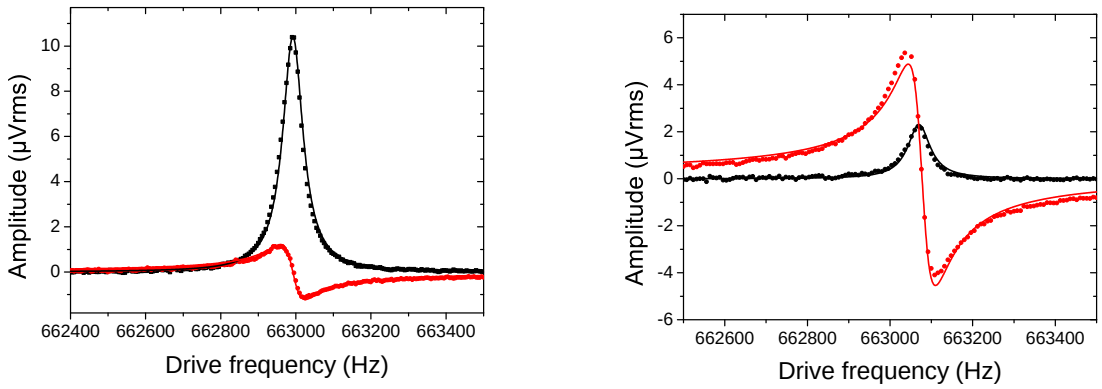

Figure 2.31: typical resonance lines measured on a 300 μm NEMS in the parametric amplification ($\phi = -\pi/4$, left panel) and squeezing ($\phi = +\pi/4$, right panel) regimes, for the same pumping factor h, with resonant displacement amplified by a factor 4.75 and squeezed by a factor 1.75, respectively. Solid lines are fits from Eq. (2.79) with $\mathrm{h} = 0.77$.

The two quadratures are then asymmetrized, as seen in Fig. 2.31. Note that whether motion is amplified or squeezed, in both cases, the in-phase response is still a Lorentzian in the high-Q approximation, with renormalized amplitude and linewidth:

$$\begin{cases} X(\omega_{res}) &= \dfrac{F_0 Q}{k} \cdot \dfrac{1}{1 \pm \mathrm{h}}, \\ \\ \Gamma_r &= \Gamma\sqrt{1-\mathrm{h}^2}. \end{cases} \tag{2.80}$$

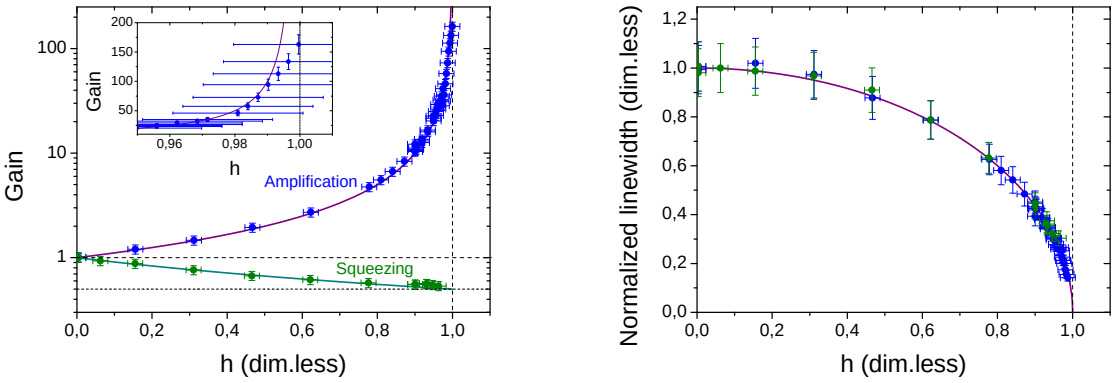

Figure 2.32: left: gain in parametric amplification (blue dots) and squeezing (green dots) regimes for the same device as in Fig. 2.31 as a function of the pumping factor h. Error bars on h are estimated from typical offset voltage fluctuations on the gate of about 5 mV. Solid lines reproduce Eq. (2.80) for the resonant amplitude. Inset: zoom on the $h \to 1$ region. Right: effective linewidth normalized to the zero pumping value, with the same conventions as left panel. The purple solid line follows Eq. (2.80) for the renormalized linewidth.

In addition, we see that in both cases, for both quadratures, the effective linewidth goes to zero the same way as $\mathrm{h} \to 1$. That, and the divergence for the same limit in the amplification case, indicate that there is an instability appearing at $\mathrm{h} = 1$. This is the threshold for the transition to the parametric oscillation regime, where oscillations are self-sustained.

Close to the threshold, the resonant amplitude, as well as the effective Q factor, are supposed to diverge in the parametric amplification regime. However, saturations are observed, which are due to nonlinearities, either geometric [29] or coming from the anelasticity of the constitutive materials. Here, gains up to 100 were measured in a perfectly linear regime, as shown in Fig. 2.32 (left panel). A saturation seems to appear beyond a pump factor $\mathrm{h} = 0.99$ (Fig. 2.32, left panel inset). However, one must be cautious in analyzing its origin: voltage fluctuations on the gate at the mV scale as well as errors of even a few percent in the pump phase setting can lead to increasingly dramatic errors in h close to the threshold, as discussed in Ref. [64]. This is captured in the error bars, which are big even for large DC bias voltages on the gate (5 V at best).

2.10 Conclusion and perspectives

In this chapter the basics of our experimental techniques along with some necessary theoretical grounds have been described. Their purpose is to set safe grounds for more sophisticated model studies which will be detailed in the chapters to come. Indeed, they rely on careful, comprehensive calibrations, and our procedure can allow one to obtain unprecedented agreements between experimental data and theoretical models without need of free parameters. Therefore, in the following, measurements will be presented calibrated as much as possible, that is, in real units. Future works on other actuation and detection schemes such as the capacitive ones [63] can nonetheless be considered. Even with the magnetomotive scheme, tilting the sample holder at 45° should allow to address mode coupling between two flexural modes of different families of nearby frequencies, in the same fashion as Refs. [23, 24] where energy can be exchanged between the two modes, acting as a classical two-level system that can be driven coherently.

Despite the characterization of external electrical damping, the issue of the fundamental origin of damping mechanisms was eluded in this chapter. The dissipation measured between 1 K and 30 K is almost constant, which is a characteristic feature of dissipation mediated by two-level systems in the framework of the Standard Tunneling Model. In the third part of this manuscript these mechanisms are investigated with more details, especially below 1 K. In addition, unusual features observed for gas damping will also be reported, that are attributed to the interaction with a gas in confined geometries.

Last but not least, these characterizations provide us with a solid basis to embed beam-based NEMS structures in more sophisticated detectors that can operate at the quantum limit, to eventually reach the quantum ground state of motion [18]. For this purpose, dedicated actuation/detection schemes are needed, by far more sensitive than the magnetomotive scheme and also enabling quantum-limited operations [19].

2.11 Résumé en français

Dans ce chapitre, nous introduisons d'une part les techniques nécessaires à la conduite de nos expériences, d'autre part les bases théoriques permettant l'utilisation de modèles plus complexes introduits par la suite. Nous présentons le procédé de fabrication en salle blanche de nos nano-poutres doublement encastrées ainsi que les outils cryogéniques et électroniques permettant de les manipuler à basse température, aussi bien à 4 Kelvin qu'en dilution. Nous présentons également la technique magnétomotive utilisée pour mettre en mouvement la structure ainsi que pour détecter ce mouvement. Ce mouvement est décrit en premier lieu par la mécanique des poutres et la décomposition modale dans l'équation d'Euler-Bernoulli découlant des conditions aux limites imposées par la géométrie du système. Afin d'obtenir des quantités

en unités réelles (force appliquée en Newton, amplitude détectée en mètres), nous décrivons une technique de calibration in-situ du résonateur, reposant sur le chauffage local dû à la circulation d'un fort courant électrique dans la couche métallique déposée sur la poutre. La fiabilité de cette procédure est testée avec la caractérisation sans paramètre ajustable de phénomènes non-linéaires tels que le tirage de fréquence et le couplage de modes mécaniques de vibration, qui ont pour origine le raidissement d'une poutre doublement encastrée subissant une déformation, ou l'accordage de fréquence et l'amplification paramétrique rendus possibles par la modulation de fréquence obtenue par couplage électrostatique de la poutre à une électrode de grille. L'accord obtenu est excellent, ce qui nous permet entre autres d'invoquer ces phénomènes de façon quantitative dans les chapitres à venir. Les phénomènes de dissipation électro-mécanique sont brièvement introduits à travers l'étude de l'amortissement causé par les courants induits par la technique magnétomotive. Certains mécanismes mal connus à ce jour causant l'amortissement mécanique seront approfondis dans la dernière partie de ce manuscrit.

Part I

Non-linear fluctuating model NEMS

Chapter 3

Interplay between non-linear dynamics and position fluctuations

Contents

3.1 Introduction

The present chapter, together with the next one, attempts to propose an in-depth, quantitative study of a phenomenon which is ubiquitous in vibrating nanostructures: frequency fluctuations. Identifying intrinsic frequency noise sources in vibrating resonators has drawn a lot of attention recently for essentially two reasons. The first one is obviously of practical nature: a huge effort in the two last decades has been made on using nanomechanical systems as mass sensors [74], with increasingly good accuracy, to a tremendous mass sensitivity at the proton level [10]. This last point relies crucially on the frequency resolution of a mechanical oscillator: a change in the resonator's mass due to e.g. a single protein sticking on it provokes a small change of its eigenfrequency. Thus, damping must be minimized, but also dephasing of the mechanical signal, as it also leads to spectral broadening [75]. In particular, while being promising candidates due to their extremely low mass, graphene and carbon nanotubes mechanical resonators suffer a lot from excess spectral broadening. Several papers in the last few years have addressed the issue, e.g. Refs. [32, 76, 77], while signatures of noise which does not fall into known sources and whose origin remain unclear [78] have been reported. But on a more fundamental basis, these can lead to elegant, in-depth experimental studies. The stochastic behaviour of (nano-)mechanical systems is in itself a teeming topic: recent theoretical and experimental studies have shown that their dynamics when coupled to various noises sources is highly non-trivial and requires subtle descriptions [79, 80, 15, 81, 31], which go far beyond the mere technical issue of stability.

In the following Chapter we focus on one mechanism which is ubiquitous in micro/nanomechanical systems: thermal position fluctuations experienced by the resonator are transduced through geometric, dispersive non-linear interactions (Duffing and mode-coupling) into frequency fluctuations. This interplay between position fluctuations and non-linearities has already been addressed experimentally in a few papers [14, 30], but always in a limited range, which always prevented previous studies to obtain a full description of the problem. Here, we take advantage of our experimental schemes to address the physics over an unprecedented wide range. While the temperature is artificially tuned, the mechanism is deeply intrinsic, as all nanomechanical structures present some geometric non-linearity. Our experimental findings are captured by a theoretical description largely based on Ref. [31], which we try to explain in simple terms here. An effort is made on drawing parallels with Nuclear Magnetic Resonance (NMR), with whom the studied phenomenon shares some common features. We also propose a derivation of an ultimate limit to frequency resolution imposed by

this mechanism, which appears to be significant for low-mass, low-stress structures such as carbon nanotubes. Finally, we extend experimentally the study to the bistable regime of the NEMS response, where position fluctuations are themselves modified by the Duffing nonlinearity, revealing a great richness especially close to bifurcation and spinodal points [82]. Our discussion on this last point will nonetheless stay at a phenomenological level and ignore the frequency fluctuation aspect.

3.2 Fluctuation-dissipation theorem

As discussed previously, the NEMS is not isolated from its environment: phonons of the resonant mode are coupled to different thermal baths, among which bulk traveling phonons (coupling through the clamps), electrons in the metallic layer and external impedances, defects, two-level systems, etc. These are all couplings to uncontrolled degrees of freedom, towards which the resonator dissipates kinetic energy in an irreversible way while moving. This irreversibility appears through the first derivative in the dynamics equation, which breaks time-reversal symmetry. The coefficient Γ associated to the first derivative term is a phenomenological quantity, the damping rate, i.e. the rate at which the system will return to equilibrium after a small perturbation by losing energy towards these degrees of freedom. From a macroscopic perspective, an analogous Mathiessen's rule makes this electromechanical damping rate the sum of the damping rates assigned to each bath:

$$\Gamma = \sum_{\{\mu\}} \Gamma_\mu, \tag{3.1}$$

where the sum is formally made over all dissipative channels. Here we assume that all baths degrees of freedom are statistically independent. A more detailed discussion on microscopic mechanisms from which damping channels emerge will be given in the next part. As mechanical energy is dissipated, it is converted into heat to its surroundings, which in turn favours scattering between bath constituents and mode phonons: such processes thus turn heat (which is incoherent) into kinetic energy by creating a random motion, the well-known Brownian motion.

In the canonical picture of Brownian motion, the position of a potential-free motion variable follows standard diffusion laws and its average spatial extension grows with time as $\sqrt{t}$. In our case, the resonator's collective mode variable $x(t)$ also experiences Brownian motion, however its spatial extension remains confined within the restoring potential, as the latter counteracts the diffusion process. On timescales larger than Γ^{-1}, the spatial extension $\Delta x^2 = \langle x^2 \rangle$ keeps a finite, constant value. Note that here brackets indicate statistical averaging over realizations of the Hamiltonian; yet the ergodicity principle ensures that for long measurement times $\gg \Gamma^{-1}$, time averaging is equivalent to statistical averaging. The spatial extension is easily obtained through

the equipartition theorem: the mean potential energy $U = m\omega_0^2\langle x^2\rangle/2$ associated to the motional degree of freedom x is $k_BT/2$, and therefore:

$$\Delta x^2 = \frac{k_BT}{m\omega_0^2}. \tag{3.2}$$

We see that the same mechanism links Brownian motion (position fluctuations) and damping (energy dissipation). This link has been mathematically demonstrated in a more general context by several authors in the 20$^{\text{th}}$ century [83, 84], and constitutes the **fluctuation-dissipation theorem**, referred to as FDT in the following. It states that the autocorrelation function, which quantifies the resonator's position fluctuations at thermodynamic equilibrium, is proportional to the retarded (i.e., dissipative) response of the system to an external perturbation. Assuming we are in the linear response regime, in the classical limit $\hbar\omega \ll k_BT$, the FDT writes in the frequency domain [84] for a degree of freedom x with a susceptibility χ:

$$S_x(\omega) = \frac{2k_BT}{\omega}\mathrm{Im}\left[\chi(\omega)\right], \tag{3.3}$$

where S_x is the power spectral density of position fluctuations, i.e. the spread in frequency of the position noise power. Wiener-Khinchin theorem establishes that it is merely the Fourier transform of the autocorrelation function $\langle x(t)x(t+\tau)\rangle$, which is characteristic of the fluctuations, acting a "memory":

$$S_x(\omega) = \int_{-\infty}^{+\infty}\langle x(t)x(t+\tau)\rangle \mathrm{e}^{i\omega\tau}\mathrm{d}\tau. \tag{3.4}$$

On the other hand the imaginary part $\mathrm{Im}[\chi(\omega)]$ of the mechanical susceptibility in frequency domain corresponds to the retarded part of the susceptibility in time domain: thus it represents dissipation. Note that integration of the relation (3.3) leads to the equipartition theorem relation (3.2). It is also worth noticing that in the linear response regime one should have for the power spectrum:

$$S_x(\omega) = |\chi(\omega)|^2 S_F(\omega), \tag{3.5}$$

where S_F is the spectrum of the Langevin force F_{th} responsible for position fluctuations. We assume here that this force is zero on average, and is δ-correlated, which in fact is a requirement of the FDT: in the so-called Markovian approximation, the correlation time τ_b of any bath's degrees of freedom is assumed to be very small compared to the NEMS decay rate. Using the fact that $\mathrm{Im}[\chi(\omega)] = m\omega\Gamma|\chi(\omega)|^2$, or integrating Eq. (3.5), one obtains a quantitative expression for the spectrum of the equivalent Langevin force F_{th} exerted by the bath constituents on the resonator, responsible for

thermal fluctuations. This relation is often referred to as a second version of the FDT:

$$S_F(\omega) = 2m\Gamma k_B T. \tag{3.6}$$

Note that the amplitude of the Langevin force, as well as the position fluctuations (which are merely a linear filter to the force noise) are assumed to follow a Gaussian distribution: we have made the approximation that $\tau_b \ll \Gamma^{-1}$, and therefore statistics is made on an infinite number of independent collision events. This leads to Gaussian fluctuations through the central limit theorem.

3.3 Dispersive coupling to Brownian motion through geometric nonlinearities

3.3.1 General framework

The previous section concerns an ideal, linear system, e.g. a perfectly linear NEMS with uncoupled eigenmodes. However, this picture will partially break if one goes beyond linear response. In particular, the FDT as written in Eq. (3.3) is not valid anymore.

Let us now consider the case of a real structure, where geometric nonlinearities will impose *de facto* coupling between the different eigenmodes of the structures. The typical situation during our experiments will correspond to the case where we focus on the dynamics of a peculiar driven mode with index n. In the simplest case, the Hamiltonian describing the driven mode and encompassing the situation writes:

$$\mathcal{H} = \frac{p_n^2}{2m_n} + \frac{1}{2}m_n\omega_n^2 x_n^2 + \frac{1}{4}m_n\gamma_n x_n^4 + \frac{3}{4}m_n\sum_{m\neq n}\gamma_{m,n}x_m^2 x_n^2 - F_n x_n\cos(\omega t), \tag{3.7}$$

where $p_n = m_n\dot{x}_n$ is the momentum, F_n is the driving force amplitude, γ_n is the term describing the Duffing interaction, while the bi-quadratic terms in the sum together with their coefficients $\gamma_{m,n}$ account for the dispersive modal coupling to *all the other eigenmodes* by construction, as defined in section 2.9.3. One can obtain the global equation of motion of a mode n from a generalized Hamilton-Jacobi equation:

$$m_n\ddot{x}_n + \frac{\partial\mathcal{H}}{\partial x_n} = -m_n\Gamma_n\dot{x}_n + F_{th,n}(t). \tag{3.8}$$

The right hand side term describes phenomenologically the energy decay of the n-th resonator mode at a rate Γ_n into the thermal bath, which acts in return on the resonator's dynamics through the Langevin force $F_{th,n}$. A set of equations of motion for

each mode n is obtained through Eq. (3.8):

$$\ddot{x}_n + \Gamma_n \dot{x}_n + \omega_n^2 x_n + \left(\gamma_{n,n} x_n^2 + \frac{3}{2} \sum_{m \neq n} \gamma_{n,m} x_m^2 \right) x_n = \frac{F_{th,n}(t)}{m_n} + \frac{F_n \cos(\omega t)}{m_n}. \quad (3.9)$$

The last term on the left hand side acts as a global non-linear restoring force which directly translates the energy stored in the involved modes into frequency pulling through geometric nonlinearities as an anharmonic correction. As this sum is proportional to the displacement, nonlinear terms act, within this model, as a correction to the harmonic potential.

If now the energy stored in the modes is only of thermal origin (i.e. arising from the modes coupling to a thermal bath, see section 3.2), the displacement variables of all the undriven modes are noises. As a result, the thermal displacement noise on a mode is transduced as a frequency noise in another through nonlinear mode coupling and intra-mode coupling, i.e. Duffing nonlinearity.

3.3.2 Frequency noise correlator and spectral density

Before going deeper into calculations, it is useful to qualtitatively describe the frequency noise introduced in the previous section. In what follows, for the sake of simplicity we restrict ourselves to the case where one mode n is driven, with a certain response x_n, and coupled to only one another undriven mode m of amplitude δx_m. The response can also be coupled to its own fluctuations with the Duffing interaction term, in the same fashion as the intermodal coupling case, with simply a numerical renormalization factor. In fact, we will see later that our experimental scheme can allow us to address these ideal situations.

From above, we know that the mode m will create a frequency fluctuation $\delta\omega_{n,m} \propto \delta x_m^2$ on the probed mode. The autocorrelation function for this frequency noise can be obtained through Wick's theorem, separating a 4-point correlator into a sum involving only 2-point correlators:

$$\langle \delta x_m^2(0) \delta x_m^2(\tau) \rangle = \Delta x_m^4 + 2 \langle \delta x_m(0) \delta x_m(\tau) \rangle^2. \quad (3.10)$$

The corresponding noise spectral density is then readily obtained:

$$S_{x_m^2}(\omega) = \Delta x_m^4 \delta(\omega) + \frac{1}{\pi} \int_{-\infty}^{+\infty} S_{x_m}(\omega - \omega') S_{x_m}(\omega') \mathrm{d}\omega'. \quad (3.11)$$

The frequency domain expression gives an intuitive picture of the noise contributions. A sketch of the situation is represented in Fig. 3.1:

- The "δ-peak" term is a DC contribution which is simply the average value (first order moment) of the frequency fluctuations. Indeed, the position fluctuations of every mode have a Gaussian distribution centered in zero. Then, by construction, the frequency fluctuations are highly non-Gaussian and asymmetric, having a non-zero average value.

- The convolution term can be split into two parts. The high-frequency one, centered around $2\omega_m$, represents a variation on a timescale $(2\omega_n)^{-1}$ too short to be followed by the resonator whose dynamics is set on a timescale Γ_m^{-1}. As such, within the high-Q mode approximation, this fast varying term is filtered out, which is the philosophy of the rotating wave approximation. Meanwhile, the low-frequency part of the noise spectral density is spread over a width $\sim \Gamma_m$ and will be responsible for slow variations of the modes resonance frequencies, which are the key aspect of the work presented here: the driven mode will have its frequency adiabatically following the frequency change.

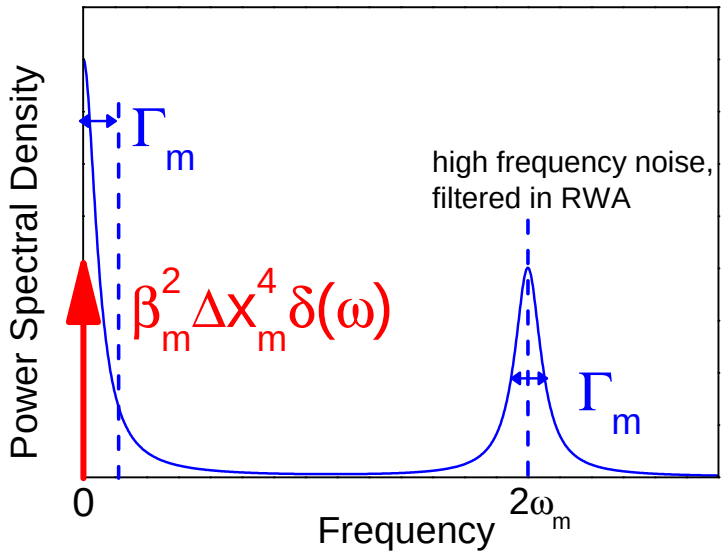

Figure 3.1: Schematic spectrum of the n^{th} mode frequency fluctuations induced by nonlinear coupling to the m^{th} mode Brownian motion.

In the high-Q limit, the correlator of position fluctuations simply follows an exponential decay law of rate $\Gamma_m/2$, as one can derive from the fluctuating mode Langevin equation. According to Eq.(3.10) and within the approximation made above (filtering of fast frequency fluctuations), this implies that the AC part of the frequency fluctuations decay as follows:

$$\langle \delta\omega_{n,m}(0)\delta\omega_{n,m}(\tau)\rangle_{\mathrm{AC}} \propto e^{-\Gamma_m \tau}. \tag{3.12}$$

The obtained correlation decay rate Γ_m of the frequency fluctuations is a crucial parameter that will set the physics of the problem. Equivalently, a typical correlation time $\tau_c = 1/\Gamma_m$ can be defined for the fluctuations. It represents the "memory" time of the fluctuations, and its value will set the crossover between the different regimes experimentally observed. We see that even though the process described does not allow additional energy transfer, it is limited by the energy relaxation rate of the fluctuating mode creating frequency noise.

3.3.3 Langevin equations in the rotating wave approximation

The problem at hand is tedious to solve in its raw form, yet the approximations stated above make a considerable simplification possible. We write the motion variables in terms of slow motion amplitudes, in the so-called **rotating frame**: $x_n(t) = \left(A_n(t)e^{i\omega t} + A_n^*(t)e^{-i\omega t}\right)/2$ with ω the driving field frequency and A_n the slow complex amplitude of motion. This decomposition can be re-injected in Eq. (3.9). Here, since we are in the high Q limit, we can make the following approximations:

- Terms which are not resonant with the driving frequency, i.e. proportional to $e^{-i\omega t}, e^{\pm 2i\omega t}, e^{\pm 3i\omega t}$, are dropped.
- Since the amplitude term is varying on timescales comparable to Γ_n^{-1}, we can neglect most of the derivative terms: $\ddot{A}_n, \Gamma_n \dot{A}_n \ll \omega^2 A_n, \omega\Gamma_n A_n$.

The same transformation can be applied to mode m, with its slow amplitude δA_m. Such a notation is a reminder of the fluctuating nature of mode m. As the latter is undriven, so its rotating frame frequency will be taken as ω_m. In addition, we consider first the case where the driving force F_n is small enough not to significantly distort the response, which in fact amounts to neglecting the terms $\beta_{n,m}|A_n|^2\delta A_m$. Note that if this approximation cannot be made, new phenomena emerge, which are described in the last section of this Chapter.

This leads to a linearized version of the problem. The equations of motion write for modes m and n, respectively:

$$\begin{cases} \dot{\delta A}_m + \dfrac{\Gamma_m}{2}\delta A_m &= \dfrac{F_{th,m}(t)e^{-i\omega_m t}}{2m_m\omega_m}, \\ \dot{A}_n + \dfrac{\Gamma_n}{2}A_n + i\left(\omega - \omega_n - \underbrace{\beta_{n,m}(1+\delta_{n,m})|\delta A_m|^2}_{\delta\omega_{n,m}}\right)A_n &= \dfrac{F_n e^{i\phi}}{4m_n\omega_n}. \end{cases} \tag{3.13}$$

The probe mode n is then affected by noise on the mode m, through an effective frequency noise $\delta\omega_{n,m}(t) = (1+\delta_{n,m})\,\beta_{n,m}|\delta A_m(t)|^2$, where $\delta_{n,m}$ is Kronecker's symbol. The latter allows a unified description of the inter-mode coupling and intra-mode coupling ("self-coupling" of the response to its own position noise) cases. To allow such a unified description, here we have assumed that the fluctuating mode is linear as far as its fluctuations are concerned. The case where the non-linearity comes into play will be addressed in section 3.5. For the time being we are only concerned with the fluctuations statistics, and one can show that the deviation to Gaussian statistics in the steady-state is significant only if the Q factor is of order 1 [85], hence negligible in our high Q devices.

We can decompose the slow complex amplitude into its quadratures $\delta A_m = \delta X_m + i\delta Y_m$. These two quadratures are uncorrelated (within our linearization), and are both so-called Ornstein-Uhlenbeck noises, i.e. are Gaussian processes with a finite steady-state variance due to the restoring potential. They satisfy the following Langevin equations:

$$\begin{cases} \delta\dot{X}_m + \dfrac{\Gamma_m}{2}\delta X_m &= \dfrac{F_{th,m}(t)\cos(\omega_m t)}{2m_m\omega_m}, \\ \delta\dot{Y}_m + \dfrac{\Gamma_m}{2}\delta Y_m &= -\dfrac{F_{th,m}(t)\sin(\omega_m t)}{2m_m\omega_m}, \end{cases} \tag{3.14}$$

with autcorrelation functions $\langle\delta X_m(0)\delta X_m(\tau)\rangle = \langle\delta Y_m(0)\delta Y_m(\tau)\rangle = \Delta x_m^2\exp(-\Gamma_m\tau/2)$, and $\langle\delta X_m(0)\delta Y_m(\tau)\rangle = 0$. While δX_m, δY_m are Gaussian and centered, it is obvious that the effective frequency noise $\delta\omega_{n,m}$ is neither Gaussian nor centered. Moreover, the spectrum of the noise is similar to the position spectrum, thus providing a good example of a highly colored noise.

3.3.4 Averaging over the frequency noise: two interesting limit behaviours

Our measurements always yield quantities that are averaged. To model this theoretically in the situation at hand is not a simple task for two reasons. First, as said above, the frequency fluctuation at a time t is not distributed according to a Gaussian law: since position fluctuations are Gaussian, frequency jumps take only positive values and are distributed according to an exponential law. The stationary joint probability density for the displacement noise of the fluctuating mode is:

$$p(\delta X_m, \delta Y_m) = \frac{1}{2\pi\Delta x_m^2} e^{-\dfrac{\delta X_m^2 + \delta Y_m^2}{2\Delta x_m^2}}. \tag{3.15}$$

The mode-coupling induced frequency noise variable writes $\delta\omega_{n,m} = (1+\delta_{n,m})\beta_{n,m}(\delta X_m^2 + \delta Y_m^2)$, with its magnitude $\Sigma_{n,m} = 2(1+\delta_{n,m})\beta_{n,m}\Delta x_m^2$. The frequency noise stationary probability density is readily obtained through a Jacobian transform:

$$\mathrm{d}p(\delta\omega_{n,m}) = \frac{\Theta(\delta\omega_{n,m})}{\Sigma_{n,m}} e^{-\frac{\delta\omega_{n,m}}{\Sigma_{n,m}}} \mathrm{d}\delta\omega_{n,m} \frac{\mathrm{d}\theta}{2\pi}, \tag{3.16}$$

with Θ the Heaviside function. However, due to the finite decay rate of the fluctuations, one cannot always simply average the susceptibility over time-independent distributions. A simple picture can clarify the situation: if we assume that the resonator experiences at a time t a frequency change of typical magnitude $\Sigma_{n,m}$, the minimum time needed by the resonator to synchronize with the jump and "sample" this change of frequency accurately will be $\sim \Sigma_{n,m}^{-1}$. This is the characteristic time to be compared with the typical decay time $\tau_c = \Gamma_m^{-1}$, or "memory", of the frequency noise correlations. Two limits exist, which are detailed below.

Inhomogeneous broadening limit

The first limit situation occurs when $\Sigma_{n,m}\tau_c \gg 1$ (see Fig. 3.2): in this regime, the fluctuations are essentially correlated over an infinitely long time, which means that every change in frequency will be well resolved and adiabatically followed by the resonator: the latter can sample the change with increasingly good accuracy. Provided that the averaging measurement is done over a infinitely long time, say $\gg \Gamma_m^{-1}$ and Γ_n^{-1}, it is equivalent to say, by ergodicity, that the average susceptibility in the frequency domain is the simple sum of partial stochastic susceptibilities $\chi_(\omega - \delta\omega_{n,m})$ over all realizations of $\delta\omega_{n,m}$ with the exponential distribution derived above:

$$\chi(\omega) = \int_{-\infty}^{+\infty} \chi(\omega - \delta\omega_{n,m})\Theta(\delta\omega_{n,m}) \frac{e^{-\delta\omega_{n,m}/\Sigma_{n,m}}}{\Sigma_{n,m}} \mathrm{d}\delta\omega_{n,m}. \tag{3.17}$$

The distribution involed is none other than the Boltzmann weight, as noticed in Ref. [14]: frequency fluctuations are directly proportional to the fluctuating mode's stored energy. One notes the treatment similar to Nuclear Magnetic Resonance [86], where the effective experienced field is averaged over spatial inhomogeneities. This analogy must be taken carefully: of course, here the system experiences time-controlled disorder instead of spatial. In the experiment described here, this analogous regime can be reached for frequency noise magnitudes high enough. The physics is then reduced to the interplay of two parameters: the frequency noise magnitude and the probe mode's decay time. This will be addressed in greater detail in Chapter 4.

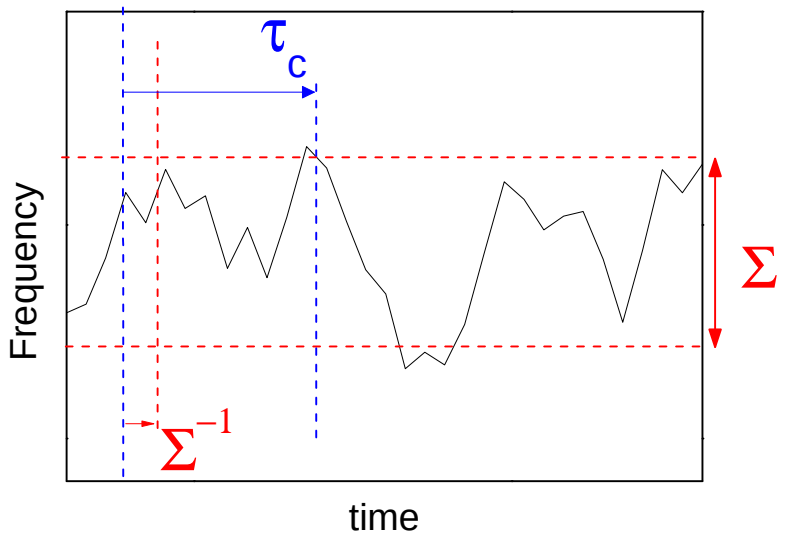

Figure 3.2: schematics of the frequency noise in the inhomogeneous broadening situation.

Motional narrowing limit

In the opposite limit where $\Sigma_{n,m}\tau_c \ll 1$ (see Fig. 3.3) correlations decay too fast for the NEMS to resolve a small frequency change: the memory of this change is erased faster than the time required to sample it. Then, the effective distribution "seen" by the probe's mode is not obtained from the full reservoir's dynamics but only from a truncated part of it, as only a fraction of the realizations on the time disorder are accessible.

This is somehow analoguous to NMR again: by replacing a spatial disorder on the surrounding magnetic field by a time disorder on the frequency, we observe a crossover from the previously described **inhomogeneous broadening** (abbreviated IB) to a **motional narrowing** regime (abbreviated MN), where essentially the NEMS will only have its parameters renormalized by the first (resonance shift) and second (linewidth broadening) moments of the fluctuating frequency distribution. This transition was observed in mechanical devices in the case of artificially created telegraph frequency noise in Ref. [81], where the authors varied the noise correlation time rather than its magnitude. From a well resolved two-peak structure in the inhomogeneous broadening regime due to the two only possible values of the frequency noise, they observed the transition towards the MN regime where the two peaks merged into a single one which gets closer to the original resonance as the correlations decay time is reduced. The originality in the case described in this manuscript is that it relies on really **intrinsic properties** of the resonator: its thermal fluctuations and its geometric nonlinearities.

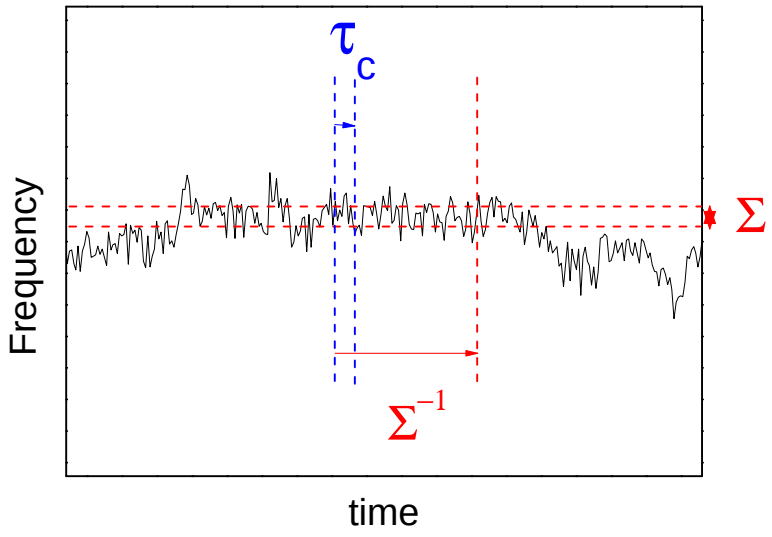

Figure 3.3: schematics of the frequency noise in the motional narrowing situation.

In the context of NMR, motional narrowing arises from fast diffusion of the inhomogeneous field sources [86], and therefore it increases with temperature. Here the phenomenon is smeared out as the effective temperature $T_{\text{eff}} \propto \Delta x_m^2$ increases. This has led authors who observed a similar phenomenon in the optical emission spectrum of quantum dots to name it an "unconventional" motional narrowing [87], "unconventional" referring to the unusual temperature dependence. However, in the present context temperature does not play an analogous role as in NMR. In the original context, it speeds up (spatial) inhomogeneities sources, whereas here it somehow slows the (time) sources down with respect to the memory time.

3.3.5 Joining the two limits with a stochastic path integral approach

The previous section provides rather intuitive ways to consider the phenomenon. However, our experimental results often fall in between the two marginal cases, and a simple quantitative formulation is not easy to find in that situation. Nonetheless, there is an elegant way to obtain the susceptibility averaged over frequency fluctuations in the whole dynamic range through a stochastic path integral formulation [31].

The idea is that in a given time interval, between known initial and final positions in the phase space, the Brownian motion of the mode creating frequency noise can take many possible paths in the phase space, and that the statistical averaging procedure is merely taking into account all these paths with their weight. Therefore, the accu-

mulated phase can also take many paths, and in fact, experiences diffusion, as shown in Fig. 3.4. Each path's weight can be obtained from the Langevin dynamics of the fluctuating mode in the Markovian bath approximation. From what we have described above, we know that the average susceptibility will be a function of the scaling parameter called "motional narrowing parameter" $\alpha_{n,m} = \Sigma_{n,m}\tau_c = 2\beta_{n,m}(1+\delta_{n,m})\Delta x^2/\Gamma_m$.

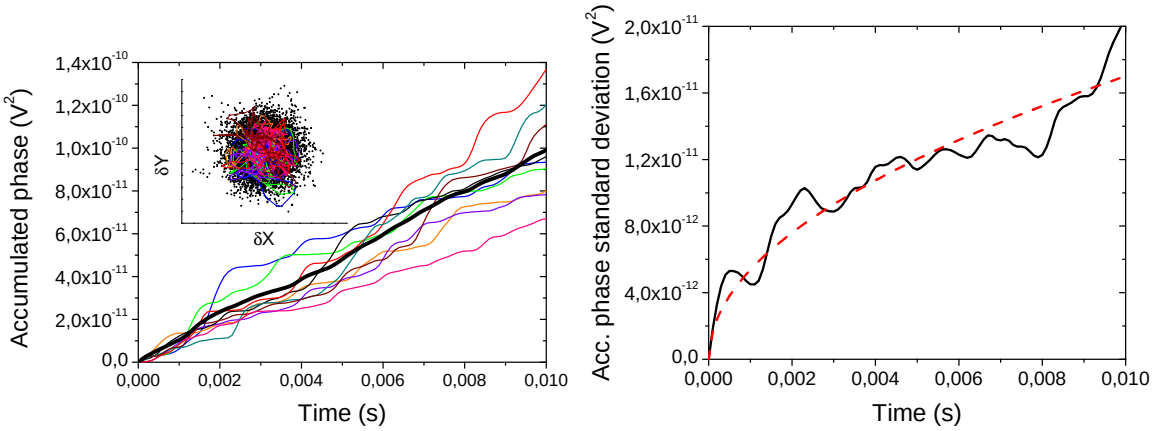

Figure 3.4: left: phase accumulated through the nonlinear mechanism along different Brownian trajectories (inset) of the first mode of the sample "250 µmn° 1". The thick black line is an average over these trajectories. Right: standard deviation around the average accumulated phase path. The red dashed line is a fit $\propto \sqrt{t}$ following diffusion laws. The accumulated phase is shown in units of Brownian motion as measured at the lock-in level with the technique described in section 3.5.

Integrating Eq. (3.13) for the driven mode n, one obtains the slow amplitude in time domain. Due to the presence of a stochastic frequency term, the response itself has a stochastic nature:

$$A_n(t) = \int_{-\infty}^{t} \frac{\mathrm{d}t' F_n e^{i\phi}}{4m_n\omega_n} \exp\left(-\left[\frac{\Gamma_n}{2} + i(\omega-\omega_n)\right](t-t') + i\int_{t'}^{t}\delta\omega_{n,m}(t'')\mathrm{d}t''\right). \tag{3.18}$$

This solution is simple to interpret: indeed, the exponential term is merely a slow time domain susceptibility $\chi_{sl}(t,t')$, relating the response at a time t after a perturbation at a time t', modulated by a stochastic accumulated phase term, such that:

$$A_n(t) = \int_{-\infty}^{t} \frac{F_n e^{i\phi}}{4m_n\omega_n}\chi^*_{sl}(t,t')\mathrm{d}t'. \tag{3.19}$$

By definition, the lock-in amplifier measures an averaged response at a given frequency. Within the applied force factor and calibration coefficients, this is just the susceptibility in frequency domain, which is by construction:

$$\chi_n(\omega) = \frac{i}{2m_n\omega_n}\int_0^t \langle\chi_{sl}(t',0)\rangle \mathrm{d}t'. \tag{3.20}$$

We can now write an averaged slow susceptibility, which amounts to the usual certain part times the averaged stochastic modulation:

$$\langle\chi_{sl}(t,0)\rangle = \exp\left(-\left[\frac{\Gamma_n}{2} + i(\omega-\omega_n)\right]t\right)\left\langle e^{i\Delta\phi_{n,m}(t)}\right\rangle, \tag{3.21}$$

where $\Delta\phi_{n,m}(t) = \int_0^t \delta\omega_{n,m}(t')\mathrm{d}t'$ is the accumulated phase during one Brownian trajectory of the mode m between time 0 and t. From the integral form in the exponential argument one can see that the averaging has to take into account all realizations of a **full trajectory** in the phase space of the Langevin process $(\delta X_m, \delta Y_m)$ between time 0 and time t. It is useful to notice that averaging over the frequency noise is equivalent to average over the two quadratures which are uncorrelated in the limit of small driving fields: thus each averaging can be done separately. Since the bath is Markovian, one can convert Langevin equations (3.14) on quadratures into Fokker-Planck equations, which govern the evolution of transition probabilities. We note $W^X_{i,f} \equiv W(\delta X_{m,f}, t_f|\delta X_{m,i}, t_i)$ the probability to be at the position $\delta X_{m,f}$ at a time t_f starting from position $\delta X_{m,i}$ at time t_i, and equivalently for δY_m. The Fokker-Planck equation writes:

$$\frac{\partial W^X_{i,f}}{\partial t_f} = \frac{\Gamma_m}{2}\frac{\partial\left(\delta X_{m,f} W^X_{i,f}\right)}{\partial \delta X_{m,f}} + \frac{\Gamma_m \Delta x_m^2}{2}\frac{\partial^2 W^X_{i,f}}{\partial \delta X^2_{m,f}}. \tag{3.22}$$

The same equation applies also to $W^Y_{i,f} \equiv W(\delta Y_{m,f}, t_f|\delta Y_{m,i}, t_i)$. The general solution to this equation writes:

$$W^X_{i,f} = \sqrt{\frac{1}{2\pi\Delta x_m^2(1-e^{-\Gamma_m(t_f-t_i)})}}\exp\left(-\frac{\left[\delta X_{m,f} - \delta X_{m,i}e^{-\Gamma_m(t_f-t_i)/2}\right]^2}{2\Delta x_m^2\left(1-e^{-\Gamma_m(t_f-t_i)}\right)}\right). \tag{3.23}$$

For long times the memory of the initial position $(\delta X_{m,i}, \delta Y_{m,i})$ is erased in the phase space, and we recover the steady-state, Gaussian probability distribution (3.15) on $\delta X_{m,f}$. More interestingly, in the limit of short time intervals $\delta t = t_f - t_i \ll \tau_c \sim \Gamma_m^{-1}$, one obtains the propagator:

$$W^X_{i,f} \underset{\delta t \ll \Gamma_m^{-1}}{\approx} \sqrt{\frac{1}{2\pi\Gamma_m\Delta x_m^2\delta t}}\exp\left(-\frac{\left[\delta X_{m,f} - \delta X_{m,i}(1-\Gamma_m\delta t/2)\right]^2}{2\Gamma_m\Delta x_m^2\delta t}\right). \tag{3.24}$$

It is now possible to reconstruct, from this propagator, the probability associated to the realization of one path. Let us cut the time interval $[0,t]$ into N small equal intervals, such that $\delta t = t/N$. Since the process is assumed to be Markovian, one can

derive the probability density associated to one path using conditional probabilities:

$$\begin{aligned}\mathcal{W}[\delta X_m]_{[0,t]} &= \prod_{i=1}^{N-1} W_{i,i+1}^{X} \\ &= \left(\frac{1}{2\pi\Gamma_m\Delta x_m^2\delta t}\right)^{N/2} \exp\left(-\frac{\sum_{i=1}^{N-1}\left[\frac{\delta X_{m,i+1}-\delta X_{m,i}}{\delta t} - \frac{\Gamma_m}{2}\delta X_{m,i}\right]^2\delta t}{2\Gamma_m\Delta x_m^2}\right). \end{aligned} \tag{3.25}$$

Taking the limit $N \to \infty$, i.e. $\delta t \to 0$, the probability density functional on the path δX_m between 0 and t is:

$$\mathcal{P}[\delta X_m(t)] = \exp\left[-\frac{1}{2\Gamma_m\Delta x_m^2}\int_0^t \left(\delta\dot{X}_m(t') + \frac{\Gamma_m}{2}\delta X_m(t')\right)^2 \mathrm{d}t'\right]. \tag{3.26}$$

The expectation value for the accumulated phase can then be expressed through the functional integral:

$$\left\langle e^{i\Delta\phi_{n,m}(t)}\right\rangle = \iint \mathcal{D}\delta X_m \mathcal{D}\delta Y_m e^{i\int_0^t (1+\delta_{n,m})\beta_{n,m}(\delta X_m^2(t')+\delta Y_m^2(t'))\mathrm{d}t'}\mathcal{P}[\delta X_m]\mathcal{P}[\delta Y_m], \tag{3.27}$$

with the formal differential term in the trajectories space:

$$\mathcal{D}\delta X_m(t) \underset{N\to\infty}{=} \prod_{i=1}^{N}\frac{\mathrm{d}\delta X_{m,i}}{(2\pi\Gamma_m\Delta x_m^2\delta t)^{1/2}}. \tag{3.28}$$

Calculating the average dephasing term from Eq. (3.27) is no easy task. Basically, one has to discretize once more the integral, which decomposes over sums on Gaussian variables. This tedious task is performed in Ref. [31]. After calculation, one gets explicitly the expectation value of the accumulated phase term $\left\langle e^{i\Delta\phi_{n,m}(t)}\right\rangle \equiv G(t)$:

$$G(t) = \frac{e^{\Gamma_m t/2}}{\cosh(a_{n,m}t) + \dfrac{\Gamma_m\left(1+2i\alpha_{n,m}\right)}{2a_{n,m}}\sinh(a_{n,m}t)}. \tag{3.29}$$

where $a_{n,m} = \frac{\Gamma_m}{2}\sqrt{1+4i\alpha_{n,m}}$. Note that this path integral approach provides us with another level of interpretation. At the most basic level, a mechanically resonant mode is merely the constructive interference of an incoming and a reflected sound wave in the beam, which acts as an acoustic cavity. As the nonlinear interaction creates an additional stochastic phase, this interference is blurred, because each wave of the sum is partially incoherent: the stochastic phase term competes with the background phase coherent term of the standard response.

In the motional narrowing limit, the initial phase coherence is more protected since noise correlations, decaying too fast, become localized in time. Therefore the effect of phase diffusion on resonance properties is limited, as the most noisy paths have a reduced impact.

In the opposite, inhomogeneous broadening regime, the impact of phase diffusion is not attenuated anymore by time localization effects and therefore blurring masks the background phase coherence. To paraphrase Ref. [79], the average (3.17) can be interpreted as an incoherent sum over partial susceptibilities $\chi(\omega_n - \delta\omega_{n,m})$, as described in paragraph 3.3.4.

Even though the expression of G is quite unpractical, one can expand it in the motional narrowing limit, finding again the results obtained in Section 3.3.4:

$$G(t) \approx e^{i\alpha_{n,m}\Gamma_m t - \Gamma_m \alpha_{n,m}^2 t/2}. \tag{3.30}$$

The complex term corresponds to a frequency shift, the real one is an additional decay term. In frequency domain, it leads to a complex Lorentzian averaged response $\mathcal{G}(\omega)$ with renormalized resonance frequency ω_{res} and linewidth $\Delta\omega$:

$$\omega_{res} \approx \omega_0 + \Gamma_m \alpha_{n,m} = \omega_0 + 2\beta_{n,m}(1+\delta_{n,m})\Delta x_m^2, \tag{3.31}$$

$$\Delta\omega \approx \Gamma_n + \frac{\Gamma_m \alpha_{n,m}^2}{2} = \Gamma_n + \frac{2\left[2\beta_{n,m}(1+\delta_{n,m})\Delta x_m^2\right]^2}{\Gamma_m}. \tag{3.32}$$

3.4 Results in the driven case

3.4.1 Experimental setup

The experimental setup is shown in Fig. 3.5. As the fundamental (noted 1) and third (noted 3) mode are rather easy to actuate and detect, we will focus our study on them. Thermal fluctuations at 4 K are way below our sensitivity limit and too small to reach the inhomogeneous broadening limit, in particular for a doubly-clamped structure which does not move too much. Thus we deliberately feed the first mode with a current noise. The latter goes through injection line with the additioner used for the calibration procedure (see paragraph 2.8.2) and is translated by the magnetomotive scheme into a noise force.

In principle, this puts the noise-fed mode highly out of equilibrium. However, the force noise is strictly equivalent to an effective temperature defined through the FDT relation (3.6) at which fluctuations are easily measurable and have a significant effect on the driven responses. Noise calibration and measurement procedures are detailed below in Section 3.5. The voltage noise is delivered with an arbitrary waveform generator Agilent HP A33120 with real noise bandwidth 10 MHz, such that at the scale

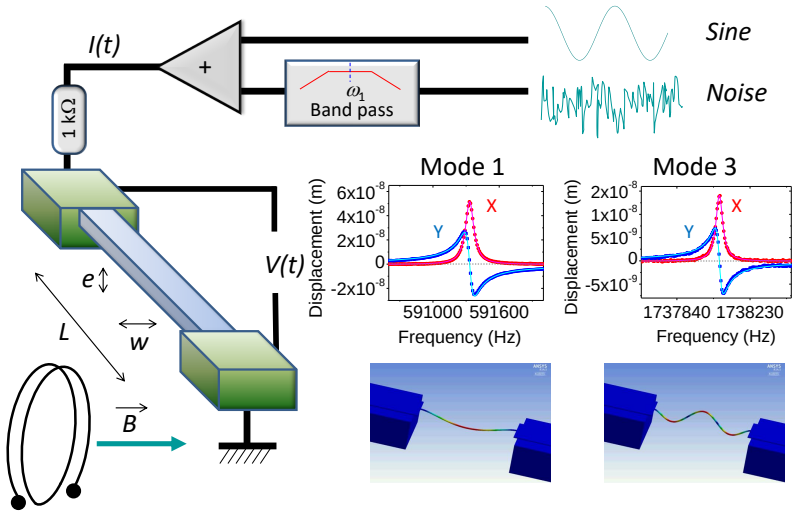

Figure 3.5: schematics of the experimental setup. Note that the sine wave injection can be a signal at the first mode frequency, or the third one, or removed if we are only interested in the position fluctuation spectrum.

of the resonator, the noise power spectral density $S_F(\omega)$ is flat. Thus, the effective temperature mentioned above is defined such that $S_F(\omega) = 2m_1\Gamma_1 k_B T_{\text{eff}}$.

We carefully characterized the delivered noise: from spectrum analyzer measurements we know that there is only a 5% decreasing slope between 0 and 10 MHz, irrelevant at the NEMS scale, and made sure the noise is Gaussian, centered, as shown in Fig. 3.6, left panel. Besides, as shown below, high effective temperatures ($10^6 - 10^{10}$ K) are needed to witness e.g. inhomogeneous broadening. Reaching such effective temperatures requires large noise powers. Thus, to avoid overheating of the sample and selectively put the first mode at high effective temperatures, a bandpass filter is inserted after the generator. The filter gain curve is shown in Fig. 3.6, right panel. Its integrated bandwidth is 0.7 MHz, with a maximum transmission factor 0.95.

With such a scheme, we are able to tune one mode's effective temperature and study its coupling to the driven mode while leaving the other modes utterly irrelevant to the study, as thermomechanical noise at 4 K is completely negligible in comparison.

In addition, we carefully characterize both modes, following the procedure described in Chapter 2: applied forces as well as displacements are known in real units, which enable to know nonlinear coefficients $\beta_{i,j}, \{i,j\} = \{1,3\}$. These calibrations put together give us a 20 % margin. The experiments have been performed on 4 different devices, whose characteristics are gathered in the following table.

Starting from a voltage noise δV_{in} shown in peak-to-peak (V_{pp}) units, we can recalculate the current noise spectrum $S_I(\omega)$ (force S_F) flowing through the NEMS: we have

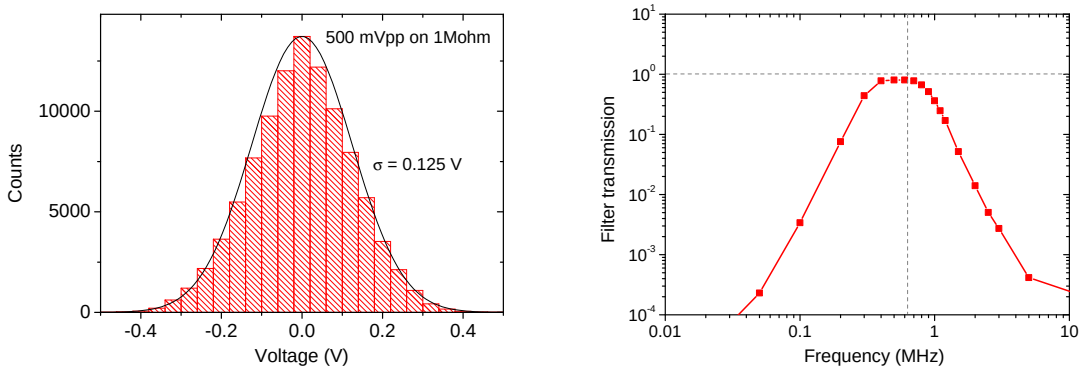

Figure 3.6: left: AWG output voltage noise histogram for an applied noise 1 V_{pp}, with a Gaussian fit. Right: amplitude gain of the bandpass filter. The dashed line corresponds to the resonance frequency of a 300 µm beam.

	spring k_n	freq. $\omega_n/2\pi$	$\Gamma_n/2\pi$	non-lin. $\beta_{n,m}/2\pi$
$n=1$ 300 μm-n°1	0.40 N/m	0.59 MHz	100 Hz	$\beta_{1,1} = 1.35\,10^{15}$ Hz/m^2
$n=1$ 300 μm-n°2	0.45 N/m	0.66 MHz	140 Hz	$\beta_{1,1} = 1.70\,10^{15}$ Hz/m^2
$n=1$ 15 μm-n°1	1.2 N/m	6.9 MHz	550 Hz	$\beta_{1,1} = 5.0\,10^{19}$ Hz/m^2
$n=3$ 300 μm-n°1	3.4 N/m	1.74 MHz	40 Hz	$\beta_{3,1} = 2.75\,10^{15}$ Hz/m^2
$n=1$ 250 μm-n°1	0.45 N/m	0.9 MHz	190 Hz	$\beta_{1,1} = 8.5\,10^{15}$ Hz/m^2
$n=3$ 250 μm-n°1	4.0 N/m	2.7 MHz	25 Hz	$\beta_{3,1} = 1.6\,10^{16}$ Hz/m^2

Table 3.1: Measured mode parameters relevant to the data presented here, with loaded linewidths at a field $B = 0.84$ T. All agree fairly well with analytic computation.

checked that the root mean square (rms) value delivered by the generator is defined such that the peak-to-peak value displayed is 8 times the rms value, as shown in Fig. 3.6 left panel. Besides, this noise is spread over the output bandwidth (9.5 MHz) of the AFG, hence a value given in $V_{rms}/\sqrt{\text{Hz}}$. The resulting voltage noise goes through the bandpass filter (described in the above paragraph), and the injection line, which sets an integrated value for the voltage noise applied to the NEMS+bias resistance ensemble. Within a numerical shape factor, the current noise spectrum in A^2/Hz units that flows through the NEMS is then:

$$S_I(\omega) = \left[\frac{0.95\sqrt{\pi}G_I(\omega_1)}{8(R_N+R_b)}\frac{\delta V_{in}}{\sqrt{9.5\text{ MHz}}}\right]^2. \tag{3.33}$$

3.4.2 Measured resonance lines under nonlinearity-induced frequency fluctuations

The derived accumulated dephasing term (3.29) acts as a slow modulation of the time domain signal, both in amplitude and frequency. In frequency domain, the measured averaged response is then the standard frequency domain susceptibility, with a noisy eigenfrequency, convoluted with a complex-valued pseudo-distribution which is the Fourier transform $\mathcal{G}(\omega)$ of the average accumulated phase term (3.29):

$$\chi_n(\omega) = \int_{-\infty}^{+\infty} \chi_n(\omega - \delta\omega_{n,m})\Theta(\delta\omega_{n,m})\mathcal{G}(\delta\omega_{n,m})\mathrm{d}\delta\omega_{n,m}. \tag{3.34}$$

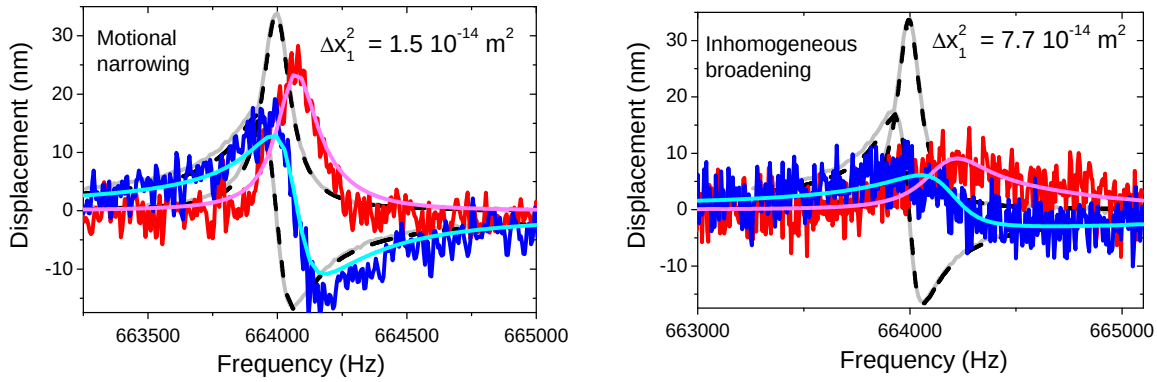

Figure 3.7: Fundamental mode resonance lines in phase (blue) and quadrature (red) measured with the device 300 µm n^{o}2 (see Table 3.1), in the motional narrowing (left panel) and inhomogeneous broadening (right panel) regimes in the case of intra-mode, Duffing mediated frequency fluctuations, at a constant driving excitation. Solid lines are direct applications of Eq. (3.34). The grey line is a measurement of the standard response at the same drive tone for comparison, with complex Lorentzian fits (dashed lines).

The susceptibility is probed through our standard response measurements, with long enough ($\gg \Gamma_m^{-1}, \Gamma_n^{-1}$) lock-in time constants so as to integrate all realizations of the slow frequency fluctuations. One important point is to keep coherent driving excitations at a low enough level, in order not to enhance other, unwanted non-linear interaction terms that go beyond the linearized model presented in section 3.3.3. These additional terms can indeed result in correlations between the two quadratures of the fluctuating mode, and extensions of the model would have to be considered (see section 3.7). In our case, a good criterion is to apply drive forces such that the unperturbed response (grey dots in Fig. 3.7) still appears symmetric (or anti-symmetric, for the in-phase response). Two resonance lines for the "self-coupling" case, i.e. the driven mode coupled to its own Brownian motion are shown in Fig. 3.7. Each one is representative

of an asymptotic regime, for the same sinusoidal excitation. One can see that for low frequency noise (left panel), i.e. in the motional narrowing regime, the lineshape remains essentially Lorentzian. This is not surprising, as the calculated lines are simply renormalizations of the noiseless lines in this regime (see previous sections). This is equivalent to say that the pseudo-distribution is simply a Lorentzian which carries only the first and second moments of the "full" exponential distribution. The resonance shift, being proportional to α_{11} is significant, while linewidth broadening, being proportional to α_{11}^2 remains marginal. Thus, phase diffusion is rather limited, while its drift, seen through the resonance frequency shift, is consequent.

On the contrary, the shift does not increase much more in the high amplitude noise (inhomogeneous broadening, right panel) limit, because the distribution gets closer to the real one, which is real-valued, exponential. Note that as it gets closer, its asymmetric shape leaves an imprint on the response, which also becomes highly asymmetric as a result of the convolution. Indeed, the fluctuations take only positive values, which explains the long-tail feature in the frequency region above the resonance frequency. As a matter of fact, the line gets closer to an exponential shape, i.e. the stationary frequency noise distribution. We use the most simple convention: the chosen inhomogeneous linewidth parameter is the full width at half height (FWHH, or FWHM). It allows to easily extract numerically the parameter from the theoretical expression (3.34), which is neither explicit nor easy to manipulate in its most general form. Note also that the signal-to-noise ratio worsens as the noise becomes larger, because a much longer averaging time is required to obtain cleaner lines: yet it is unrealistic to measure for too long, as uncontrolled drifts due e.g. to two-level fluctuators (see Chapter 6) can perturb significantly the measured lines on long timescales. The theoretical lines reproduce rather well the measured lines, with no free parameters.

The evolution of the two relevant parameters (shift, broadening) as a function of the Brownian motion amplitude, i.e. the magnitude of the frequency noise (or equivalently, the effective temperature) is shown in Fig. 3.8, with broadening obtained from FWHH measurements. The agreement between experimental data and theory is rather good, and there is no free parameter, as our noise source is calibrated within ± 15 %.

The case of inter-modal coupling is also addressed, with again representative examples in Fig. 3.9. Note that the line with the highest level of noise applied is still close to the motional narrowing limit. This is due to values for inter-mode nonlinear coefficients smaller than for Duffing ones, as mode overlaps are significantly smaller. Thus, to witness an effect, very high noise excitations are required, which explains why the most noisy lines are still rather close to a Lorentzian. Note, however, that the agreement between theoretical expressions and experimental data is not as good as in the Duffing case, and higher noise would result in even poorer resolution: thus the inhomogeneous broadening regime could not be properly observed. This can also explain why the work presented in Ref. [30] was limited to the low noise, motional narrowing limit: although temperature could also be enhanced by a few orders of

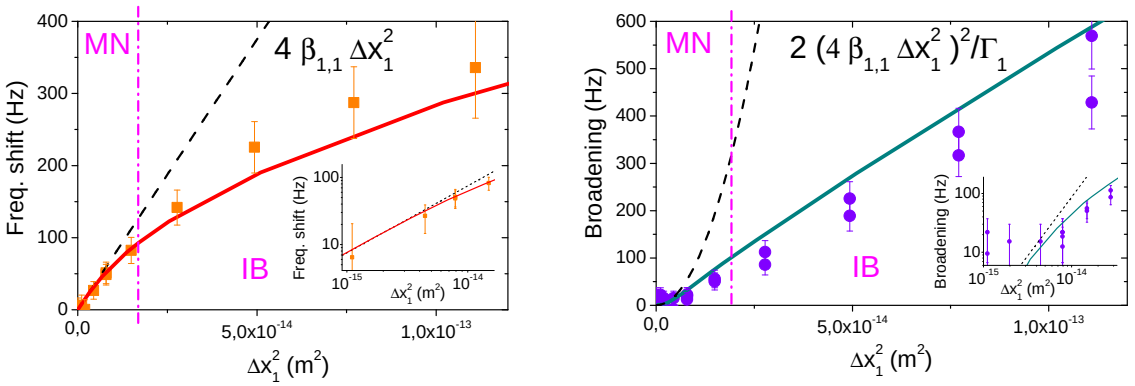

Figure 3.8: frequency shift (left) and linewidth broadening (right) of the fundamental mode resonance as a function of its own Brownian motion amplitude, with the two discussed regimes denoted. The solid lines are theoretical curves extracted numerically from Eq. (3.34), while dashed lines show the laws obtained in the motional narrowing regime (Eqs. (3.31) and (3.32) for shift and broadening respectively). Insets in both graphs are zooms on the data obtained in the motional narrowing regime. The pink line roughly marks the transition between the two regimes at $\alpha_{1,1} = 1$.

magnitude, mode-coupling geometric nonlinear coefficients were too small to observe a transition, a situation expected for a cantilever.

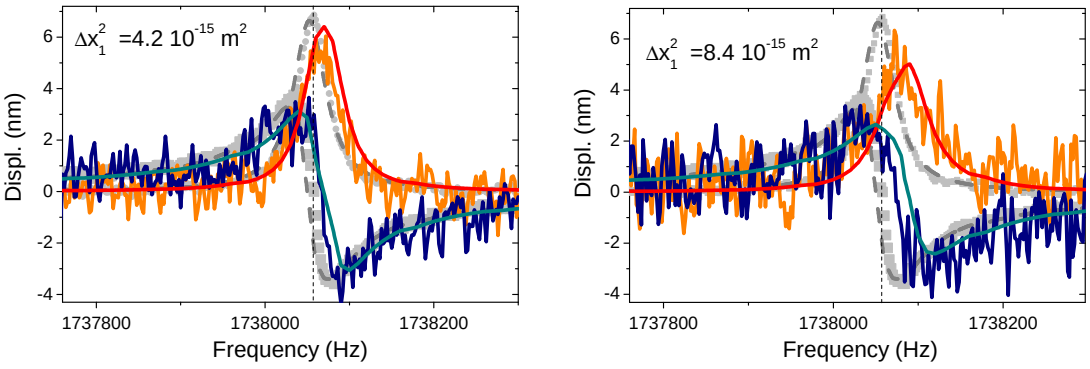

Figure 3.9: third mode in phase (blue) and quadrature (orange) resonance lines measured for a 300 µm long device, for low (left) and intermediate (right) noise levels on the first mode, at a constant driving excitation. Solid lines are the direct application of Eq. (3.34). Grey lines are measurements of the standard response at the same drive tone for comparison, with complex Lorentzian fits (dashed lines).

The resonance shift and the broadening over the experimentally studied noise range are shown in Fig. 3.10. We see first that data taken remain close to the motional narrowing limit even for high noises, as mentioned above. Besides, the agreement in the case of the shift is not as good, again, as in the Duffing case, with discrepancies

up to 20 %. This is likely due to a competition between the mode coupling effect, hardening the resonator, and the fact that the required noise starts to significantly overheat the structure physically, leading to softening of the resonator (see Section 2.7): this competition would thus result in a smaller shift than expected.

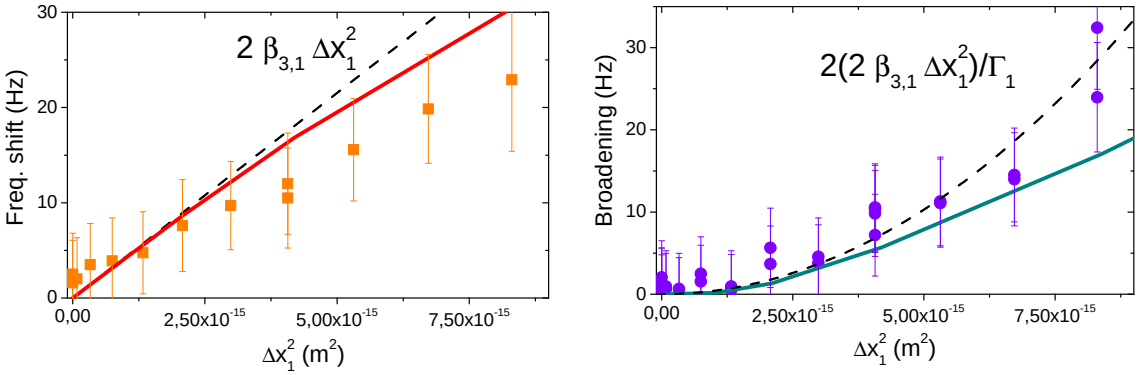

Figure 3.10: frequency shift (left) and linewidth broadening (right) of the third mode resonance as a function of the fundamental mode Brownian motion extension, with the two discussed regimes denoted. The red solid lines are the parameters extracted numerically from Eq.(3.34), while dashed lines show the laws obtained in the motional narrowing regime.

From these measurements one thing is clear: in the linear regime of driving force, the observed effect only depends on the dynamics of the noisy mode, while the probe's dynamics has little influence, whether the probe is another mode or the noisy mode response itself. This shows that the two effects differ only quantitatively. Only in the case where $\Gamma_n \gg \Gamma_m$ one might observe a departure from the model, because then a fraction of the effective frequency fluctuations would be too fast to be followed by the probe mode, which in fact means that this fraction would fall outside of the rotating wave approximation, i.e. would be filtered by the probe's dynamics.

In addition, measurements for very small position fluctuations unambiguously demonstrate the motional narrowing effect. While we have not used noises large enough to depart from the motional narrowing regime on the 250 µm sample, the resolution is excellent: in Fig. 3.11 we see that for an integrated position noise on the fundamental mode $\Delta x_1^2 = 6.1 \times 10^{-16}$ m^2, theoretical curves obtained through full averaging with Eq. (3.34) and through averaging with Eq. (3.17) are significantly different: while the application of the full theory matches well the resonance lines, the IB-type averaging clearly fails to reproduce the data.

An interesting feature is that this discrepancy appears only on the right side of the response: this is expected, as the motional narrowing process prevents large excursions in frequency, and those happen by construction towards higher frequencies since $\delta x_m^2 \geq 0$. If one considers the unperturbed driven response as the result of a frequency noise magnitude going to zero, the motional narrowing is merely the onset of the constructive

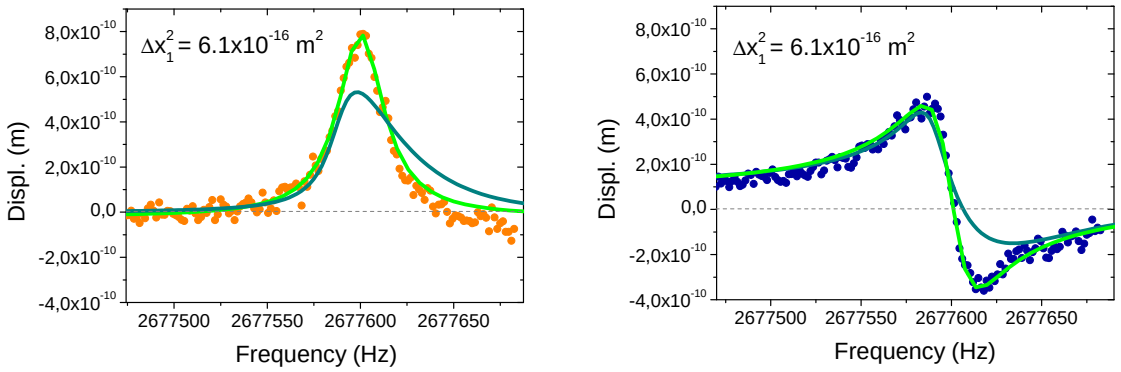

Figure 3.11: X (left) and Y (right) response curves taken for a small position noise, in the motional narrowing limit. Two fits are presented: one (light green) is from the analytic result (3.34), while the other (dark green) is obtained by averaging with the static exponential distribution on frequency noise, with a manually added shift in the latter case to allow a visual comparison.

interference at the origin of the mechanical resonance. As the noise magnitude, i.e. the disorder, goes to zero, there is less diffusion around the most probable accumulated phase path (the black line in Fig. 3.4 left panel), which enhances phase coherence and results in more Lorentzian lines.

3.5 Observation of non-linear position noise spectra

As seen in section 3.2, the response and the position noise spectrum are linked through the fluctuation-dissipation theorem in the linear regime. Yet, in presence of a nonlinear interaction, even though the phenomenological explanation should still hold, a direct relation such as Eq. (3.3) is not necessarily valid anymore.

Nonetheless, the results obtained in the previous sections for a driven mode obviously apply qualitatively when looking at the position spectrum of the fluctuating mode, without any driving sine force. Under high force noises, the nonlinear restoring force term becomes increasingly relevant. This impacts the position spectrum, which undergoes frequency noise and line shape distortion as the driven responses. Including now a non-linear term $\gamma_{m,m}\delta x_m^3(t)$ on the dynamics of the noisy mode in Eq. 3.9 and performing a RWA, its Langevin equation writes now:

$$\dot{\delta A}_m + \frac{\Gamma_m}{2}\delta A_m + \beta_{m,m}|\delta A_m|^2\delta A_m = \frac{F_{th,m}(t)e^{-i\omega_m t}}{2m_m\omega_m}. \tag{3.35}$$

From rules on derivation of correlation functions, and using $\delta A_m = \delta X_m + i\delta Y_m$, one can write coupled Langevin equations on both quadratures. The procedure is detailed in [31] and follows the same idea as what has been exposed above. In the end, the

average accumulated phase term is rather similar to the driving case:

$$G_s(t) = \frac{e^{\Gamma_m t}}{\cosh(a_{m,m}t) + \dfrac{\Gamma_m\,(1+2i\alpha_{m,m})}{2a_{m,m}}\sinh(a_{m,m}t)}. \tag{3.36}$$

The non-linear spectrum thus writes:

$$S_x(\omega) = \int_{-\infty}^{+\infty} S_x(\omega - \delta\omega_{n,m})\Theta(\delta\omega_{n,m})\mathcal{G}_s(\delta\omega_{n,m})\mathrm{d}\delta\omega_{n,m}, \tag{3.37}$$

where $\mathcal{G}_s$ is the Fourier transform of G_s. This section presents our technique to measure the spectrum of position fluctuations, as well as the results obtained under large fluctuations.

3.5.1 Acquisition of noise spectra

The most conventional way to measure noise is to use a spectrum analyzer, which measures the autocorrelation function of the noise signal in a given bandwidth and display its Fast Fourier Transform (FFT). While it is a straightforward measurement procedure, having the measured quantities in real units can be tedious, as the displayed spectra are only relative to a certain reference level and go through a complex chain of processing. In the present experiment, having real units is crucial to quantitatively address the phenomenon. Meanwhile, lock-in amplifier measurements are already calibrated so that forces and displacements are known in real units. Thus, we developed an alternative way to measure position spectra using only the lock-in amplifier. Another advantage of this technique is the possibility to obtain phase-resolved information on the fluctuations, which proves useful when nonlinearities break the symmetry of the 2D Gaussian statistics in the phase space (see section 3.7 below).

By definition, a lock-in amplifier demodulates in amplitude a given input signal by mixing it with a reference signal. The resulting voltage is averaged during a time set by the lock-in time constant and long enough in principle, so that only the signal present at the reference frequency remains with minimum noise. In the frequency domain, this procedure is the convolution of the input signal with a narrow filter centered around the swept reference frequency, of bandwidth inversely proportional to the time constant. Therefore, the narrower the filter, the better the resolution on the measured quantity, at the expense of a fast measurement.

However, it is implied that the wanted signal, in such a procedure, is a deterministic one, obtained through a response to a drive signal synchronized in frequency with the reference signal. What we want to measure here is a noise, which by definition is spread over a large range of frequencies. Therefore, one can use the lock-in amplifier

in a reverse way by opening the bandwidth centered around the reference frequency, to acquire as much noise as possible coming from the system.

Within this bandwidth BW, a signal is acquired and digitized with a DAQ card operating much faster than the lock-in time constant. The acquired signal length is proportional to the bandwidth, but we loop the measurement to obtain a trace with a number of samples N statistically significant. A computer routine then calculates numerical correlators $C_{XX}[j] = \langle \delta X_i \delta X_{i+j} \rangle_i$, $C_{YY}[j] = \langle \delta Y_i \delta Y_{i+j} \rangle_i$, $C_{XY}[j] = \langle \delta X_i \delta Y_{i+j} \rangle_i$, where the average notation $\langle ... \rangle_i \equiv \sum_{i=0}^{N-1} /N$, using cycling notations when $i + j \geq N$. The SR844 lock-in has a filter with asymptotes falling at 24 dB/oct, and the equivalent measurement bandwidth BW is obtained from the lock-in time constant τ_m through the relation $\mathrm{BW} \times \tau_m = 5/64$. By definition $S_\Lambda(\omega) = \pi C_\Lambda[0]/\mathrm{BW}$, where $\Lambda = \mathrm{XX}, \mathrm{YY}$ or XY. Note that by construction, if the linearized description still holds, X and Y are uncorrelated, i.e. $S_{XY}(\omega) = 0$, and $S_x(\omega) = S_{XX}(\omega) = S_{YY}(\omega)$, where S_x is the position noise spectrum defined through Wiener-Khinchin theorem (3.4).

3.5.2 Pulling Brownian motion out of the measured signal

The procedure explained above does not take into account the fact that the NEMS is actuated in an invasive way through current feeding and is inserted in a disadapted transmission line. These factors will be responsible for additional parasitic noise sources, which will result in dramatically limited performances of our setup compared to, say, optical means [4]. Let us now focus more on these different contributions. The noise current injected writes in the rotating frame $\delta I(t) = \delta I^c(t)\cos(\omega t) - \delta I^s(t)\sin(\omega t)$. $\delta V(t)$, the detected signal at the level of the lock-in, is the sum of:

- the electromotive force noise corresponding to the Brownian motion itself:

$$\delta V_B(t) = -(\xi l B)^2 \frac{\mathrm{d}}{\mathrm{d}t}(\chi * \delta I)(t), \tag{3.38}$$

- the Ohmic response of the conducting layer having a resistance R_N:

$$\delta V_{\mathrm{ohm}} = R_N \delta I(t), \tag{3.39}$$

- a capacitive response due to the finite transmission line capacitance C_{eq}:

$$\delta V_{\mathrm{capa}}(t) = \int \frac{\delta I(t')}{C_{eq}} \mathrm{d}t', \tag{3.40}$$

- all the other noise contributions that do not arise from the electrical noise current, e.g. the lock-in amplifier input noise. These are gathered in a quantity $\delta V_{\mathrm{oth}}(t)$.

The voltage noise spectrum is the Fourier transform of the total voltage noise auto-correlation function $\langle \delta V(t)\delta V(t+\tau)\rangle$. Within the rotating wave approximation, the terms $\dot{\delta I}^c, \dot{\delta I}^s$ can be neglected. Moreover, the noise current is filtered with a 0.7 MHz bandwidth filter, and thus has a typical correlation time ~ 1 µs, which is reasonable when compared to the NEMS decay time in the ms range. Therefore the background noise can be safely approximated as δ-correlated. In addition, noise arising from uncontrolled sources is uncorrelated with the current noise. The main drawback of this technique is a cross correlation appearing between the Brownian motion term and the ohmic/capacitive contributions. Especially, the Brownian-capacitive cross-correlation will introduce, in the frequency domain, a term proportional to $\mathrm{Re}\,[\chi(\omega)]$, which is anti-symmetric, as opposed to the Brownian spectrum and the Ohmic contribution cross-terms. This will result in a distorted total spectrum lineshape, as shown in Fig. 3.12 left panel. The total spectrum writes:

$$S_V(\omega) = S_{th}(\omega) + S_{\mathrm{cross}}(\omega) + S_{\mathrm{back}}(\omega), \tag{3.41}$$

with each contribution:

$$S_{th}(\omega) = |\chi(\omega)|^2(\xi l B)^4\omega^2 S_I(\omega), \tag{3.42}$$

$$S_{\mathrm{cross}}(\omega) = \left(-2R_N \mathrm{Im}\,[\chi(\omega)] + \frac{2}{C_{eq}\omega}\mathrm{Re}\,[\chi(\omega)]\right)(\xi l B)^2\omega S_I(\omega), \tag{3.43}$$

$$S_{\mathrm{back}}(\omega) = S_{\mathrm{oth}}(\omega) + \left[R_N^2 + \left(\frac{1}{C_{eq}\omega}\right)^2\right] S_I(\omega). \tag{3.44}$$

Knowing the metallic layer resistance R_N, only the transmission line capacitance C_{eq} and the noise level $S_{\mathrm{oth}}(\omega)$ (supposedly white in the frequency range considered) are left as free parameters to fit the measured spectra. An example of application of this procedure is shown in Fig. 3.12.

By subtracting the cross correlation term and the background term to the raw, measured spectrum, one is left only with the actual Brownian motion spectrum. Since this rectification procedure involves subtraction of unwanted contributions, it introduces negative values in the spectrum, but these are mere artefacts. We measure spectra for different applied (current) noises, checking that the equipartition relation (3.2) holds, with mode parameters (spring, mass) measured independently, e.g. through standard driven response procedures (see Fig. 3.13). Note that points taken at very high effective temperatures ($\sim 10^8 - 10^{10}$ K) are already in the Duffing regime concerning the spectra lineshape (see paragraph below).

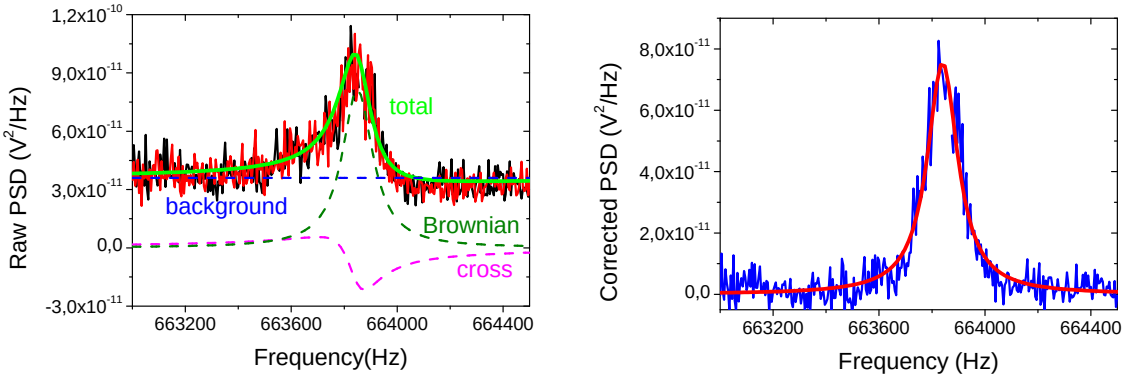

Figure 3.12: left: raw measured power spectral density on X and Y quadratures at the level of the lock-in amplifier, on sample 300 µm n°1. The green solid line is the application of Eq. (3.41), with a fit line capacitance $C_{eq} = 500$ pF, while dashed lines show contributions of Eq. (3.42) (green), (3.43) (pink) and (3.44) (blue). Right: corrected power spectral density, where parasitic contributions S_{cross} and S_{back} have been substracted. The red solid line is a Lorentzian fit yielding a linewidth $\Gamma_1 = 140$ Hz in agreement with the linewidth obtained through sine wave response measurements.

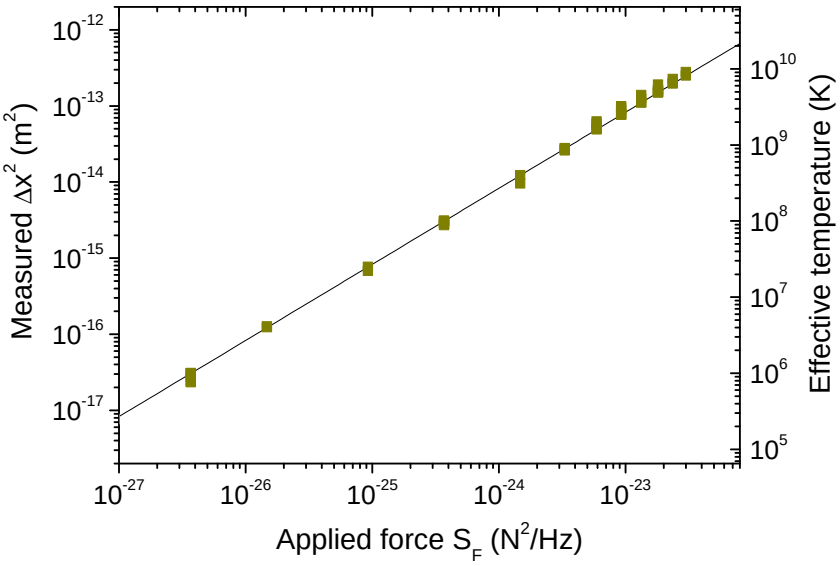

Figure 3.13: integrated value of the Brownian motion spectrum in real units, with its corresponding effective mode temperature, as a function of the force noise spectrum in real units. The solid line follows the equipartition relation (3.2) even though the spectrum is distorted (see below), with mode parameters measured independently.

It is useful to notice that each contribution has a different field dependence. Therefore, to ensure that the procedure is valid in the whole parameter range for the chosen fit parameter C_{eq}, we measure spectra at different fields and report the fitted magnitudes of each contribution at the NEMS resonance as a function of the magnetic field, as shown in Fig. 3.14. The agreement between the fitted contribution and Eqs. (3.42), (3.43), and (3.44) is rather good, within 15 % of the measured values. Note that since the current noise injected is high, the uncorrelated noise contribution, estimated to 10 nV/$\sqrt{\text{Hz}}$ at most, is very small compared to the ohmic/capacitive noise contribution to the background.

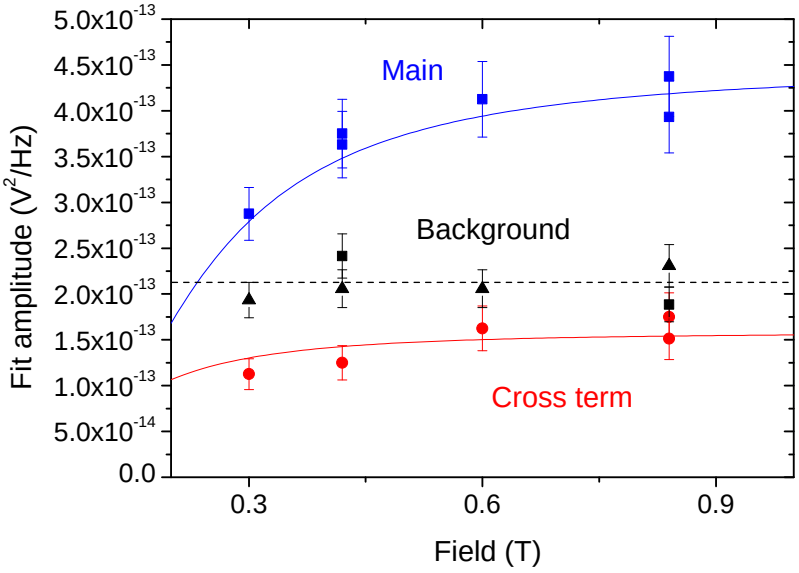

Figure 3.14: spectral peak height in raw units as a function of the magnetic field. "Main" refers to the Brownian motion spectrum, "Background" is the sum of ohmic, capacitive and uncorrelated contributions, and "Cross term" is the contribution arising from the cross-coupling between the ohmic/capacitive noise and the Brownian motion. With a transmission line capacitance estimated at C_{eq} = 500 pF, which is consistent with the disadapted cable length (a few meters), all fitted contributions are captured by the model within 15 %. The blue solid, red solid and black dashed lines reproduce Eqs. (3.42), (3.43), and (3.44) respectively.

Last but not least, one must find an optimal bandwidth BW with respect to the Brownian spectrum width. In the ideal case, taking a working point at the highest possible field with the smallest bandwidth would be the best option. However, doing so is time consuming, so the bandwidth chosen is generally not the smallest one. Yet, as the useful noise has a spectral spreading equal to the system linewidth, an upper limit on the measurement bandwidth exists. Indeed, if this bandwidth is too large,

the effective thermomechanical noise will be artificially broadened and its resonance height decreased, since the peak will be "diluted" over the measurement bandwidth due to the convolution process. Therefore, a trade-off bandwidth must be found so that the mechanical spectrum has its true linewidth, while the signal is measured over reasonable times. We have measured spectra for different electromechanical linewidths tuned with the magnetic field, as reported in Fig. 3.15. We have checked that all background contributions scale as BW as expected for a white noise.

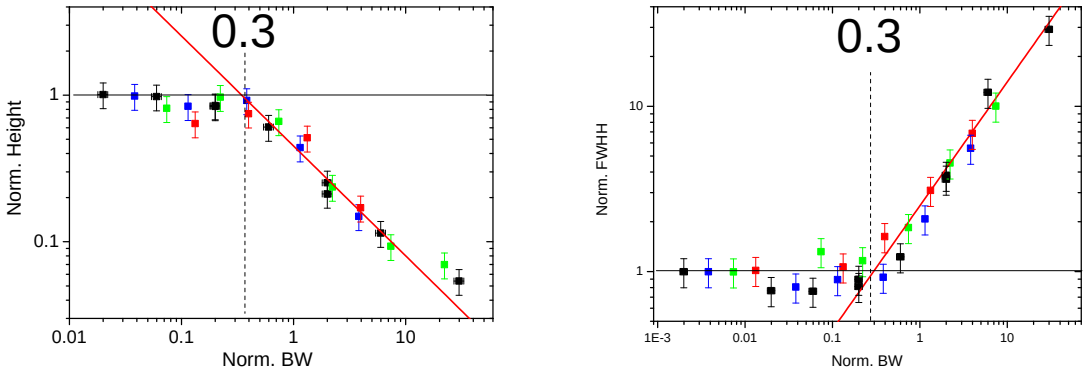

Figure 3.15: height (left panel, normalized to the maximum value) and width (right panel, normalized to the NEMS linewidth) of the spectrum peak, as a function of the lock-in amplifier bandwidth normalized to the NEMS linewidth, at 0.84 T (black), 0.6 T (blue), 0.42 T (green), and 0.3 T (red), hence for damping rates 140, 70, 36 and 20 Hz respectively. Solid lines are guides, while the dashed line shows the optimal bandwidth with respect to the electromechanical linewidth.

These peak height and width plots, normalized to mechanical parameters (true height, true damping rate at a given field) show that the data taken at different damping rates all collapse on the same curve when the measurement bandwidth is normalized to the damping rate. An optimum value in this case is a lock-in bandwidth equal to 30 % of the damping rate.

One important point is that in all these measurements, the intercorrelation spectrum S_{XY} has always been 0, and spectra measured on both quadratures were identical $S_{XX} = S_{YY}$. This does not hold anymore if a strong sine wave driving excitation is used (see section 3.7), as the linearization used to obtain Eq. (3.13) is not valid anymore in the self-coupling case: the term $|A_n|^2 \delta A_n$ cannot be discarded in this situation.

3.5.3 Distortion of position spectra at high effective temperatures

In the limit of high effective temperatures, the nonlinearly-induced shift and broadening observed for response measurements becomes also visible for the position spectrum, with its two limit behaviors (MN and IB). However, one has to take into account overheating of the structure due to high injected powers, which becomes relevant in the very high effective temperature limit ($10^9 - 10^{10}$ K). The total power due to injected noise is recalculated by integrating the injected voltage noise spectrum over the filter's bandwidth, yielding values as high as 10 nW directly injected in the nanomechanical beam. This is taken into account in the fit procedure following our thermal model (see Chapter 2, section 2.7). Examples for both limits are shown in Fig. 3.16, with theoretical lines obtained from Eq. (3.37) without free parameters. Again, the spectra observed for high effective temperatures appear strongly asymmetric, with a long tailed structure which is reminiscent of the exponential distribution (3.16). In addition, no cross-correlation between the two quadratures was observed.

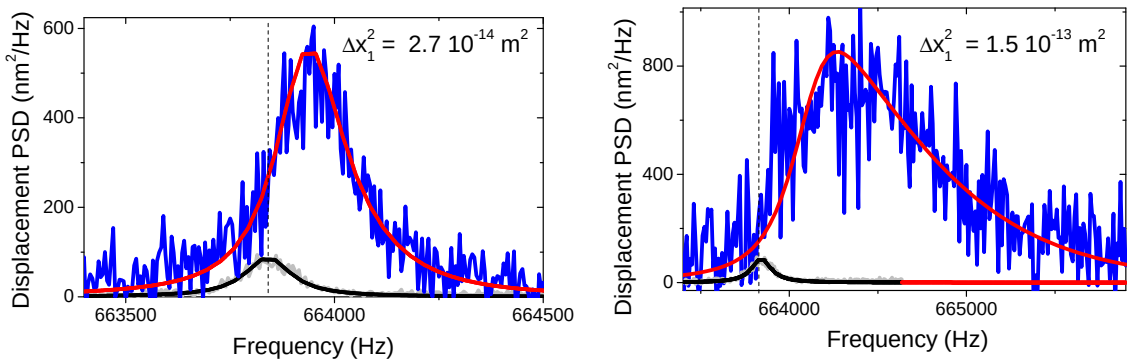

Figure 3.16: position noise spectra of the fundamental mode obtained in the motional narrowing (left) and inhomogeneous broadening (right) regimes. Solid lines are the application of Eq. (3.37). The grey line is a spectrum obtained in the linear regime, for low enough effective temperatures so that the effect of Duffing non-linearities can be neglected, while the dashed line is a Lorentzian fit with the linewidth corresponding to that of the driven response.

An interesting point is that numerical integration of the spectra, i.e., the spatial extension of the Brownian motion Δx_1^2, matches well the expected value insofar as $\Delta x_1^2 = Q_1^2 S_F / k_1^2$, as shown in Fig. 3.13. Thus, the equipartition hypothesis is not affected by the reported phenomenon. If it were the case, the features observed in driven response measurements in section 3.4 would anyway be incorrectly reproduced by theory: indeed, these features are dependent on the integrated position noise, which in the case of driven measurements was inferred through the equipartition hypothesis.

The fact that energy is conserved is another evidence that we genuinely witness a distortion due only to frequency noise, a purely dispersive phenomenon, mathematically described by the convolution. Measured shifts and FWHH as a function of position noise magnitude are plotted in Fig. 3.17. The agreement between data and theoretical lines is unprecedented: to our knowledge, only one study reported thermally non-linear spectra [14] in the case of levitated nanoparticles in an anharmonic trap, and no quantitative agreement could be found, while the discussion only considered the case where the partial susceptibilities were weighted by Boltzmann's distribution, i.e. the inhomogeneous broadening regime.

Interestingly, one sees that the lines obtained for the spectrum and the imaginary part of the response are **not the same**. Therefore, even though the equipartition hypothesis is still valid, the fluctuation-dissipation relation (3.3) does not hold anymore. This is not surprising, however, since the present study actually goes beyond the simple linear response, which is a prerequisite for the validity of the relation.

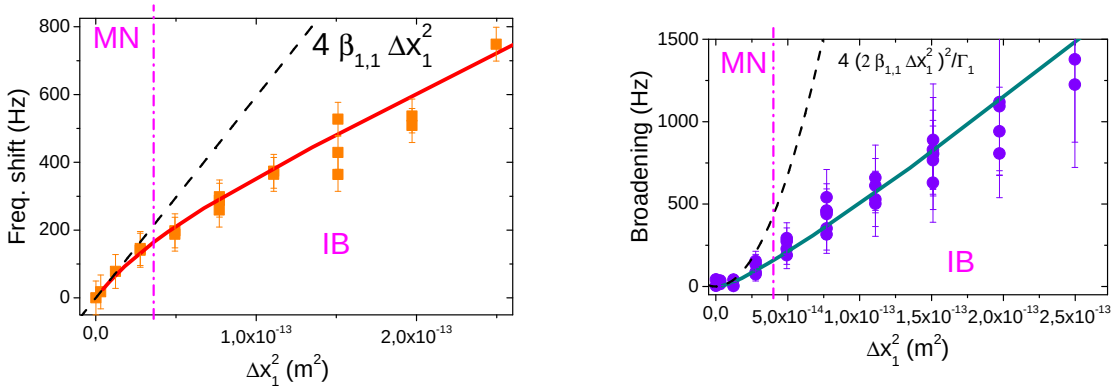

Figure 3.17: frequency shift (left) and linewidth broadening (right) of the fundamental mode position power spectrum as a function of its intensity. Solid lines are the theoretical parameters extracted numerically from Eq. (3.37), while dashed lines show the laws obtained in the motional narrowing regime.

3.6 Consequences on fundamental limitations to frequency resolution

Previous sections focused on the subtleties of the Duffing-mediated frequency noise. However, it also presents some important consequences for applications. Indeed this effect is ubiquitous, relying only on really intrinsic and genuine properties such as the dissipative coupling to a thermal bath and geometric nonlinearities. In addition, while we focused on the effect due to one mode for the sake of demonstration, any real vibrating structure will have a collection of modes which will contribute to the

observed frequency noise. In particular, while geometric nonlinearity-mediated mode coupling was long observed within a given family of modes, recent works have shown that geometric mode coupling was also possible between two flexural modes of different families in nanomechanical structures [88]. Coupling to longitudinal or torsional modes is however overlooked here, as it is in practice very small and falls outside standard beam theory.

In essentially all situations where real nonlinearity-induced frequency noise is observable, the temperature is such that the phenomenon occurs in the motional narrowing limit. Therefore, the resonance will be a dressed Lorentzian, with a frequency shift $\propto T$ analogous to a "thermal" mechanical Lamb shift and a thermal decoherence-like broadening $\propto T^2$. Including another family of flexural modes with motion variables $\{\delta y_{m'}\}$, the renormalized parameters for a driven mode n write:

$$\omega_n = \omega_n^0 + 4\beta_{n,n}\Delta x_n^2 + 2\sum_{m\neq n}\beta_{n,m}\Delta x_m^2 + 2\sum_{m'}\beta_{n,m'}\Delta y_{m'}^2, \tag{3.45}$$

$$\Delta\omega_n = \Gamma_n + \frac{2(4\beta_{n,n}\Delta x_n^2)^2}{\Gamma_n} + 2\sum_{m\neq n}\frac{(2\beta_{n,m}\Delta x_m^2)^2}{\Gamma_m} + 2\sum_{m'}\frac{(2\beta_{n,m'}\Delta y_{m'}^2)^2}{\Gamma_{m'}}. \tag{3.46}$$

These expressions are generic. In the case of doubly-clamped beams, one can use expressions for βs derived from the nonlinear description of beams (see Chapter 2, section 2.9). Within numerical sum factors, and after application of the equipartition hypothesis (3.2) to Δx_m and $\Delta y_{m'}$, the dependencies on the in-built parameters appear as follows:

$$\frac{\omega_n - \omega_n^0}{\omega_n^0} = \mathcal{A}_n \times \left(\frac{E_{beam}A}{2L^3}\right)\left(\frac{k_BT}{2k_n^2}\right), \tag{3.47}$$

$$\frac{\Delta\omega_n - \Gamma_n}{\Gamma_n} = \mathcal{B}_n \times \left(\frac{E_{beam}A}{2L^3}\right)^2\left(\frac{k_BT}{2k_n^2}\right)^2 Q_n^2. \tag{3.48}$$

Numerical prefactors $\mathcal{A}_n$ and $\mathcal{B}_n$ include sums over all the coupled modes, introducing the integrals defined with the mode function overlaps (as defined in Chapter 2):

$$\mathcal{A}_n = \sum_m \frac{I_{n,n} + I_{m,m} + 2I_{n,m}^2}{k_m/k_n} + \sum_{m'}\frac{I_{n,n} + I_{m',m'} + 2I_{n,m'}^2}{k'_m/k_n}, \tag{3.49}$$

$$\mathcal{B}_n = \sum_m \frac{Q_m}{Q_n}\frac{\left(I_{n,n} + I_{m,m} + 2I_{n,m}^2\right)^2}{(k_m/k_n)^2(\omega_m^0/\omega_n^0)} + \sum_{m'}\frac{Q_{m'}}{Q_n}\frac{\left(I_{n,n} + I_{m',m'} + 2I_{n,m'}^2\right)^2}{(k_{m'}/k_n)^2(\omega_{m'}^0/\omega_n^0)}, \tag{3.50}$$

where we deliberately made a distinct sum over the other family of eigenmodes, as their modal functions are slightly different in the case of a rectangular beam, where moments of area differ. Note that in both limiting cases (high and low stress), overlap

integrals, resonance frequencies and spring constants ratios can be simplified, yielding only dependencies in mode numbers in the sums [33].

However, $\mathcal{A}_n$ and $\mathcal{B}_n$ do depend on the type of dispersion relation $\omega_m(\lambda_m)$, and no analytic expression can join the high and low stress limits. Left alone is the dependence of the Q factor with the mechanical mode number for the thermal dephasing prefactor $\mathcal{B}_n$. Although there is currently no universal description of loss mechanisms in nanomechanical resonators, observations [39, 89] suggest that for SiN beams the Q factor depends on the bending energy as: $Q_m = (U_{bend} + U_{tension})/\Delta U_{bend}$, with $U_{bend} + U_{tension}$ the total potential energy defined by Eq. (2.40). The phenomenological model does not propose a microscopic analysis of the damping, but assumes that losses ΔU_{bend} are proportional to the bending energy and introduces a complex Young's modulus to account for it which is left as the only free parameter in the model. Previous studies of our SiN beams showed rather good agreement with this approach, and a mode dependent expression can be found in Ref. [42]. The approach is phenomenological, with the mode dependence fit to the model with one free parameter ΔU_{bend}.

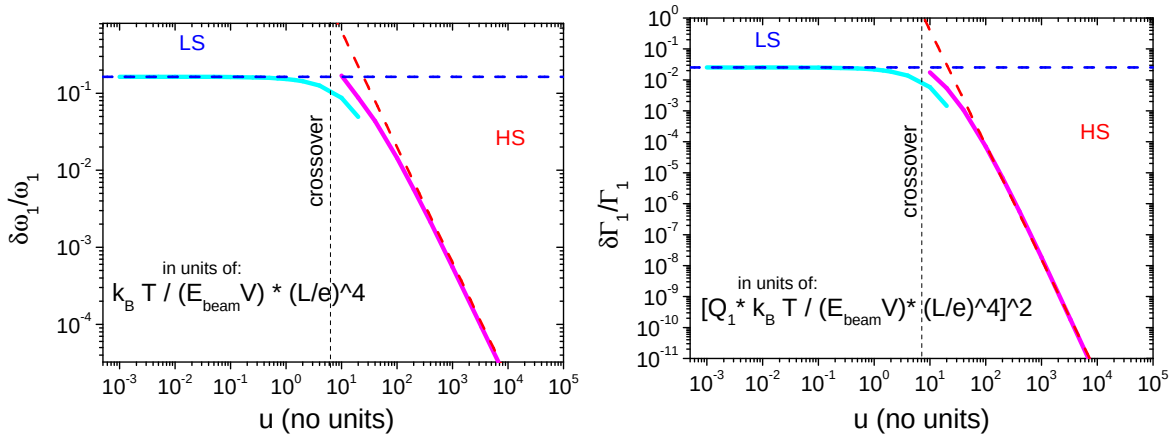

Figure 3.18: thermal frequency dressing (left) and broadening (right) for the fundamental flexure, with units shown in figures, as a function of the dimensionless stress parameter $u = \frac{\sigma A L^2}{E_{beam} I}$. Solid lines are the result of numerical sum calculations, while dashed lines show both limit cases (high and low stress), calculated for a single family of modes.

The results of the computation for the fundamental flexure are summarized in Fig. 3.18, for a single family of modes. It essentially doubles for a square beam, taking into account the other family. Note that the frequency dressing term is simply a shift, but this term would lead to extra dephasing if temperature were not stable. Furthermore, the limitation imposed by thermal decoherence crucially depends on the aspect ratio L/e. In particular, we see that the effect quickly decreases with added stress, but for low stress structures with high aspect ratio, the fundamental limit imposed by this mechanism is not negligible, e.g. for carbon nanotubes. This could be an explanation for recent observations [76, 32], where the mechanism was qualitatively mentioned. The

authors from Ref. [76] reached the same conclusion, although with a very different, microscopic approach.

3.7 Anomalous fluctuations for non-linear driving fields

3.7.1 Beyond linearization

The results exposed in the sections above are obtained and well described in a linearization approximation: in order to obtain the set of equations (3.13), we have neglected the term $|A_n|^2\delta A_m$, which corresponds experimentally to a drive low enough so the response remains linear in the driving force. In other words, the interplay between the fluctuations and the drive was unilateral, and modifying the driving force did not affect the fluctuations. However, as shown in Fig. 3.19, in the "self-coupling" situation, the linear relation $x_n \propto F_n$ does not hold anymore when the NEMS is strongly driven: its peak value is lower than expected, as if there were an excess position noise transduced into frequency noise, which over-deteriorates the response. Moreover, this effect is asymmetric: while the X quadrature is over-blurred, the Y one is less affected (see Fig. 3.19 inset).

In fact, keeping the full non-linear term in the RWA introduces a new phenomenology that has been overlooked so far in this Chapter. It arises from the possibility for the driven motion to act back on its own fluctuations, if the nonlinearity is strong enough, i.e. $\beta x_{max}^2 \sim \Gamma$. In that limit where the system is driven far from its equilibrium, it is not possible to obtain separate equations such as the system (3.13). While a complete resolution is tedious, we shall expose qualitative theoretical and experimental features that we believe can explain the excess frequency noise observed. The interested reader may find a more detailed derivation of the fluctuation problem for a strongly driven nonlinear resonator in Refs. [82, 42]. On the experimental side, let us mention that at this stage the apparatus was not developed enough to enable systematic and quantitative measurements. Therefore, the results obtained in this section are only preliminary and used as a qualitative demonstration.

It is convenient to start from the Duffing equation (2.67), first without considering fluctuations. Within the rotating wave approximation, and introducing reduced parameters $Z(\theta) = \sqrt{\frac{3\gamma}{16\omega\Gamma}} A\left(\frac{2\theta}{\Gamma}\right), g_0 = \frac{\sqrt{3\gamma}F_0}{8(\omega\Gamma)^{3/2}m}, g_{th} = \frac{\sqrt{3\gamma}F_{th}}{4(\omega\Gamma)^{3/2}m} e^{-i\omega t}, \Omega = 2(\omega-\omega_0)/\Gamma$ with a dimensionless slow time $\theta = \Gamma t/2$, one obtains:

$$\dot{Z}(\theta) = -(i\Omega + 1)Z(\theta) + i|Z(\theta)|^2 Z(\theta) - ig_0 - ig_{th}(\theta), \tag{3.51}$$

where the dot notation refers to the derivative with respect to θ, A is the slow, deterministic complex amplitude in the rotating frame and all indexes are dropped since we are only interested in one mode. First we consider a situation without noise, i.e.

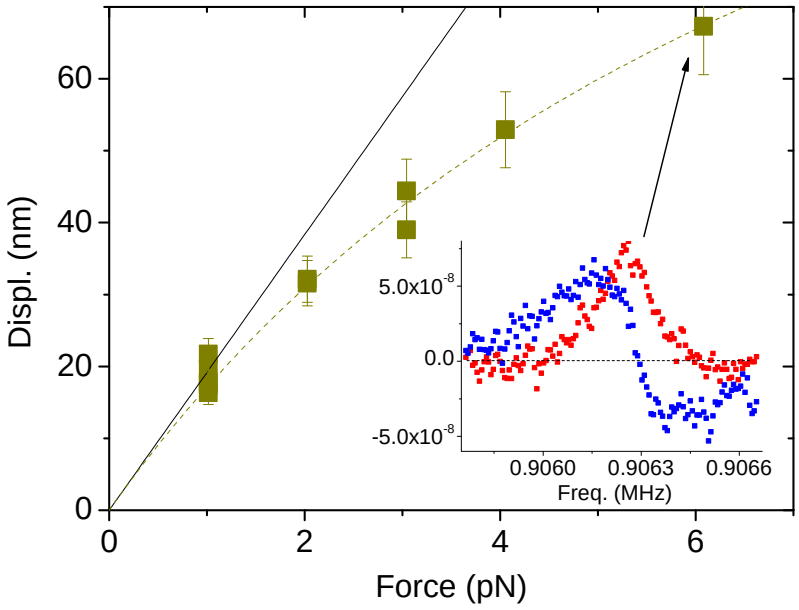

Figure 3.19: amplitude at resonance of the first mode sine-wave response experiencing a constant position noise $\Delta x_1^2 = 2.2 \times 10^{-15}$ m^2 ($T_{\text{eff}} = 7 \times 10^7$ K), as a function of the driving force amplitude, for the sample 250 µm n° 1. The black solid line is the linear drive prediction, while the dark yellow dashed line is a guide for the eyes. Inset: in-phase and quadrature responses for an applied force $F_1 = 6.1$ pN.

$g_{th} = 0$. The steady state solution writes:

$$Z_0 = \frac{g_0}{|Z_0|^2 - \Omega + i} = |Z_0(\Omega)|e^{i\phi_0(\Omega)}. \tag{3.52}$$

To simplify, we introduce the variable $\tilde{Z}(\Omega) = Z(\Omega)e^{-i\phi_0(\Omega)}$, such that the steady state solution is real-valued. If now we introduce a small perturbation (created e.g. by the Langevin force g_{th}), we can linearize Eq. (3.51) in the fluctuations around the steady-state solution. We introduce $\tilde{Z}_R = \text{Re}[\tilde{Z}]$ and $\tilde{Z}_I = \text{Im}[\tilde{Z}]$ the quadratures of the motion along the reference phase ϕ_0, and allow them to fluctuate (in practice, they do so because of the Langevin force): $\tilde{Z}_R = \tilde{Z}_0 + \delta Z_R$ and $\tilde{Z}_I = \delta Z_I$ (since the steady state solution is real). Using the real and imaginary parts of Eq. (3.52) for the steady state solution multiplied by $e^{-i\phi_0}$, and injecting in Eq. (3.51) one obtains the dynamics equation for the fluctuations $(\delta Z_R, \delta Z_I)$:

$$\begin{pmatrix} \delta\dot{Z}_R \\ \delta\dot{Z}_I \end{pmatrix} = \begin{pmatrix} -1 & \Omega - \tilde{Z}_0^2 \\ 3\tilde{Z}_0^2 - \Omega & -1 \end{pmatrix} \begin{pmatrix} \delta Z_R \\ \delta Z_I \end{pmatrix}. \tag{3.53}$$

This equation is the core of the issue: without the Duffing interaction there would not be a dependence in the stationary solution and the eigenvalues of the system would give the usual relaxation time $2/\Gamma$ in both directions. Here we can expect the Duffing nonlinearity to break this symmetry, as the eigenvalues yield:

$$v_{1,2} = -1 \pm \sqrt{\left(3\tilde{Z}_0^2 - \Omega\right)\left(\Omega - \tilde{Z}_0^2\right)}. \tag{3.54}$$

We see that as soon as the oscillation is large enough to distort a resonance line, there is a separation of the two quadratures decay rates: indeed, in real units, the decay rates write $\Delta\omega_{1,2} = -\Gamma\mathrm{Re}[v_{1,2}]$, and we see clearly that $\mathrm{Re}[v_1] \neq \mathrm{Re}[v_2]$ even for moderately distorted lines. This appears clearly in Fig. 3.20: one relaxation rate increases while the other decreases. Let us mention that analogies can be made with Landau's theory of phase transitions [90]: for a given force close to the critical force (when considering a sweep in frequency) or a given frequency close to the spinodal point (when considering a force ramped through the critical force), the quartic Hamiltonian (3.7) in displacement is on the verge to allow a new stable motional state to develop. Therefore, according to Landau's theory of phase transitions we can expect fluctuations near this critical point to diverge, while their dynamical timescales are slowed down, even though the analysis in terms of scaling laws and is unfortunately beyond the scope of this work and calls for further analysis.

The separation, at a constant force, is triggered as soon as $\Omega \geq \Omega_{res}$, as shown in Fig. 3.20. For forces close to the critical point, there is a clear separation of timescales on quadratures, and when the critical force is applied, the relaxation rate of the slow quadrature reaches zero, at the spinodal point, while the other is doubled compared to the bare relaxation rate. This behaviour remains beyond the critical force, when the driving force is brought close to both bifurcation points: for instance, at the upper branch bifurcation where the high amplitude metastable state and the unstable state merge, we have $v_1 = 0$ and $v_2 = -2$, that is, system-independent eigenvalues, which do not depend on the amplitude and frequency anymore. The quadratures in the eigenbasis $(\delta Z_1, \delta Z_2)$ behave according to:

$$\begin{cases} \delta\dot{Z}_1 = 0, \\ \\ \delta\dot{Z}_2 = -2\delta Z_2. \end{cases} \tag{3.55}$$

Therefore, in the eigenbasis, one quadrature can be discarded while the other has very slow timescales, thus reducing the physics to a simple one dimensional problem. Since the resonance frequency asymptotically merges with the upper bifurcation frequency at very large forces, the range where the timescales depart reduces as the force is increases, as seen in Fig. 3.20. This timescale separation allows for instance

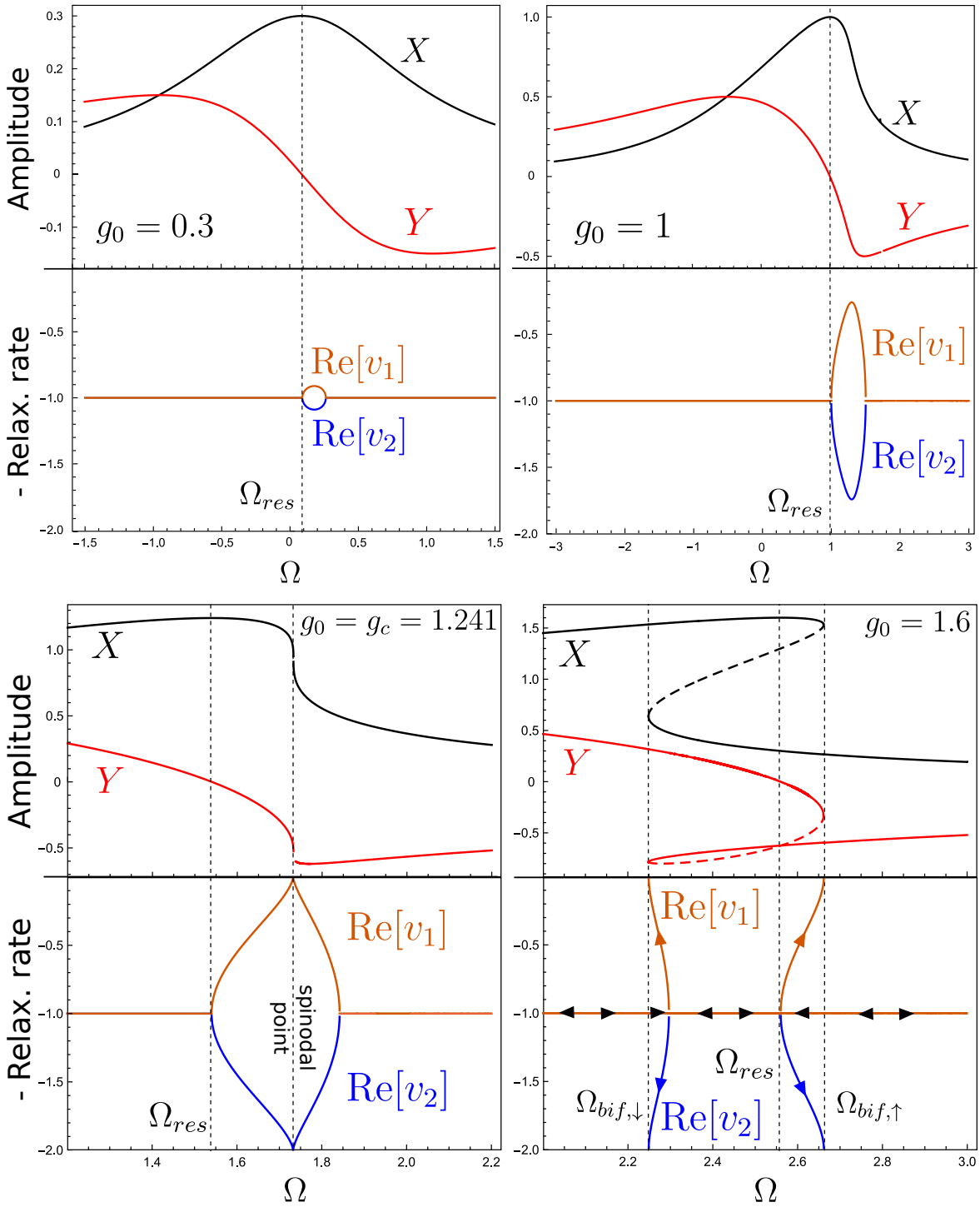

Figure 3.20: mechanical responses in dimensionless units (see text, the dashed parts represent the unstable solution) plotted with relaxation rates $-\mathrm{Re}[v_{1,2}]$ in dimensionless units computed from Eq. (3.54) as a function of the reduced driving frequency, for reduced driving forces $g_0 = 0.3$ (weakly non-linear), $g_0 = 1$, $g_0 = g_c = 1.241$ (critical force where the hysteresis opens), $g_0 = 1.6$ (strongly non-linear, bistable). On the last panel, arrows represent the frequency sweep direction.

to study quantitatively escape dynamics from the metastable state [71]. This phenomenon should be visible directly if one measures the correlation functions on both quadratures with different phases, to extract these decay times. We do so instead of measuring the spectrum: indeed, since this time we drive the NEMS while we measure the fluctuations, we obtain an integrated r.m.s. information for each drive frequency, but not the full spectral information. Since the latter is supposed to depend on the driving field, we can only have a partial information if we use our spectrum reconstruction technique. However, by measuring the correlation function at each drive setting with a bandwidth wide enough (i.e. a good resolution in time), we have access to the relaxation time at each drive and we can observe its evolution along the frequency sweep. The correlators computed from both quadratures are obtained from a noise sample digitized by the DAQ card (see section 3.5.1), and averaged over many samples.

To obtain a clean signal on the correlation functions and remove the background-mechanical cross component (3.43) that will alter the exponential decay, we have designed a simple opposition line based on a LC circuit with a tunable capacitance that is mounted in parallel with the NEMS circuit (see Fig. 3.21): the incoming voltage noise is splitted between the two lines, and the LC circuit acts as a dephaser with an adjustable gain, so that the voltage noise obtained at the end is subtracted to the background voltage noise obtained at the cryostat output. The Ohmic component of the cryostat output is, within a numerical factor, the same as the opposition line signal, plus a constant dephasing due to lineic capacitances. This holds true as long as the bandwidth of the RLC circuit is large compared to the mechanical bandwidth, which is the case in practice with our setup. With the right tuning of the capacitance (between 0 and 200 pF) and the appropriate cable length for the opposition line, it is possible in theory to catch up the dephasing, match the level of Ohmic noise and significantly cancel the background noise. However, due to the noisy nature of the signal, the task is tedious. Nevertheless, we manage to suppress the background by a factor 5 in power, which is enough to significantly suppress the cross component (3.43) as well.

3.7.2 Slowing down the decay of position noise correlations near bifurcation points

We have measured correlation functions $C_{\mathrm{XX}}(t), C_{\mathrm{YY}}(t), C_{\mathrm{XY}}(t)$ for a force near the critical point where the hysteresis opens (see Chapter 2 paragraph 2.9.2). We see while sweeping the frequency Ω that the dynamics is slowed down as we run across the spinodal point x_s where $\omega_{bif,\uparrow} = \omega_{bif,\downarrow}$, with a decay time for correlations that is multiplied by a factor up to 20, as shown in Fig. 3.22, left panel.

The increase in relaxation times is concentrated for driving frequencies near the spinodal point in the (ω, x) plane (which is not the resonance position, i.e. the maximum in amplitude: $\omega_{bif,\uparrow,\downarrow} \neq \omega_{res}$). As seen in Fig. 3.22 (right panel), relaxation times

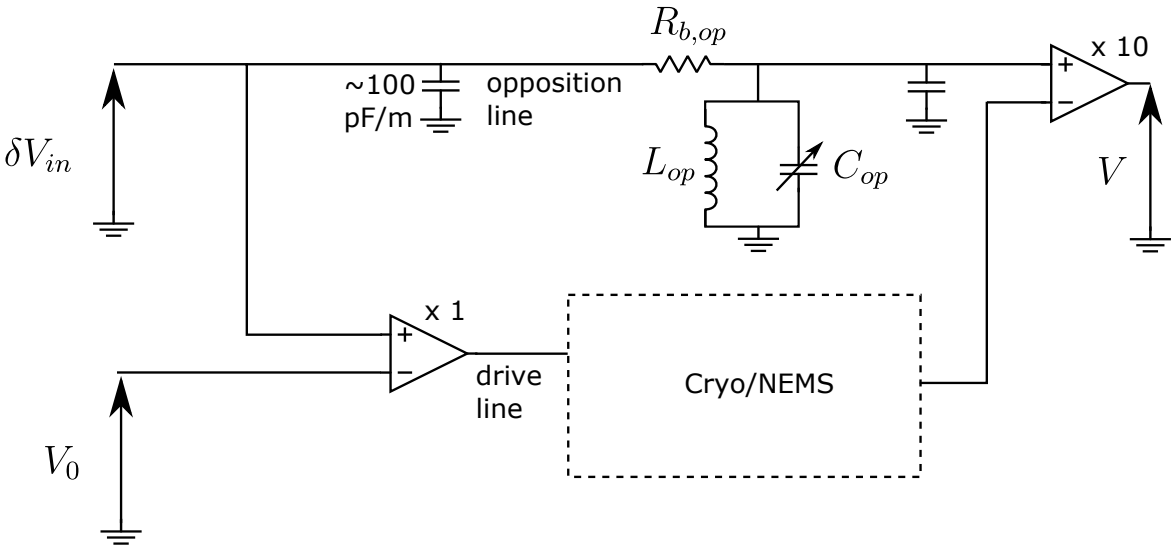

Figure 3.21: setup with a parallel opposition circuit used to cancel the resistive background (attenuators and filters not shown). The components used have values $L_{op} = 0.19$ mH, $R_{b,op} = 1$ kΩ, and the tunable capacitance can be adjusted between $C_{op} = 0$ and 200 pF. The cable length is adjusted to optimize the noise cancellation. V_0 and δV_{in} generate the driving force and noise respectively, while V is the detected voltage fed to the lock-in.

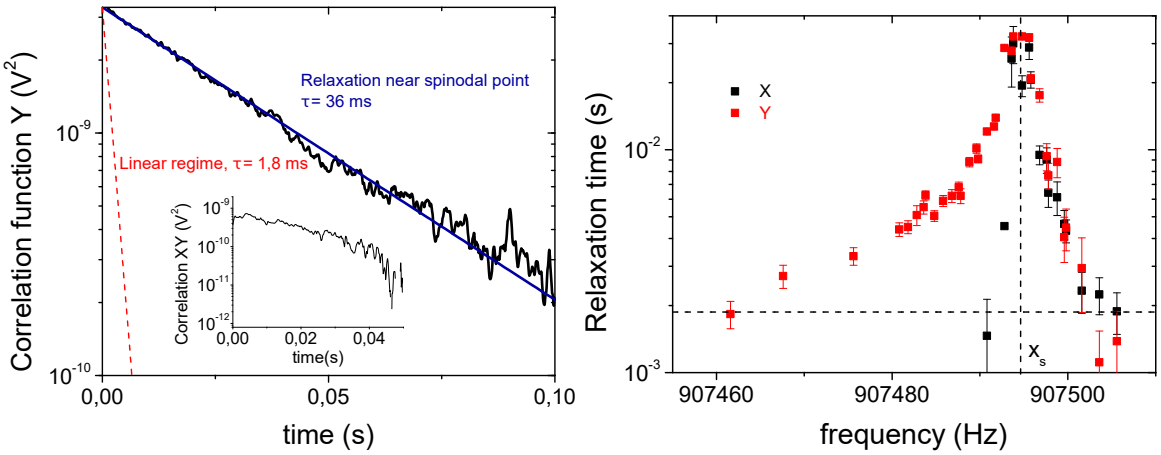

Figure 3.22: left: noise correlator $C_{YY}(t)$ on the Y quadrature in raw units for a force $F_0 = 17$ pN close to the critical point and a phase $+45°$ compared to the reference phase yielding in-phase and quadrature responses. The blue line is an exponential fit $\propto e^{-t/\tau}$, with a comparison to the pure linear case (dashed red line). The inset shows the intercorrelation function C_{XY} Right: relaxation times obtained on both quadratures correlators as a function of the driving frequency, for the same applied force. The dashed vertical line marks the spinodal point in amplitude, while the horizontal one marks the relaxation time in the linear regime.

on both quadratures are increasing, although not with the same rise. The maximum is reached at the spinodal point where both quadratures display the same decay, and then both decay times decrease likewise as the frequency is detuned away from the spinodal point x_s.

Note that the measurements presented here have been realized at fixed driving phase. Thus this (X, Y) quadrature basis **is not** the one adapted to the present problem: indeed, the eigenbasis associated to the eigenvalues is obtained by rotation from the initial basis (the one in which we have the in-phase and quadrature response) with an angle that depends on the frequency and amplitude of the oscillation. Therefore, the reference phase must be adapted with an appropriate compensation scheme for each driving frequency to follow the directions where the asymmetry is maximum, which is not the case here. The signature of this is that the correlation function C_{XY} is nonzero for some drive frequencies, as shown in Fig. 3.22 left panel inset. In any case, qualitatively, we observe a slowing down of the fluctuations dynamics, which is a first new feature compared to previous sections.

For applied forces larger than the critical force ($F_0 > F_c$), asymptotically close to $\omega_{bif,\uparrow}$, we also observe the predicted separation of timescales for the two quadratures, as shown in Fig. 3.23. Note that getting close to the bifurcation point is a delicate operation, as the frequency and the damping of the resonator are fluctuating, thus affecting the hysteresis (see Chapter 6). Moreover, being close to the bifurcation point makes the resonator likely to jump between the two states, and this likelihood exponentially increases with the force noise injected since the latter acts as an effective temperature. Thus, we cannot get too close to the bifurcation frequency, which might explain why the measured relaxation times in the privileged direction are not tremendously high.

We see that one quadrature has correlations that decay very fast while the other has a correlation time multiplied by 10, i.e. more than one order of magnitude higher than the other, thus reducing the physics to the very convenient true 1D problem through timescale separation as explained theoretically above. Note that it is unclear whether the sharp decay on the X quadrature is due to the background or the NEMS, since the signal on X is very weak.

3.7.3 Asymmetric amplification of fluctuations in the phase space

So far we have shown preliminary evidence that the dynamics of the NEMS is slowed down near peculiar points when driven in the nonlinear regime. But the magnitude of its fluctuations is also affected: for each driving frequency we have monitored the trajectory of the Brownian motion in the quadrature space in the RWA. An example near the bifurcation frequency is shown in Fig. 3.24.

Two features are noteworthy: first the Brownian motion is squeezed along one quadrature while amplified along the other (see the oval in the figure replacing the

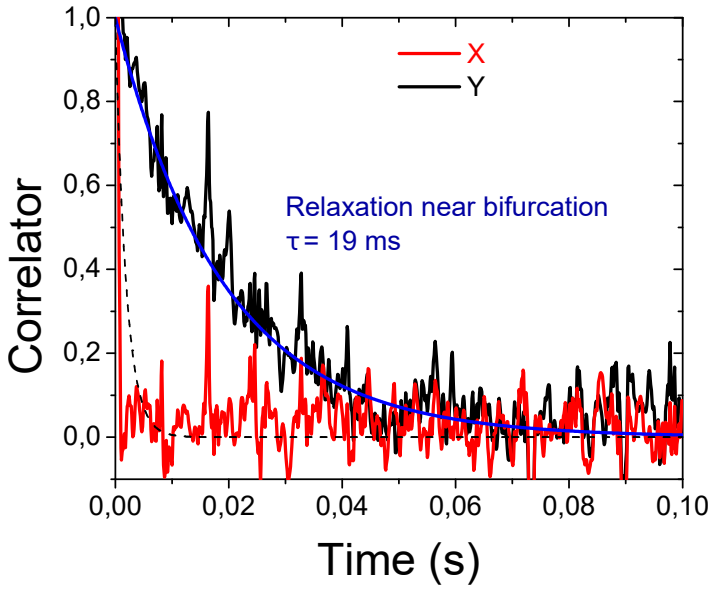

Figure 3.23: fluctuating quadratures correlators for a force $F_0 = 42$ pN, with a driving frequency a few Hz detuned from $\omega_{bif,\uparrow}$. The phase is set at $+45°$ from the reference phase in which we observe the in-phase and quadrature responses. The dashed line is the exponential decay expected in the linear regime.

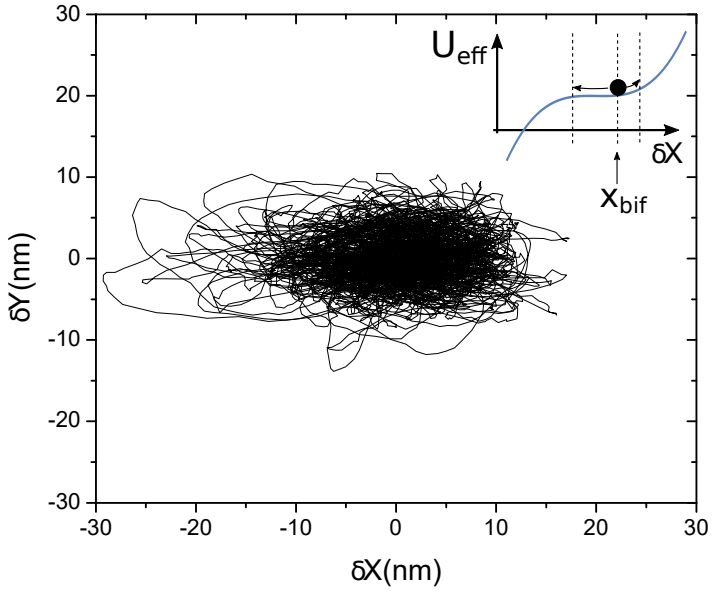

Figure 3.24: fluctuations in the quadratures space for a force $F_0 = 42$ pN $> F_c$, with a driving frequency a few Hz detuned from $\omega_{bif,\uparrow}$. The phase is set at $+45°$ from the reference phase in which we observe the in-phase and quadrature responses. Squeezing is represented by the oval shape. Inset: cubic pseudo-potential representation in the 1D approximation.

perfect circle of standard Brownian motion). It was observed in Ref. [91] in a somewhat different way, by measuring r.m.s. noise values near a bifurcation point at different reference phases. It is indeed expected, as a general consequence in a system whose frequency is modulated at twice its resonance frequency. This is the case here, because of the term $|A_n|^2\delta A_n$ that was neglected in the previous sections: the fluctuations are parametrically amplified, in a similar fashion to the gate modulation scheme detailed in Chapter 2, and used for noise reduction schemes [92]. Note that the squeezing achieved cannot be accurately evaluated, because of the residual Ohmic background, which is not affected by nonlinearities. The background eventually masks the squeezed component for strong squeezing. On the other hand, we observe a slight asymmetry in the amplified direction. This appears to be specific to the bistable regime. Indeed, one can show (see e.g. Ref. [82]) by keeping the second order in the fluctuations in Eq. (3.51) that close to the bifurcation frequency, the 1D problem is equivalent to that of a fictive particle moving in a cubic potential. This is schematically pictured in the inset of Fig. 3.24: the fluctuations are asymmetric because of the potential asymmetry. Such features are similar to what is observed for bistable optical [93] and optomechanical systems [94].

Even though the measurements presented here are only qualitative and preliminary, they comfort us in the idea that the framework used to describe the nonlinear frequency transduction of Brownian motion in the previous sections needs to be adapted when the Brownian motion itself is affected by the driving field: indeed the magnitude of fluctuations as well as their correlation time is deeply changed, which in return affects the nonlinearity-mediated frequency fluctuations of the NEMS.

3.8 Conclusion and prospects

Summary of the results

In this chapter, we have reported the experimental demonstration of non-linear transduction of Brownian motion into frequency noise over an unprecedented parameter range. We showed that this transduction followed a non-trivial evolution, scaling with the ratio between the magnitude of the created frequency noise (Σ) and its decay rate (τ_c^{-1}). This led us to observe two asymptotic regimes that are identified by analogy with NMR: inhomogeneous broadening ($\Sigma\tau_c \gg 1$) where the noise is "static", infinitely correlated with respect to the fluctuating mode's dynamics, and motional narrowing ($\Sigma\tau_c \ll 1$), where fluctuations correlations decay too fast to have a full impact on the probe mode's dynamics. The two limits are analytically encompassed in a path integral model of the susceptibility's expectation value. This model reproduces well the experimental data within 20 % at worst without free parameters.

In addition, we have developed a measurement technique that allows us to obtain phase-resolved position noise spectra. It allowed us to observe the same signatures

on the spectrum, where the usual Lorentzian peak was undergoing a transition from a weak "dressing" (Lorentzian with renormalized parameters) to an asymmetric, inhomogeneous shape due to full averaging over partial susceptibilities. While thermal non-linearities for position fluctuations spectra had been reported in Ref. [14], the description stayed mainly phenomenological, and limited to the inhomogeneous broadening case. We demonstrate here the phenomenon from low to high noise limit, with an excellent theoretical agreement.

To further develop on the transduction phenomenon with a more applied approach, we derived as quantitatively as possible the ultimate limit on frequency resolution imposed by this mechanism. In-built stress is found to dramatically improve the performance of the device. Yet, for low-stress devices, the strong dependence on the devices' aspect ratio can lead to non-negligible limitations, which are crucial as far as their potential for sensing is concerned.

Finally, we have shown the limitations of our model when the NEMS driven motion is in the nonlinear range: here the motion back-acts on its fluctuations, creating an anomalous position and frequency noise. This anomaly is explained qualitatively with squeezing/amplification of position fluctuations and slowing down of timescales, even though the obtained results are still preliminary and cannot be yet described quantitatively.

Prospects

Regarding the frequency noise transduction experiment itself in its current form, a rather quick investigation might be done by keeping a constant force noise while tuning the damping rate of the fluctuating mode with the magnetic field (loading effect, see 2.6.3), i.e. the frequency noise correlation time. This is the other way of tuning the motional narrowing parameter α, and it is in fact the approach adopted by authors in Ref. [81] in the case of telegraph frequency noise.

Another in-depth investigation would be to access the position spectrum while a driving force is applied. It is predicted in Ref. [31] that unusual spectral features would appear: in particular, one expects a pedestal structure to form around the sine drive δ peak and an excess spectrum due to the non-linear interaction between the probe driving and the fluctuating mode. Such features were reported in Ref. [15] for a carbon nanotube resonator, although through a different mechanism involving a gate electrode. In the current state of our experiment, however, it is rather difficult to probe this effect, as the method used for measuring spectra is not well adapted: close to the driving frequency, the drive amplitude will necessarily pollute the spectrum due to bandwidth opening. Therefore, a spectrum analyzer would be more adapted, but it does not avoid the issue of additional spectral contributions described in section 3.5.

Besides, while some further efforts are required to explain quantitatively the anomaly reported in the last section, we see also that a subtle phenomenology is at stake: on

some peculiar points of the mechanical hysteresis, position fluctuations are diverging, both in magnitude and in correlation times. This could be further developed quantitatively in the framework of critical phenomena and phase transitions.

Other schemes could be foreseen: engineering more sophisticated structures with a more sensitive read-out technique, one could couple modes (not necessarily of the same family) with clever schemes that allow one to observe e.g. anomalous phase diffusion [95]. Moreover, if a quantum-limited read-out of a mechanical resonator is made possible, the extension of the presented results to the quantum regime [96] is naturally appealing. An educated guess is that in the limit where all modes are in the quantum ground state, i.e. $\hbar\omega_m \gg k_B T$, the mechanism survives only in the form of a mechanical Lamb shift [97], where a mode eigenfrequency is dressed by the interaction with quantum vacuum fluctuations of all the other modes. It could also be implemented for quantum non-demolition (QND) measurements of another mode Fock states, since the interaction Hamiltonian is bi-quadratic. To witness these effects, however, is far beyond the current reach of state-of-the-art quantum nanomechanics.

3.9 Résumé en français

Dans ce chapitre nous montrons comment le bruit de position d'un mode mécanique, c'est-à-dire son mouvement Brownien, est transduit en bruit en fréquence sur la résonance du mode lui-même ainsi que des modes auxquels il est couplé, par le biais de la non-linéarité géométrique introduite dans le Chapitre précédent. Ce bruit en fréquence est basse fréquence, hautement structuré, non-Gaussien, et sa largeur spectrale est fixée par le temps de relaxation du mode fluctuant en position. Nous montrons que ce bruit induit une dynamique non-triviale du mode sondé subissant le bruit en fréquence : il y a une compétition entre le temps de corrélation (mémoire) fini du bruit en fréquence et la diffusion de la phase du mode sonde (diffusion spectrale). Nous mettons en évidence deux limites importantes. La première concerne des fluctuations grandes, telles qu'un saut en fréquence provoqué par le bruit dans le référentiel tournant est échantillonné sur un temps suffisamment court pour que l'auto-corrélation du signal de saut en fréquence soit encore importante: cela provoque un décalage en fréquence de la raie (car le bruit en fréquence est de moyenne non nulle), et un élargissement inhomogène de la raie de résonance dû à la diffusion spectrale. Dans le cas inverse, lorsque les corrélations du bruit s'effacent sur des temps très courts devant le temps nécessaire au mode sonde pour suivre le saut en fréquence, seule une partie des fluctuations est effectivement intégrée par le mode sonde et la diffusion spectrale est donc limitée : c'est le pénomène de rétrécissement par le mouvement, qu'on retrouve également sous une autre forme en Résonance Magnétique Nucléaire. Les deux limites sont capturées par une approche théorique reposant sur une intégrale de chemin introduite dans [31]: la phase accumulée par le mode sonde est moyennée sur les différentes réalisations de

trajectoires Browniennes, en tenant compte de la relaxation du mode subissant un mouvement Brownien.

L'expérience est réalisée sur plusieurs NEMS de tailles différentes, et nous observons l'effet dans trois configurations essentielles: pour un couplage entre un mode Brownien et un mode sonde forcé différents, dans le cas où le mode sous forçage est couplé à ses propres fluctuations (via l'interaction de Duffing) et dans le cas où les fluctuations de position sont suffisamment grandes pour induire une distorsion du spectre de bruit de position lui-même. Afin de pouvoir observer de façon certaine l'effet du bruit de position tout en palliant la faible sensibilité de la mesure magnétomotive, nous avons soumis le mode sous mouvement Brownien à un bruit en force externe équivalent à une température de mode effective. Par ailleurs, nous avons développé une technique utilisant la détection synchrone pour mesurer la densité spectrale de bruit de position. Les résultats expérimentaux, reportés dans [33], sont en bon accord avec l'approche théorique en intégrale de chemin dans tous les cas de figure, lorsque l'excitation sinusoïdale est suffisamment faible pour rester en régime linéaire. Si cette condition n'est pas remplie, nous observons un écart significatif à la théorie, que nous pensons dû à l'action en retour de l'oscillation forcée sur les fluctuations de position. Ce phénomène est étudié expérimentalement de façon qualitative dans le cadre de la théorie de la bifurcation dynamique, en lien avec les phénomènes critiques : nous observons en particulier un ralentissement de la dynamique du système ainsi qu'une compression asymétrique des fluctuations de position près du point critique d'ouverture d'une hystérésis et près des points de bifurcation.

Nous abordons également un aspect plus appliqué, qui concerne la limite fixée sur la résolution en fréquence due au phénomène étudié: en effet, la non-linéarité géométrique ainsi que les fluctuations thermiques de positions sont des caractéristiques intrinsèques au système. Ainsi, tout système nanomécanique subira les fluctuations de fréquence telles que nous les avons décrites. Nous montrons par des estimations quantitatives que la contrainte interne dans le matériau permet de réduire l'effet, et que des structures à faible contrainte interne comme les nanotubes de carbone sont particulièrement sensible à ces fluctuations, ce qui explique certaines observations d'élargissement spectral, qui invoquaient déjà le mécanisme de façon qualitative [32].

Chapter 4

A model experimental approach to classical decoherence for mechanical systems

Contents

4.1 Introduction

4.1.1 Motivations

As described in Chapter 3, fluctuations of a mode's resonance frequency lead to spectral broadening. We mentioned earlier the limitations caused by such broadening mechanisms on sensing applications. Yet, fundamentally, it is not necessarily a simple task to distinguish damping and spectral diffusion, as they both lead to spectral broadening. Most often in the nanomechanics literature until recently, the difference

between the two has been overlooked, since dephasing effects were assumed to be small enough to attribute spectral broadening only to dissipative processes. Recently, the rise of graphene and carbon nanotubes as mechanical resonators has led to reconsider non-dissipative processes, which also limit spectral resolution to a non negligible extent [98, 77, 15], as shown in Chapter 3. In particular, recent experiments have investigated non-linear damping signatures in graphene and carbon nanotube mechanical resonators [9, 99]. Another study showed a non-linear dephasing signature in such devices, where non-linear damping was ruled out thanks to time-resolved measurements [75]: a significant discrepancy was observed between the spectral Q factor and the one obtained in time domain. Let us mention that such signatures were not observed for atomically thin vibrating MoS_2 membranes [100], which strongly suggests a carbon-based mechanism. Generally speaking, this dephasing is due to dispersive coupling to a noisy signal, which could be e. g. a gate electrode voltage due to fluctuating offset charges.

In the present chapter we detail a comprehensive approach which enables to thoroughly separate dissipative from non-dissipative processes in a nanomechanical measurement. We first present a generic way to calculate analytically the broadening induced by frequency fluctuations in the case where the latter are Gaussian, i.e. the reservoir quantity is linearly coupled to the motion. We present the corresponding measurements in frequency domain, which bear some similarities with the previous Chapter's results. We then extend our measurements to the case of quadratic coupling to the reservoir, which leads to asymmetric noise. In addition, we perform time domain measurements which enable to separate damping from dephasing.

4.1.2 Analogy with Nuclear Magnetic Resonance

The separation between damping and dephasing processes immediately recalls the context of Nuclear Magnetic Resonance (NMR). In NMR, dissipation arises from the resonant energy exchange between an out-of-equilibrium 1/2-spin and the environment to which it is coupled, bringing back the system to equilibrium over a characteristic time T_1 [86]. On the Bloch sphere, it corresponds to the longitudinal relaxation time that characterizes the decay of the projection of the magnetic moment on the z axis.

Meanwhile, decoherence is characterized by the transverse relaxation time T_2, characterizing the decay of the projection of the magnetic moment on the transverse plane (x, y). Thus, it is sensitive to damping processes but also to fluctuations along the z axis, i.e. fluctuations of the energy splitting $\hbar\omega_{01}$ (ω_{01} is the so-called Larmor frequency) between the two spin states that can be induced by the environment. In the frame rotating at the Larmor frequency, these fluctuations will be effective only if their typical timescale is comparable with or lower than the spin dynamics timescale, i.e. T_1. As these fluctuations cannot involve energy exchange between the spin and its environment, they only introduce what we call an **adiabatic dephasing**, since there

is an accumulated phase $\int \omega_{01}(t)\mathrm{d}t$.

Using Bloch equations describing the evolution of the magnetization, one can show that for fully dissipative processes $T_2 = 2T_1$. If adiabatic dephasing is added, the transverse relaxation time will actually be shorter, leading to $T_2 < 2T_1$. One can introduce the pure dephasing rate $\Gamma_\phi = T_2^{-1} - T_1^{-1}/2$ that accounts only for adiabatic processes. Bloch-Redfield theory establishes that the longitudinal relaxation time can be linked to fast fluctuations of an environment variable X coupled to the spin's transverse components. Typically, treating the coupling to the environment as a perturbation, one establishes that $T_1^{-1} \propto S_X(\omega_{01})$. Meanwhile, adiabatic dephasing is determined by the low-frequency spectrum of the environment variable coupled to the longitudinal spin component, and in the zero frequency limit the pure dephasing rate $\Gamma_\phi \propto S_X(0)$.

Obviously the NEMS is a classical oscillator, not a quantum spin. Its dynamics is not described by Bloch-type equations. Yet, conceptually, some analogies are still possible, especially with respect to pure dephasing. Indeed the bare Lorentzian linewidth Γ accounts for dissipation and thus the usual relaxation time $2/\Gamma$ can be identified with a T_1 time. Meanwhile, as pointed out in Chapter 3, if the NEMS undergoes fluctuations of its resonance frequency that are slow enough, it adiabatically follows them. Under sinusoidal excitation, the response accumulates dephasing, and for long enough measurement times, it is averaged over all realizations of the fluctuations assuming ergodicity. This leads to inhomogeneous broadening, hence to a change in the linewidth. This change is not caused by additional dissipative processes and thus, one can define by analogy a measurable (classical) decoherence time $T_2 = 2/\Delta\omega$, where $\Delta\omega$ is this inhomogeneous linewidth. As quadratures include the phase dependence, averaging over fluctuations independently on both would lead to quadratures decaying with a time constant T_2 in free decay experiments. Building on these analogies, one can introduce a pure dephasing rate $\Gamma_\phi = T_1^{-1} - T_2^{-1}$. Note that here there is no factor 2 as opposed to NMR. This factor appears because of the peculiar structure of the spin space, which does not come into play here.

Generally speaking, noise sources leading to frequency fluctuations, e.g. $1/f$ noise, do not have a sharp, DC contribution, or a smoothly varying contribution spread over Γ_ϕ, resulting in non-exponential decay. Therefore, the T_2 time has an arbitrary definition, which depends on the noise characteristics. This will be addressed below. Meanwhile, measuring T_1 is possible through decay measurements (not to be confused with free induction decay in NMR leading to T_2 measurements): ideally, the NEMS is resonantly excited at $t < 0$, and relaxes to its rest position as the excitation is turned off at $t = 0$. Obviously, the NEMS will return to equilibrium by oscillating at its natural frequency ω_0 but with a noisy accumulated phase term $\Delta\phi = \int \delta\Omega(t)\mathrm{d}t$, where $\delta\Omega(t) = \omega(t) - \omega_0$. However, measuring and averaging over many realizations the decay of the squared amplitude R^2 eliminates the phase dependence, leading to a true T_1 measurement.

4.1.3 The gate electrode as a source of frequency fluctuations

To separate damping and dephasing contributions, we need to implement a measurement scheme that allows us to observe the resonator's decay, i.e. its return to equilibrium after a perturbation, in real time. Since the response is a small signal competing with instrumental noise, in time domain, one needs to average over many decays to obtain reasonable error bars on the exponential decay time constant. However, our best (i.e. longest) resonators display at best linewidths above 1 Hz, which translates as decay times $T_2 \leq 300$ ms at best. In addition we need a magnetic field high enough to address their motion with a good signal to noise ratio, but we know that long devices are more affected by external loading losses (see Chapter 2 section 2.6.3). The best compromise is thus to use long devices with small magnetic fields: with the device used in this experiment for time-resolved measurements (see Chapter 3, Table 3.1, sample 300 µm n°2), which has an intrinsic linewidth of 3.6 Hz, clean signals are obtained with a field $B = 100$ mT, which yields a loaded linewidth $\Gamma = 2\pi \times 5.6$ Hz (i.e. a decoherence time $T_2 = 57$ ms). Therefore, the mode remains mostly mechanical with respect to damping/dephasing mechanisms. This is crucial if one wants to unveil dephasing mechanisms of mechanical origin, for instance in the non-linear regime.

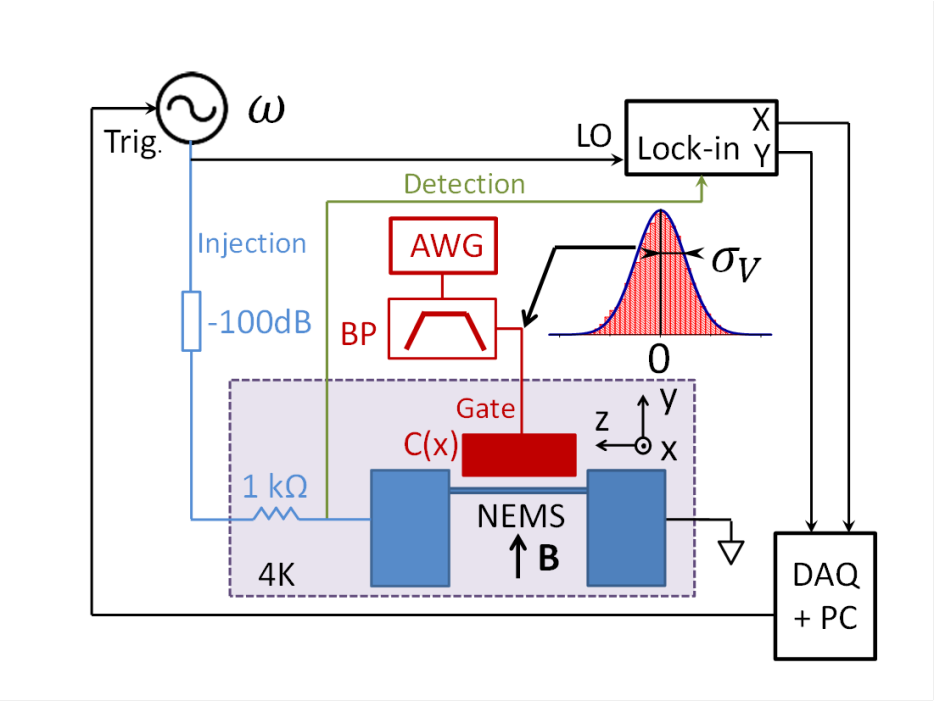

Figure 4.1: schematics of the experimental setup. The DAQ card enables fast communication between the computer software and the generator, which permits to perform well resolved time domain measurements.

A sketch of the experimental setup is shown in Fig. 4.1. In addition to the usual

actuation and detection setup, the same voltage noise source that is used in Chapter 3 is connected to the gate electrode. The sample used in this experiment has a gate electrode separated from the beam by a gap $g = 3$ µm. The gate coupling characterization is the one shown as example in Chapter 2, Fig. 2.24, with a gate-NEMS coupling strength $\partial^2 C_g/\partial x^2 = -4.3 \times 10^{-5}$ F/m^2. As fast fluctuations would be filtered out by the mechanical mode, the typical correlation time of the frequency noise must be comparable with or larger than T_1, while the noise spectrum must be low frequency. To be in this situation, we insert a bandpass filter in the line with -3 dB cut-off frequencies at 40 mHz (low) and 0.8 Hz (high). The choice to introduce a low cut-off frequency is justified by the need to rule out parasitic sources such as $1/f$ noise, which is ubiquitous in any kind of electrical component.

Since the filtering reduces by many orders of magnitude the effective noise level on the gate, we put a pre-amplifier after the filter so as to maintain it at a level where dephasing effects are observable, with a power gain $G = 2.5 \times 10^7$. The filter's spectral characteristics are summarized in Fig. 4.2. A polynomial fraction $\mathcal{F}(\omega)$ interpolates the measured points to capture the spectral characteristic. It enables a quantitative shaping of the gate controlled frequency noise. At the gate level, the standard deviation of the voltage noise σ_g can be linked to that of the voltage noise delivered by the AWG σ_A:

$$\sigma_g^2 = \frac{\mathrm{BW_F}}{\mathrm{BW_A}} G \sigma_A^2, \tag{4.1}$$

where $\mathrm{BW_F} = 1.2$ Hz, $\mathrm{BW_A} = 10$ MHz are the integrated bandwidths of the filter and the noise source, respectively. The agreement between calculated values of σ_g and measured values is rather good, with at most 10 % discrepancy between the two.

Moreover, since $\mathcal{F}(\omega)$ is measured, we can quantitatively infer the voltage noise spectrum $S_V(\omega)$ at the level of the gate electrode:

$$S_V(\omega) = \frac{\pi G \sigma_A^2}{\mathrm{BW_A}} \mathcal{F}(\omega). \tag{4.2}$$

Therefore, the voltage noise spectrum is only the image of the filter's spectral response. This is useful to quantitatively obtain the frequency noise spectrum (see below).

The noise on the resonance frequency is directly obtained from the gate-NEMS capacitive coupling, through Eq. (2.61):

$$\delta\Omega(t) = -\frac{1}{4m\omega_0} \frac{\partial^2 C_g(0)}{\partial x^2} V_g^2 = \alpha V_g^2. \tag{4.3}$$

Here the gate voltage V_g is not explicit: it can either be pure noise, i.e. $V_g \equiv \delta V_g$ or a noise added to a voltage bias V_0, i.e. $V_g = V_0 + \delta V_g$. This results in either quadratic

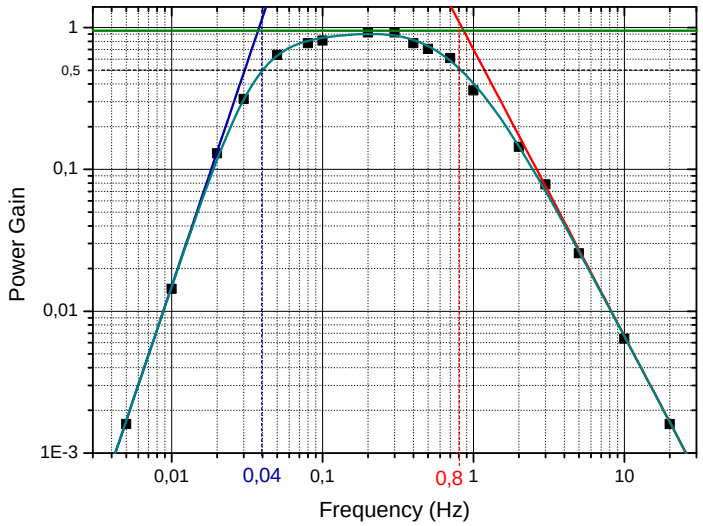

Figure 4.2: power gain characteristic of the low-frequency filter used in this experiment. -3 dB cutoff frequencies are displayed (blue and red dotted lines) with asymptots, while the dark green solid line is an interpolation function used for calculations.

or linear coupling to a Gaussian noise source, yielding qualitatively and quantitatively different results.

4.2 Linear coupling to a Gaussian noise source

4.2.1 Generic formalism

Let us assume that a noise source $\delta\Omega(t)$ featuring a Gaussian distribution and having a correlation time τ_c (which can be finite) is coupled linearly to the NEMS displacement $x(t)$, creating a stochastic restoring force:

$$F_g(t) = -2m\omega_0\delta\Omega(t)x(t). \tag{4.4}$$

$\delta\Omega(t)$ can originate e.g. from gate voltage fluctuations coupled to our NEMS. From this generic coupling term one can write the accumulated phase $\Delta\phi(t)$ for one noise trajectory between a reference time $t = 0$ and a time t, in the same fashion as in the previous chapter:

$$\Delta\phi(t) = \int_0^t \delta\Omega(t')\mathrm{d}t'. \tag{4.5}$$

Obviously this dephasing is a stochastic quantity. The experimental approach is to measure an average one. We can use the same procedure as in Chapter 3: solving the standard equation of motion in the rotating frame leads to a mechanical susceptibility which is, in time domain, the product of the usual, certain susceptibility $\chi_0(t)$ by an accumulated phase term. The latter is averaged over the ensemble of realizations between 0 and t:

$$\chi_a(0,t) = \chi_0(0,t)\left\langle e^{i\Delta\phi(t)}\right\rangle . \tag{4.6}$$

Instead of using the path integral approach described before, we have used another equivalent technique, which is more convenient in this context. We write the exponential term in Taylor series:

$$\left\langle e^{i\Delta\phi(t)}\right\rangle = \sum_{k=0}^{+\infty} \frac{i^k}{k!}\left\langle \Delta\phi^k(t)\right\rangle . \tag{4.7}$$

Each k term of the sum, i.e. k^{th} moment of the dephasing, can be explicited:

$$\left\langle \Delta\phi^k(t)\right\rangle = \left\langle \left(\int_0^t \delta\Omega(t')\mathrm{d}t'\right)^k \right\rangle = \int_0^t \mathrm{d}t_k ... \int_0^t \mathrm{d}t_1 \langle \delta\Omega(t_1)...\delta\Omega(t_k)\rangle. \tag{4.8}$$

To calculate the term between brackets we can use the Wick formula for k Gaussian, centered variables:

$$\langle \delta\Omega(t_1)...\delta\Omega(t_k)\rangle = \sum_{\mathcal{C}_k}\prod_{i\neq j}\langle \delta\Omega(t_i)\delta\Omega(t_j)\rangle, \tag{4.9}$$

where the sum is taken over the ensemble $\mathcal{C}_k$ of possible simultaneous pairing configurations for an ensemble of k stochastic processes with the same Gaussian distribution. Here we have reduced the calculation to an integration over products of two-point correlation functions. This is quite convenient: assuming causality as well as an exponential decay for correlations, a generic two-point correlation function has the form:

$$\langle \delta\Omega(t_i)\delta\Omega(t_j)\rangle = \sigma^2 \exp\left(-\frac{|t_i - t_j|}{\tau_c}\right). \tag{4.10}$$

Since pairings are simultaneous in a configuration, one cannot use twice the function $\delta\Omega$ at the same time t_j in a given configuration. In other words, there is a one-to-one correspondence between a two-point correlator and the integrals over the times considered in the correlator. In addition, to get rid of the absolute value which is a

consequence of causality we can use the time-ordering property of a double integral:

$$\int_0^t \mathrm{d}t_i \int_0^t \mathrm{d}t_j \langle \delta\Omega(t_i)\delta\Omega(t_j)\rangle = 2\sigma^2 \int_0^t \mathrm{d}t_i \int_0^{t_i} \mathrm{d}t_j \exp\left(-\frac{t_i - t_j}{\tau_c}\right). \tag{4.11}$$

Then, the calculation is straightforward, and the contribution of each integrated two-point correlator to the k^{th} moment writes, independently of any intermediate time:

$$\int_0^t \mathrm{d}t_i \int_0^t \mathrm{d}t_j \langle \delta\Omega(t_i)\delta\Omega(t_j)\rangle = 2\sigma^2\tau_c \left[t + \tau_c\left(e^{-t/\tau_c} - 1\right)\right]. \tag{4.12}$$

From Wick formula we know that only configurations with an even number of variables, i.e. even moments of $\Delta\phi$, will be non-zero. That said, since all k variables are paired, the number of pairs in a given configuration of $\mathcal{C}_k$ must be $k/2$. The only unknown left is the number N_k of pairing configurations in $\mathcal{C}_k$. To discard double occurrences, one should consider how many times one configuration can occur as pairings are identical but picked up in a different order. This number is equal to the number of couples permutations in an ensemble of $k/2$ couples, which is simply $(k/2)!$. Thus, the number of possible combinations contributing to an even k-th moment is:

$$N_k = \binom{k}{2}\binom{k-2}{2}\ldots\binom{2}{2}/(k/2)! = \frac{k!}{2^{k/2}\left(\frac{k}{2}\right)!}. \tag{4.13}$$

Since all contributions have the same value calculated in Eq. (4.12), an even k-th moment of the dephasing writes:

$$\left\langle \Delta\phi^k(t)\right\rangle = N_k\left(2\sigma^2\tau_c\right)^{k/2}\left[t + \tau_c\left(e^{-t/\tau_c} - 1\right)\right]^{k/2}, \tag{4.14}$$

while odd k-th moments are zero. Doing the replacement $k \to 2k$ in the sum, the averaged term can thus be evaluated:

$$\left\langle e^{i\Delta\phi(t)}\right\rangle = \sum_{k=0}^{+\infty} \frac{(-1)^k}{(2k)!}\frac{(2k)!}{k!2^k}\left(2\sigma^2\tau_c\right)^k\left[t + \tau_c\left(e^{-t/\tau_c} - 1\right)\right]^k. \tag{4.15}$$

Finally, the averaged susceptibility in time domain is:

$$\chi_a(0,t) = \chi_0(0,t)\exp\left[-\left(\sigma\tau_c\right)^2\left(\frac{|t|}{\tau_c} + e^{-|t|/\tau_c} - 1\right)\right], \tag{4.16}$$

where we have included the case $t < 0$ through the use of the absolute value. The asymptotic regimes underlined in Chapter 3 can be again highlighted here: if a typical frequency jump of magnitude σ occurs such that $\sigma\tau_c \gg 1$, the sampling time σ^{-1} will

be small compared to τ_c, and then only short times t compared to τ_c will matter in the additional decay to the susceptibility. If we expand the inner exponential term in Eq. (4.16) at second order, we are left with a Gaussian decay, which yields equivalently, when translated to the frequency domain, to a Gaussian probability density for frequency fluctuations:

$$\chi_a^{\mathrm{IB}}(0,t) = \chi_0(0,t)\exp\left[-\frac{\sigma^2 t^2}{2}\right]. \tag{4.17}$$

Note that the correlation time, approximated as infinite, has disappeared from the problem. This is the so-called "inhomogeneous broadening limit", where the frequency fluctuations imprint directly the shape of the resonance (see Chapter 3). Inversely, if a typical frequency jump of magnitude σ occurs such that $\sigma\tau_c \ll 1$, the inner exponential term will be very small on short timescales, while the linear part of the exponent will be large. Thus, we can approximate the average susceptibility with:

$$\chi_a^{\mathrm{MN}}(0,t) = \chi_0(0,t)\exp\left[-\sigma^2\tau_c t\right]. \tag{4.18}$$

In other words, the imaginary response is Lorentzian, with a linewidth that is renormalized by a factor $(1+\sigma^2\tau_c)$. This corresponds to the "motional narrowing limit", as discussed in Chapter 3 in another context.

4.2.2 Results

To address the linear coupling situation, an additioner of gain 1 is inserted after the preamplifier, such that the DC voltage and the voltage noise level can be tuned independently. Including the DC term in a statically shifted resonance frequency, the frequency noise in Eq. (4.3) rewrites:

$$\delta\Omega = \alpha\delta V_g^2 + 2\alpha V_0\delta V_g. \tag{4.19}$$

By choosing a large enough DC bias one can favour the linear coupling to the Gaussian noise source while keeping a low enough quadratic term. Thus in this section we assume $\delta\Omega(t) \approx 2\alpha V_0\delta V_g(t)$, meaning that the frequency noise is essentially Gaussian, with a zero average value (hence no resonance shift due to the fluctuations) and a standard deviation $\sigma = 2\alpha V_0\sigma_g$. For the 300 µm NEMS used in the experiment reported in this section, we measure a coupling constant $\alpha = 2\pi \times 13.8$ Hz/V^2. Note that the DC voltage that is computed is the **effective** one, i.e. the one that takes into account the offset on the gate. The latter is measured during the coupling strength characterization, as shown in Chapter 2, section 2.8.3. The typical offset voltage in

this experiment was about 300 mV, which is rather large (more typical values are about 100 mV). The σ_g values are given in r.m.s. units, that is, $\sigma_g = \left\langle \delta V_g^2 \right\rangle^{1/2}$.

The spectral lines observed should be, in this configuration, the Fourier transform of Eq. (4.16). In other words, the average susceptibility in frequency domain is the convolution of the bare susceptibility by the Fourier transform of the exponential term, called $p(\delta\Omega)$:

$$\langle \chi(\omega) \rangle = \int_{-\infty}^{+\infty} \chi(\omega - \delta\Omega) p(\delta\Omega) \mathrm{d}\delta\Omega. \tag{4.20}$$

The p term is, in the inhomogeneous broadening (IB) regime, the probability distribution that weights the partial responses $X(\omega - \delta\Omega)$, and is Gaussian, centered:

$$p_{\mathrm{IB}}(\delta\Omega) = \frac{1}{\sigma\sqrt{2\pi}} \exp\left(-\frac{\delta\Omega^2}{2\sigma^2}\right). \tag{4.21}$$

In the low noise limit, the resolution is not good enough to clearly make the difference between the IB regime and the full theory. Indeed the NEMS used in the linear coupling case is slightly below average in terms of Q factor: its has a 8.25 Hz loaded linewidth at 100 mT, while the filter's integrated bandwidth is 1.2 Hz, leading to an estimated correlation time 0.15 s for the frequency noise. Note that the filter does not exactly shape the noise as an exponentially correlated quantity (for instance because of the low-frequency filtering), which limits in any case our experiment for a perfect match with theory. In Fig. 4.3, we see that for typical noises used in this study the difference between the IB regime and the full expression for the average accumulated phase term quickly vanishes. The theoretical broadening is also plotted in Fig. 4.6 for an averaging in the IB approximation (black) or with the full theory (orange). The discrepancy between the two falls well within our error bars, which are set at 10 % of the initial linewidth, i.e. around 0.8 Hz.

In the inhomogeneous broadening regime, the averaged quadrature X is a Voigt profile, i.e. the convolution of a Lorentzian by a Gaussian. Therefore, the averaged response will depend on the interplay between the noise magnitude σ and the damping rate Γ, as they characterize the Lorentzian and noise distribution width, respectively. If one is large compared to the other, the narrow peak can be approximated as a δ peak with small corrections, and the response is either Lorentzian for weak noise ($\sigma \ll \Gamma$), with weakly renormalized parameters, or Gaussian ($\sigma \gg \Gamma$), i.e. dominated by noise properties.

In the case of weak noise, a typical jump in frequency due to the gate voltage noise does not exceed a fraction of the linewidth and therefore, the distribution p_{IB} is very narrow around the drive frequency, close to a δ peak in the vicinity of the Lorentzian. As a result the average response $\langle X \rangle$ at a frequency ω close to the resonance remains Lorentzian at first order and can be expanded within the integral (4.20) in powers of

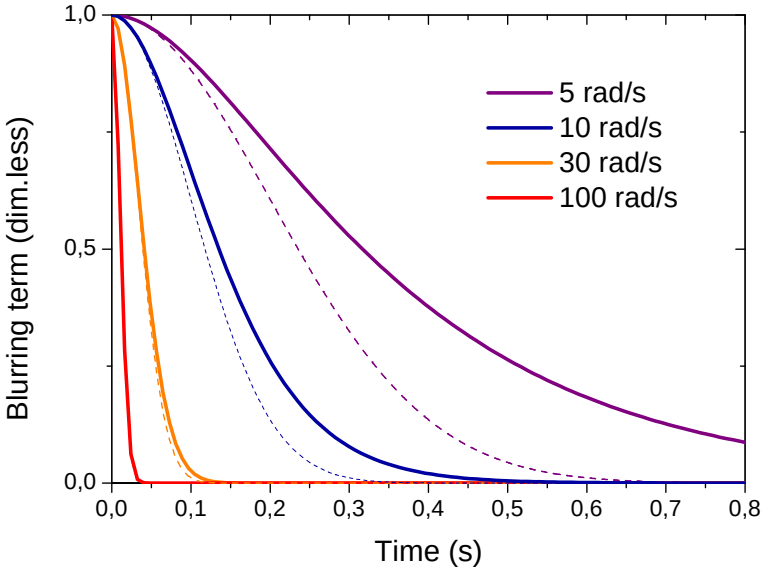

Figure 4.3: averaged dephasing term ("blurring") in (4.20) for different noise magnitudes with a noise correlation time $\tau_c = 0.15$ s. Dashed lines are the corresponding Gaussian approximations, i.e. the average dephasing term in Eq. (4.28).

$\delta\Omega$, which makes a calculation of noise-renormalized parameters (resonance frequency, linewidth) possible. Note that the method is fairly generic and can be used for any type of distribution that is **peaked enough at zero for low noise magnitudes**. If we expand Eq. (4.20) at second order:

$$\langle X(\omega)\rangle \approx X(\omega) - \mathcal{M}_1 \frac{\mathrm{d}X}{\mathrm{d}\omega} + \frac{\mathcal{M}_2}{2}\frac{\mathrm{d}^2X}{\mathrm{d}\omega^2}, \tag{4.22}$$

where we have introduced the n^{th} order moments of the noise distribution p_{IB}: $\mathcal{M}_n = \langle \delta\Omega^n \rangle = \int \delta\Omega^n p_{\text{IB}}(\delta\Omega)\mathrm{d}\delta\Omega$. To obtain the noise-dressed resonance frequency $\omega_{res} = \omega_0 + \varepsilon$ one has to solve:

$$\left.\frac{\mathrm{d}\langle X(\omega)\rangle}{\mathrm{d}\omega}\right|_{\omega=\omega_{res}} = 0. \tag{4.23}$$

Finding ω_{res} is easy by combining Eq. (4.22) and Eq. (4.23). Assuming the noise-induced shift ε is small (since the noise is weak), Eq. (4.22) can then be expanded at first order in ε around ω_0. As X is Lorentzian, its value and that of its derivatives at ω_0 are well known. At first order, we finally obtain:

$$\omega_{res} = \omega_0 + \mathcal{M}_1. \tag{4.24}$$

This result is rather simple and not surprising: in the weak noise limit, the frequency is shifted by the mean value of the distribution. If the latter is Gaussian, centered, as in this section, $\mathcal{M}_1 = 0$ and the response does not experience any frequency shift.

One can also evaluate the noise-induced broadening (decoherence) in the weak noise limit where this broadening is small. The starting point is the mere definition of a FWHM:

$$\frac{1}{2}\langle X\left(\omega_{res}\right)\rangle = \left\langle X\left(\omega_{res} + \frac{\Gamma}{2} + \Delta\omega_r\right)\right\rangle = \left\langle X\left(\omega_{res} - \frac{\Gamma}{2} - \Delta\omega_l\right)\right\rangle, \tag{4.25}$$

where we have introduced the left (right) hand side broadening $\Delta\omega_l$ ($\Delta\omega_r$), in case the total broadening is asymmetric. Using Eq. (4.22), combined with expansions at first order in $\Delta\omega_l$, $\Delta\omega_r$, ε around $\omega_0 \pm \Gamma/2$ and the fact that X is Lorentzian with known first and second derivatives at $\omega_0, \omega_0 \pm \Gamma/2$, one obtains in the end that $\Delta\omega_r = \Delta\omega_l$, and the inhomogeneous linewidth $\Delta\omega = \Gamma + \Delta\omega_l + \Delta\omega_r$ in the weak noise limit is then:

$$\Delta\omega = \Gamma + \frac{6\left(\mathcal{M}_2 - \mathcal{M}_1^2\right)}{\Gamma}. \tag{4.26}$$

For the centered Gaussian noise case that we address in this section, $\mathcal{M}_2 = \sigma^2$ and thus:

$$\Delta\omega = \Gamma + \frac{6\sigma^2}{\Gamma}. \tag{4.27}$$

An example of weakly perturbed response is shown in Fig. 4.4 where a Lorentzian and a Gaussian fit are compared. The Gaussian fit is much less convincing, as it does not reproduce well the experimental shape. In the weak noise limit, the relevant linewidth is therefore the Lorentzian one.

Meanwhile, the strong noise limit $\sigma \gg \Gamma$ cannot provide generic expressions for the resonance lines, as they will be dominated by the fluctuations distribution and thus will have properties specific to p_{IB}: as the distribution's width is controlled by σ, the Lorentzian line is thus close to a δ peak in the convolution (4.21). For the case studied here, the line will essentially be Gaussian centered around the natural frequency:

$$\langle X(\omega)\rangle \approx \frac{F_0}{m\omega_0}\sqrt{\frac{\pi}{8\sigma^2}}e^{-\frac{(\omega-\omega_0)^2}{2\sigma^2}}. \tag{4.28}$$

Thus, the resonance frequency still does not shift, and the linewidth is governed by the noise statistical properties. This is highlighted by the absence of the mechanical

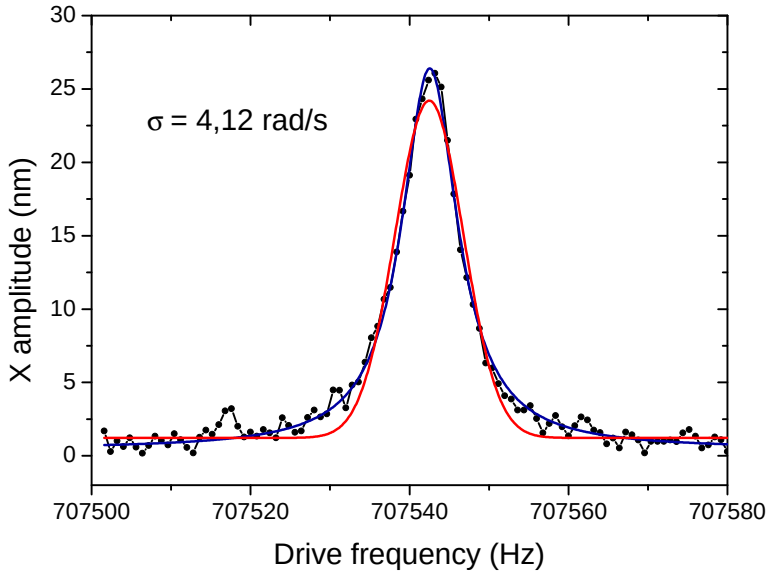

Figure 4.4: resonance line (X quadrature) measured for an applied DC gate voltage $V_0 = 1.37$ V and a voltage noise $\sigma_g = 17.3$ mV_{rms}, hence a frequency noise magnitude $\sigma = 4.12$ rad/s. The red curve is a Gaussian fit, while the blue curve is a Lorentzian one.

damping rate in the expression. Instead, the resulting profile has a Gaussian linewidth:

$$\Delta\omega \approx \sigma\sqrt{8\ln 2}. \tag{4.29}$$

A typical example is shown in Fig. 4.5, again with Gaussian and Lorentzian fits. The latter is less convincing in capturing the experimental curve, although this appears less obviously than for the weak coupling case, due to higher instrumental noise. Therefore, the Gaussian width is favored, even though the discrepancy with the Lorentzian one is not tremendous.

The picture in this situation is analogous to Doppler broadening in an atomic ensemble, where atomic spectral emission or absorption lines often have a linewidth much bigger than that given by the excited state lifetime: as the gas atoms move randomly due to thermal agitation with a Gaussian distribution on velocities v of typical spreading $v_{th} \sim \sqrt{k_B T/m}$, they see in their frame a radiation frequency corrected by a factor $1 - v/c$ (c is the speed of light), which increases the frequency range allowed for radiation emission/absorption. If thermal agitation is important, the "thermal width" is much bigger than the intrinsic lifetime and thus the spectral line becomes Gaussian with the so-called Doppler width [101].

The experimental results in the linear coupling case are summarized in Fig. 4.6.

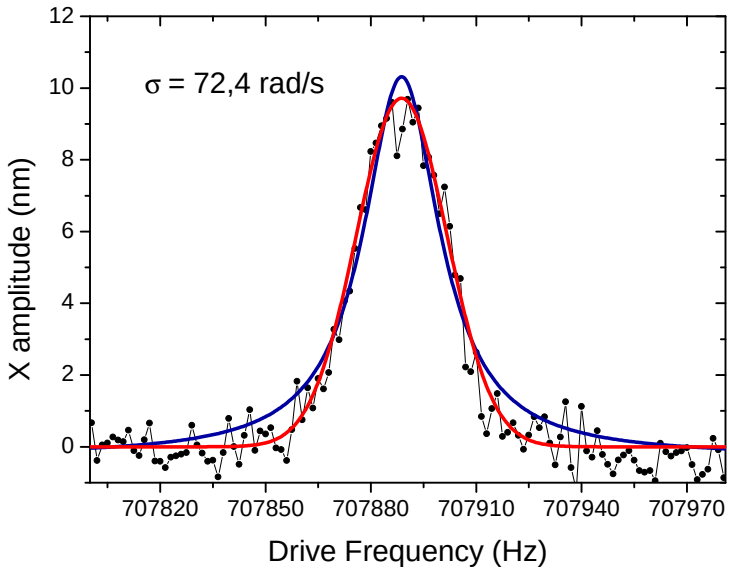

Figure 4.5: resonance line (X quadrature) measured for an applied DC gate voltage $V_0 = 5.29$ V and a voltage noise $\sigma_g = 78\,\mathrm{mV}_{rms}$, hence a frequency noise magnitude $\sigma = 72.4$ rad/s. The red curve is a Gaussian fit, while the blue curve is a Lorentzian one.

Clearly, the Gaussian width approximation is out of range in the weak renormalization limit. In the limit where responses are dominated by noise properties, this time the Lorentzian with falls slightly below the theoretical prediction. In each range, the appropriate data are rather well reproduced by theory, within an error bar set by the natural linewidth (10 % of Γ). Again, the full theory and the inhomogeneous broadening approximation are, within this error bar, not distinguishable. The bar set at $\Gamma/2$ underlines the transition from Lorentzian-dominated response to noise-dominated properties.

4.3 Quadratic coupling

4.3.1 Framework

In this section, we do not apply a DC voltage on the gate electrode and make sure the offset voltage remains small enough compared to typical noise voltages applied. Therefore, the frequency noise (4.3) rewrites simply: $\delta\Omega \approx \alpha\delta V_g^2$. However, using the same approach as in the linear case is more difficult, as we have to consider two types of pairings in the correlation function decomposition instead of one, which makes the counting more involved. Yet, we have shown above that for typical noise values used here, the inhomogeneous broadening approximation holds reasonably well. With the

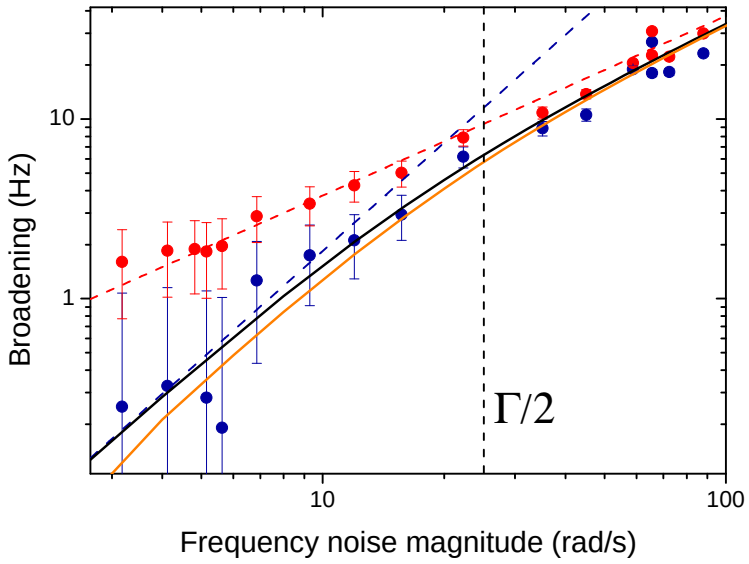

Figure 4.6: broadening of the resonance line as a function of gate-controlled frequency noise. Blue dots are obtained from the FWHM of a Lorentzian fit of the resonance line, red dots come from the FWHM of a Gaussian fit. The error bars represent 10 % of the bare resonance linewidth. Dashed lines are the two asymptotic behaviours of the linewidth broadening, i.e. applications of Eq. (4.27) (blue) and Eq. (4.29) (red). The solid black line is the broadening extracted from the IB approximation, while the orange line comes from the full theory. The dashed vertical line is a guide marking the transition from weak renormalization to noise-dominated response.

bandpass filter described above (see Fig. 4.2), we make sure that the injected noise is a low-frequency one. As the voltage noise delivered by the AWG is white, Gaussian, centered, the frequency fluctuation spectrum can be written from the filtered gate voltage noise δV_g using Wick's formula:

$$\langle \delta\Omega(t)\delta\Omega(t+\tau)\rangle = \alpha^2\sigma_g^4 + 2\alpha^2\langle \delta V_g(t)\delta V_g(t+\tau)\rangle^2. \tag{4.30}$$

Therefore, in the frequency domain, the frequency noise spectrum can be obtained in a similar fashion to Eq. (3.11), with a true DC term and a convolution part:

$$S_\Omega(\omega) = \alpha^2\sigma_g^4\delta(\omega) + \frac{\alpha^2}{\pi}\int_{-\infty}^{+\infty} S_V(\omega')S_V(\omega-\omega')\mathrm{d}\omega'. \tag{4.31}$$

The situation is slightly different from that of Chapter 3. The initial noise is already low frequency, which means that the convolution will entirely result in a low frequency

spectrum for frequency noise. We have established an expression for the voltage noise spectrum and its integrated value through Eqs. (4.1) and (4.2). Therefore, the frequency fluctuations spectrum can be written in terms of experimentally measurable quantities:

$$S_\Omega(\omega) = \alpha^2 G^2 \left(\frac{\mathrm{BW_F}}{\mathrm{BW_A}}\right)^2 \sigma_A^4 \delta(\omega) + \pi \left(\frac{\alpha G \sigma_A^2}{\mathrm{BW_A}}\right)^2 \underbrace{\int_{-\infty}^{+\infty} \mathcal{F}(\omega')\mathcal{F}(\omega-\omega')\mathrm{d}\omega'}_{S_C(\omega)}. \quad (4.32)$$

A numerical computation of $S_C(\omega)$ is shown in Fig. 4.7. The fluctuations remain

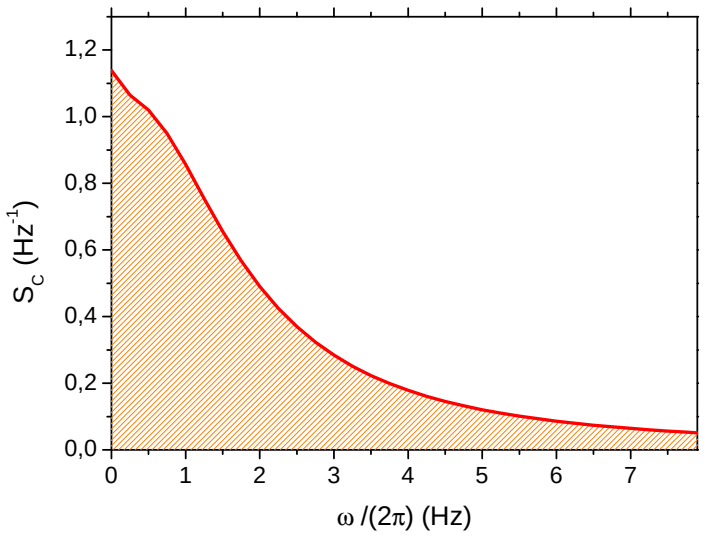

Figure 4.7: convolution part of the frequency fluctuations power spectral density $S_c(\omega)$, recalculated from the low-frequency filter gain characteristic, with colored area.

essentially slow insofar as it is weighted much more in the frequency region $\leq \Gamma$. Note that there is also a DC contribution (in fact the first moment) leading to a frequency shift, which is overlooked here, as we are focusing on the distinction between damping and decoherence. One can obtain the probability distribution on $\delta\Omega$ from the Gaussian distribution on δV_g:

$$p(\delta\Omega) = \Theta(\delta\Omega) \left(\frac{1}{\sqrt{2}\pi\sigma\delta\Omega}\right)^{1/2} \exp\left(-\frac{\delta\Omega}{\sqrt{2}\sigma}\right), \quad (4.33)$$

with $\sigma = \sqrt{2}\alpha\sigma_g^2$. The choice to leave a $\sqrt{2}$ outside this definition is a matter of convention, such that σ is without numerical factors the frequency noise standard deviation. Again, due to the quadratic nature of the coupling, frequency fluctuations

take only positive values, which appears through the Heaviside function $\Theta(\delta\Omega)$. The n^{th} moment of this distribution, $\mathcal{M}_n = \langle \delta\Omega^n \rangle$, writes:

$$\mathcal{M}_n = \int_{-\infty}^{+\infty} \delta\Omega^n p(\delta\Omega) \mathrm{d}\delta\Omega = \frac{(2n)!}{n!} \left(\frac{\sigma}{2\sqrt{2}} \right)^n . \tag{4.34}$$

Therefore, the standard deviation is indeed $\sqrt{M_2 - M_1^2} = \sigma$, with $\mathcal{M}_1 = \sigma/\sqrt{2}$ being in fact the DC shift. Note that physically, σ is also linked to the integrated frequency fluctuations spectrum:

$$\mathcal{M}_2 = \frac{1}{2\pi} \int_{-\infty}^{+\infty} S_\Omega(\omega) \mathrm{d}\omega = \frac{3\sigma^2}{2}. \tag{4.35}$$

4.3.2 Protocol for time-domain measurements

The procedure to perform time-resolved measurements is similar to that of Ref. [69], where it was implemented for MEMS with much larger time constants. Here the only modification is instrumental, through the use of a DAQ card with a 300 kHz sampling rate that permits to address smaller timescales. The protocol is schematized in Fig. 4.8: for $t \leq 0$ the driving force is swept adiabatically (i.e. around 1 Hz/s for this experiment) up to the resonance frequency, where it stays for 1 s. In parallel, a "trigger" signal is set with an amplitude higher than a given threshold. After 1 s, at $t = 0$, the "trigger" signal drops below the threshold value: at this precise moment the driving force is suddenly detuned far from resonance, with a detuning frequency Δ of typically a few linewidths. Therefore, the NEMS relaxes from its steady-state amplitude towards its rest position while oscillating at its natural frequency ω_{res}. As the lock-in amplifier reference signal is synchronized in frequency with the excitation, it records the beating between the mechanical oscillation and the local oscillator on both quadratures. The two quadratures in time domain in the local oscillator's reference frame thus write:

$$\begin{cases} X(t) &= e^{-t/T_1} \left[X_0(\omega_{res}) \cos(\Delta t) - Y_0(\omega_{res}) \sin(\Delta t) \right], \\ Y(t) &= e^{-t/T_1} \left[X_0(\omega_{res}) \sin(\Delta t) + Y_0(\omega_{res}) \cos(\Delta t) \right]. \end{cases} \tag{4.36}$$

Therefore, the exponentially decaying envelope $R(t)$ and thus T_1 can be obtained through $R^2 = X^2 + Y^2$, if the averaging is done on R^2 rather than on X and Y separately. Otherwise, in presence of noise, such that the beating frequency is now $\Delta + \delta\Omega$ the time constant observed through independent averaging of the quadratures is smaller, due to averaging on noisy sinusoidal terms. We formally call this average $\langle R \rangle^2 \equiv \langle X \rangle^2 + \langle Y \rangle^2$ Note that this can be turned into another technique to measure the T_2 time, which we will call $\overline{T}_2$ to make the distinction with the frequency-resolved technique.

Observing the beating is the reason why the frequency detuning procedure is chosen, rather than staying locked at resonance and just switching off the excitation. Note

that in order to acquire a well-sampled time-resolved signal, the lock-in time constant must be much smaller than the decay time. We set a measurement time constant $\tau_m = 100$ µs. Thus, the detuning must be small enough so as to remain within the lock-in bandwidth, while being greater than the linewidth so that the NEMS truly relaxes to its rest position.

This technique can be extended without difficulty to the non-linear regime. However, in the bistable regime, we took care not to park too close to the bifurcation frequency, to avoid parasitic jumps from the high to the low amplitude state, or jumps due to the shift of the hysteresis under the influence of intrinsic frequency noise (see Chapter 6). An acquisition card NI-DAQ operating up to 300 kHz per channel was used to record data points and synthesize a trigger signal with a jitter in the trigger time smaller than 2 ms, which is reasonable as far as our NEMS is concerned. Since opening the lock-in bandwidth comes with more instrumental noise, the procedure is repeated, and the signal is averaged over typically 1000 realizations.

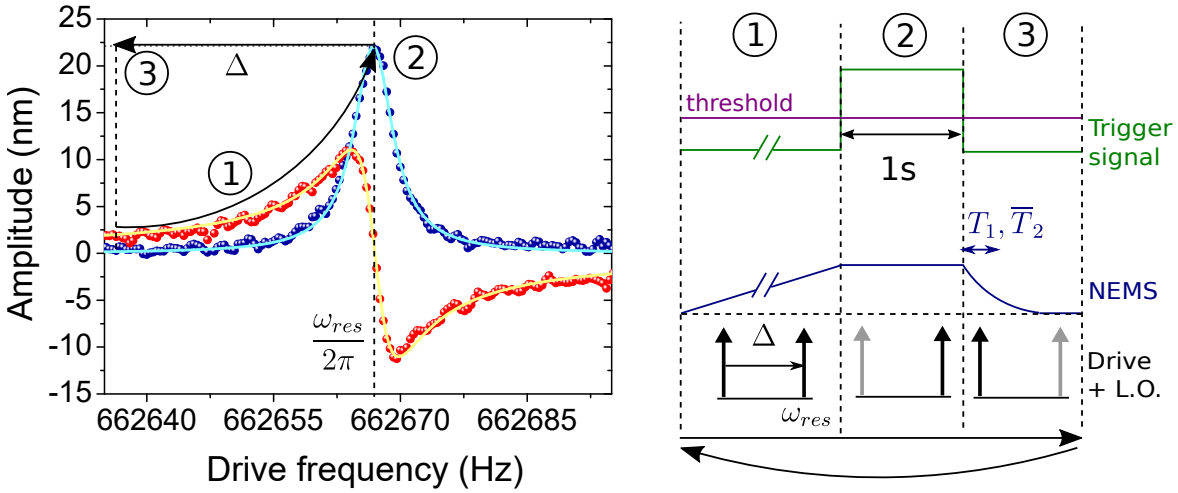

Figure 4.8: protocol for time-domain measurements, with a frequency response in the left panel as a guide, and the time sequence represented in the right panel. 1: the excitation tone is swept at a low speed up to the resonance frequency ω_{res}. 2: when the resonance frequency is reached, a "trigger" signal is set at a high amplitude. It is maintained during 1 second. 3: after 1 second, at $t = 0$, the trigger signal goes below a threshold value, which triggers the drive frequency to be suddenly detuned at a frequency $\omega_{res} + \Delta$. The decay is recorded with the DAQ card, and the procedure is repeated. The last row of the time sequence chart shows the frequency of the excitation (black arrow), which is synchronized with the local oscillator, at each step of the sequence.

To test this procedure while checking whether intrinsic dephasing is measurable or not, we measured decay times T_1 and T_2 both in frequency and time domain up to large displacement amplitudes: at most the displacement amplitude was four times the resonator's thickness, thus strongly in the non-linear regime. A comparison between

the two measurements for the same displacement amplitude is shown in Fig. 4.9. Each point of the frequency domain response was averaged over 3 s to be as sensitive as possible to hypothetical intrinsic dephasing.

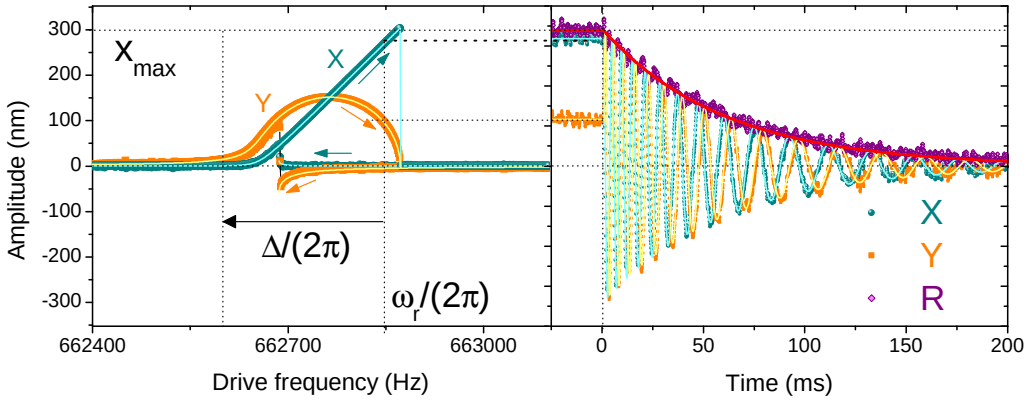

Figure 4.9: frequency (left) and time (right) domain responses of the resonator for an excitation force $F_0 = 1.1$ pN bringing the resonator far into the bistable regime. The free decay of the steady-state resonant response is triggered by detuning the excitation force away from the resonance frequency by $\Delta = -2\pi \times 250$ Hz at $t = 0$. Solid lines on the left panel are the application of the Duffing model through Eq. (2.67) with $\beta = 1.8$ mHz/nm^2, while those reproducing the experimentally observed non-linear oscillations on the right panel follow the expression obtained through Lindstedt-Poincaré method and $\kappa = 2$ mHz/nm^2 (see text). The magenta points represent the free decay of the amplitude $R = \sqrt{X^2 + Y^2}$, while the red solid line is an exponential fit yielding the energy decay time $T_1 = 57$ ms.

Remarkably, the beating between the NEMS and the local oscillator is a non-linear oscillation. While the period is initially equal to the detuning, it gradually becomes larger, until it reaches a value equal to $[\Delta + (\omega_{res} - \omega_0)]^{-1}$, where ω_0 is the natural resonance frequency in the linear regime (mind the minus sign on Δ). This feature can be explained by the geometric non-linearity: as the motion goes to zero, the non-linear frequency pulling gradually weakens, and the pseudo-oscillation synchronizes with the decreasing resonance frequency. Using the Lindstedt-Poincaré method of solving non-linear differential equations, a secular perturbation theory approach detailed in Ref. [69], one can fit the non-linear oscillation with a time-varying frequency $\omega_{res}(t) - \omega_0 = \kappa x^2(t = 0)\varpi(t)$, where κ is left first as a free parameter and where:

$$\varpi(t) = \frac{1 - e^{-2t/T_1}}{2t/T_1}. \tag{4.37}$$

Besides, theory predicts that the coefficient κ should coincide with the Duffing coefficient β. Over the whole dynamic range we verified experimentally that $\kappa = \beta$ within 10 %, where $\beta = 1.8$ mHz/nm^2. Moreover, we did not observe any discrepancy between relaxation and decoherence times for our device, nor any non-linear damping, as shown in Fig. 4.10, within error bars over the range explored (see Chap. 6 for further discussion).

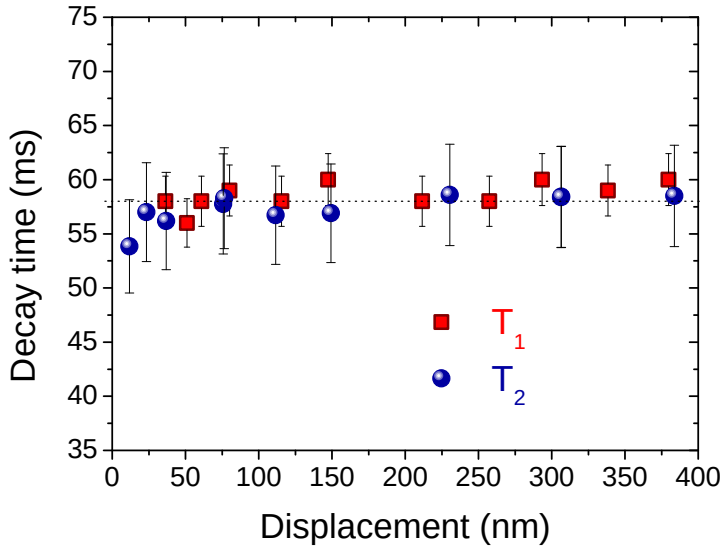

Figure 4.10: T_1 and T_2 times obtained with the methods described in the main text, as a function of mechanical displacement. The dotted line is set at 58 ms.

While being in itself a negative result, it gives confidence that our structure is ideal to model through external means the impact of frequency noise on the measured modes. Note that in Ref. [24], measurements on a similar SiN beam also showed that $T_1 = T_2$.

4.3.3 Results

From then on, the experiment is rather simple: as we control the level of noise on the gate electrode through the voltage source, we measure response lines in the frequency domain to obtain T_2, and decays in time domain to obtain T_1 and $\overline{T}_2$. Response lines (X and Y) measured at different noise levels are shown in Fig. 4.11.

Basically two limits exist, which are this time fully captured by the convolution picture, in contrast to Chapter 3: the correlation time of the frequency noise is assumed to be very long and thus does not appear in the calculation. For a frequency noise magnitude small compared to the NEMS damping rate, the frequency noise distribution

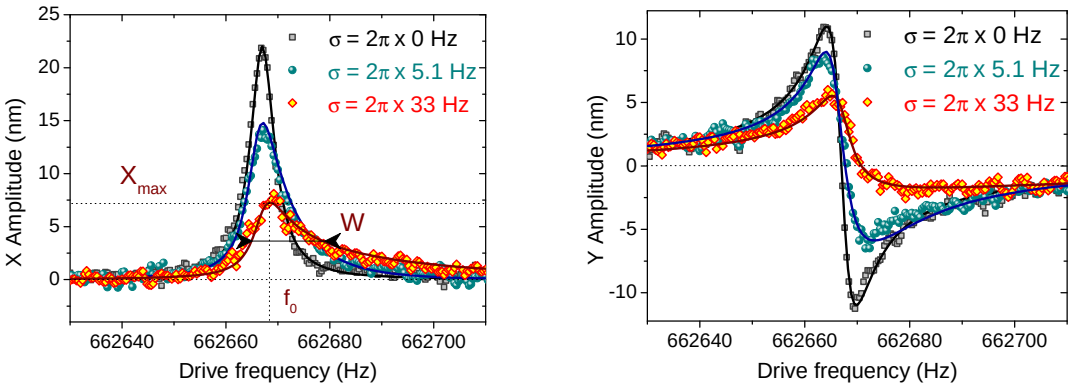

Figure 4.11: in-phase (left) and quadrature (right) responses in frequency domain with an applied force $F_0 = 83$ fN, for three levels of gate induced frequency noise. The extracted parameters (FWHM W, resonance frequency, maximum amplitude) are shown for the response undergoing a frequency noise magnitude $\sigma = 2\pi \times 33$ Hz. Solid lines are the application of Eq. (3.34).

is close to a δ function, and therefore the Lorentzian response is not too perturbed: its parameters are simply renormalized by low-order moments of the frequency noise distribution (first for the shift, second for broadening). As the frequency noise magnitude is increased, i.e. $\sigma \sim \Gamma$ the response gradually deteriorates from a Lorentzian lineshape to an asymmetric resonance which is a "mix" of the bare response and the frequency noise distribution. In the limit $\sigma \gg \Gamma$ the bare Lorentzian response gets closer to a δ function in the vicinity of the noise distribution, and therefore the altered response is highly asymmetric, close to the noise distribution. This is reflected in the fact that the asymmetry takes the form of a long tail towards higher frequencies, as a consequence of having only positive fluctuations values.

From an altered line we extract the FWHM $\Delta\omega = 1/(\pi T_2)$. The decrease of the decoherence time T_2 down to less than half its maximum value while increasing the level of noise applied is shown below in Fig. 4.13, left panel. The data are found to be in good agreement with the theoretical curve extracted from numerical computation of the FWHM of the altered response, Eq. (4.20). We can therefore claim that we measure the loss of phase coherence due to low frequency fluctuations that are adiabatically followed by the NEMS.

We now turn to time domain measurements, with the procedure detailed above. As the level of frequency noise is increased, the ringdown time T_1 of the averaged square amplitude $\langle R^2 \rangle$ remains at 57 $\pm$ 5 ms, up to the highest noise applied in this work. Thus it is truly insensitive to frequency fluctuations. The ringdown curve measured for $\sigma = 2\pi \times 33$ Hz is shown in Fig. 4.12, in magenta.

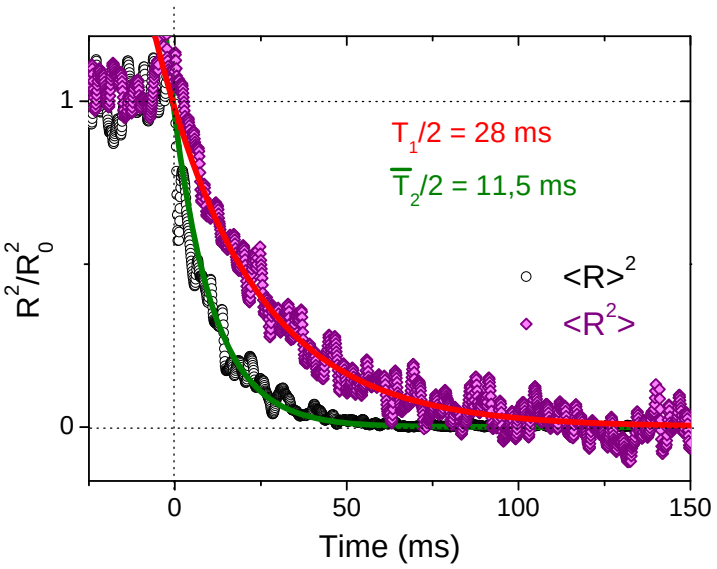

Figure 4.12: decay from the normalized steady-state resonant amplitude, measured through the two ways explained in the main text, averaged over approximately 1000 realizations, for an applied force $F_0 = 83$ fN and a frequency noise magnitude $\sigma = 2\pi \times 33$ Hz. The notation $\langle R \rangle^2$ stands symbolically for $\langle X \rangle^2 + \langle Y \rangle^2$. Solid lines are exponential fits yielding $T_1/2$ and $\overline{T}_2/2$.

As pointed out before, the ringdown technique can also be used to measure decoherence by measuring and averaging separately the two quadratures decaying and extracting a $\overline{T}_2$ (fit of the so-called $\langle R \rangle^2$. For each T_1 measured we also extracted $\overline{T}_2$. An example is shown in comparison with the T_1 measurement in Fig. 4.12. The measured values are reported in Fig. 4.13, where the discrepancy between T_1 and T_2 appears unambiguously even for modest levels of noise applied. This demonstrates that we indeed measure energy relaxation through the ringdown, while measuring the loss of phase coherence (which obviously includes the energy loss) with the usual frequency sweep.

From then on, the pure dephasing rate $\Gamma_\phi = T_2^{-1} - T_1^{-1}$ accounting only for dispersive processes leading to decoherence can be deduced, whether it is obtained from T_2 or $\overline{T}_2$. The extracted values are shown in Fig. 4.13 right panel, with $\overline{\Gamma}_\phi$ corresponding to the pure dephasing rate calculated from $\overline{T}_2$. Thus, we find a quantitative link between the analogous pure dephasing rate and the integrated power spectral density of frequency noise, as in the case of quantum bit circuits [102].

The agreement with theory, with discrepancies lower than ± 15 %, is rather good for both methods (T_2 and $\overline{T}_2$ fits), and validates our approach. Yet one issue remains: a characteristic time is not an absolute quantity insofar as it is defined arbitrarily,

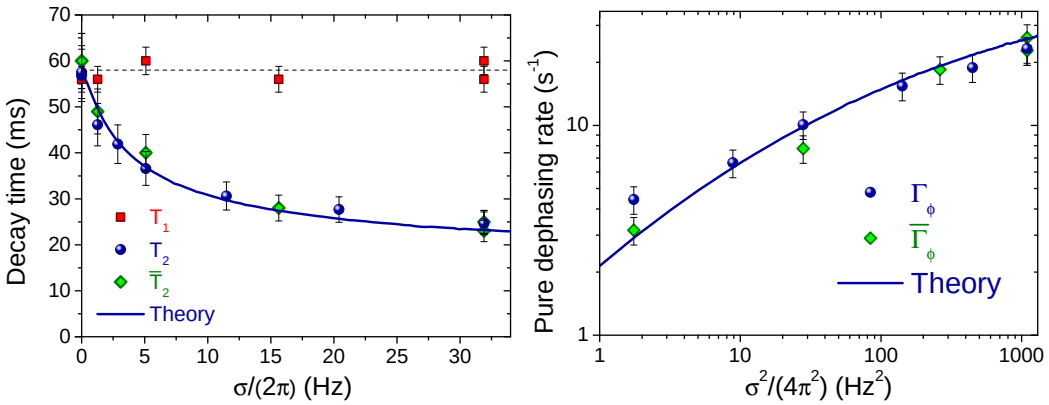

Figure 4.13: left: measured decay times as a function of injected noise level σ. The blue solid line is obtained by numerically extracting the linewidth from the convolution. The dashed line is a guide for the eyes. Right: analogous pure dephasing rate as defined in the main text, extracted from T_2 and $\overline{T}_2$ measurements, with a reference $T_1 = 57$ ms. The blue solid line is calculated from the T_2, which is numerically extracted from the convolution formula.

for instance through an exponential decay, i.e. from a Lorentzian linewidth in the frequency domain. Nonetheless, the altered responses are obviously not Lorentzian, and T_2 and $\overline{T}_2$ are merely practical estimates of decoherence which amount to approximating the measured lines with Lorentzian shapes, or decays with exponential fits, as is shown in Fig. 4.14.

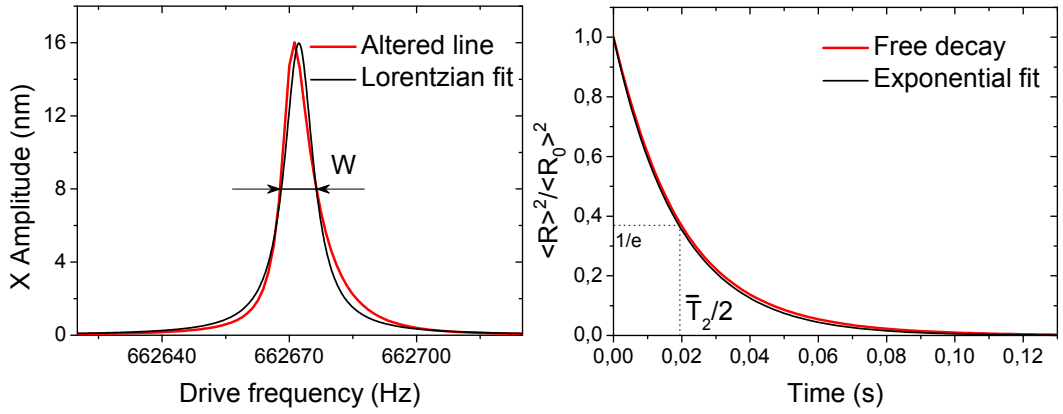

Figure 4.14: left: frequency domain response with a frequency noise magnitude $\sigma = 2\pi \times 5.1$ Hz, and the Lorentzian fit having the same FWHM. Right: time domain response of $\langle X \rangle^2 + \langle Y^2 \rangle$ with the same frequency noise magnitude, and the exponential fit which is the inverse Fourier transform of the Lorentzian fit on the left panel.

While such approximations might seem crude at first glance, their accuracy can be checked by introducing the following shape factor $\mathcal{S}$:

$$\mathcal{S} = \frac{\Delta\omega x_{\max}}{\int \mathrm{Im}[\chi_0(\omega)]F_0 \mathrm{d}\omega}. \tag{4.38}$$

The product $\Delta\omega x_{\max}$ in the numerator corresponds, within a numerical factor, to the area that the quadrature would have if it were Lorentzian. It is normalized to the area of the noiseless Lorentzian. For a pure Lorentzian line $\mathcal{S} = 2/\pi$. The measured shape factors are shown in Fig. 4.15.

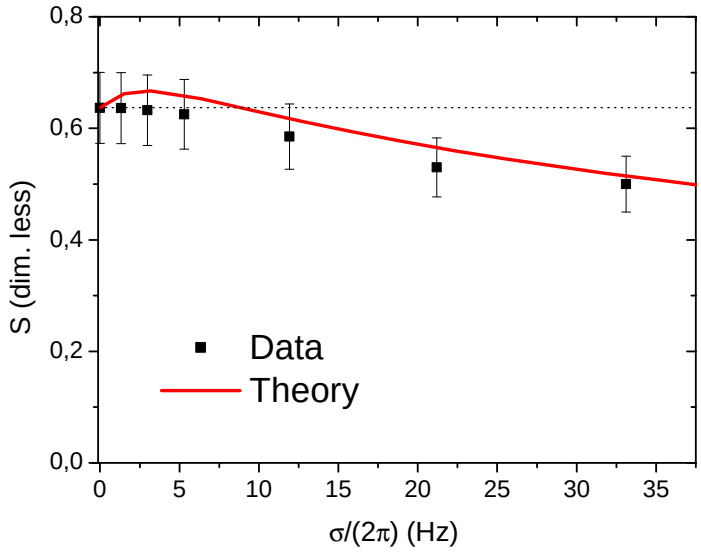

Figure 4.15: measured shape factor as a function of the noise magnitude. The red solid line is the shape factor with $\Delta\omega$ calculated from Eq. (4.20).

The experimental shape factors agree well with the theoretical calculation based on Eq. (4.20), and do not deviate more than 20 % from the initial value at the strongest level of applied noise. This ultimately proves the accuracy of our Lorentzian approximation. Note that as the lines in frequency domain are simply Fourier transforms of the quadrature ringdowns, the exponential approximation also holds well.

Needless to say, the shape itself under fluctuations contains extremely valuable information, which is another reason why we created a non-Gaussian, asymmetric noise taking only positive values. Deconvoluting a line is a non-trivial task but remains feasible, which is of fundamental importance when intrinsic, unknown mechanisms leading to spectral broadening are addressed. A recent proposal addresses the issue in the context of nanomechanics [103], suggesting that computing the moments of the response could lead to the identification of these decoherence mechanisms.

4.4 Conclusion and prospects

In this Chapter, time and frequency domain responses of a mechanical mode have been measured and its relaxation T_1 and decoherence T_2 times compared so as to separate, within a framework analogous to NMR, the contribution of energy relaxation and pure dephasing among processes limiting the NEMS performance. We have established that with no external noise biases, within our resolution, our SiN nanomechanical devices are not subject to non-linear damping or dephasing over a very large range, as opposed to observations made with carbon based systems [9, 75]. This issue shall be addressed further in Chapter 6. Having ruled out internal mechanisms, we have engineered slow fluctuations of the resonance frequency, by capacitively coupling gate voltage fluctuations controlled with an external source to the nanomechanical motion. The coupling could be made linear, with a DC gate voltage bias, or quadratic in the voltage fluctuations. With engineered slow fluctuations we unravel signatures of pure dephasing. Using the analogy with studies done on quantum bit circuits, we link quantitatively the pure dephasing rate to the integrated power spectral density. The shape of noise-altered resonance lines is found to intimately depend on the nature of the coupling, i.e. on the frequency noise statistics, a feature already observed in the experiment described in Chapter 3. In a "reverse engineering" approach, this can be useful: for devices suffering from actual intrinsic dephasing, the shape can provide information on the noise sources by computing its moments, which provide information on the fluctuation statistics.

4.5 Résumé en français

Dans ce chapitre, complémentaire du précédent, nous décrivons une expérience ayant pour but de modéliser la décohérence classique d'un système nano-mécanique par analogie avec la Résonance Magnétique Nucléaire (RMN) ou les systèmes d'information quantique. Des concepts issus de ces champs d'étude sont introduits, tels que le temps de relaxation T_1 qui est le temps caractéristique sur lequel s'effectue le transfert irréversible d'énergie du système à son bain, et le temps de décohérence, qui inclut les pertes d'énergie mais incorpore aussi la perte de cohérence (ici classique) de la phase associée à l'oscillation du système. La décohérence est artificiellement créée par une source de bruit lent (spectre piqué en-dessous de 1 Hz) en tension couplée capacitivement à la vibration mécanique par une électrode de grille: le bruit est alors transduit en fluctuations lentes de la fréquence de résonance du mode étudié, ce qui introduit un déphasage accumulé sur une échelle de temps comparable à T_1, responsable d'une perte de cohérence de phase du signal bien que la relaxation d'énergie reste inchangée. La procédure est similaire à celle du chapitre précédent bien qu'ici le mécanisme à l'origine des fluctuations de fréquence soit extérieur à la nano-poutre (nous utilisons une grille externe au lieu de la non-linéarité intrinsèque). En revanche, l'objet du

chapitre est différent: il s'agit simplement ici de séparer pertes d'énergie et perte de cohérence de phase.

Nous mesurons le temps de décohérence du mode fondamental de flexion hors du plan d'une longue poutre nano-mécanique par la technique habituelle de balayage en fréquence de la raie de résonance mécanique. En effet, chaque point de la raie est moyenné sur des temps suffisamment longs pour intégrer statistiquement toutes les réalisations des fluctuations de fréquence. En présence de déphasage adiabatique, la raie est élargie. La largeur de raie inhomogène (par analogie avec la RMN) est directement une mesure du temps de décoherence T_2, tandis que la forme de la raie nous renseigne sur la statistique des fluctuations: ceci est démontré en créant deux types de bruit en fréquence, l'un Gaussien, l'autre fortement asymétrique.

Afin de mesurer le temps de relaxation T_1 en s'affranchissant de la contribution du déphasage adiabatique, nous développons une technique résolue en temps de mesure de l'oscillation mécanique, insensible à la phase de l'oscillation. En coupant l'excitation initialement à résonance, nous mesurons l'enveloppe des pseudo-oscillations du signal relaxant á l'équilibre sur le temps caractéristique T_1. En l'absence de fluctuations, nous montrons que le déphasage adiabatique est négligeable avec notre niveau de résolution, et qu'il n'y a pas de phénomène de relaxation ou déphasage non-linéaire visible comme cela peut être le cas pour des résonateurs à base de graphène ou de nanotubes de carbone. Lorsque le bruit en fréquence est artificiellement ajouté, nous observons clairement une séparation des deux temps caractéristiques T_1 et T_2, qui est capturée quantitativement par un modèle théorique simple. Nous pouvons en particulier extraire un taux de déphasage adiabatique pur, qui peut être quantitativement lié au spectre intégré des fluctuations lentes de fréquence. Ces résultats, reportés dans [34], reposent sur des techniques simples à mettre en œuvre, et invitent à une réflexion sur le caractère fondamentalement quantique de certains phénomènes à l'œuvre dans les systèmes mésoscopiques et/ou à la limite quantique.

Part II

NEMS coupled to microscopic degrees of freedom

Chapter 5

Energy relaxation in a surrounding fluid

Contents

5.1 Introduction

While the previous part of this manuscript was addressing fluctuation and damping processes in a model way, that is, with engineered situations, this part now deals with

processes that are physically taking place either in the surroundings or within the constitutive materials of the nano-electro-mechanical system. It is part of a widespread effort to acquire an exhaustive knowledge of fundamental mechanisms truly acting at mesoscopic scale and limiting the mechanical object's performance by reducing its relaxation or coherence time. Indeed these mechanisms are still far from being completely understood. Still, every friction or pure dephasing mechanism is set over a typical lengthscale, which in some cases becomes comparable with at least one of the oscillator's dimensions. Therefore, while this endeavour may suggest practical reasons, the NEMS can nevertheless be seen from the basic researcher's point of view as a tremendous tool to investigate these often complex but rich mesoscale mechanisms [104, 58, 11, 28, 105]. In the end, their knowledge is a prerequisite to engineer structures that are as free as possible from these mechanisms, so that other, elusive but extremely fundamental decoherence sources could be probed [20]. Note that the philosophy is rather different from that of the previous part: while we still attempt to stay quantitative, some strong assumptions must be occasionally made to explain our findings, as we do not pretend to bring definite answers to questions that remain open to a large extent. In particular, some parameters strongly depend on materials and are, by essence, not completely under control. They often rely on measurements prior to this work.

The first Chapter of this part deals with an ubiquitous source of damping: even though the NEMS is put in a vacuum cell, there is always some residual amount of gas. While it can be neglected in the first place for most of our experiments, one can wonder what happens if a portion of gas is deliberately introduced in the cell: the gas acts as a fluid interacting with the mechanical object. Such a friction process should naturally be addressed in the framework of fluid dynamics, in the same fashion as vibrating wires used as viscosimeters for quantum fluid studies [51]. Besides, NEMS and MEMS are now at the core of micro- and nano-fluidics because of their ability to probe small lengthscales of a fluid, be it for fundamental purposes tackling the refinements of kinetic theory [106] or applied ones such as biosensing [107]. Here, as a preamble to study more complex classical or quantum matter, we propose to investigate refinements of the interaction between the NEMS probe and Helium-4 gas at cryogenic temperatures. It is a simple experiment insofar as Helium is a very well known gas, almost ideal, with tabulated properties [108]. Thus, very quantitative predictions can be made to support our measurements. The relevant length to address these interactions, and especially friction processes, is the gas **mean free path** λ, which writes:

$$\lambda = \frac{1}{\sqrt{2} n \sigma_{\mathrm{He}}} = \frac{k_B T}{\sqrt{2} \sigma_{\mathrm{He}} P}, \tag{5.1}$$

where n is the gas density, and σ_{He} the cross-section of collisions for Helium-4 atoms.

The latter is computed in Ref. [108], including a small temperature. Depending on the ratio between the mean free path and some geometric dimension of the device (the so-called Knudsen number), the physics at stake is indeed very different, and the geometry of our doubly-clamped nanobeams, suspended over a well-resolved length, make them good candidates to probe several lengthscales. While this gas damping experiment was initially dedicated to characterize the interaction between the fluid and the NEMS according to well established properties, it yielded rather unexpected results at the limit of very low pressures: a reduction of damping has been observed below the standard prediction (linear in pressure). The results thus cover a wide pressure range, from the high pressure limit where the flow of gas around the NEMS is laminar and behaves well according to Navier-Stokes equations, down to very low pressures where the flow is molecular and exhibits unusual features. By "flow" we mean that even though there is no externally created flow, there is one in the NEMS reference frame since the latter is oscillating in the fluid.

5.2 Experimental apparatus

5.2.1 Gas handling system

The experiment at stake relies on the control of pressure into a cell. Therefore, two runs have been made on two different helium bath cryostats in order to demonstrate the reproducibility of the results and rule out any extra geometrical features. Some characteristics are gathered in Table 5.1.

	Cryostat n°1	Cryostat n°2
Sample holder	copper rod (massive)	copper plate (thin)
Pumping line diameter	2 mm	5 mm
Cell diameter	2 cm	4 cm
Capillary tube length	1 m	1 m

Table 5.1: relevant geometrical characteristics varying from one cryostat to the other.

The experimental cell, initially under cryogenic vacuum ($P < 10^{-6}$ mbar), is connected to a capillary tube going up to an external gas handling system set at room temperature. A valve controls the connection between the capillary tube and the gas handling system. The latter is a pipe into which portions of gas are added in a controlled way by an external source made of pure (> 99.99 %) ^{4}He: it comes from a needle valve connected to a helium dewar evaporation. In addition, impurities finding their way towards the cell should be adsorbed on the cell's walls at cryogenic temperatures. Since pumping down to truly 10^{-6} mbar at 4.2 K once helium gas has been

added is time consuming, we choose to start from the low pressure range and go to high pressures by gradually increasing gas portions. The pressure is monitored from 10^{-3} Torr to 100 Torr at room temperature by a Baratron gauge which truly measures pressure. It offers a resolution at the mTorr scale, and displays a zero value usually around -5 mTorr and drifting also at the mTorr scale over approximately an hour. Since these drifts are slow and measured, they can easily be captured and corrected for the data analysis. In addition the experiments were carried out over several thermal cycles to make sure they were reproducible.

We also made sure that thermomolecular corrections all along the pumping line were negligible, so that the pressure read with the gauge is truly that of the cell. We checked that the results were the same with the cryostat full of Helium or almost empty, so that its upper part is above 4.2 K. Besides, estimates of the effect depend on tube dimensions and lead to negligible corrections [109], only becoming relevant below 10^{-3} mbar. Moreover, as we will see later, measurements from one cryostat to the other yield the same results despite different tube diameters and cryostat sizes.

From then on the procedure is simple: when we want to increase the pressure in the cell, we first close the valve and introduce a portion in the pipe. We then open the valve, thus circulating gas into the cell, and let the pressure reach equilibrium. Once it is reached, the valve is closed, and the pipe is pumped again to vacuum.

5.2.2 Samples used in this experiment

The experiments have been run on three different samples, each one being rather long so as to acquire a lot of signal, while reducing the amount of geometrical features: as the length is much bigger than the cross-dimensions, we can approximate our wires as infinitely long strings (and infinitely thin in the low pressure limit). Their characteristics are gathered in Table 5.2, and pictures are shown in Fig. 5.1. Note that the 150 µm long device has an intrinsic linewidth Γ_{int} which is rather large, resulting in bigger error bars for very low pressure measurements than with the other devices. This is likely due to the fabrication process. Most importantly, the three devices have been designed such that their gaps g between the wire and the bottom spread over one order of magnitude, while all gaps are way larger than the devices cross-dimensions. Usual XeF_2 does not permit an etching depth beyond 20 µm: the undercut would be too big for the structure to stay suspended (see Fig. 5.1 right panel). Thus a new process has been developed by our collaborator Thierry Crozes, which relies on two lithography steps. It led to develop a sample with a bottom trench located 40 µm below the string (see Fig. 5.1 left panel).

As stated through Eq. (3.1), any gas damping contribution will be added to the intrinsic damping rate Γ_{int}. Therefore, to adress gas damping, we simply subtract this vacuum value, using low fields so as to minimize the loading contribution and gain in resolution: the lower the intrinsic value, the better resolution is obtained since

	freq. $\omega_0/2\pi$	$\Gamma_{vac}/2\pi$	gap g
mode 1 100 µm	2.2 MHz	9 Hz	4 µm
mode 3 100 µm	6.7 MHz	30 Hz	4 µm
mode 5 100 µm	11 MHz	55 Hz	4 µm
mode 1 300 µm	0.66 MHz	3 Hz	40 µm
mode 3 300 µm	1.98 MHz	10 Hz	40 µm
mode 1 150 µm	1.65 MHz	90 Hz	20 µm

Table 5.2: relevant parameters for the three samples measured. The damping rates indicated are obtained in vacuum ($P < 10^{-6}$ mbar) for a magnetic field $B = 100$ or 200 mT, depending on the sample.

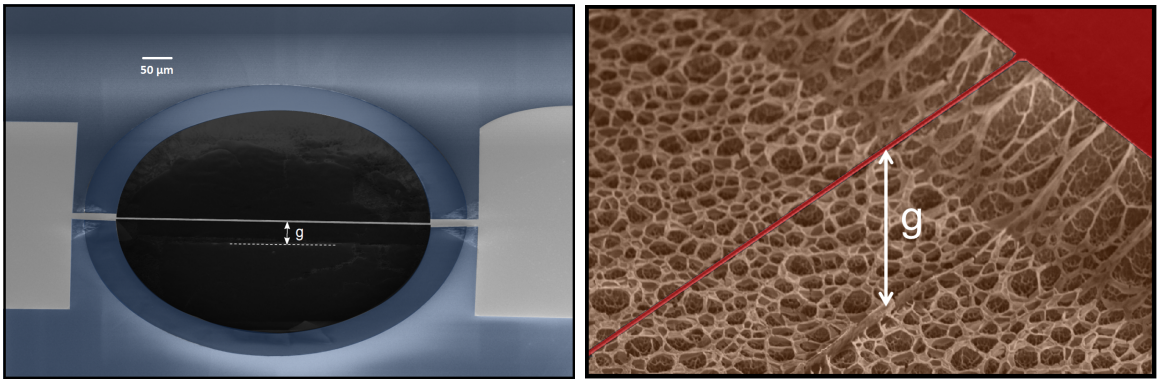

Figure 5.1: left: colorized SEM picture of the 300 µm device, with $g = 40$ µm the gap between the string and the bottom trench. Right: zoom on the right clamp of the 150 µm device ($g = 20$ µm), which emphasizes the spongy bottom resulting from the XeF_2 etching. The shadowed region is a good marker of the undercut digging length.

for our lowest pressures a relative error is already existing on the vacuum linewidth. However, all measured vacuum linewidths were found to be reproducible within 5 % of the indicated value at worst, which enable rather precise measurements. Note that all measurements were done with driving forces low enough in order to remain in the linear regime.

A typical example is shown in Fig. 5.2, with the pressure changed by one order of magnitude between the two measured resonance lines and with an excitation force adapted to obtain the same amplitude of motion. The difference is striking, with lines much broader than in vacuum, which gives us confidence concerning our resolution.

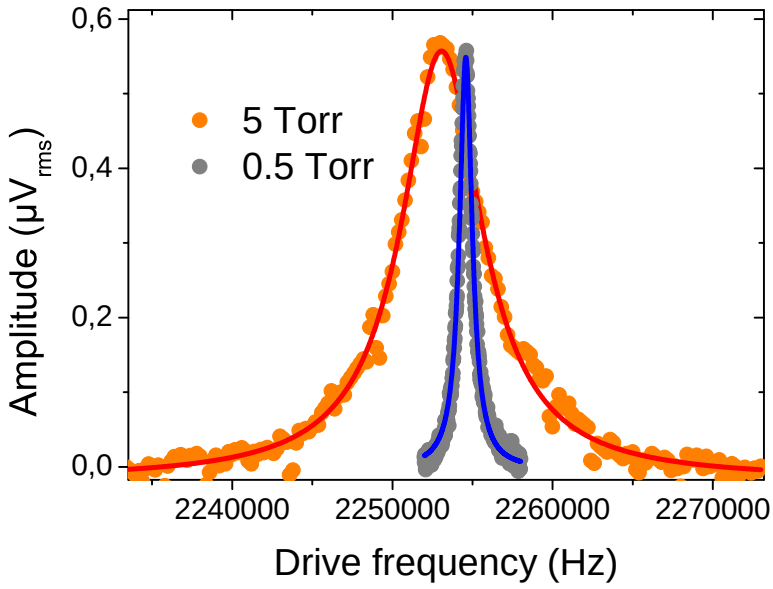

Figure 5.2: resonance lines measured at 5 Torr (orange dots) and 0.5 Torr (grey dots) with the 100 μm sample. Solid lines are Lorentzian fits, yielding resonance frequencies $\omega_0(P = 5 \text{ Torr}) = 2\pi \times 2.2531$ MHz and $\omega_0(P = 0.5 \text{ Torr}) = 2\pi \times 2.2548$ MHz, and damping rates $\Gamma(P = 5 \text{ Torr}) = 2\pi \times 6$ kHz and $\Gamma(P = 0.5 \text{ Torr}) = 2\pi \times 1$ kHz.

5.3 NEMS in a viscous fluid: the Navier-Stokes regime

5.3.1 Hydrodynamic description of the NEMS damping by a fluid

At a cell pressure $P \sim 10 - 100$ Torr, the gas mean free path λ is much smaller than the NEMS cross-dimensions w, e. Thus the NEMS can be described as an oscillating body moving in a **continuous**, viscous fluid having a shear (or dynamic) viscosity η. The transition regime where this approach progressively deteriorates, with so-called slippage corrections in the first place, is addressed in Section 5.3.3. The NEMS velocity $\omega_0 x(\omega_0)$ is at most ~ 1 m/s, i.e. small compared to the speed of sound in helium (100 m/s), and thus second viscosity (linked to volume change) can be neglected. To derive the friction force between a fluid particle of mass density ρ_g and the solid body one needs to find the fluid velocity field $\mathbf{v}_g$ around the NEMS, which is described by the Navier-Stokes equation:

$$\rho_g \left[\frac{\partial \mathbf{v}_g}{\partial t} + (\mathbf{v}_g \cdot \nabla)\mathbf{v}_g \right] = -\nabla P + \eta \nabla^2 \mathbf{v}_g. \tag{5.2}$$

Such a problem for a square cross-section is addressed in Ref. [110]. The damping

force per unit length in the frequency domain writes:

$$\frac{\partial F_g(z,\omega)}{\partial z} = \rho_g A_c\, \omega^2 \Lambda(\omega) \Psi(z) x(\omega), \tag{5.3}$$

where ρ_g is the gas mass density and $A_c = \pi w^2/4$ the effective cross-section of the beam experiencing friction. $\Lambda(\omega)$ is the friction coefficient that is calculated from Eq. (5.2). By effective we mean that it is the cross-section for a cylinder of diameter w, and the correction to match the rectangular case will further be incorporated in the friction coefficient. To detail physically the viscous force acting on the whole beam, one can write the instantaneous power injected into the fluid due to the damping force integrated over the whole beam in time domain:

$$P_g = \dot{x}(t) \left[-\rho_g A_c \,\mathrm{Re}\left[\Lambda(\omega)\right] \int \Psi^2(z) \mathrm{d}z\, \ddot{x}(t) + \rho_g A_c\, \omega\, \mathrm{Im}\left[\Lambda(\omega)\right] \int \Psi^2(z) \mathrm{d}z\, \dot{x}(t) \right]. \tag{5.4}$$

From then on the viscous force that appears into the brackets can be decomposed into two different components. The one proportional to $\ddot{x}$ is said to be **reactive**, adding inertia as if the effective mass of the NEMS were renormalized by the surrounding fluid, dragged together by the motion. This contribution leads to a shift of the resonance frequency. On the other hand, the term proportional to $\dot{x}$ acts as the **dissipative** component, leading to the linewidth broadening. What is left now to compute is the friction coefficient $\Lambda(\omega)$. It can be explicited as $\Lambda(\omega) = \Sigma(\omega)\Omega(\omega)$, where $\Sigma(\omega)$ is the Stokes solution for an infinite cylinder [111]. $\Omega(\omega)$ is a small correction used to match the rectangular cross-section term [110, 112], which renormalizes the damping by at most 15 %. The Stokes solution writes:

$$\Sigma(\omega) = k' + ik'' = \frac{4}{\frac{1+i}{u}} \cdot \frac{J_1\left(\frac{1+i}{u}\right) + iY_1\left(\frac{1+i}{u}\right)}{J_0\left(\frac{1+i}{u}\right) + iY_0\left(\frac{1+i}{u}\right)}, \tag{5.5}$$

where $u = \sqrt{2}\delta/w$ and $\delta = 2\sqrt{\eta/(\rho_g \omega)}$. δ is called the **viscous penetration depth**. It is the characteristic length over which the harmonic motion propagates in the fluid, that is, over which the fluid is perturbed by the oscillation. J and Y are the Bessel functions of first and second kind.

We have written the power injected, and the dissipative part P_d can be related to the linewidth broadening Γ_v through $P_d = -m\Gamma_v(\omega)\dot{x}^2(t)$. In the end, the damping rate in the viscous regime depends on the oscillation frequency:

$$\Gamma_v(\omega) = \frac{\rho_g A_c \, \omega k''(\omega)\Omega(\omega) \int \Psi^2(z)\mathrm{d}z}{m}. \tag{5.6}$$

Note that there is no geometric modal dependence, as $m \propto \int \Psi^2(z)\mathrm{d}z$. Thus, the only mode dependence is on $\omega k''(\omega)\Omega(\omega)$.

5.3.2 Acoustic wave radiation

In addition to friction processes at the NEMS-fluid boundary, another source of damping could come from the fact that while oscillating, the beam modulates the pressure field around it, which is none other than sound radiation emission, the same way a guitar string produces sound in the air. Here, sound radiation is expected to be irrelevant due to the NEMS small dimensions. We can nonetheless give an estimate, assuming the NEMS is a cylinder in first approximation. By solving the sound equation [113] which yields the pressure field P and calculating then the sound intensity $\mathbf{I} = \mathrm{Re}\,[P\mathbf{v}_g]$ at the NEMS/fluid boundary, one obtains the radiated power, and thus the contribution to the damping [35]:

$$\Gamma_s(\omega) \sim \frac{\omega^3 \rho_g w^4 l}{m c_g^2}, \tag{5.7}$$

where $c_g \sim 100$ m/s is the speed of sound in helium. This estimate is plotted in Fig. 5.5, and appears to be at best four orders of magnitude lower than fluid friction for our experiment, and thus completely irrelevant in the pressure range investigated. Therefore it shall be disregarded in what follows.

5.3.3 Slippage correction

Now the damping is explicit, there should be no free parameter. This approach was indeed valid in the case of a MEMS device [112]. However, it does not exactly match the experimentally measured damping, as shown in Fig. 5.4. In fact, the reduction of dimensions makes the nanomechanical device much more sensitive to **slippage** corrections. Indeed, for a bulk fluid (with respect to the NEMS) the tangential velocity decreases linearly as it gets closer to the boundary between the object and the fluid, and becomes zero at the boundary in good approximation because the fluid is clamped on surface irregularities: this is the so-called no-slip condition [114]. Yet, by decreasing the cell pressure, the mean free path λ of the gas is increased and eventually becomes comparable with the device cross-dimensions e, w. In that case the approximation breaks, and tangential velocity does not necessarily go to zero at the boundary between the solid object and the fluid: this is the definition of slippage. At the lowest order (i.e. before adopting a fully statistical approach, see below), a so-called **slip**

length l_{slip} takes into account the effect [115]. This is the length over which the tangential velocity field would go to zero if it were extrapolated beyond the NEMS-fluid boundary. Following Refs. [116, 117], we introduce a renormalization of the damping coefficient by the slip length:

$$\Lambda(\omega) - 1 \to \frac{1}{(\Lambda(\omega) - 1)^{-1} - \frac{1}{2u^2}\left(\frac{l_{slip}}{l_{slip} + w/2}\right)}. \tag{5.8}$$

A quantitative definition of the slip length involves the scattering processes at the NEMS-fluid interface. Indeed, this length becomes relevant when λ is a fraction of e, w which means that the NEMS is able to resolve individual gas particles collisions on its surface. It is clear that the nature of these collisions will be important in the definition of the slip length. Even though microscopic mechanisms are very difficult to model, one can sort them into two classes:

- collisions where the NEMS surface essentially acts as a mirror for the incoming particle, which are called **specular** reflections. These are called elastic, as there is no net energy transfer.

- collisions with a surface for which roughness is important due to defects, and permits many (specular) collisions before the particle bounces off the surface, with a momentum direction uncorrelated to its initial one. These collisions are said to be **diffusive**. The relevance of this effect can be appreciated by comparing the size of typical defects, about $20 - 30$ nm for our samples (see Fig. 5.3), with the De Broglie wavelength for ^{4}He atoms $\lambda_{DB} = 2\pi\hbar/\sqrt{3m_g k_B T}$ [118], which is about 0.6 nm at 4 K. No net energy is transferred, as the momentum change only affects the direction. As such, these collisions are elastic.

- collisions such that the atom "sticks" to the surface, i.e. is adsorbed. To ensure global energy conservation, this implies that another atom somewhere on the surface must be desorbed [119, 120]. By stating so, we make the assumption that the NEMS surface and the gas are at the same temperature, since the atom that is emitted is initially in equilibrium with and thus thermalized to the surface. Measurements of the sticking coefficient at 4.2 K show that it can be rather high [119, 120]. Therefore it can significantly contribute to **diffusive** scattering.

Here we merely separate diffusive from specular scattering processes with a so-called specular fraction s that is 0 for pure diffusive scattering and 1 for pure specular reflection. The slip length then writes [121]:

$$l_{slip} \approx 1.15 \left(\frac{1+s}{1-s}\right) \lambda. \tag{5.9}$$

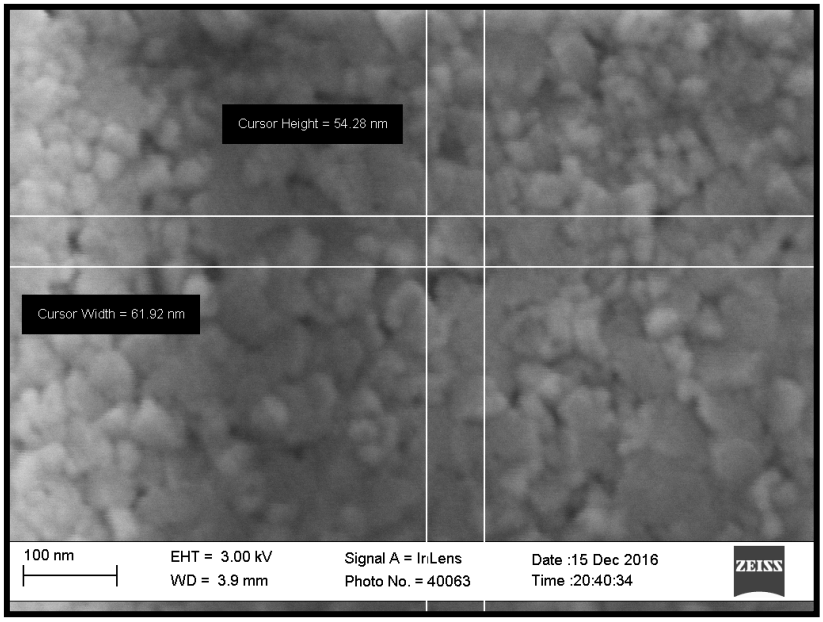

Figure 5.3: SEM picture of the Al surface. The typical size of the grains is about 30 nm, with a size varying between 10 and 60 nm.

We see that for pure specular reflection, the slip length diverges. This is expected: by definition, in the case of pure specular reflection, the NEMS merely acts as a mirror and therefore does not impact the particles equilibrium properties: there is no reason why the tangential velocity field would decrease to zero in the vicinity of the surface. In contrast, diffusive reflection, by definition, tends to slow down particles. To achieve a perfectly specular surface is challenging, and yet spectacular slippage signatures have been reported for carbon [122] and boron nitride [123] nanotubes, which likely owe to their cleanliness.

The data in Fig. 5.4 are rather well captured from 100 Torr down to about 10 Torr, where essentially $\lambda \sim w$, with a fit specular fraction $s = 0.5$ consistent with the sticking effect explained earlier. Unfortunately the third and fifth modes damping rates could not be measured up to high enough pressures to capture the viscous regime and confirm the frequency dependence, essentially because the signal was too weak to obtain reliable data: this comes from the combination of a poor Q factor and small transmission coefficients in the setup wiring. For pressures below 10 Torr the mean free path eventually becomes bigger than the NEMS cross dimensions and neither the continuous fluid description nor the first order correction (slippage) hold anymore. Thus, for $P < 10$ Torr we must find another approach, so-called **ballistic**, to describe the gas damping.

In fact, the transition regime between a laminar description and a ballistic one, which sets in over about an order of magnitude in our experiment, is a highly non-

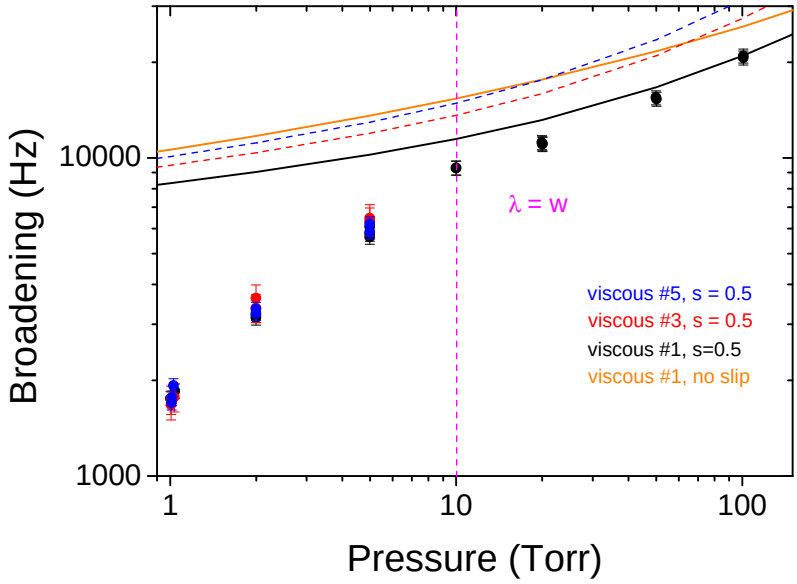

Figure 5.4: gas damping contribution as a function of the cell pressure in the high pressure limit, i.e. from 1 to 100 Torr, measured with the 100 µm long NEMS at 4.2 K. For the first mode, theoretical predictions with (black solid line) and without (orange solid line) slippage correction are represented.

trivial problem, and a universal description for oscillating flows is still missing [124]. Beyond the slippage correction, we will simply use an interpolation that makes the link between the viscous regime prediction and the ballistic one in the transition range. In the transition regime, in principle, the friction is affected by the finite response time of the fluid, which leads to the definition of a generalized Knudsen number involving not only λ/w but also the penetration depth δ [106]. Finite time effects are relevant when $\lambda \sim \delta$, which happens here around 0.5 Torr for the 100 µm device, far below the purely geometrical transition range. In addition, experimentally, such an effect would depend on the oscillation frequency, and we measured the same gas damping with the three modes, that are spaced at worst by one order of magnitude in frequency. Therefore we can safely neglect finite time effects and concentrate on finite size effects.

5.4 NEMS in a ballistic gas: the molecular regime

5.4.1 Statistical description of the damping

In the low pressure limit, the continuum description for the surrounding fluid breaks down. It is understood here that the low pressure regime corresponds to a limit when the mean free path λ of the surrounding medium atoms is large in comparison with

the device transverse dimensions. Then, from the point of view of the device, the gas is not a homogeneous ensemble but a collection of discrete, ballistic particles carrying momentum and colliding at random times on its surface as often as between themselves. Hence one must adopt a statistical approach: the measured properties (resonance frequency, damping rate) are averaged over a gas particles distribution of velocities (or possibly, spatial coordinates), and they must give a reliable account of this interaction, which does not necessarily hold true if the gas is too rarefied, in the very low pressure limit. A simple estimate can illustrate the situation with the most conservative experimentally reachable parameters: at $T = 15$ K, $P = 10$ mTorr, the number N of an ideal gas particles in a square volume $V = (200\text{ nm})^3$ of lateral dimensions typical of the NEMS cross-dimensions and small compared to its length is:

$$N = \frac{PV}{k_B T} \sim 50 \text{ particles}, \tag{5.10}$$

with a relative fluctuation on the number of particles:

$$\frac{\delta N}{N} = \frac{1}{\sqrt{N}} \sim 14\ \%. \tag{5.11}$$

While the typical number of particles shows how far we are from the continuum description, its relative fluctuations are small enough so we can use a statistical description based on gas kinetic theory. The starting point is the Maxwellian distribution on the bulk gas velocities at equilibrium:

$$f_M\left(v_x, v_y, v_z\right) = \left(\frac{m_g}{2\pi k_B T}\right)^{3/2} \times \exp\left(-\frac{m_g\left[(v_x - v_{x,0})^2 + (v_y - v_{y,0})^2 + (v_z - v_{z,0})^2\right]}{2k_B T}\right), \tag{5.12}$$

where m_g is the ^{4}He atomic mass: $m_g = 6.65 \times 10^{-27}$ kg. Here, we have considered the case of an existing flow in the gas by keeping an average velocity field $\mathbf{v}_{g,0} = (v_{x,0}, v_{y,0}, v_{z,0})$. Indeed, one should take into account the fact that the NEMS is oscillating while immersed in the gas. Therefore, even though the gas does not experience any externally imposed macroscopic flow, there exists one in the NEMS frame, which moves at a velocity $\sim \omega_0 x(\omega_0)$. In practice, one can expect $v_{z,0}$ to be zero and the profile $(v_{x,0}, v_{y,0})$ around the beam to have the same symmetries as in the laminar case.

5.4.2 Computing the damping force

It is clear from then on that the mechanism responsible for mechanical damping through the gas is the transfer of momentum from the NEMS to the ballistic particles colliding on its surface. The average force per unit area dydz exerted by a particle colliding with the device oscillating around the n^{th} mode resonance frequency is obtained by computing the total average momentum transfer:

$$\frac{\partial^2 F_g(z,t)}{\partial y \partial z} = -\rho_g \overline{v}_g \Psi_n(z) \dot{x}_n(t), \tag{5.13}$$

with v_g the incoming gas particle velocity and the bar denoting the gas average absolute velocity. Besides, when $\lambda \sim w$, particles start to collide with the NEMS as often as between themselves. This can be encompassed in the above description by simply stating a small correction to the usual Maxwell-Boltzmann distribution. We introduce a modified distribution $f(v_x, v_y, v_z) = [1 + \varepsilon(v_x, v_y, v_z)]\, f_M(\mathbf{v})$, where ε is a correction function [35]:

$$\begin{aligned}\varepsilon(v_x, v_y, v_z) = \sqrt{\frac{m_g}{2k_BT}} \sum_{i=x,y,z} a_i (v_i - v_{i,0}) \\ + \frac{m_g}{2k_BT} \sum_{i,j} a_{ij} (v_i - v_{i,0})(v_j - v_{j,0}) \\ + \left(\frac{m_g}{2k_BT}\right)^{3/2} \sum_{i,j,k} a_{ijk} (v_i - v_{i,0})(v_j - v_{j,0})(v_k - v_{k,0}) \\ + \ldots.\end{aligned} \tag{5.14}$$

Coefficients $a_{i\ldots}$ should be nonzero only in the vicinity of the NEMS, and should vanish to zero within the mean free path towards the bulk gas. Rules on the distribution allow to link some of these coefficients between themselves [125]. First, the distribution should be normalized to 1, which leads to:

$$\sum_{i=x,y,z} a_{ii} = 0. \tag{5.15}$$

In addition, the average velocity field $\int v_i f(\mathbf{v}) \mathrm{d}^3\mathbf{v}$ in each direction $i = x, y$ and z must be equal to $v_{x,0}, v_{y,0}$ and $v_{z,0}$, respectively, which leads to:

$$2a_i + 3a_{iii} + \sum_{j \neq i} a_{ijj} = 0. \tag{5.16}$$

From that, we can compute the total damping force acting on the NEMS, by integrating the total momentum transfer. Contributions in $v_{y,0}, v_{z,0}$ can be computed but their

integration over dydz will lead to a zero net contribution. Therefore, only coefficients a_x, a_{xx}, a_{xxx} are needed for the calculation. If diffusive reflection is indeed significant, the equilibrium conditions of the NEMS will have an influence on the surrounding gas due to the re-emitted particles, allegedly small since the NEMS has very small cross-dimensions. Gathering the two contributions, the damping force per unit length writes:

$$\frac{\partial F_g(z,t)}{\partial z} = -2\vartheta\rho_g\overline{v}_g w\Psi_n(z)\dot{x}_n(t), \tag{5.17}$$

with $\vartheta = s + (1-s)\left(1+\frac{\pi}{4}\sqrt{T_N/T}\right)/2$. Therefore, the presence of disorder and diffusive reflection at the level of the NEMS adds only a small renormalization of the damping force compared to an ideal case of pure specular reflection. Note that the $a_{i...}$ coefficients have disappeared from the expression and contribute only as corrections which involve the beam velocity. These terms are negligible, a fact that is experimentally justified: as opposed to the Navier-Stokes limit, the measured damping rate depends here neither on the mode, nor on the NEMS velocity (or current injected) for the driving forces used, as seen in Fig. 5.5. A detailed justification can be found in Ref. [35]. The NEMS temperature T_N could be slightly different from the gas one due to the injected drive current, but we used drive forces small enough to stay in the linear regime, and according to our thermal model (see Chapter 2 section 2.7) these should not heat up the device to more than 5 K when $T = 4.2$ K in the most conservative case, that is, when the NEMS is highly damped, and large currents are needed, in the Navier-Stokes limit. In the molecular regime the Q factor remains high and thus current-induced heating is negligible. Therefore the parameter ϑ is not very sensitive to the specularity fraction (since $[1+\pi/4]/2 \approx 0.89$) and will remain between 0.89 (purely diffusive) and 1 (purely specular). High pressure fits, where the specular fraction plays a role due to slippage, suggest that a specularity fraction $s = 0.5$ is adequate [35]. Following the same procedure as in the viscous regime, we write the dissipated power and obtain the damping rate contribution due to the rarefied gas:

$$\Gamma_{mol} = \frac{2\vartheta\rho_g\overline{v}_g w\int\Psi^2(z)\mathrm{d}z}{m}. \tag{5.18}$$

Since $\overline{v}_g \propto \sqrt{T}$ is independent of P and $\rho_g \propto P/T$ the measured broadening simply scales as $P/\sqrt{T}$. In addition, for a string, $\int\Psi^2(z)\mathrm{d}z$ is $1/2$ and $m = M/2$ for all modes. Thus, the damping in the ballistic regime does not depend on the mode for a string structure.

An example is shown in Fig. 5.5, where the gas contribution to the damping is reported for the three first symmetric modes. The fit is from Eq. (5.17) with $\vartheta = 0.95$ in the low pressure limit (i.e. a specularity fraction $s = 0.5$). The rounded part between 3 and 10 Torr captures phenomenologically the transition to the Navier-Stokes regime for low velocities [126]. However, we see that almost as soon as we catch up with

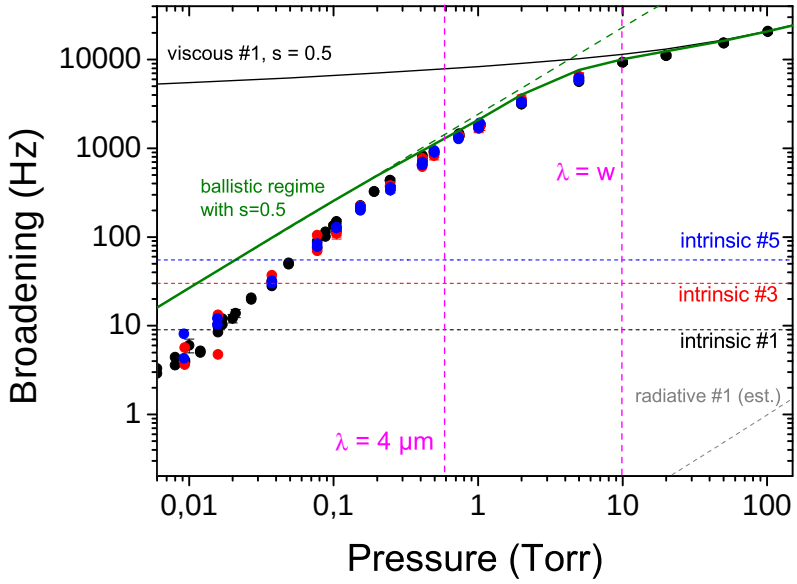

Figure 5.5: gas damping contribution versus cell pressure for the 100 µm long NEMS at 4.2 K [35]. The green dashed line is the molecular damping prediction, proportional to P. The green solid line interpolates the data in the transition range between molecular (P below 1 Torr) and viscous (above 10 Torr) regimes. The dashed line is a low pressure asymptote. The black solid line is a fit from the Navier-Stokes regime for the first mode, incorporating slippage corrections. The grey dashed line is an estimate of the acoustic radiation contribution, while the horizontal dashed lines mark the intrinsic linewidths of each mode for comparison. The vertical pink dashed lines are markers for the transition to the molecular regime ($\lambda = w$) and to the regime featuring an anomalous damping reduction ($\lambda = g = 4$ µm).

the truly molecular regime at low pressures (below 1 Torr), a **reduction** of damping is observed compared with the simple ballistic prediction, up to almost a factor of 10. This cannot be explained by the simple corrections to the Maxwell-Boltzmann distribution on the NEMS introduced above: these would lead to at most a 5 % deviation compared to the prediction (5.18) for the velocities used [35].

5.5 Unveiling the Knudsen layer at the lowest pressures

5.5.1 Main features and reproducibility

The reduction of gas damping below the molecular regime prediction is observed on the three devices used in this experiment, as shown in Figs. 5.5 and 5.6. Thus

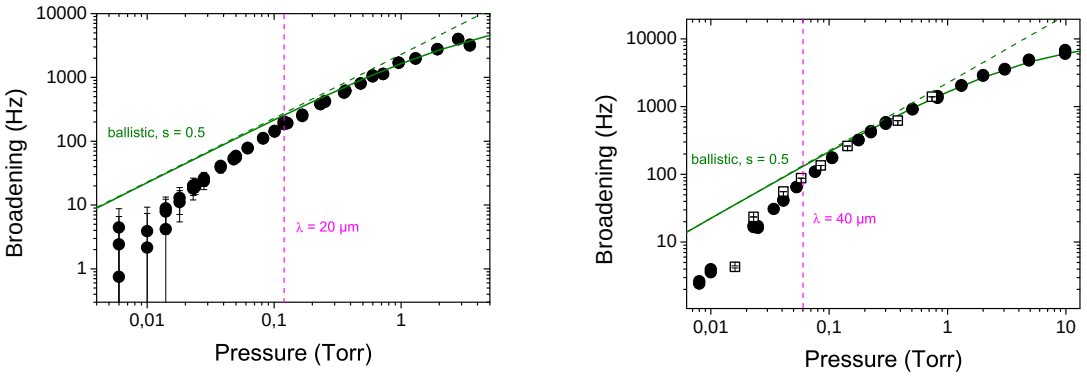

Figure 5.6: left: gas damping as a function of pressure, for the 150 μm sample ($g = 20$ μm). The solid line is the molecular regime prediction, with corrections at high pressures [126]. The magenta dashed line marks the pressure for which $\lambda = g$. The rather important error bars come from the significant intrinsic linewidth, limiting the resolution. Right: same graph for the 300 μm sample ($g = 40$ μm). Dots are data taken with the cryostat n°1 (see Table 5.1), while hollow squares are data taken with the cryostat n°2. All the data are taken at $T = 4.2$ K.

we demonstrate that the effect is genuine and independent of the cryostat by doing the same measurement on the same 300 μm device, on both cryostats 1 and 2 and finding the same result. Interestingly, the observations suggest that the effect, for all devices, manifests when the pressure is low enough so that the mean free path becomes comparable with the gap g between the NEMS and the bottom trench. To confirm this, we measure the effect at other temperatures, since the mean free path can also be tuned with temperature. The result is shown in Fig. 5.7 left panel for a temperature $T = 1.5$ K obtained by pumping on the ^{4}He bath (see Chapter 2, section 2.3): at constant pressure the damping is increased along with the molecular regime prediction, by a factor $\sqrt{4.2/1.5} \approx 1.67$ as expected. Moreover, the departure from the standard ballistic prediction is also shifted towards lower pressures, arguing in favor of a gap-driven effect: at lower temperatures, the condition $\lambda = g$ is met for lower pressures than at 4.2 K.

Up to now the temperature was homogeneous over the entire cell since it was imposed by the ^{4}He bath. To proceed, we realized experiments where the sample holder temperature alone was regulated above the bath temperature. The idea is that if no turbulent convection phenomenon takes place (which should be the case at such low pressures), the temperature gradient should be small enough on the scale of g to identify the gas temperature surrounding the NEMS with the sample holder temperature. A crude estimate of the thermal gradient at the level of the NEMS $\delta T/T_0$ (T_0 is sample holder temperature) can be given for the 150 μm sample which was used for temperature measurements: with a cell radius $\approx$ 2 cm and assuming a linear

temperature gradient between the sample holder at T_0 and the cell contour at 4.2 K, the thermal decoupling is roughly $\delta T/T_0 \approx 7 \times 10^{-4}$ at 15 K. This is clearly negligible, and we can consider $T_{gas} = T_0$. In addition, this has been confirmed experimentally: while the surrounding helium bath was cooled down to 1.3 K, we heated the sample holder up to 4.2 K with a power $\sim$ 100 mW while regulating the temperature and measured the 150 µm NEMS damping in the same pressure range as before.

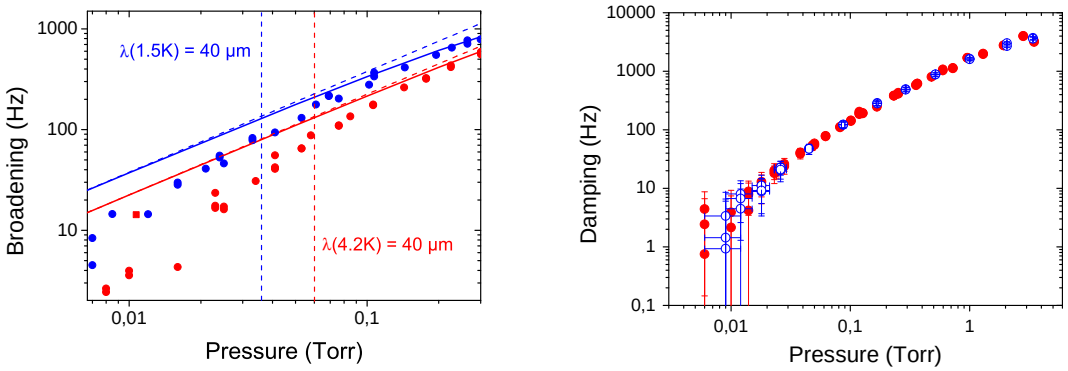

Figure 5.7: left: gas damping measured at 4.2 K (red dots) and at 1.5 K (blue dots) with the 300 µm device. The temperature was homogeneous over the whole cell. The dashed lines mark, for the two temperatures, the condition $\lambda = g$. Right: gas damping measured with the 150 µm device. Red full dots: gas damping measured with a cryostat temperature 4.2 K, with no heating of the sample holder (data shown in Fig. 5.5). Blue empty dots: gas damping measured with the cryostat cooled down to 1.3 K while regulating the sample holder temperature at 4.2 K.

The results for a regulated temperature are found to match perfectly those obtained by simply staying at 4.2 K, as seen in Fig. 5.7 right panel. Therefore we can claim that the properties of the gas near the NEMS are those determined by the sample holder temperature T_0. It demonstrates that we can safely investigate the effect for temperatures higher than 4.2 K using this method.

Our findings are strong arguments in favor of a new regime that manifests when the gas mean free path becomes commensurate with or bigger than the gap between the NEMS and the bottom trench. In other words, this corresponds to a regime where **collisions with the wall become as frequent as collisions between gas particles** for the gas portion in the NEMS region: the NEMS enters the so-called **Knudsen layer** (also sometimes referred to as "kinetic boundary layer" in the literature), of typical spread λ next to a wall, where a reduction of the (effective) viscosity is expected [127].

5.5.2 Fit procedure and results

The data measured on three different samples with rather different sizes show qualitatively similar features if we plot the gas damping contribution normalized to the molecular regime prediction. As noticed above, the discrepancy between the molecular regime prediction and the experimental data seem to become significant around a Knudsen number $\mathrm{Kn} = \lambda/g$ equal to 1. Therefore, we try to fit all the data with the same phenomenological expression, that takes the form of a polynomial fraction in the scaling variable Kn, a so-called Padé approximant $\mathcal{P}(\mathrm{Kn})$. The gas damping is fit with $\Gamma = \mathcal{P}(\mathrm{Kn})\Gamma_{mol}$, where:

$$\mathcal{P}\left(\mathrm{Kn}\right) = \frac{1 + c\,\mathrm{Kn}}{1 + (c - \alpha)\mathrm{Kn} + \dfrac{c}{\alpha'}\mathrm{Kn}^2}. \tag{5.19}$$

Such an expression captures both limits [36]. In the low mean free path limit $g \gtrsim \lambda$ (i.e. around 1 Torr for the 150 µm device), the normalized damping essentially reduces to $1 + \alpha\lambda/g$. In the other limit $\lambda \gg g$, it becomes $\alpha' g/\lambda$. The c factor is merely a parameter that makes the link between the two limits by rounding the shape of the fit. Fig. 5.8 represents the damping normalized to the molecular regime prediction, as

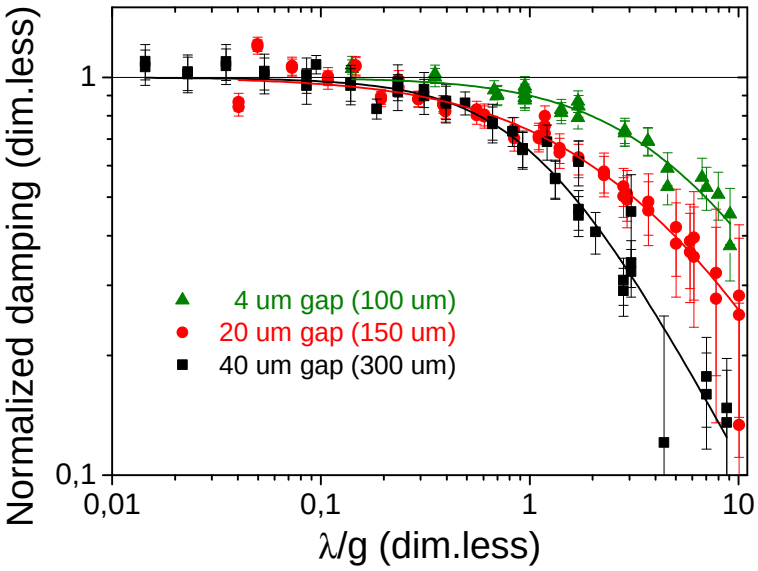

Figure 5.8: gas contribution to the NEMS damping normalized to the molecular regime prediction Γ_{mol} of Eq. (5.18), as a function of the mean free path normalized to the gap λ/g, for the three samples measured throughout the experiment, at 4.2 K. Solid lines are $\mathcal{P}(\mathrm{Kn})$ fits from Eq. (5.19).

a function of a reduced scaling parameter, namely the Knudsen number Kn. All data

sets are fit with the Padé approximant, with different coefficients for each device. We now turn to analyze the dependences of fit coefficients in temperature and gap. To minimize possible experimentalist biases we used three procedures for a fit. An example is shown in Fig. 5.9 for the 150 µm ($g = 20$ µm) device at different temperatures. We first let the computer fit all the data sets with the three parameters α, α', c left free (squares). From this tentative it appears that coefficients α and c are roughly temperature-independent. Then we keep c fixed at the average value of the previous (all free parameters) outcome and let the computer fit α and α' (empty dots). Again, α stays roughly constant, with less spreading around the mean value than with the previous routine. For the last routine c and α are kept constant, with only α' left as a free parameter (triangles). All three routines give results in rather good agreement and lead to $\alpha \approx -0.3$ and $c = 1.2$, for all temperatures and gaps. This proves that the onset of damping reduction is a purely dimensional effect, free from materials or frequency dependence: the obtained scaling appears somewhat universal at first order in the Knudsen number.

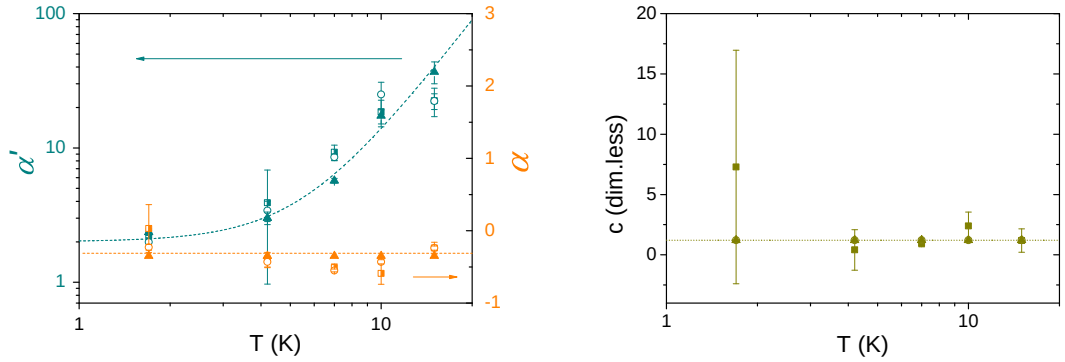

Figure 5.9: left: fit parameters α and α' as a function of temperature for the 150 µm sample with $g = 20$ µm. The different symbols account for the three fitting routines explained in the text. Dashed lines are guides for the eyes. Right: c parameter rounding the $\mathcal{P}$ function between the two asymptotic regimes. The dashed line is set at $c = 1.21$.

Meanwhile, the α' coefficient is found to scale with $1/g$, as shown in Fig. 5.10. Therefore, the normalized damping is **independent** of the gap g in the very low pressure (very high mean free path) limit. This is somehow natural: the mismatch between the wall and the gas equilibrium should be qualitatively set over a distance equal to a few λ. As the distance between the NEMS and the bottom becomes gradually small compared to the gas mean free path, the two lengthscales are not comparable anymore, and as far as the gas properties are concerned, the gap g is not a relevant lengthscale anymore. In fact, we can argue that in this limit the portion of the gas surrounding the NEMS has equilibrium properties that are essentially that of the wall, and therefore, the NEMS is in a sense a **local probe** that is directly impacted by scattering processes

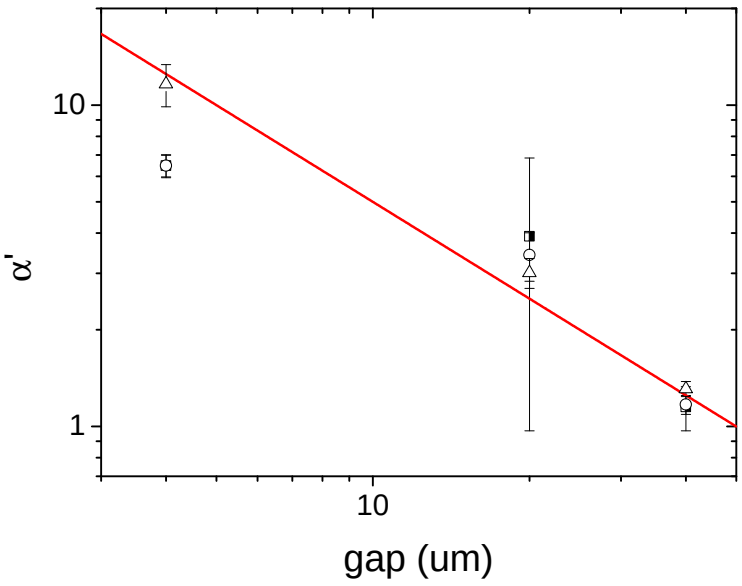

Figure 5.10: fit parameter α' as a function of the gap g between the NEMS and the bottom trench. The different symbols account for the three fitting routines explained in the text. The red solid line is a fit function $\alpha' = 50/g$.

occurring at the wall that establishes its equilibrium. Besides, the coefficient α' shows a huge dependence on temperature (we fit a quadratic + cubic dependence, see Fig. 5.9), which strengthens this hypothesis.

5.5.3 Role of gas adsorption and film growth

As explained above, our measurements point out the role of the Knudsen layer, and thus of the bottom wall, in the gas damping mechanisms. Yet, the boundary and slippage regime discussed in the literature are mostly trying to describe the mechanisms taking place when a temperature gradient is present between the wall and the fluid, or when a flow is present. This is essentially the case discussed above in paragraph 5.4.2, considering the oscillatory flow around the NEMS itself, which could indeed lead to corrections. The phenomenon we discuss here is of another nature: the system is macroscopically at rest in equilibrium, but locally these conditions are broken by the presence of the boundary: if gas particles were undergoing pure specular reflection at the wall, the latter would merely act as a mirror and no change in the thermodynamic and statistical properties of the gas near the wall should occur.

We must therefore invoke the diffusive nature of boundary scattering at the wall, e.g. sticking events, in order to circumscribe the microscopic origin of the effect. Indeed, the fit α' parameter (see Fig. 5.9 right panel) shows a dramatic temperature

dependence, especially significant above 10 K, and since it accounts for processes very close to the wall with respect to the mean free path, it strongly suggests a surface-triggered boundary phenomenon.

It is possible to characterize qualitatively the energy landscape at the wall as a function of temperature through the measurement of the quantity of adsorbed atomic layers. As typical binding energies of helium on a surface are known to be in the $10 - 100$ K range for the first layers, we expect helium atoms to be adsorbed on the NEMS surface at our working temperatures, thus adding a mass δm to the total NEMS mass M. This will result in a change of the resonance frequency $\delta\omega_0$ downwards:

$$\delta\omega_0 = \omega_0\sqrt{\frac{M}{M+\delta m}} - \omega_0 \approx -\frac{\omega_0}{2}\frac{\delta m}{M}. \tag{5.20}$$

One can then monitor the frequency shift as a function of pressure and temperature to compute the number of helium atoms adsorbed on the surface, and then find the typical energy scales involved. At cryogenic temperatures, there is always one solid layer that is well anchored to the NEMS surface, even for our lowest pressures, of typical adsorption energy 70 K [128]. The adsorbed mass is expressed in units of adsorbed helium density (see Fig. 5.11), using the bare ^{4}He atomic mass and the geometric NEMS surface $2l(w+e)$. Knowing the layer density for helium $\rho_{at} = 11.6 \times 10^{18}$ atoms/m^2 [129], we can compute how many layers are adsorbed on the NEMS.

The NEMS surface as well as the bottom trench are rather disordered. For instance, at the NEMS upper side surface Al grains have a typical size 20 µm (see Fig. 5.3). Thus we can expect that adsorbed atoms do not complete uniformly a layer but rather fill stronger binding sites (e.g. at the junction of grains) that are somewhat equivalent to "pores" in a spongy material [130]. We thus found that the adsorption isotherms (completion at a given temperature, as a function of pressure) are well described by the Dubinin-Astakhov (D-A) model, which indeed applies to disordered surfaces. In this model, the number of adsorbed atoms write:

$$N_{ads} = N_m \exp\left[-\left(\frac{k_B T \ln\left(\frac{P_s(T)}{P}\right)}{E}\right)^n\right]. \tag{5.21}$$

Here N_m is the maximal adsorbed quantity at the saturated vapour pressure $P_s(T)$, and E is a characteristic adsorption energy. n is a parameter that depends on the disorder at the surface, referred to in the literature as a "surface heterogeneity factor" [131]. The frequency shift data, converted in adsorbed atoms density for the 150 µm long device, are plotted in Fig. 5.11. Also shown are measurements on the two other devices (see Table 5.2), rescaled to the 150 µm sample dimensions. All data sets are rather well fit in the low pressure region with $N_m = 3$ layers, $E = k_B \times 30$ K, and $n = 1.3$. The values for $P_s(T)$ are taken from reference works [44]. The accuracy of

the model is surprisingly good, given that homogeneity and characteristic energies are likely to differ between the Al-coated side of the NEMS and the bare SiN one. This shall be enough, however, for a discussion on a qualitative basis. Note that above the critical point temperature of ^{4}He ($T_c = 5.19$ K at $P_c = 2.25$ bar), saturated vapour pressure is not defined anymore. Yet, we can still fit consistently the data sets at higher temperatures with $P_s = P_c$. In fact, the sensitivity in P_s is only logarithmic here.

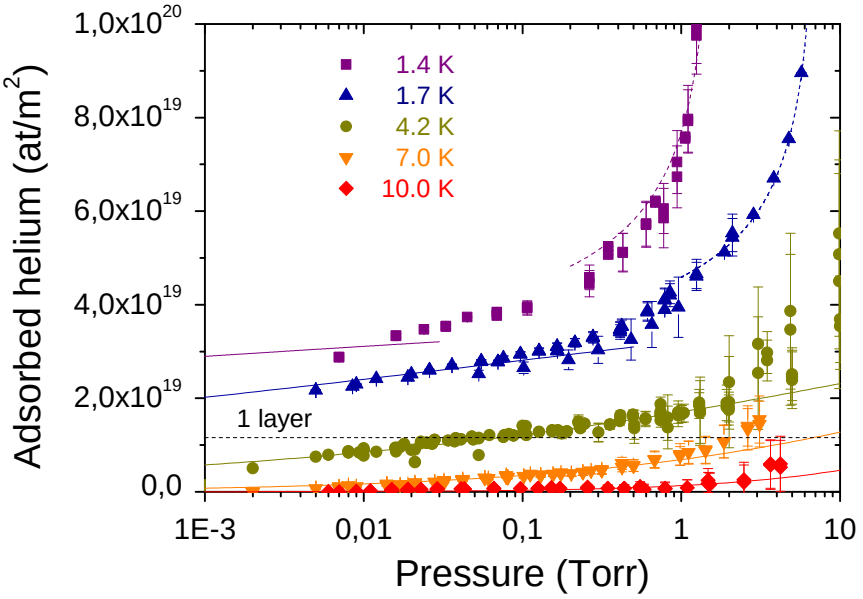

Figure 5.11: added mass on the 150 µm resonator probed by resonance shift measurements, in units of area density of adsorbed atoms, for different temperatures. Solid lines at low pressures follow the Dubinin-Astakhov isotherm model (Eq. (5.21), see text for the fit parameters), while dashed lines at high pressures for temperatures below 2 K are the application of Eq. (5.25) for the unsaturated film growth. Above 2 K, the high pressure growth is interpreted as the reactive component of the viscous flow taking place (see Section 5.3.1).

Some more information on the potential landscape can be obtained: in fact, following Ref. [132] the D-A isotherm can be seen as an averaged property over the disordered surface, which is made of independent, homogenous domains whose adsorption isotherms are simple Langmuir ones: $N \propto (1 - P_0/P)^{-1}$, where P_0 is linked to a characteristic adsorption energy ε. From then on the typical energy obtained in the D-A isotherm is then an average obtained over the distribution of domain adsoption energies [130]:

$$g(\varepsilon) = n\frac{(\varepsilon - \varepsilon_m)^{n-1}}{E^n} \exp\left[-\left(\frac{\varepsilon - \varepsilon_m}{E}\right)^n\right], \tag{5.22}$$

where ε_m is the local minimum of adsorption energy due to intermolecular forces ~ 10 K for ^{4}He atoms. The distribution (5.22) is plotted in Fig. 5.12 for $E = k_B \times 30$ K and $n = 1.3$: it yields a maximum at 20 K with a typical asymmetric spread ~ 40 K around the peak value. This energy scale seems to match the growth of α' with temperature reported in Fig. 5.9 left panel. This strongly suggests a link between the boundary layer effect reported here and the adsorbed surface dynamics. Note however that the isotherm plot in Fig. 5.11 probes the surface of the NEMS device, while the boundary layer depends on properties of the spongy bottom of the trench (e.g. Fig. 5.1 right panel). The analysis done here nonetheless gives us some idea about the adsorption energies involved, and the amount of layers present on surfaces. We will come back to these issues at the very end of the Section.

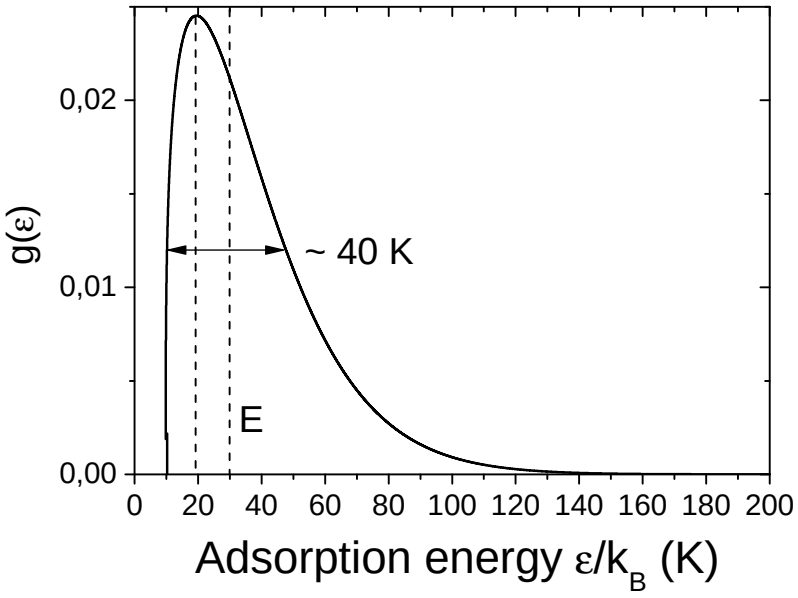

Figure 5.12: adsorption distribution function $g(\varepsilon)$, obtained from Eq. (5.22).

Of course, this description does not hold anymore at high coverages (i.e. $N > N_m$, as surface inhomogeneities are smeared out by the now completed layers. Therefore, the potential seen by the gas atoms is not exactly that of the porous silicon substrate surface (or the NEMS one): the latter is now partly screened by the helium layers. As atoms are adsorbed and layers are completed, the adsorption potential seen by remaining gas atoms venturing near the wall is closer to that created by helium atoms, with a typical energy scale that depends on the number of layers already completed. In addition, layers become more uniformly completed [133]. At high pressures > 0.5 Torr for low temperatures (below typically 4 K), the number of layers is larger and exceeds $N_m = 3$ (see Fig. 5.11). Therefore we can treat the NEMS as a uniform solid

this time, and the interaction potential V_{vw} between a gas atom and the solid at a distance d is of Van der Waals type:

$$V_{vw}(d) = -\frac{2\pi\varepsilon_m n_s a^6}{3d^3} = -\frac{A}{d^3}, \tag{5.23}$$

where $n_s = 60$ atoms/nm^3 is the solid atomic density for aluminum (50 atoms/nm^3 for silicon) and $a = 2.56$ Å the van der Waals atomic radius (similar for silicon). As one layer is about 0.36 nm thick (the helium spacing in bulk [44]), we have $\frac{A}{k_B \times (0.36\ \text{nm})^3} = \alpha_K N_m^3 = 7.73$ K.layers^3. In this experiment we kept a pressure $P < P_s$, and the high coverage situation only applies for temperatures below the superfluid transition at 2.17 K. If the pressure is high enough, an unsaturated film grows: it arises from the competition between the van der Waals force exerted by the surface on the film and gravity. The thickness of this unsaturated film depends on the gas pressure at the level h of the NEMS from the bottom of the cell which is at saturated vapour pressure P_s:

$$P(h) = P_s(T) \exp\left(-\frac{\delta m g_0 h}{k_B T}\right), \tag{5.24}$$

where g_0 is the gravitational field, labeled so to avoid any confusion with the gap g. If one equates the gravitational potential (obtained by inverting the equation above) with the van der Waals potential (5.23), one can obtain the number of adsorbed layers $N = d/(0.36\ \text{nm})$:

$$N = N_m \left[\frac{\alpha_K}{T \ln\left(\frac{P_s(T)}{P}\right)}\right]^{1/3}. \tag{5.25}$$

Here $N_m = 3$ is the value obtained from low coverage fits. The high coverage curves following Eq. (5.25) are represented in Fig. 5.21 with dashed lines, with no free parameters. Note that at these temperatures, the film is superfluid (the so-called Rollin film) and thus creeps over surfaces [44]. However, we do not probe its superfluid properties in this experiment, and data focusing on superfluid properties are not reported in this manuscript.

5.5.4 Interpretation in terms of density reduction near the wall

While signatures of the Knudsen layer manifest clearly and can be correlated to the adsorption dynamics at the wall, we have not explained so far why this dynamics should lead to an effective damping reduction on the NEMS. To get a deeper understanding, even at a qualitative level, it is useful to focus on the distribution of particles in

the vicinity of the wall, since in the ballistic regime the damping is a statistical quantity. With no external forcing, the evolution of the particles distribution $n(\mathbf{r})f(\mathbf{v}_g, t)$ in a given volume $\mathrm{d}^3\mathbf{r}\mathrm{d}^3\mathbf{v}_g$ of the phase space follows the well-known Boltzmann equation:

$$\frac{\partial(nf)}{\partial t} + \mathbf{v}_g.\frac{\partial(nf)}{\partial \mathbf{r}} = \mathcal{C}[nf], \tag{5.26}$$

where $\mathcal{C}$ is the so-called **collision integral**, i.e. the functional gathering the scattering processes that bring the portion of gas in the elementary volume back to thermal equilibrium. It formally writes:

$$\mathcal{C}[nf] = n^2(\mathbf{r}) \iint \mathrm{d}\Omega\mathrm{d}^3\mathbf{v}_{g,1}\,(f'f'_1 - ff_1)\,K(\mathbf{v}_g, \mathbf{v}_{g,1}, \Omega). \tag{5.27}$$

Here K is the so-called **scattering kernel**, which accounts for a scattering process $(\mathbf{v}_g, \mathbf{v}_{g,1}) \rightarrow (\mathbf{v}'_g, \mathbf{v}'_{g,1})$ within a solid angle Ω. The condensed notations read $f^{(\prime)}_{(1)} \equiv f(\mathbf{v}^{(\prime)}_{g(,1)}, t)$. In the steady-state regime, the equation to solve reduces to:

$$\mathbf{v}_g.\frac{\partial(nf)}{\partial \mathbf{r}} = \mathcal{C}[nf]. \tag{5.28}$$

As the dynamics at the wall is very different from that of the gas because of diffusive scattering, there is a mismatch that reflects in the collision integral (5.27). At equilibrium in the bulk gas, the collision integral is equal to zero, from which we deduce the Maxwell-Boltzmann distribution f_M (5.12) as the equilibrium distribution. At the wall in the steady-state regime the collision integral is not zeroed anymore, which implies that the distribution $f \neq f_M$ on the boundary [134].

Therefore, the dynamics at the wall introduces a deviation to the Maxwellian distribution that propagates off the surface within a characteristic length comparable with the mean free path λ. The latter argument is justified *a posteriori* by our experiment, but also qualitatively: if there is a gradient of the distribution, there should be one for thermodynamic quantities that are derived from the distribution through its moments. From this non-equilibrium steady state, the return to equilibrium in the gas is defined by scattering processes that will naturally take place over a typical distance λ.

Note that the deviation from the Maxwell-Boltzmann distribution is not necessarily small. There is currently no exhaustive knowledge of the microscopic mechanisms occurring at the wall, and the statistical description far within the Knudsen layer remains an extremely challenging problem, largely unsolved theoretically. The key feature here is that at the onset of the boundary layer ($\lambda/g \gtrsim 0.1$), the NEMS, which is closer to the bulk spatially, is essentially sensitive to small reminiscences of this gradient, which appear to be universal, since the α parameter is independent of the gap and the cell temperature.

While we do not attempt to solve the Boltzmann equation (5.28), which would be a considerable theoretical challenge far outside the scope of this work, we can use again the approach developed in the previous section, in paragraph 5.4.2, to describe the onset of the damping reduction, from a modification of the equilibrium distribution f_M. This is justified insofar as the behaviour seems universal and the departure from the molecular prediction is not too big in the region $\lambda/g \gtrsim 0.1$. We use the polynomial correction (5.14) to the Maxwell-Boltzmann distribution, and keep average velocities $v_{x,0}, v_{y,0}, v_{z,0}$ in the expansion. The coefficients $a_{i...}$ are not explicited so far, but they should be space-dependent, as the average velocities should also. As seen earlier, it is possible to connect these coefficients through sum rules [125]. Moreover, the average kinetic energy defines the temperature through $m_g\overline{|\mathbf{v}_g - \mathbf{v}_{g,0}|^2}/2 = 3k_BT/2$. This relation imposes additional sum rules on coefficients because of the averaging. In addition, symmetries of the problem are such that there should not be any dependence of thermodynamic quantities on y, z. Very conveniently, the first three moments of the collision kernel are zeroed because of mass, momentum and energy conservation, which leads to the well-known transport equations. The mass conservation equation is the moment of order zero of Eq. (5.28) projected along $\mathbf{x}$ and writes:

$$\frac{\partial}{\partial x}\left(\int f(v_x, v_y, v_z) v_x n(x) \mathrm{d}^3\mathbf{v}_g\right) = 0. \tag{5.29}$$

In fact, from the application of sum rules, this moment of order zero is already zero. The first moment gives the conservation of momentum along the $\mathbf{x}$ direction:

$$\frac{\partial}{\partial x}\left(\int f(v_x, v_y, v_z)(m_g v_x) v_x n(x) \mathrm{d}^3\mathbf{v}_g\right) = 0. \tag{5.30}$$

The second moment yields the conservation of energy:

$$\frac{\partial}{\partial x}\left(\int f(v_x, v_y, v_z)\left(\frac{1}{2}m_g v_x^2\right) v_x n(x) \mathrm{d}^3\mathbf{v}_g\right) = 0. \tag{5.31}$$

This set of transport equations, through the application of sum rules, leads to 2 equations on only four independent variables among the $a_{i...}$ coefficients, which are functions of x, identified to g the position of the NEMS in the vicinity of the bottom (at which $x = 0$). These four coefficients are the only ones relevant to our problem, when the expansion 5.14 is truncated at third order. The next step is to write thermodynamic quantities as slightly perturbed at the onset of the Knudsen layer $n = n_0 + \delta n(x)$ and $T = T_0 + \delta T(x)$. From the hierarchy of conservation equations (5.29),(5.30),(5.31), we can then link the quantity $\delta n/n_0$ to $\delta T/T_0$ and the $a_{i...}$.

Coming back to the Boltzmann equation, we can follow the Chapman-Enskog method [135] for the left-hand side term of Eq. (5.28): the $a_{i...}$ coefficients are de-

veloped in series of $\mathrm{Kn} = T/x$: $a_{i...} = b_{i...}^{(1)}\mathrm{Kn} + b_{i...}^{(2)}\mathrm{Kn}^2 + ...$ Here, coefficients $b_{i...}^{(k)}$ do have a physical meaning: they express the near-field induced deviation to bulk equilibrium due to the scattering processes at the wall. With such a definition, $a_{i...}$ coefficients will be nonzero at the onset of the Knudsen layer, and zero in the bulk when $x \to +\infty$. The temperature gradient is also developed as $\delta T/T_0 = d_1\mathrm{Kn} + d_2\mathrm{Kn}^2 + ...$

Obviously, the knowledge of the collision integral is required from now on. The problem can be defined in a self-consistent way by also writing the collision integral in powers of the velocity field, with coefficients that are also powers of Kn:

$$\begin{aligned}\mathcal{C}[nf] \approx n_0\sqrt{\frac{m_g}{2\pi k_B T}}\exp\left[-\frac{m_g(v_x - v_{x,0})^2}{2k_B T}\right] \\ \times \Big[\frac{\kappa_1(\mathrm{Kn})(v_x - v_{x,0})}{\lambda} \\ + \frac{\kappa_2(\mathrm{Kn})\left(\dfrac{m_g}{2k_B T}\right)^{1/2}(v_x - v_{x,0})^2}{\lambda} \\ + \frac{\kappa_3(\mathrm{Kn})\left(\dfrac{m_g}{2k_B T}\right)^{3/2}(v_x - v_{x,0})^3}{\lambda} + ...\Big] \quad (5.32)\end{aligned}$$

with $\kappa_i(\mathrm{Kn}) = \nu_i^{(1)}\mathrm{Kn} + \nu_i^{(2)}\mathrm{Kn}^2 + ...$ Such a development seems licit, since we are close to the bulk with $\mathrm{Kn} \lesssim 0.1$, where the collision integral should be zero as the distribution tends towards f_M. In addition, constraints can be obtained on these parameters, using the fact that the three first collision kernel moments should be zero (conservation laws). Using this phenomenological approach permits to overlook the scattering kernel, which is elusive since we do not know in detail the wall's dynamics: the only quantities one can extract are characteristic energies, as shown in the previous paragraph, and are meant to bring only qualitative arguments here.

From then on, the problem is self-consistent if we truncate expansions at order $n+1$ in velocities and order n in Kn on the left-hand side of Eq. (5.28), $n+2$ in velocities and $n+1$ in Kn in the collision integral $\mathcal{C}[nf]$. We chose to stop at $n = 3$, after which the problem is not easy to handle regarding the calculation. The full procedure is tedious and carried out in Mathematica, and we finally obtain that the average velocity field is zero: $\overline{\mathbf{v}}_{g,0} = 0$, while all introduced coefficients can be expressed as functions of parameters $b_{i...}^{(j)}$.

The next step is to compute macroscopic parameters, evaluated at the position of the NEMS $x = g$, i.e. $\mathrm{Kn} = \lambda/g$. We already have $\delta T/T_0$ and $\delta n/n_0$. Meanwhile the kinetic pressure tensor component P_{ij} is by definition the flow of momentum $m_g v_i$ in the direction $\mathbf{j}$: $P_{ij} = \iiint n m_g v_i v_j f(v_x, v_y, v_z)\mathrm{d}^3\mathbf{v}$, from which we obtain the thermodynamic pressure $P = (P_{xx} + P_{yy} + P_{zz})/3$. Note that in the end we still have

$P = n_0 k_B T$, but each of the tensor components does not necessarily follow the same law. Again, for symmetry reasons only $P_{xx} = P_{xx,0} + \delta P(\mathrm{Kn})$ should be affected, with $P_{xx,0}$ the bulk value. The calculation shows that:

- the kinetic pressure field remains actually constant, i.e. $\delta P(\mathrm{Kn}) = 0$. This is reassuring, as a deviation would mean that in general no manometer could be accurate as soon as the surface is not perfectly specular.
- there is a **temperature gradient**, only quadratic in Kn and $b_{i\ldots}^{(j)}$ coefficients, which should thus be weak enough so it can be disregarded in the first place. Note that this temperature drop is known to occur in the boundary layer, and takes the form of a temperature jump at the wall, since the wall itself should be thermalized at T_0 [125, 134].
- the density gradient is a **first order** correction in the Knudsen number, and in the $b_{i\ldots}^{(n)}$:

$$\frac{\delta n(\mathrm{Kn})}{n_0} = -\frac{1}{2}\left[2b_{xx}^{(1)} + 6b_{xxxx}^{(1)} + \left(b_{xxyy}^{(1)} + b_{xxzz}^{(1)}\right)\right]\mathrm{Kn}. \tag{5.33}$$

This last point shows that the observed reduction of damping is the result of a **rarefaction phenomenon** (see schematic in Fig. 5.13), induced by the dynamics at the wall which translates into a deviation to the Maxwell-Boltzmann distribution f_M in the Knudsen layer. As the effective density in the gas is reduced, so is the number of collisions on the surface of the NEMS: this ultimately explains the reduction of damping observed in our experiments. Indeed, since the damping rate calculation involves an average over the particles distribution, we can write an **effective near-field** coefficient ϑ_{nf} instead of ϑ in the damping rate expression (5.18), which incorporates the density reduction term $\delta n(\mathrm{Kn})/n_0$ to match the observed damping reduction:

$$\vartheta_{nf}(\mathrm{Kn}) \approx \vartheta + \underbrace{\frac{1}{2}\left[s + (1-s)\left(\frac{\pi}{4}\sqrt{\frac{T_N}{T_0}} + \frac{1}{2}\right)\right]\frac{\delta n(\mathrm{Kn})}{n_0} - \frac{1}{8}(1+s)b_{xxxx}^{(1)}\mathrm{Kn}}_{\equiv\, \vartheta\alpha\mathrm{Kn}}. \tag{5.34}$$

It goes without saying that the expression into brackets in Eq. (5.33) can only constitute a single free parameter, because of the lack of information on scattering processes at the wall: thus we recover the $\mathcal{P}$ function in the low Knudsen number limit, through $\vartheta_{nf} \approx \vartheta(1+\alpha\mathrm{Kn})$, with alpha the fit parameter already introduced in section 5.5.2 and Eq. (5.34). Therefore, assuming $s = 0.5$ holds in the whole temperature range and taking again $T_N \approx T_0$, only the $b_{i\ldots}^{(1)}$ are free parameters to describe the damping reduction, which accounts for surface scattering. The link between the measured effect and surface properties suggests that it could depend on the sample. Yet, the fits presented in paragraph 5.5.2 suggest that the deviation at first order, i.e. the α parameter, is independent of the device. Nevertheless, we can argue that all three devices are made

of the same materials (SiN thin film on silicon substrate), and suspended the same way with the XeF_2 etching, which results in a similar spongy bottom for all the devices (see Fig. 5.1). This may explain the absence of discrepancy in α from one sample to the other. The other explanation would be that the first order deviation is not affected by the details of the diffusive scattering mechanisms at the wall, making this term truly **universal**. This hypothesis is favored by the fact that we obtain an α which is temperature independent. This suggests once more that the coefficients $b^{(1)}_{i...}$ originate only from a mismatch in the distribution which has nothing to do with temperature, i.e. with the excitations at the wall, since these excitations depend on temperature. Thus, higher order coefficients $b^{(2),(3)..}_{i...}$ **must depend** on temperature and bear the information on the wall excitations, since α' strongly depends on temperature.

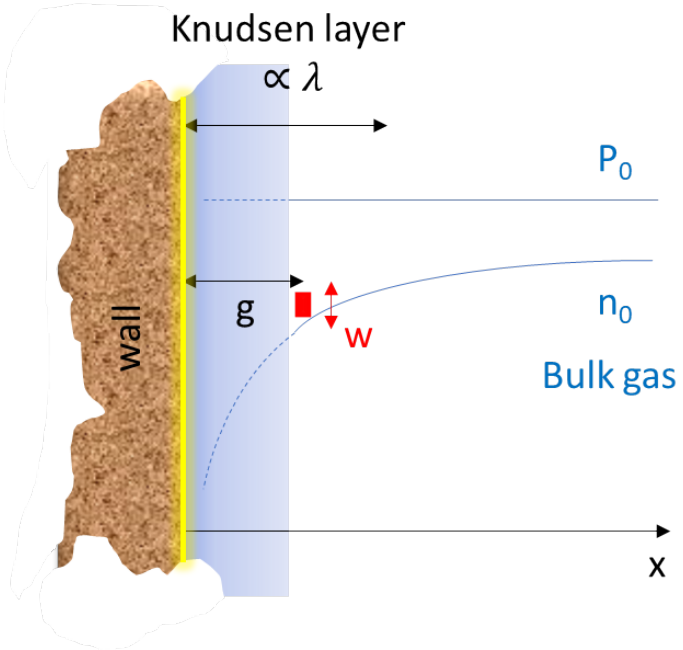

Figure 5.13: schematics of the physical situation probed by the NEMS when entering the Knudsen layer. The brown trench is the bottom of the sample, clamped and thermalized to the sample holder. The shaded region corresponds to the situation where our expansions fail, and more involved theory and/or simulations are required.

Note that the damping reduction is almost proportional to the density reduction, within an additional term $-(1+s)b^{(1)}_{xxxx}\mathrm{Kn}/8$ for the former damping reduction. Since this term comes from an expansion at order 4 in velocities, one can argue that it should be small compared with the lower order coefficient $b^{(1)}_{xx}$ appearing in the density reduction. This leads us to the introduction of an effective density defined in the Knudsen regime (when $\lambda > g$), following Eq. (5.18):

$$n \approx \frac{m\Gamma_{mol}\mathcal{P}(\mathrm{Kn})}{2\vartheta m_g w \int \Psi^2(z)\mathrm{d}z} = n_0\mathcal{P}(\mathrm{Kn}). \tag{5.35}$$

This recalculation operated on the measured data is represented for three different temperatures in Fig. 5.14 and fit with $n = n_0\mathcal{P}(\mathrm{Kn})$. Therefore, deep in the boundary layer, that is, close to the wall, the density should evolve as $n_w \approx n_0\alpha' g/\lambda$, i.e.:

$$n_w \propto \alpha'(T_0)P^2/T_0^2. \tag{5.36}$$

This anomalous pressure dependence is the dashed asymptote represented in Fig. 5.14 in the low pressure regime for each temperature [36].

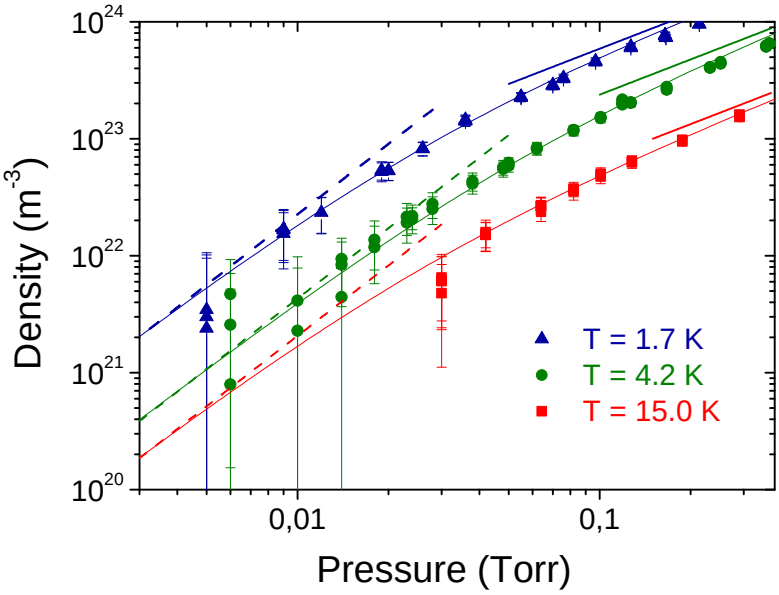

Figure 5.14: effective density recalculated from the damping data at 3 different temperatures as a function of the cell pressure, for the 150 µm device. Thin solid lines are calculated with the fits from Eq. (5.19), while asymptotes are shown in the low ($\propto P^2$) and high ($\propto P$, bulk density n_0) pressure regimes.

Eq. (5.36) is in fact a powerful result, because of the huge dependence of α' in temperature (Fig. 5.9 left panel). If α' were temperature independent, the transition range between the anomalous P^2 and the standard $\propto P$ regime would increase linearly with the temperature, since the physics would be set only by the mean free path $\lambda \propto T_0/P$. The observed behaviour is more complex: at 15 K, the density reduction is still close to the standard bulk prediction even at rather low pressures (below 0.1 Torr), and the anomalous regime is not truly reached: the cusp is drifting up, but is less salient,

and the data would reach the asymptote at even lower pressures. We believe that it is the result of the competition between the mean free path increase and the dramatic change of energy landscape at temperatures comparable with the typical adsorption energies, which is monitored through the strong dependence of α' in temperature (see Fig. 5.9 left panel). We thus stress out the fact that this effect is truly visible only at **low temperatures**, meaning temperatures smaller/comparable to the adsoption energy. It originates from mechanisms that take place at low energy scales, and which should be suppressed at room temperature. Our observations regarding the transition range from $n \propto P$ to $n \propto P^2$ might explain why higher temperature experiments failed to reproduce this Knudsen layer signatures [136]: even though this effect should be present, it would manifest itself at pressures that are not attainable experimentally.

Another aspect of this scaling near the wall is that at very low pressures the damping does not depend on the gap g anymore. In Fig. 5.15, we indeed see that the damping data (rescaled in units of effective density) for all three devices in the asymptotic limit collapse on the $n \propto P^2$ curve. In that sense, we believe that in this limit we are truly sensing the wall's properties, and that the anomalous pressure dependence is a direct signature of its dynamics. This last point highlights the advantage of using a nanomechanical string within the Knudsen layer. Indeed its cross-dimensions are much smaller than the relevant lengthscales. Therefore, while the Knudsen layer is an out-of-equilibrium property (since it involves gradients of thermodynamic quantities), a local equilibrium can be defined at the level of the NEMS, which then acts as a **non-invasive** probe for a non-equilibrium medium.

5.6 Conclusion and prospects

Summary of the results

The aim of the measurements reported in this Chapter was to characterize one ubiquitous damping source for nanomechanical devices, namely the friction due to the fluid in which it is immersed. In particular, the NEMS small cross-dimensions make it particularly sensitive to features that are otherwise negligible with larger oscillators, such as slippage. In contrast with measurements performed in air at room temperature, we realized a model experiment were an almost ideal gas was used (^{4}He around a Kelvin), which properties are tabulated. We thus have measured the gas damping contribution by varying the pressure in the experimental cell over five orders of magnitude and the temperature between 1.5 and 15 K, thus tuning considerably the gas mean free path. At low pressures when the gas becomes rarefied, i.e. has its mean free path comparable with the NEMS cross-dimensions, slippage features become visible for the NEMS, and for even larger mean free paths (even lower pressures), a description relying on kinetic theory for a ballistic gas accounts for the damping properties. Unexpectedly, we observed a reduction of the damping up to one order of magnitude below the simple

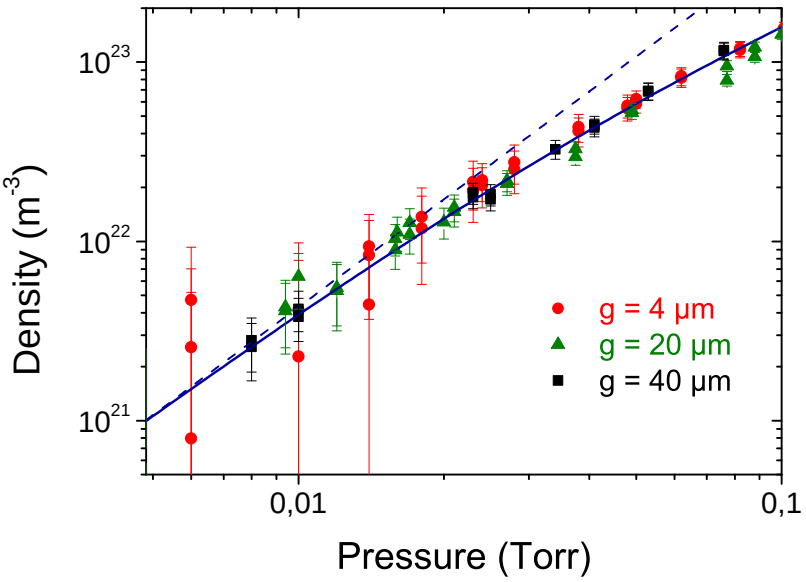

Figure 5.15: effective density as a function of pressure for the 3 different devices, i.e. 3 different gaps, for the same temperature $T_0 = 4.2$ K. The solid line is the application of Eq. (5.35) for Kn defined with $g = 40$ µm, while the dashed line is the low ($n \propto P^2$) pressure asymptote.

ballistic prediction. Possible experimental artefacts have been ruled out by measuring this deviation for three different samples, in two cryostats having different configurations. We interpret this reduction as a finite-size effect due to the proximity of the bottom trench when the mean free path is comparable with or bigger than the distance between the NEMS and the bottom trench. We show that this geometric region, referred to in the literature as the Knudsen layer, exists because of the diffusive scattering processes occurring at the wall for incoming gas particles, and qualitatively put an energy scale on them by monitoring the gas adsorption on surfaces for different temperatures and pressures. We show with a qualitative transport model that these processes create a non-equilibrium region near the wall where the gas statistical properties, and thus its thermodynamic parameters, are renormalized. The most striking feature is a gas density reduction near the wall, which causes directly the damping reduction. We also emphasize the crucial role played by low temperatures, which favor adsorption mechanisms. These measurements demonstrate the importance of surface coatings, while showing that the NEMS can be used as an efficient near-field probe for surface science.

Prospects

Obviously, many aspects have been overlooked, which deserve consideration: firstly, the transition range between the continuous fluid description and the statistical one, and its consequences on friction, still lacks of a universal description beyond the slippage correction, despite recent investigations [124, 105, 106]. Meanwhile, more quantitative information might be obtained on surfaces by combining our measurements with AFM studies which could detail the granular structure at the NEMS surface or the spongy one at the bottom.

In addition, the sensor aspect was not exploited further from computing the number of adsorbed atoms. With a better resolution one could push it to study the structural properties of the formed film, as proposed in Ref. [137], or the coupling between the resonator and the film at the single excitation level, as proposed in Ref. [138]. Besides, our study was restricted to a Helium gas. It instantly comes to mind that the same experiment could be done with a different gas, as what was done in Ref. [136] at higher temperatures, or with a liquid [139]. Since we showed the crucial role of low temperatures, however, this appears to be difficult: most elements will be condensed at helium temperatures, with the exception of hydrogen at 20 K. Such an experiment thus requires an update of the apparatus in order to be able to measure at this temperature while operating in safe conditions.

Finally, a most exciting endeavour is the use of a nano-probe to investigate yet unknown mechanisms in quantum fluids such as superfluid ^{4}He or ^{3}He. Some preliminary results have been obtained in ^{4}He, which are not shown in this manuscript. Other recent results have highlighted the potential of nanobeams for such purposes, through the mapping of the superfluid transition in ^{4}He [140]. A collaboration with Lancaster University has allowed to immerse our NEMS in superfluid ^{4}He down to mK temperatures, revealing the damping due to the superfluid excitations [141]. The case of superfluid ^{3}He is even more appealing, because of its much richer phase diagram [142]. Indeed, superfluid ^{3}He is a BCS superfluid (atoms form Cooper pairs) with a coherence length ("size" of a Cooper pair) typically lying in the $10 - 100$ nm range. Using a probe with cross dimensions comparable with the coherence length could open a new range of investigation on the intimate structure of superfluid ^{3}He, with an unprecedented accuracy [143]. The results shown in this Chapter also highlight their potential to study the superfluid in confined geometries, where elusive topological features such as Majorana states are theoretically predicted to exist [144]. This of course requires a huge experimental development far beyond the results of this Chapter, with e.g. the use of a nuclear demagnetization stage [44, 51] to cool ^{3}He down to 100 μK, where most of its thermal excitations are removed.

5.7 Résumé en français

Dans ce chapitre nous étudions l'interaction entre un résonateur nano-mécanique et un fluide simple, ici l'hélium 4 gazeux, dans la perspective d'étudier les fluides quantiques tels que l'^{4}He superfluide et l'^{3}He liquide et superfluide, à des échelles de longeur jusqu'ici inexplorées. Nous mesurons le taux de dissipation mécanique dû à l'interaction avec le fluide de 10 Torr à 5 mTorr, et nous développons différents modèles qui capturent avec un minimum d'hypothèses les résultats sur 2 ordres de grandeur en pression: de 100 Torr où le fluide est bien décrit par les équations de l'hydrodynamique classique, jusqu'à $\sim$ 1 Torr dans la limite du gaz raréfié, où nous faisons appel à une description ballistique qui explique la dissipation par le transfert d'impulsion des atomes du gaz au résonateur lors de chocs aléatoires. Une correction au régime hydrodynamique prenant en compte le glissement du fluide sur les parois du résonateur permet de décrire le début de la transition entre les deux régimes. Aux plus basses pressions, nous observons une déviation par rapport à la prédiction du régime moléculaire, reportée dans [35]. Cette déviation est observée pour des températures allant de 1.4 K à 15 K pour trois échantillons de différentes tailles, et dans deux cryostats aux caractéristiques différentes, ce qui confirme que le phénomène est reproductible.

Nous remarquons que la déviation apparaît dans tous les cas pour un libre parcours moyen λ du gaz qui devient comparable à la distance g entre la sonde nano-mécanique et le fond de l'échantillon. Le rapport entre la courbe expérimentale et la prédiction du régime moléculaire suit une loi d'échelle simple du nombre de Knudsen λ/g lorsque $0.1 < \lambda/g < 1$, qui semble universelle. Nous développons un modèle phénoménologique qui explique la déviation par rapport au régime moléculaire par les processus d'interaction entre les particules du gaz et le mur du fond. La nature diffusive de cette interaction, déjà soulignée aux plus hautes pressions pour expliquer le glissement, indique que les particules proches du fond vis-à-vis du libre parcours moyen sont en équilibre avec le mur plutôt qu'avec le gaz en volume. Ces processus diffusifs sont qualitativement sondés pour plusieurs températures à travers le dépôt de couches adsorbées de gaz sur le NEMS, qui augmentent sa masse et donc diminuent sa fréquence. Nous mettons en lumière le rôle du potentiel d'adsorption, prédominant aux basses températures. La nature même du paysage énergétique au mur a donc pour conséquence une désadaptation des propriétés d'équilibre du gaz près du mur, donc une déviation à la statistique d'équilibre de Maxwell-Boltzmann caractéristique des propriétés en volume. Cette déviation s'établit sur une distance de l'ordre de λ en partant du mur, au-delà de laquelle les collisions sont plus fréquentes entre atomes issus du volume qu'avec des atomes issus de la zone proche du mur, dite couche de Knudsen. Dans la couche de Knudsen, en revanche, les collisions sont fréquentes entre particules du gaz hors équilibre et le NEMS voit donc une statistique du gaz modifiée lorsque $g \sim \lambda$: nous montrons par la hiérarchie des équations de conservation (densité, quan-

tité de mouvement, énergie) et une résolution approchée de l'équation de Boltzmann utilisant la méthode de Grad-Chapman-Enskog (développement des quantités thermodynamiques et de l'opérateur de collision en $\lambda/x, x \equiv g$ et en les vitesses d'atomes), qu'une raréfaction du gaz a lieu dans la couche de Knudsen, avec une dépendance en pression de la densité effective du gaz asymptotiquement quadratique plutôt que linéaire comme c'est le cas en volume. Cette raréfaction a pour effet mesurable une réduction de l'amortissement mécanique par le gaz du NEMS : ce dernier agit comme une sonde non-invasive du milieu hors-équilibre du fait de ses très petites dimensions transverses.

Chapter 6

Internal energy relaxation and frequency noise in nano-mechanical systems

Contents

6.1 Introduction

The last Chapter of this manuscript focuses on intrinsic sources of mechanical damping and frequency noise. It is motivated by a puzzling fact: the Q factor of nanomechanical oscillators, that is, the ratio between the stored energy and the dissipated energy over an oscillation cycle, is found to roughly decrease with the decreasing volume [145]. While proving a major limitation for applications (more energy is required to enable motion if the Q factor is low) as well as for studies of quantum mechanical effects (a good Q factor is needed to resolve tiny effects), it also poses very fundamental questions: such features must be caused by effects that take place at mesoscale, as the competition between reduced dimensions and the typical lengthscales involved in these processes becomes significant.

To address this process, we remove all known external contributions (e.g. loading [53], or gas [36]) and take advantage of low temperatures, where already known multiphonon processes are suppressed, leaving less and less uncontrolled thermally activated microscopic degrees of freedom [43]. In the same spirit, internal spectral diffusion processes activated by temperature, such as the one described in Chapter 3 are negligible. Yet, we will see that mechanisms that limit the NEMS lifetime and coherence still exist at low temperatures. These are commonly assumed to be some sorts of defects in the materials that can transit between equivalent position states, thus causing retarded stress response to a strain perturbation, hence dissipation. In nanomechanical structures, there are only a handful of studies attempting to clarify their role, which is made even more unclear due to the size reduction. We will see in this chapter that these defects might also explain internal frequency noise features by measuring not only the damping, but also frequency fluctuations at slow timescales thanks to a newly developed technique. Thus, we begin with a detailed account on how this technique is used and applied to "high" (4 K) temperature frequency fluctuations. Then, in order to investigate more their microscopic origin, we take advantage of the dilution temperatures to cool the NEMS down to 10 mK, where the behaviour of these hypothetical defects is thought to be dominant and their signatures on the damping striking, even though complexity (or physical richness) is added by the metallic layer of the NEMS. We thus compare our damping data to frequency noise measurements made in this range and discuss a possible mechanism.

6.2 Measuring intrinsic frequency noise

6.2.1 Dynamical bifurcation as a tool to measure frequency noise

To address intrinsic frequency noise we use a technique adapted from what was proposed in Ref. [12]: since the jump associated to a bifurcation event is sharp by

contruction, the bifurcation frequency is extremely well defined, with a resolution arbitrarily set by external, user-defined parameters. These bifurcation frequencies can be linked readily to resonance frequencies. Indeed the bifurcation frequency on the upper branch writes:

$$\omega_{bif,\uparrow} = \omega_0 + 2\beta|x_{bif,\uparrow}|^2 - \sqrt{\left(\beta|x_{bif,\uparrow}|^2\right)^2 - \frac{\Gamma^2}{4}}. \tag{6.1}$$

The case of the lower branch is slightly more involved. As one increases the driving force, the lower branch amplitude at its bifurcation point $x_{bif,\downarrow}$ initially decreases below x_s, and the bifurcation frequency follows the same law as the upper branch bifurcation frequency, see Eq. (6.1). Once $x_{bif,\downarrow} = 3^{1/4}x_s/\sqrt{2}$, a turning point is reached and increasing the driving force results in an increase of $x_{bif,\downarrow}$. In that case, the bifurcation frequency writes:

$$\omega_{bif,\downarrow} = \omega_0 + 2\beta|x_{bif,\downarrow}|^2 + \sqrt{\left(\beta|x_{bif,\downarrow}|^2\right)^2 - \frac{\Gamma^2}{4}}. \tag{6.2}$$

For large displacements, the upper bifurcation frequency merges asymptotically with the resonance frequency that shifts as in Eq. (2.70) (reminder: $\omega_{bif,\uparrow} \approx \omega_0 + \beta x_{bif,\uparrow}^2$), while the lower bifurcation frequency follows asymptotically $\omega_{bif,\downarrow} \approx \omega_0 + 3\beta x_{bif,\downarrow}^2$. A representation of the bifurcation frequencies diagram is shown in Fig. 6.1. The key message is that there is a simple correspondence between both bifurcation frequencies and the resonance frequencies through Eqs. (6.1) and (6.2), and therefore, measuring the bifurcation frequency fluctuations is a way to access frequency noise on ω_0 if we assume that thermal fluctuations on position are small, which is the case at 4 K, and that force or damping fluctuations are negligible, a point which shall be discussed explicitly below. A practical consequence is that the bifurcation frequency cannot be defined with a better resolution than that obtained for the resonance frequency.

We performed experiments measuring the statistics of the two bifurcation points mostly on a 250 µm high stress SiN device. The procedure to measure the bifurcation frequency noise is schematized in Fig. 6.2: for the upper branch, the frequency sweep starts from low frequencies with a large sweep step and a high speed to enable reasonable measurement time, up to about half the hysteresis: from then on, the step is set at a low enough value so as to minimize sampling noise on the resulting bifurcation frequencies, and the sweep is done at a speed $\sim 0.1-1$ Hz/s enough to be in an adiabatic regime. The last point is important, as it is known that too large speeds exacerbate escape events from the metastable state, which are not bifurcation events [42]. We have verified that for speeds up to one order of magnitude different from the reference one used, the results were identical within our error bars. When the bifurcation event

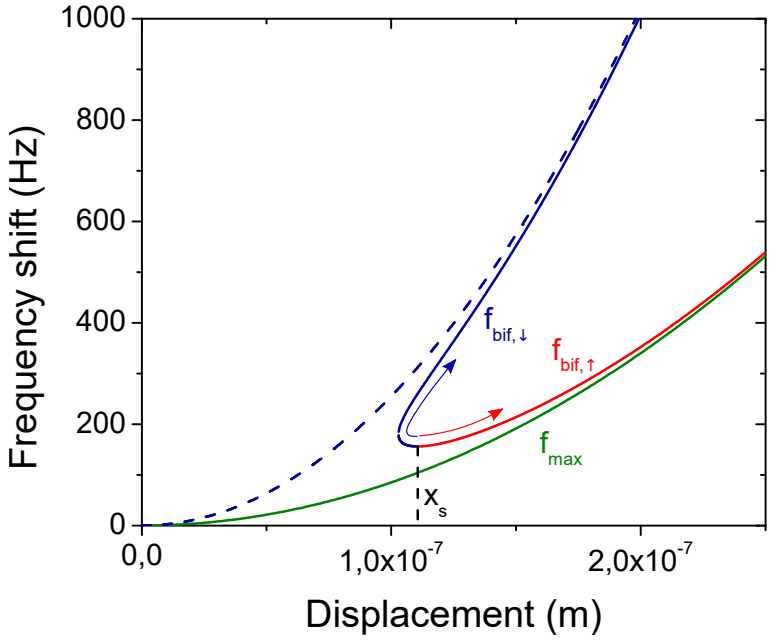

Figure 6.1: Shift of the resonance frequency and diagram of the bifurcation frequencies as a function of the motion amplitude, with the parameters of the 250 µm long NEMS. The arrows indicate the direction of the evolution of bifurcation frequencies along with an increase in the applied force. The red solid line is the application of Eq. (6.1). The blue solid line is made of two parts. Beyond the turning point when following the arrow, the line is the application of Eq. (6.2). Between x_s and the turning point, it is simply Eq. (6.1) applied to the lower branch bifurcation frequency. The green solid line is the Duffing shift of the resonance frequency, following Eq. (2.70). The blue dotted line is the asymptotic behaviour of $\omega_{bif,\downarrow}$ (see text).

occurs, the amplitude switches sharply from the metastable state (high amplitude) now made unstable to the only remaining stable one, which is a low amplitude one: as the amplitude goes below a user-fixed threshold value, the frequency at which the amplitude crosses the threshold is recorded, and the frequency sweep is stopped. The sequence is then repeated, and a track and a histogram of bifurcation frequencies is eventually built. Therefore, we have an access to the resonance frequency noise, as discussed above. We checked that the procedure was threshold-independent as long as the threshold remains within the amplitude region between the two states.

Besides, another source of frequency fluctuations could come from the jitter on the internal clock of the generator, due e.g. to room temperature fluctuations. We characterize it using one generator's signal on the input port of the lock-in amplifier while using another identical generator as a reference signal. Once the certain shift due to the discrepancy between the two reference clocks is corrected, we observe a phase drift $\sim$ 1 mHz over a few minutes at 1 MHz, and $\sim$ 10 mHz over a few minutes at 10 MHz. Assuming the two generators undergo a similar phase noise, we can assume

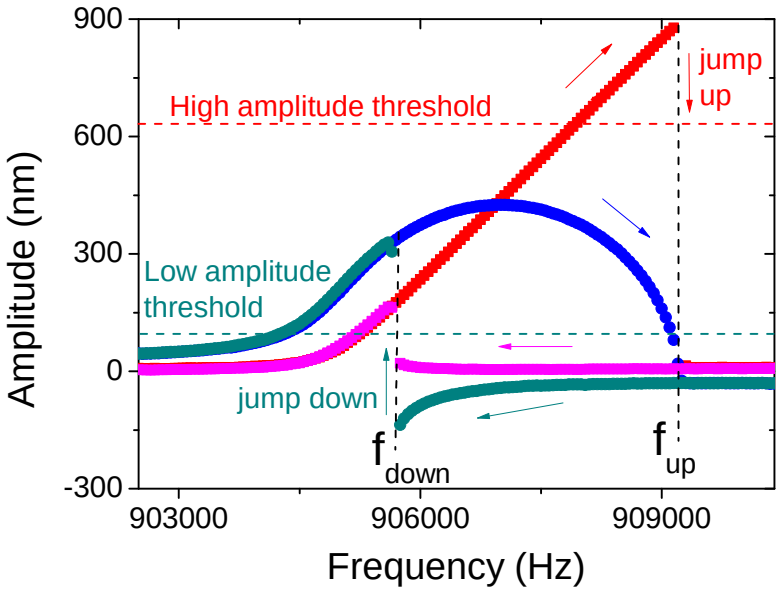

Figure 6.2: Bistable resonance line, with markers used in defining the procedure (threshold and jumps, see text). This resonance line corresponds to a force $F_0 = 81$ pN applied to our 250 µm device, measured at 4 K in a 1 T field.

that the latter is evenly distributed, which leads to a frequency noise in the ppb range, that is, two orders of magnitude below the lowest frequency noise values reported in our experiments.

The procedure allows to record a bifurcation frequency with an arbitrary precision, with measurement times ranging from 10 s to 1 min, and is repeated over a few hours to acquire enough statistics.

Note that we described the measurement operated with the upper state branch, i.e. with the upper bifurcation frequency and higher amplitude. Obviously, it can be operated without supplementary effort on the lower state branch by reversing the protocol. A typical frequency noise track taken while operating on the lower branch is shown in Fig. 6.3, with a reference frequency (the average one) subtracted. From such a track one can extract a few key informations, which are described below.

6.2.2 Analysis procedure and spectral features

A few steps are necessary to extract information from a frequency noise track. A typical frequency noise such as in Fig. 6.3 indeed features fast jumps, on the order of the measurement times, but also slow drifts that make a brute force estimate of the noise magnitude unreliable since they forbid reproducible measurements. First we can obtain a quantitative spectral information by performing a Fast Fourier Transform (FFT) on

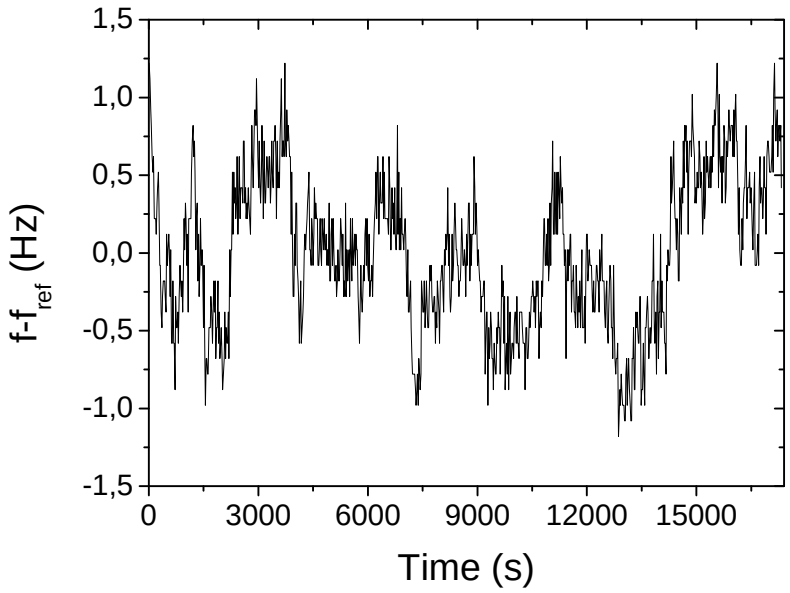

Figure 6.3: typical frequency noise track, taken over about 4 hours, with a step 0.03 Hz. Down sweep measured on the 250 um device, for the setup of Fig. 6.2.

the measured signal autocorrelation. This yields the frequency fluctuations spectrum $S_f(\omega)$. The power spectral density associated to the frequency noise displayed in Fig. 6.3 is shown in Fig. 6.4.

The spectrum clearly is that of a so-called **non-stationary noise**, fit with a $1/f^{1+\mu}$-type law, where μ is an exponent smaller than 0.5. Possible origins of such a noise will be addressed later, but for the time being, it makes the problem a little harder: one cannot estimate precisely a frequency noise magnitude by integrating the spectrum (which yields the variance), as this integral strongly depends on the time over which a track is taken: this measurement time imposes a low cut-off frequency ω_{low}. Besides, the sampling time (time between two neighbour frequencies) also imposes a high cut-off frequency ω_{high}, even though it does not crucially affect the integral here since the weight is bigger at low frequencies. For a noise power spectral density $S_f(\omega) = A_0/\omega^{1+\mu}$, the variance is:

$$\sigma_f^2 = \frac{1}{\pi}\int_{\omega_{low}}^{\omega_{high}} S_f(\omega)\mathrm{d}\omega = \frac{A_0}{\pi\mu\,\omega_{low}^{\mu}}\left[1-\left(\frac{\omega_{low}}{\omega_{high}}\right)^{\mu}\right], \tag{6.3}$$

where we have assumed that the spectrum was symmetric in zero, hence the integral over positive frequencies and the factor $1/\pi$ instead of $1/(2\pi)$. Note that the case $\mu = 0$ is divergent in the last expression in Eq. (6.3), but the limit $\mu \to 0$ is easily found, yielding also a strong dependence in the measurement bandwidth:

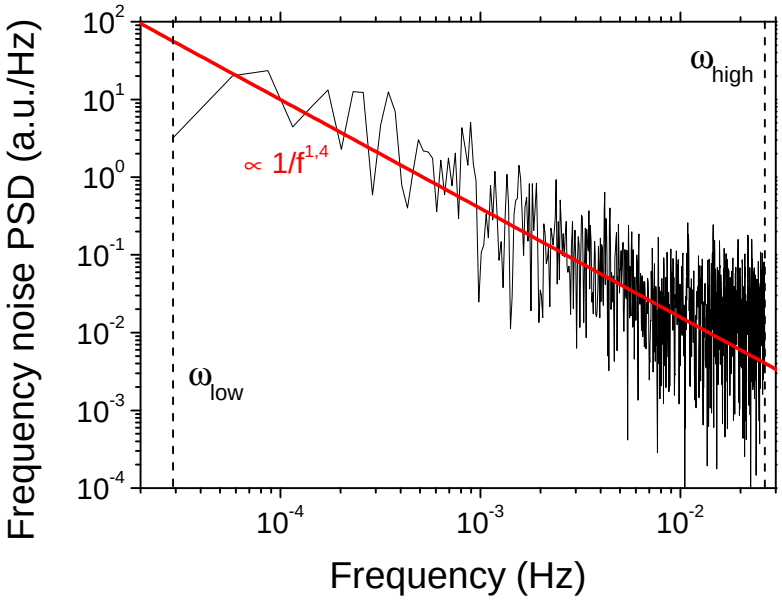

Figure 6.4: frequency noise power spectral density $S_f(\omega)$, obtained from FFT on the auto-correlation signal of the frequency noise track shown in Fig. 6.3. The two cut-off frequencies correspond to the global measurement time (ω_{low}) and the acquisition time for one resonance frequency (ω_{high}). The red solid line is a $1/\omega^{1+\mu}$-type fit, here with $\mu = 0.4$.

$\sigma_f^2 = \frac{A_0}{2\pi}\ln(\omega_{high}/\omega_{low})$. Since our measurement technique does not allow to always have fixed measurement and sampling times from one frequency track to another, we cannot extract reproducible quantities from the bare spectrum. Therefore, to get rid as much as possible from edge effects, one can conveniently compute the statistics on **jumps** $\delta f(t_i)$ from a frequency $f_i \equiv f_{bif}(t_i)$ at a time t_i to the next one measured f_{i+1}. In fact, this is almost equivalent to apply a high-pass filter to the frequency noise track, since we can write in the limit where the sampling time $\Delta t_{min} \to 0$:

$$\delta f(t) \approx \frac{\mathrm{d}f_{bif}(t)}{\mathrm{d}t}\Delta t_{min}. \tag{6.4}$$

From then on, the original spectral information is kept. Indeed, the spectral density on jumps writes:

$$S_{\delta f}(\omega) \approx (\Delta t_{min}\omega)^2 S_f(\omega). \tag{6.5}$$

The ω^2 illustrates the fact that we have applied a high-pass filter to the raw frequency noise by computing jumps, since it puts more weight on high frequencies. Long term drifts are thus canceled and do not affect our estimates of frequency noise. The inte-

grated value of the jumps spectrum is calculated as follows, and can be considered as the characteristic magnitude of frequency noise:

$$\sigma_{\delta f}^2 = \frac{1}{\pi}\int_{\omega_{low}}^{\omega_{high}} S_{\delta f}(\omega)\mathrm{d}\omega = \frac{A_0(\Delta t_{min}\omega_{high})^2}{\pi\omega_{high}^{\mu}(2-\mu)}\left[1-\left(\frac{\omega_{low}}{\omega_{high}}\right)^{2-\mu}\right]. \tag{6.6}$$

This expression can be simplified: first, since μ is close to 0, the second term into brackets is very small, as the two experimental cut-off frequencies are always separated by at least two orders of magnitude. Second, the Fourier transform properties impose that $\Delta t_{min}\omega_{high} = \pi$. Thus, the jumps variance is:

$$\sigma_{\delta f}^2 \approx \frac{\pi A_0}{\omega_{high}^{\mu}(2-\mu)}. \tag{6.7}$$

We see that this variance is rather weakly dependent on the sampling frequency, since μ is small. We can estimate the discrepancy between two successive measurements with only different sampling frequencies, in the most extreme case: the maximum μ observed was 0.4 and sampling times varied between 10 and 60 seconds at most. This leads to discrepancies of at most $(\sigma_{\delta_{f,2}} - \sigma_{\delta_{f,1}})/\sigma_{\delta_{f,1}} = (\omega_{high,1}/\omega_{high,2})^{\mu/2} - 1 \approx 38$ %, and usual sampling times are less spread. Therefore, our measurements combined with the jump analysis provide safe grounds for a quantitative study of intrinsic frequency fluctuations. Note that there is no dependence on the higher cut-off if $\mu = 0$. Besides, a $1/\omega$-type spectrum is rather convenient in that we do not need fast measurement times, since the weight is on low frequencies.

Usually, we compute the discretized version of Eq. (6.6), which is easily accessible through the jumps histogram. If we assume that jumps are independent events, they should reasonably follow a Gaussian distribution of width $\sigma_{\delta f}$. This width is the so-called **Allan deviation** [104], and its experimental version for a finite number N of samples is expressed as follows:

$$\sigma_{\delta f} = \sqrt{\langle \delta f^2\rangle - \langle \delta f\rangle^2} = \sqrt{\frac{1}{N-1}\sum_{i=1}^{N-1}(f_{i+1}-f_i)^2}. \tag{6.8}$$

Note that we have assumed that on average $\langle \delta f\rangle = 0$ to write the last equality. The frequency histogram associated to the frequency noise track of Fig. 6.3 is shown in Fig. 6.5. left panel. The histogram is not clearly well fit by a Gaussian, which is likely due to the slow drift component. In fact, most histograms taken from raw data do not feature a clear Gaussian shape. The jump histogram is plotted in Fig. 6.5 right panel for comparison. The Gaussian fit is good, and yields a typical width that is 1) reproducible and 2) smaller than the one obtained from raw data, which is expected since we have removed the slow drift. Besides, as a proof of robustness, insets show

that the jumps are kept around zero with time, and that the spectrum of jumps is well fitted with Eq. (6.5), where the frequency noise spectrum is the one fit in Fig. 6.4. This demonstrates that finite time corrections which were neglected to write Eq. (6.4) can be overlooked in our analysis.

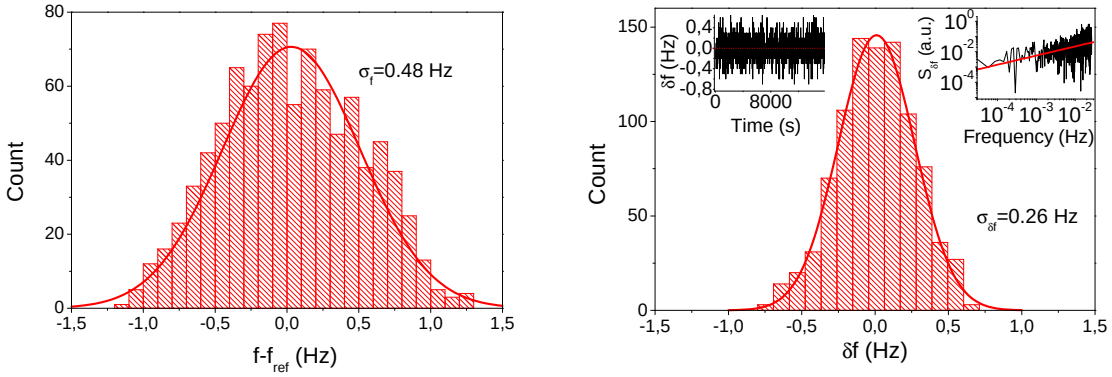

Figure 6.5: left panel: histogram of the frequency noise track shown in Fig. 6.3. Right: histogram on jump events, computed from the same track. Red solid lines on both histograms are Gaussian fits. Insets: time track of jumps (left) and jumps spectrum (right), with the red curve being the application of Eq. (6.5).

Remarkably, if one can obtain a reliable estimate of σ_f through the histogram, it provides a good way to predict and fit the exponent μ in the spectrum. Indeed, just as the spectra on jumps and on frequency noise can be linked, the two variances can be related combining Eq. (6.8) and Eq. (6.3):

$$\sigma_f^2 = \frac{2-\mu}{\pi^2 \mu} \left[\left(\frac{\omega_{high}}{\omega_{low}} \right)^{\mu} - 1 \right] \sigma_{\delta f}^2. \tag{6.9}$$

This relation strongly depends on μ, which is the only free parameter if the two variances are extracted from histogram computations. Applying this relation to the two magnitudes measured in the case of Fig. 6.5, we find that $\mu = 0.4$ with a 10 % margin on the value if we assume a 15 % error on the measured estimates. This value is consistent with the $1/\omega^{1.4}$ fit in Fig. 6.4. Albeit appealing, this method suffers from a major drawback: as we said above, most of the time, the distribution on frequency noise is not Gaussian enough to properly extract σ_f because of slow drifts.

Note that using the nonlinear properties of the resonator should not involve significantly the Brownian motion transduction mechanism described in Chapter 3: first, the resulting statistics on the frequency noise would be strongly asymmetric [33]. On the other hand, a quick estimate, given typical nonlinear coefficients for our beams and the true thermal fluctuations at 4 K yield a spectral broadening in the µHz range. To make sure that the interplay between nonlinearities and fluctuations is negligible,

we measure frequency noise with an added noise force: the statistics starts to be altered for equivalent temperatures in the 10^6 K range. Thus this mechanism is here irrelevant.

6.2.3 Results and discussion

Since the technique is demonstrated to be reliable, we use it to characterize thoroughly frequency noise in our device [40]. First we measure by operating on the upper branch, at high motion amplitude. The results yield similar frequency power spectra with a $1/\omega^{1+\mu}$ characteristic, where $\mu = 0.4 \pm 0.05$ for all measurements on the same 250 μm long device, and a Gaussian distribution on frequency jumps.

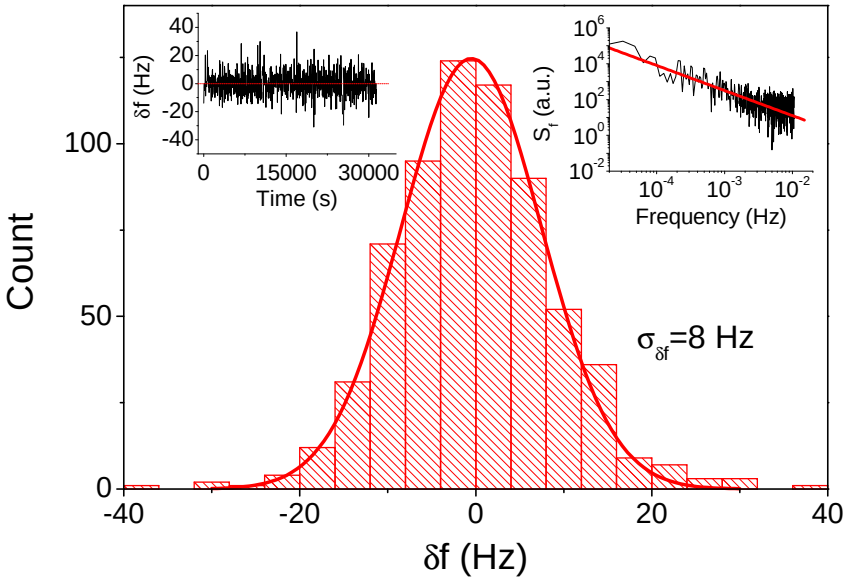

Figure 6.6: histogram of the frequency jumps taken on the upper branch of the bistable resonance shown in Fig. 6.2. Right: histogram on jump events. Insets: time track of jumps (left) and frequency spectrum (right), with the red curve being the $1/\omega^{1+\mu}$ fit.

An example is shown in Fig. 6.6. Unexpectedly, the Allan deviation is **much bigger** than the one measured while operating on the lower branch. We thus have measured the frequency noise over a large range of motion amplitudes (i.e. of driving forces), operating both on the upper and lower branches. The Allan deviation appears to scale quadratically with the motion amplitude on the upper branch and seems to remain rather constant on the lower branch, as seen in Fig. 6.7.

Note that there is a clear offset, which is well captured by the lower branch measurements. In addition, we tuned the Q factor of the NEMS with the magnetic field, only to find that the Allan deviation depends linearly on the Q factor at fixed motion

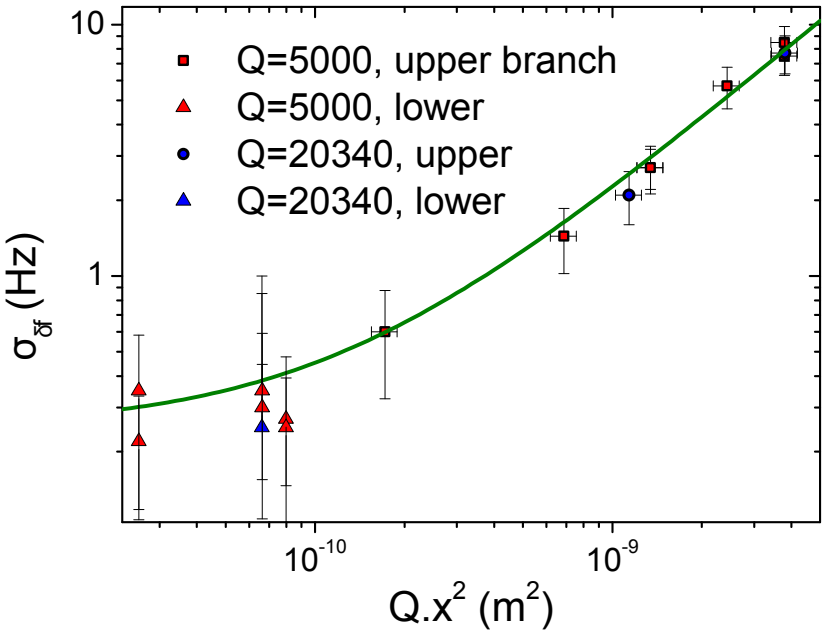

Figure 6.7: Allan deviation as a function of displacement at the two bifucation points, as a function of squared amplitude of motion multiplied by the Q factor, for two Q factors. The fit yields $\sigma_{\delta f} = 0.25 + 2.02 \times 10^9\ Qx^2$.

amplitude. The measurements were also carried on a 15 µm long SiN device with the same characteristics, apart from the length. The same dependence is observed, although with bigger error bars. Furthermore, we measured, at a high constant displacement on the upper branch and high Q factor, the dependence on temperature from 4 to 20 K. Within error bars, the Allan deviation is not clearly affected by temperature. Of course this does not mean that there is no temperature dependence, but this should be small and uncorrelated to the observed nonlinear features. To further investigate a possible temperature dependence, we measure frequency noise by operating on the lower branch, where the motion amplitude is the smallest ($x \approx x_s$) and the Allan deviation rather insensitive to it.

The result is plotted in Fig. 6.8. We observe a linear dependence of the Allan deviation in temperature from 1 to 30 K. An offset of 0.16 Hz remains if one extrapolates the linear dependence to $T = 0$ K. The observed linear dependence is consistent with the work of Ref. [146], where a similar long, stressed SiN device was studied, but the frequency noise value we measure at 4 K is one order of magnitude higher than that reported in this work. The main difference is the presence, in our case, of the Aluminium layer. In the aforementioned work, the origin of frequency noise is thought to be relaxation of two-level defects in the materials, that translates into fluctuations of stress or Young's modulus [104]. Here, it is likely that another mechanism, perhaps of the same nature, takes place in the metallic layer. This could be linked with the

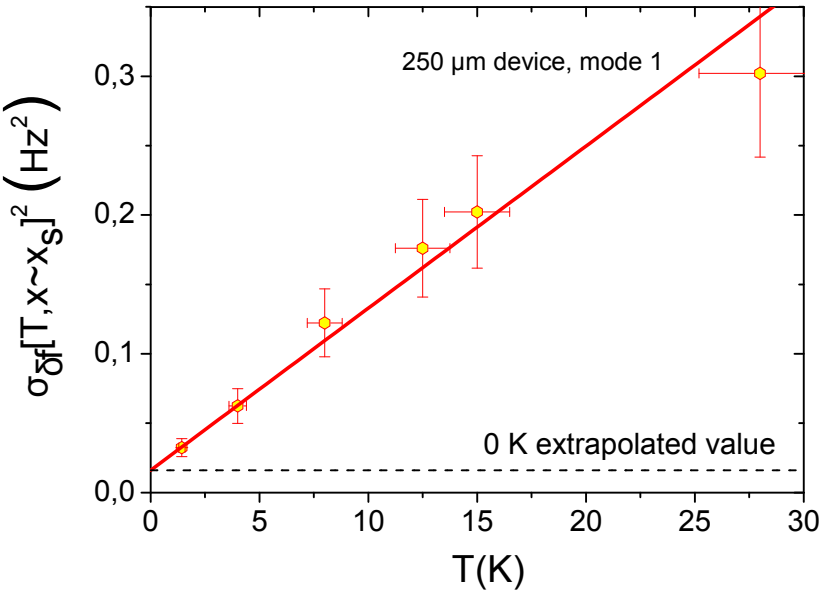

Figure 6.8: Allan deviation as a function of temperature measured on the lower branch, or on the upper branch with the quadratic dependence in displacement (small here) removed.

work done in Refs. [55, 50, 56] that report the dependence of damping on the thickness of the metallic layer, pointing towards metal-dominated dissipation mechanisms. We will focus on this below. This is further supported by the fact that our intrinsic Q factor is about 600 000, hence almost four times lower than that of the device used in Ref. [146] which is 400 µm long (we expect a linear dependence of Q in length, see Ref. [39]). For the time being, we see that the slope in temperature is rather weak, which explains why we do not see it by measuring at high amplitudes if we consider the $Q.x^2$ dependence itself as being temperature independent. Note that the extrapolation to zero temperature is such that $\sigma_{\delta f}(T = 4\text{ K}, x \sim x_s)/\sigma_{\delta f}(T = 0, x \sim x_s) \approx 2$, which again is close to what authors in Ref. [146] have obtained.

While the temperature dependence had already been reported in Ref. [146], the nonlinear dependence in the motion amplitude we observe has not been observed so far to our knowledge. The question now is: where does it come from ? The dependence in the Q factor could originate from the bifurcation process: indeed, the spinode point in the (x, ω) plane writes $x_s = \frac{1}{3^{1/4}}\sqrt{\Gamma/\beta}$. Therefore, the prefactor in the quadratic dependence could be linked to the mechanical energy at the spinode point $\propto x_s^2$. If so, the quadratic dependence should only appear for displacements above the spinode point, which makes the fit shown in Fig. 6.7 meaningless for $x \to 0$. Fig. 6.9 shows an attempt to plot the data rescaled to the spinode point energy on the X axis, with the Allan deviation extrapolated for the spinode subtracted (what is called here $x_s \sim 0$). The data for all Q factors are rather well captured by the fit, and we see that all data taken while sweeping on the lower branch are gathered at the origin.

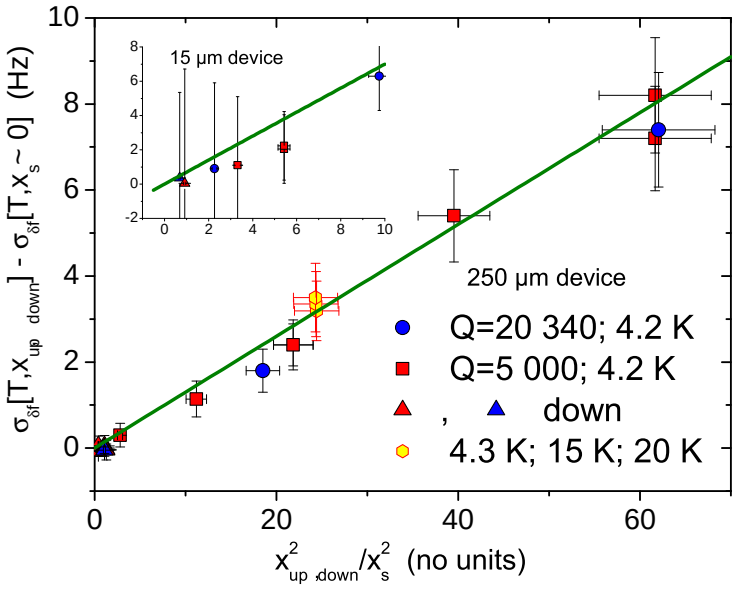

Figure 6.9: frequency noise, with the extrapolated value for the spinodal point contribution subtracted, as a function of the mechanical energy ($\propto x^2$), normalized to the spinodal point mechanical energy ($\propto x_s^2$). The green solid line is a simple linear curve of slope 0.13 Hz. Inset: same graph for the 15 µm device, with a slope 0.7 Hz.

It is nonetheless rather hard to imagine a mechanism linked to the bifurcation process that could **amplify** frequency fluctuations. It is thus quite natural to proceed by assuming that bifurcation is ideal (i.e. occurring truly instantaneously within our resolution), and that the extra noise source has to be sought in the bifurcation position expression $\omega_{bif} - \omega_0 \propto \beta x_{bif}^2$. This means that either β or x_{bif} has to be the noisy variable. We can rule out β, which is $\propto E/\omega_0$, since a Gaussian noise on the Young's modulus E having the observed signatures (mode-dependent, proportional to Γ^{-1}) seems unphysical.

Writing $\omega_{bif} - \omega_0 \propto \beta x_{bif}^2 \times (1 + \delta x_{bif}/x_{bif})$, we realize that the right scaling is obtained if $\delta x_{bif}/x_{bif} = -\delta\Gamma/\Gamma$, i.e. if the effect is produced by amplitude fluctuations generated by a fluctuating damping rate. To be quantitative, we recall that [82]:

$$\begin{cases} x_{bif,\uparrow} \approx x_{max}, \\ x_{bif,\downarrow} \approx \left(\dfrac{x_{max}\Gamma}{4\beta}\right)^{1/3}, \\ x_{max} = \dfrac{F_0}{m\omega_0\Gamma}, \end{cases} \tag{6.10}$$

which leads to:

$$\omega_{bif,\uparrow} \approx \omega_0 + \delta\omega + \beta x_{max}^2 \left(1 - \frac{\delta\Gamma}{\Gamma}\right), \tag{6.11}$$

$$\omega_{bif,\downarrow} \approx \omega_0 + \delta\omega + 3\beta x_{max}^2 \left[1 + o\left(\frac{\delta\Gamma}{\Gamma}\right)\right], \tag{6.12}$$

$$\omega_s \approx \omega_0 + \delta\omega + \frac{\sqrt{3}\Gamma}{2}\left(1 + \frac{\delta\Gamma}{\Gamma}\right). \tag{6.13}$$

We thus justify why the lower bifurcation point is amplitude independent, and why the upper branch leads to a $\beta x_{max}^2/\Gamma$ scaling of the additional noise: this shall be understood as an **amplification** of the effect of the damping fluctuations on the postition of $\omega_{bif,\uparrow}$, which at the spinodal point add up with actual frequency fluctuations through Eq. (6.13). For our measurements, we are always far from the spinodal point, thus Eqs. (6.11) for the upper branch and (6.12) for the lower one do apply instead of Eq. 6.13. Their extrapolations at $x_{max} \to 0$ do not match the spinodal expression, which is why we quoted $x_s \sim 0$ in the graphs of Figs. 6.8 and 6.9. As a final result, the damping noise is simply $\sqrt{3}/2$ times the slope extracted from the linear fit of the data in Fig. 6.9.

The nonlinear dependence was also measured on the third and fifth modes of the 250 µm beam. The quadratic behaviour is again observed on both, again with offsets. The fitted frequency noise parameters are reported for the three modes in Table 6.1. We find out that damping fluctuations are roughly 2.5 times smaller than frequency fluctuations, regardless of the intrinsic value of Γ. This means that for our highest Q devices Q factor fluctuations can be as large as 5 %, while for most devices they are of order 0.1 % or smaller. Similarly, for our best devices the frequency noise $\sigma_{\delta f}$ represents up to 20 % of the resonance width $\Gamma/(2\pi)$. This means that in frequency domain measurements, frequency noise can contribute to decoherence with a slight broadening of the resonance peak (see Chapter 4). While it is a small effect, the influence of damping noise to decoherence remains always within our error bars: defining a T_2 from x_{max} using $x_{max} = F_0/(m\omega_0\Gamma)$ (see Chapter 4), we see that $\delta\Gamma$ impacts it marginally (5 % at most). Similarly, in a time domain measurement we can wite the averaged susceptibility in complex form:

$$\langle\chi_a(t)\rangle = \langle\exp\left[i\delta\omega t\right]\rangle \left\langle \exp\left[i\beta x_{max}^2 \varpi(t)\frac{2\delta\Gamma}{\Gamma}t\right]\right\rangle \chi_{NL}(t), \tag{6.14}$$

with $\chi_{NL}(t)$ the non-linear, deterministic susceptibility in time domain, and ϖ defined in Eq. (4.37) as the time-domain non-linear oscillation factor. Assuming the statistics is Gaussian on a decay timescale on both noises, the two averages can be calculated

explicitly:

$$\langle \chi_a(t) \rangle = \exp\left[-\frac{\sigma_f^2 t^2}{2}\right] \exp\left[-\left(\beta x_{max}^2 \varpi(t) \frac{\sigma_{\delta\Gamma}}{\Gamma}\right)^2 t^2\right] \chi_{NL}(t), \tag{6.15}$$

the fluctuations being taken in the inhomogeneous broadening limit (see Chapters 3 and 4). This last point seems licit to us, as the fluctuations observed have a $1/\omega$ type spectrum leading to very slow characteristic timescales. Decoherence due to frequency noise has also a small effect in time domain for our devices having the best Q factors, seen as an extra Gaussian decay. The damping fluctuations are again amplified by a term $\beta x_{max}^2/\Gamma$, but the decaying term $\varpi(t) = (1-e^{-\Gamma t/2})/(\Gamma t/2)$ in the exponential is a rather weak dependence, and with our devices we see that extremely large motion (on the millimeter scale for our longest devices) is needed to observe a mesurable impact on the decay of the two quadratures, i.e. on $\overline{T}_2$ (see Chapter 4. Such displacements are in practice never reached. This explains why no effect could be seen in Ref. [34], leading to $T_1 \approx T_2 \approx \overline{T}_2$, where $T_1 = 2/\Gamma$ is the energy decay time. Eventually, the bifurcation method presented here appears to be a unique, simple and reliable way to access damping noise $\delta\Gamma$ quantitatively.

Mode	$\omega_1/(2\pi)$	Bare Q_1	β	$\sigma_{\delta f}$	$\sigma_{\delta\Gamma}$
n=1	0.905 MHz	600 000	8.5 mHz/nm^2	0.28 ± 0.05 Hz	0.11 Hz $\pm$ 10%
n=3	2.68 MHz	18 000	125 mHz/nm^2	0.1 ± 0.02 Hz	0.005 Hz $\pm$ 15%
n=5	4.45 MHz	4 800	570 mHz/nm^2	0.09 ± 0.05 Hz	0.0025 Hz $\pm$ 30%

Table 6.1: internal frequency noise of the three first symmetric modes at $T = 4.2$ K for the 250 µm device.

The values measured at the lowest displacement are presumably the true intrinsic frequency noises. Indeed, the typical relative frequency noise $\sigma_{\delta f}/f_1$ for the fundamental mode lies, at 4.2 K, in the $0.1 - 0.01$ ppm range, which is fairly consistent with values reported earlier in the literature. Some of these values are listed in Table 6.2 for comparison.

However, no damping fluctuations have been reported to our knowledge, and the value quoted for the goalpost device is recalculated from Ref. [42]. Interestingly, the ratio of frequency noise to damping noise seems to be also around a factor of 3 for this device, hinting that this ratio exists regardless of the differences in the resonator's nature (cantilever-type versus doubly-clamped) and materials (silicon versus silicon nitride). In addition, the spectrum measured is always of the form $1/\omega^{1+\mu}$ with no change in μ for the same device, regardless of the displacement amplitude and hence, of the fluctuation type. Therefore, it is tempting to claim that fluctuations in frequency

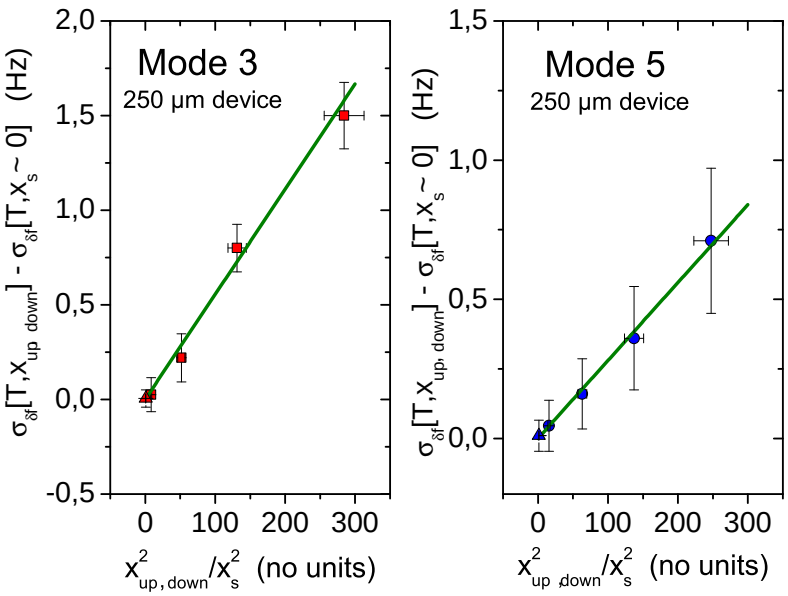

Figure 6.10: frequency noise data of the third and fifth mode of the 250 μm beam, rescaled with the same procedure as for the first mode (see Fig. 6.9).

Device	T	$\omega_1/(2\pi)$	Unloaded Q_1	$\sigma_{\delta f}$ or σ_f
250 μm SiN/Al d.c. beam	4.2 K	0.59 MHz	600 000	0.25 ± 0.05 Hz
15 μm SiN/Al d.c. beam	4.2 K	17.5 MHz	18 000	1.45 ± 0.1 Hz
2×3 μm Si/Al goalpost	4.2 K	7.1 MHz	4 800	1 ± 0.5 Hz (σ_f)
380 μm SiN d.c. beam	5 K	0.64 MHz	2 200 000	0.01 ± 0.5 Hz (σ_f)
3.2 μm cantilever	300 K	45.2 MHz	6 000	36 Hz

Device	$\sigma_{\delta f}$ or σ_f	$\sigma_{\delta\Gamma}$
250 μm SiN/Al d.c. beam	0.28 ± 0.05 Hz	0.11 Hz $\pm$ 10 %
15 μm SiN/Al d.c. beam	1.45 ± 0.1 Hz	0.6 Hz $\pm$ 10 %
2×3 μm Si/Al goalpost	1 ± 0.5 Hz (σ_f)	0.35 Hz $\pm$ 10 %
380 μm SiN d.c. beam	0.01 ± 0.5 Hz (σ_f)	X
3.2 μm cantilever	36 Hz	X

Table 6.2: internal frequency noise reported in this work (two first rows) and in some recent works (in order of appearance [42, 146, 78]). Here d.c. stands for "doubly-clamped". For the Si/Al goalpost, the values of $\sigma_{\delta\Gamma}$ have been recalculated from Fig. IV.19 in Ref. [42].

and damping are linked through the same microscopic mechanism, even though more experimental insights are needed.

We are left with the question of the actual microscopic origin of the intrinsic fre-

quency noise (and damping) measured. The temperature dependence is not unexpected: a linear dependence in the range considered could be produced through a model featuring defects acting as thermally switching two-level systems [104, 43]. As these interact with a strain field, they relax towards equilibrium, changing the local stress or the local Young's modulus as proposed in Ref. [104]. Since we are dealing with highly-stressed beams, we do believe that for our structures (and the one of Ref. [146]) it is more likely a stress fluctuation that is generating frequency noise. Therefore, we could imagine that fluctuations in the stored stress on long timescales (unlike dissipation, see below) result in the observed $\sim k_B T/\omega$ spectrum [147]. Note that the exponent is rather different from 1, ranging between 1.2 and 1.4, which poses questions on whether the mechanism at stake can be simply explained by TLS. The next sections are focused on the interaction of these two-level systems with strain fields, and measurements on dissipation and frequency noise at lower temperatures are meant to clarify their role.

6.3 Internal energy relaxation at milliKelvin temperatures: an overview of the Standard Tunneling Model (STM)

6.3.1 Structural two-level defects (TLS) in amorphous materials

We turn to analyze theoretically and experimentally microscopic sources of damping, that might also be responsible for frequency noise. For a start, it seems licit to rule out clamping losses, as they strongly depend on the beam's aspect ratio: at worst for our structures, a damping dominated by clamping losses [58] would lead to Q factors in the $10^7 - 10^8$ range, while we do not measure, for the structures of interest here, Q factors higher than 10^6. Once external contributions like gas damping [36] and high-order phonon processes leading to thermoelastic [11] or Akhiezer [43] damping are removed by lowering temperature and pressure, mechanical damping (and decoherence) at very low temperatures is thought to originate mostly from the interaction between the mechanical mode and Two-Level Systems. These low-energy excitations are described in the framework of the **Standard Tunneling Model** (STM). The STM was introduced in the early 70s by P. W. Anderson [25] and W. A. Phillips [37] to explain apparent anomalous features in thermal properties of amorphous solids at low temperatures [148], and as it was found later, in their acoustic properties. The main assumption is that the disordered lattice typical of amorphous systems allows for its atoms (or some small group of atoms) to possess two nearly equivalent metastable position states separated by an energy barrier of height V_0 over a distance d and hav-

ing an asymmetry energy Δ. These atoms can go from one potential well to the other by quantum mechanical tunneling [149] or thermal activation [150] as shown in Fig. 6.11. From then on, the acoustic (or mechanical) and thermal properties of amorphous solids are determined by the interaction between these TLS and phonons.

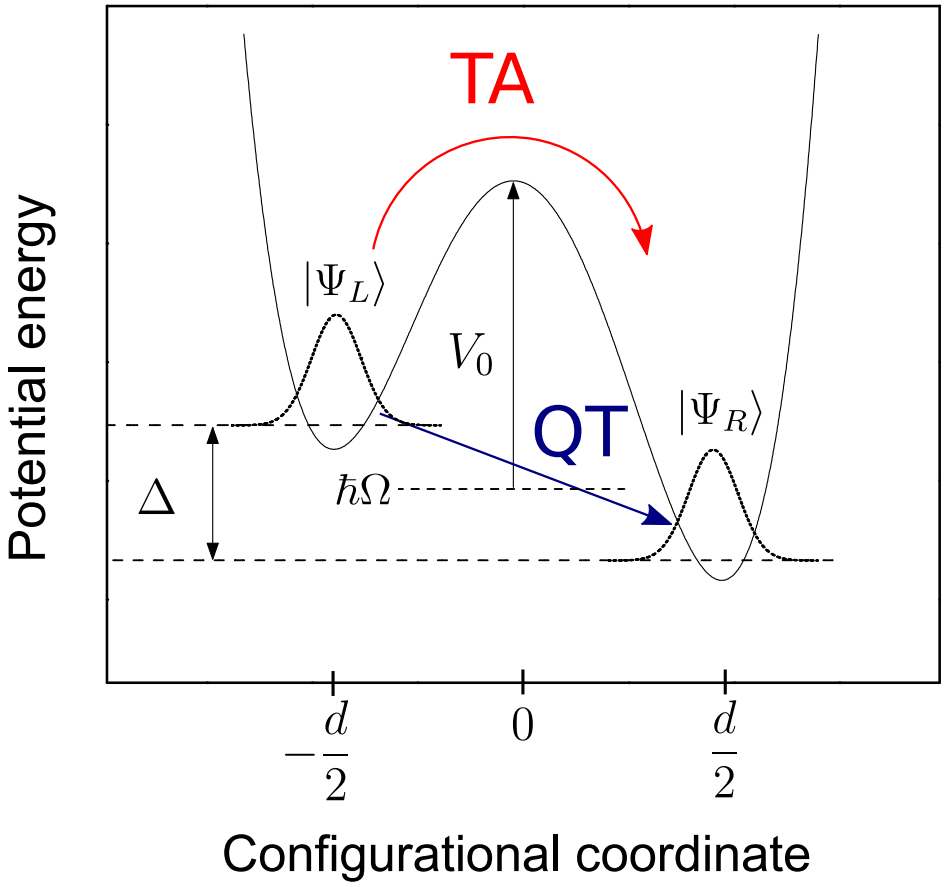

Figure 6.11: schematic representation of a two-level system with asymmetry Δ and barrier height V_0. The motion of the atom from one metastable well to the other is induced either by quantum tunneling (QT) or thermal activation (TA).

While the most salient signatures are now rather well known and characterized in bulk structures, their exact impact on nanomechanical damping is still poorly understood despite a broad range of studies, for instance Refs. [151, 26, 27, 49, 28], to mention a few. This lack of consistency from one study to the other seems to originate partly from the additional complexity brought by dimensionality aspects. For instance, while TLS are usually treated as an energy continuum distribution, it is not clear whether this description still holds in the context of nanomechanics, where the structure is so tiny that only a small number of TLS are present [38]. Furthermore, many experiments have been realized on crystalline samples (mono or poly), but the results are still treated within the STM; to be consistent, one has to invoke defects

that act as TLS [26], as opposed to the constitutive TLS of glasses, or a modified version of the STM that is consistent with long-range order present in crystals [152]. In addition, the small size of NEMS devices also makes them hard to address with non invasive probes: for instance, our magnetomotive scheme involves a metallic layer with electrons that can also act as an additional bath for TLS [28], increasing further the complexity of the problem. In this section we address the dissipation at very low temperatures of a 15 µm long nanomechanical resonator, and compare it with results obtained in Ref. [28] and on a 50 µm long sample with otherwise identical characteristics embedded in a microwave cavity for a new (microwave) optomechanics experiment. We treat here the quantum mechanical aspect of TLS, as thermal activation is exponentially suppressed with temperature and thus nearly irrelevant at $T = 1$ K or below.

6.3.2 Single TLS Hamiltonian

A generic TLS is pictured in Fig. 6.11 in the previous section. The tunneling amplitude is nonzero due to the overlap between the two potential wells wavefunctions and the finite barrier height. It is physically relevant to consider a finite overlap, as far as the spacing between two positions for an atom does not exceed a few Å. This overlap $\langle\Psi_L|\Psi_R\rangle$ is modelled to vanish exponentially in the Gamov factor λ. The latter is obtained within the WKB approximation as a function of the barrier height V_0 and the distance d, in the configurational coordinate space, between the two potential wells: $\lambda = d\sqrt{2m_aV_0}/\hbar$, with m_a the mass of the tunneling entity. Thus, the tunneling amplitude between the two wells, i.e. their coupling energy, writes:

$$\Delta_0 \approx \hbar\Omega e^{-\lambda}. \tag{6.16}$$

In the position space, the Hamiltonian of a single, isolated two-level system is then:

$$\widehat{\mathcal{H}}_0 = \frac{1}{2}\begin{pmatrix}\Delta & \Delta_0\\ \Delta_0 & -\Delta\end{pmatrix} = \frac{\Delta}{2}\widehat{\sigma}_z + \frac{\Delta_0}{2}\widehat{\sigma}_x, \tag{6.17}$$

where we have introduced Pauli matrices $\widehat{\sigma}_{x,z}$, which highlight the formal analogy with a 1/2-spin. Diagonalizing the Hamiltonian (6.17) is straightforward, and one obtains the two TLS energy eigenstates:

$$\varepsilon_\pm = \pm\frac{1}{2}\sqrt{\Delta^2 + \Delta_0^2}. \tag{6.18}$$

In the following, we will often refer to the energy spacing ε between the two eigenstates to characterize the TLS:

$$\varepsilon = \varepsilon_+ - \varepsilon_- = \sqrt{\Delta^2 + \Delta_0^2}. \tag{6.19}$$

In the following we will use the energy basis to describe the interaction between phonons and TLS, which is thought to be the dominant channel of mechanical energy relaxation at low temperatures, where the bath fights against coherent tunneling of the TLS. We later extend the formalism to the interaction between conduction electrons and TLS.

6.3.3 TLS energy distribution

Since there is no reason for a disordered material to host only one type of TLS, energy-wise, we can assume that it features instead a distribution over an energy range that should be limited by the glass transition temperature around 1000 K. Although there is no general consensus on what should be the density of energy states for two-level systems, two arguments lead to a rather simple description: first, at low temperatures, the relevant TLS which are interacting with equilibrium phonons should have energies (and hence asymmetries) that are well below the glass transition temperature (~ 1000 K). Therefore, considering that asymmetries range up to this energy, we can assume that the distribution on asymmetries is roughly constant in our range. Meanwhile, we can see through Eq. (6.16) that a small change in the barrier leads to a large variation of the tunneling matrix element Δ_0. Since at low temperatures, the range of Δ_0 spanned is small, the distribution in the λ parameter is assumed to be roughly uniform. Then, the probability distribution writes:

$$P(\Delta, \lambda)\mathrm{d}\Delta\mathrm{d}\lambda = P_0\mathrm{d}\Delta\mathrm{d}\lambda. \tag{6.20}$$

Hence P_0 is the number of TLS per unit energy per unit volume. Through a simple variable change we can obtain a distribution on asymmetries and tunneling matrix elements:

$$P(\Delta, \Delta_0)\mathrm{d}\Delta\mathrm{d}\Delta_0 = \frac{P_0}{\Delta_0}\mathrm{d}\Delta\mathrm{d}\Delta_0. \tag{6.21}$$

While this distribution explains well experimental findings, it also raises the issue of an energy cut-off, as the distribution (6.21) clearly diverges for small tunneling amplitudes. We shall see in the following that the averaging over many TLS is not very sensitive to the low cut-off energy, provided that the latter is small compared to $k_B T$. Ultimately, this cut-off is justified by the finite number of TLS in the structure.

We also introduce useful distributions on couples $(\varepsilon, \Delta), (\varepsilon, \Delta_0)$ and on reduced parameters $(u, v) = (\varepsilon/(k_B T), \Delta/\varepsilon)$:

$$P(\varepsilon,\Delta)\mathrm{d}\varepsilon\mathrm{d}\Delta = \frac{P_0\,\varepsilon}{\varepsilon^2-\Delta^2}\mathrm{d}\varepsilon\mathrm{d}\Delta, \tag{6.22}$$

$$P(\varepsilon,\Delta_0)\mathrm{d}\varepsilon\mathrm{d}\Delta_0 = \frac{P_0}{\Delta_0\sqrt{1-\dfrac{\Delta_0^2}{\varepsilon^2}}}\mathrm{d}\varepsilon\mathrm{d}\Delta_0, \tag{6.23}$$

$$P(u,v)\mathrm{d}u\mathrm{d}v = \frac{P_0 k_B T}{1-v^2}\mathrm{d}u\mathrm{d}v. \tag{6.24}$$

In particular, the distribution on dimensionless parameters (6.24) will allow to predict easily how the damping should behave at low temperature without explicit integration (see below).

6.3.4 Interaction between a mechanical mode and TLS: qualitative description

The interaction between TLS and phonons can be split into two parts, namely **relaxational** and **resonant** processes, which are predominant depending on the phonon energies at stake and lead to very different signatures. Though the two can be treated on an equal footing using Bloch equations for the pseudo-spin representing the TLS, here we describe them separately to clarify the physical picture and make the link with the NEMS macroscopic parameters clearer. One can quickly describe the two processes the following way:

- the relaxational interaction involves two parts: first, the TLS energy levels are modulated by the oscillating strain field imposed when the NEMS is driven. Hence they are put out of their equilibrium, and relax energy towards their environment over a finite time delay after the strain modulation, which represents a loss of energy. We use the **TLS susceptibility** to a strain perturbation, which contains both reactive (frequency shift) and dissipative (damping) parts, as a framework in this case.

- the resonant interaction is easier to describe: when driven, a mechanical (phonon) mode ω is put out of equilibrium, and relaxes back by interacting with TLS whose energy splitting match the mechanical energy quantum $\hbar\omega$ relative to a mode: either the TLS absorbs or emits resonant phonons. Thus the mechanical damping rate is directly the **phonon-TLS scattering rate** averaged over the whole TLS distribution.

In the following, we will describe in detail these two processes, starting with the relaxational interaction, which is more subtle to address. Besides, we believe that the reduced dimensions and beam nature of our mechanical device require a specific

treatment that is usually disregarded in the literature which essentially applies the bulk, 3D case.

6.3.5 Relaxational TLS-phonon interaction

TLS energy modulation by an applied strain field

By definition, atomic positions will be perturbed by any externally applied strain modulation. Thus, the potential landscape seen by an individual TLS will be modified, which puts the TLS out of equilibrium as it modifies its energy splitting. Since the wavelengths associated to a mechanical drive are much bigger than the distance between the two potential wells (which is typically in the Å range), at first order the driving field only modifies the asymmetry, hence the energy splitting of the TLS. The TLS will then relax towards equilibrium by exchanging energy with its environment, e.g. thermal phonons in any materials [25], or conduction electrons in metallic glasses [153].

We shall focus first on phonon-driven relaxation of TLS, which is ubiquitous and thought to be responsible for a large part of our experimental findings. Indeed, since the TLS returning to equilibrium involves tunneling, hence atomic motion in the disordered lattice, it modifies the local stress. Apart from the driving field, thermal phonon modes are assumed to be at equilibrium. Besides, phonon modes that are resonant with the TLS energy splittings involved are assumed to have wavelengths much bigger than the interwell spacing. In fact, this can be justified easily: at low temperatures, well below the Debye temperature, modes of wavevectors $\sim 1/d$, which are at energies much bigger than $k_B T$, are not thermally activated and thus do not interact with TLS. As a result, any strain field $\widehat{\mathcal{E}}$, at first order, is a tiny linear perturbation of the TLS potential landscape: the potential barrier is almost unchanged, and strain only couples to the TLS asymmetry. Therefore, the interaction Hamiltonian is diagonal in the position basis $(|\Psi_L\rangle, |\Psi_R\rangle)$:

$$\widehat{\mathcal{H}}_{int}^{ph,p} = \overrightarrow{\gamma} \cdot \overrightarrow{\widehat{\mathcal{E}}} \widehat{\sigma}_z, \tag{6.25}$$

where $\gamma_j = \frac{1}{2}\partial\Delta/\partial\mathcal{E}_j, j = 1...6$ (to match the definition of strain as a 6-vector component [43]) is the TLS asymmetry change per unit strain, i.e. the TLS-phonon interaction strength. Here we have kept the directional aspect of the coupling, due to non-zero transverse strain components in a real material with a non-zero Poisson coefficient experiencing longitudinal strain.

The interaction Hamiltonian (6.25), treated as a weak perturbation, can be rewritten in the energy eigenbasis $(|-\varepsilon/2\rangle, |\varepsilon/2\rangle) \equiv (|g\rangle, |e\rangle)$:

$$\widehat{\mathcal{H}}_{int}^{ph,\varepsilon} = -\frac{\overrightarrow{\gamma} \cdot \overrightarrow{\widehat{\mathcal{E}}}}{\varepsilon} \left(\Delta\widehat{\sigma}_z + \Delta_0\widehat{\sigma}_x\right). \tag{6.26}$$

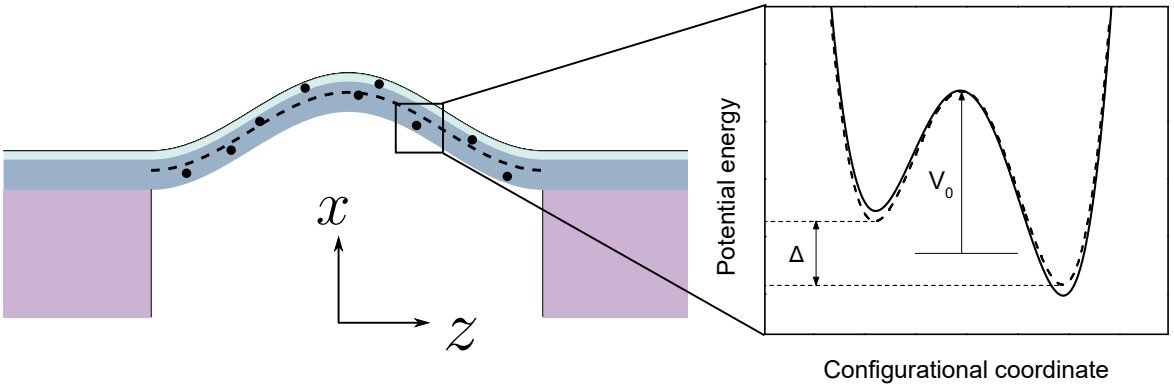

Figure 6.12: schematic representation of the relaxational interaction, detailed for one TLS: as the beam is undergoing a deformation when resonantly excited, the resulting local strain field changes the interatomic potential and modulates the TLS asymmetry. The dots represent defects randomly distributed in the beam, the dashed line on the beam is the neutral axis, where the applied strain field is zero. The TLS equilibrium configuration is the dashed potential, while the full line represents the strain-modulated potential.

This Hamiltonian is the building block of the physical picture: it describes both the strain modulation of TLS and the relaxation of TLS to phonons via thermal strain fields.

Damping rate and frequency shift due to the relaxational interaction

The relaxational interaction can be divided into two parts, that are both described by the interaction Hamiltonian (6.26). It can be treated in a similar fashion to magnetic or dipolar moments interacting with an externally applied field. We proceed through a semi-classical treatment that is close to that proposed by Philips [149]. However here we 1) keep the vectorial nature of the strain field and the couplings while taking into account macroscopic constraints such as small cross-dimensions or modal shapes [38], and 2) lead the derivation to yield, at the end of the calculation, the damping rate and the frequency shift that are our measurable quantities. The quantum aspect of the treatment will reside in the calculation of the TLS relaxation time that appears in the TLS susceptibility, i.e. the change in polarization due to an applied strain field.

We derive first the response of a TLS to a classical strain field that arises from our Laplace excitation, with a Zener-like model [154]. This yields the power dissipated by the modulating strain field, and this power can be linked to the NEMS damping. At rest, the TLS polarization $p_0 = p_e - p_g$, where $p_{e,g}$ are the states occupation probabilities, is easily obtained, as the TLS is in equilibrium with its thermal bath: $\langle\widehat{\sigma}_z\rangle_0 = \tanh[\varepsilon/(2k_BT)]$, where $\langle\widehat{\sigma}_z\rangle_0 = \mathrm{Tr}\left(e^{-\widehat{\mathcal{H}}_0/(k_BT)}\widehat{\sigma}_z\right)/\mathcal{Z}$ denotes the ensemble average at equilibrium, $\mathcal{Z}$ being the TLS partition function. First, the TLS energy is

modulated by a classical oscillating macroscopic strain field $\overrightarrow{\mathcal{E}} = \overrightarrow{\mathcal{E}_0}\cos(\omega t)$. Therefore, the polarization $p = p_0 + \delta p$ is shifted from its equilibrium by the applied strain field as the energy levels are modulated: the associated change in energy in a time interval δt, written in the classical limit from Eq. (6.26), is:

$$\delta U = -\frac{\Delta}{\varepsilon}\left(\overrightarrow{\gamma}\cdot\overrightarrow{\mathcal{E}}\right)\dot{p}\,\delta t. \tag{6.27}$$

The evolution of the TLS polarization can be written in the relaxation time approximation, i.e. for strain perturbations that do not bring the system too far from thermal equilibrium:

$$\dot{p} = -\frac{p - p_{st}}{\tau_{rel}}, \tag{6.28}$$

where p_{st} is the steady-state polarization for a given strain $\overrightarrow{\mathcal{E}}$, and τ_{rel} is the characteristic time over which the out-of-equilibrium polarization goes back to the steady state value. The latter can be linked to the thermal equilibrium polarization, at first order in the strain field:

$$p_{st} \approx p_0 + \frac{\partial p_0}{\partial \Delta}\frac{\partial \Delta}{\partial \overrightarrow{\mathcal{E}}}\cdot\overrightarrow{\mathcal{E}} = p_0 + \frac{\overrightarrow{\gamma}\cdot\overrightarrow{\mathcal{E}}}{k_B T}\frac{\Delta}{\varepsilon}\mathrm{sech}^2\left(\frac{\varepsilon}{2k_B T}\right). \tag{6.29}$$

Meanwhile, we have $\dot{\delta p} = \dot{p}$ since p_0 is time-independent. As the polarization does not follow instantly the strain oscillation, we decompose the change in polarization in an in-phase and quadrature component: $\delta p = \delta p_c\cos(\omega t) - \delta p_s\sin(\omega t)$. Rewriting Eq. (6.28), we have two equations on $(\delta p_c, \delta p_s)$, and solving them yields the TLS susceptibility $\overrightarrow{\chi}_{TLS}$ defined through $\delta p_c + i\delta p_s = \overrightarrow{\chi}_{TLS}.\overrightarrow{\mathcal{E}}_0$:

$$\begin{cases} \delta p_c &= \dfrac{1}{1+\omega^2\tau_{rel}^2}\cdot\dfrac{\overrightarrow{\gamma}\cdot\overrightarrow{\mathcal{E}_0}}{k_B T}\dfrac{\Delta}{\varepsilon}\mathrm{sech}^2\left(\dfrac{\varepsilon}{2k_B T}\right), \\ \delta p_s &= -\dfrac{\omega\tau_{rel}}{1+\omega^2\tau_{rel}^2}\cdot\dfrac{\overrightarrow{\gamma}\cdot\overrightarrow{\mathcal{E}_0}}{k_B T}\dfrac{\Delta}{\varepsilon}\mathrm{sech}^2\left(\dfrac{\varepsilon}{2k_B T}\right). \end{cases} \tag{6.30}$$

Therefore, we have $\dot{\delta p} = -\omega[\delta p_c\sin(\omega t) + \delta p_s\cos(\omega t)]$, and we can explicit the energy change (6.27):

$$\delta U = \frac{\left(\overrightarrow{\gamma}\cdot\overrightarrow{\mathcal{E}_0}\right)^2}{k_B T}\left(\frac{\Delta}{\varepsilon}\right)^2\mathrm{sech}^2\left(\frac{\varepsilon}{2k_B T}\right)\frac{\omega\left[\sin(\omega t)\cos(\omega t) - \omega\tau_{rel}\cos^2(\omega t)\right]\delta t}{1+\omega^2\tau_{rel}^2}. \tag{6.31}$$

From then on, we can write the power dissipated through the modulation of a single

TLS over one cycle of the strain oscillation: $P_c = -\frac{\omega}{2\pi}\oint\frac{\delta U}{\delta t}\mathrm{d}t$. It yields straightforwardly:

$$P_c = \frac{\left(\overrightarrow{\gamma}\cdot\overrightarrow{\mathcal{E}_0}\right)^2}{2k_BT}\left(\frac{\Delta}{\varepsilon}\right)^2\mathrm{sech}^2\left(\frac{\varepsilon}{2k_BT}\right)\frac{\omega^2\tau_{rel}}{1+\omega^2\tau_{rel}^2}. \tag{6.32}$$

The last step is to sum this dissipated power over an ensemble of two-level systems that are distributed in our resonator. The distributions introduced in paragraph 6.3.3 assume that those are numerous enough so that they indeed feature a continuous distribution per energy bandwidth per unit volume. However, in a nanomechanical resonator, the dimensions reduction might be dramatic enough so that finite size effects dominate. There is no reason not to assume that TLS are randomly distributed, and the strain dependence makes the problem strongly dependent on local properties. Thus we cannot make a quantitative guess with a model featuring a discrete ensemble of TLS. Therefore, we will keep a continuous distribution for the time being, keeping in mind that the size reduction might limit our accuracy. Introducing dimensionless variables $u = \varepsilon/(k_BT), v = \Delta/\varepsilon$ and using the distribution (6.24), the dissipated power per unit volume thus writes:

$$P_{mic,V} = \frac{P_0\,\omega}{2}\left(\overrightarrow{\gamma}\cdot\overrightarrow{\mathcal{E}_0}\right)^2\underbrace{\int_{u_{\min}}^{\infty}\mathrm{d}u\int_0^1\mathrm{d}v\frac{v^2}{1-v^2}\mathrm{sech}^2\left(\frac{u}{2}\right)\frac{\omega\tau_{rel}(u,v,T)}{1+\omega^2\tau_{rel}^2(u,v,T)}}_{\mathcal{I}(T)}. \tag{6.33}$$

This form is convenient: the prefactor does not depend on temperature, so that the dependence on temperature only comes from the TLS relaxation time τ_{rel}. Keeping a quantity per unit volume is crucial here, as there is a dependence on the local strain profile which must be taken into account when integrating over dimensions. In our experiments, only the first out-of-plane flexural mode is excited. The resulting strain field amplitude is then (written in the 6-vector form [43]):

$$\overrightarrow{\mathcal{E}_0} = x_0x_t\frac{\partial^2\Psi(z)}{\partial z^2}(\nu,\nu,-1,0,0,\nu), \tag{6.34}$$

where ν is the Poisson's ratio ($\nu = 0.3$ for silicon nitride, 0.34 for Aluminum, so we consider it uniform in our beam) and we have noted x_t the transverse coordinate to avoid any confusion with the displacement amplitude. In addition, we have considered the possibility of cross-coupling TLS-strain terms by including shear. In our definition $x_t = 0$ along the neutral line of the beam. The product $\left(\overrightarrow{\gamma}\cdot\overrightarrow{\mathcal{E}_0}\right)^2$ can thus be written:

$$\overrightarrow{\gamma}\cdot\overrightarrow{\mathcal{E}_0} = x_0x_t\frac{\partial^2\Psi(z)}{\partial z^2}\left[(\gamma_x+\gamma_y+\gamma_s)\nu-\gamma_z\right], \tag{6.35}$$

where γ_s is the coupling associated to the shear strain component of the flexural mode, i.e. $\partial\Delta/\partial\mathcal{E}_6$. Injecting the result in the power per unit volume (6.33) and integrating over the NEMS volume (for x_t ranging from $-e/2$ to $e/2$), one obtains the power dissipated by the strain modulation of TLS energies:

$$P_{mic} = [\gamma_z - \nu(\gamma_x + \gamma_y + \gamma_s)]^2 \frac{we^3}{12} \frac{P_0\,\omega\,x_0^2}{2} \mathcal{I}(T) \int_{-l/2}^{l/2} \left(\frac{\partial^2\Psi(z)}{\partial z^2}\right)^2 \mathrm{d}z. \tag{6.36}$$

This expression is obtained **from microscopic arguments**. It can be equated to the power dissipated per unit length of the NEMS over one oscillation cycle, written in a **macroscopic fashion** with the damping rate from the NEMS dynamics equation:

$$P_{mac} = \frac{1}{2} m\omega^2 x_0^2 \Gamma_{rel}, \tag{6.37}$$

where we have introduced the damping rate Γ_{rel}, that is, the contribution to the linewidth due to strain-modulated TLS relaxing to equilibrium. Equating the two expressions and identifying the moment of area $I = we^3/12$ leads to a damping rate:

$$\Gamma_{rel} = \frac{P_0\overline{\gamma}^2 I}{m\omega} \mathcal{I}(T) \int_{-l/2}^{l/2} \left(\frac{\partial^2\Psi(z)}{\partial z^2}\right)^2 \mathrm{d}z, \tag{6.38}$$

where $\overline{\gamma} = \gamma_z - \nu(\gamma_x + \gamma_y + \gamma_z)$ is an effective coupling parameter. This is formally equivalent to the formula proposed in Ref. [39] where the authors introduce *ad hoc* a retarded (imaginary in frequency domain) Young's modulus E_2, whose microscopic origin is addressed in our work. For our pre-stressed beam taken in the analytic string limit, it can be further simplified since for the fundamental mode $\Psi(z) = \cos(\pi z/l)$ and $m = \rho ewl/2 = M/2$:

$$\Gamma_{rel}(T) = \frac{\omega^3 P_0 \overline{\gamma}^2 I}{\rho ewc_f^4} \mathcal{I}(T) = C\,\omega\,\mathcal{I}(T), \tag{6.39}$$

with $c_f = \sqrt{\sigma_0/\rho}$ the sound speed for our high-stress beam flexural modes, σ_0 being the in-built stress. We have used the fact that our flexural modes have a linear dispersion relation in the string limit, i.e. $\omega = \pi c_f/l$ for ω close to the fundamental flexure resonance. The constant C is defined so in order to make the parallel with the usual C derived for bulk amorphous solids. We can now predict the two limit behaviours expected for the damping. A TLS relaxation time should depend on its energy configuration and temperature, since the latter is characteristic of a bath into which a TLS relaxes energy. In the most canonical case, e.g. a bath of phonons, environmental degrees of freedom are switched off as temperature is decreased, resulting in an increase of the relaxation time with decreasing temperature. Since we have a

finite number of TLS, there must be at least one with a minimal relaxation time. In the limit where $\omega\tau_{rel,min} \gg 1$, the ensemble of TLS never reaches thermal equilibrium. As a result, TLS do not have time to exchange energy with their surroundings, which limits their ability to rearrange the local atomic configuration. Therefore, the resulting damping must decrease as we approach this limit, by decreasing temperature. In the limit where $\omega\tau_{rel,min} \gg 1$, the integral $\mathcal{I}(T)$ can be evaluated analytically for simple expressions of the TLS relaxation time. The latter will be derived after. In the "slow" limit $\omega\tau_{rel} \ll 1$, the TLS have time to relax to equilibrium in between successive strain increments. Therefore the relaxation time should not be relevant anymore, and indeed, $\mathcal{I}(T)$ can be evaluated analytically, so that the resulting damping rate is simply a constant in temperature, the so-called "plateau":

$$\Gamma_{rel} \underset{\omega\tau_{rel}\ll 1}{=} \frac{\pi\omega C}{2}. \tag{6.40}$$

Practically, the temperature above which the damping is constant is always found around 1 K in the literature on sound attenuation in glasses, with a C constant in the $10^{-4} - 10^{-3}$ range for almost all glasses [153]. This similarity found in many works has led the community to speculate about a possible **unversality** of the glassy behaviour at low temperatures. Note however, that the usual C constant to which it has been hitherto referred is defined as $C_{bulk} = P_0\gamma^2/(\rho\, c_l^2)$, with c_l the longitudinal sound speed (or transverse one, which is of the same order), because it is derived in the case of bulk matter. Our calculation highlights the role of dimensionality, such that the C constant for our **high-stress** beam is **renormalized**:

$$C_{beam} = \left(\frac{\pi e}{l}\right)^2 \cdot \frac{E}{12\sigma_0} C_{bulk}, \tag{6.41}$$

while in the beam limit it reduces to $C_{beam} = C_{bulk}$ because of the dispersion relation 2.10 that essentially compensates the aspect ratio. Provided that the theory applies to our system and reasonably matches the experimental data, it shows that the TLS contribution to the damping rate in the plateau region, that is, for most experiments between 1 and 10 K, scales quadratically with the aspect ratio e/l, and is proportional to the ratio between Young's modulus and in-built stress. This is an important result, as it shows explicitly with a minimal set of assumptions the role of dimensionality jointly with in-built stress in the damping of nanomechanical resonators. In particular, we see that $\Gamma \propto C_{beam}\omega \propto 1/\sqrt{\sigma_0}$: in-built stress reduces the damping in the high-stress limit.

In the opposite regime of strain oscillation $\omega\tau_{rel} \gg 1$ where the TLS relax slowly compared to the strain modulation speed, the damping rate (6.39) writes:

$$\Gamma_{rel} \underset{\omega\tau_{rel}\gg 1}{=} \int_{u_{\min}}^{\infty} \mathrm{d}u \int_0^1 \mathrm{d}v \frac{v^2}{1-v^2} \mathrm{sech}^2\left(\frac{u}{2}\right) C\tau_{rel}^{-1}(u,v,T). \tag{6.42}$$

Meanwhile, the reactive contribution, i. e. the stored energy associated to the strain modulation of a TLS energy writes:

$$U(t) = -\frac{\Delta}{\varepsilon}\left(\overrightarrow{\gamma}\cdot\overrightarrow{\mathcal{E}}\right)\delta p. \tag{6.43}$$

Injecting the expression for δp in the case of an oscillating strain and integrating over an oscillation cycle, we have

$$\overline{U} = \frac{\left(\overrightarrow{\gamma}\cdot\overrightarrow{\mathcal{E}_0}\right)^2}{2k_BT}\left(\frac{\Delta}{\varepsilon}\right)^2 \mathrm{sech}^2\left(\frac{\varepsilon}{2k_BT}\right)\frac{1}{1+\omega^2\tau_{rel}^2}, \tag{6.44}$$

which is to be equated to $\delta k x_0^2/2$, the change in potential energy due to the reactive contribution, where $\delta k \approx \delta\omega_0/(2\omega_0)k_0$ is a spring constant modulation due to the real part of the TLS susceptibility (i.e. the instantaneous stress change due to an oscillating modulation strain). In the end, after integration over all TLS and over the volume as we did for the dissipated power, the relative change in the NEMS resonance frequency writes in the string limit:

$$\left.\frac{\delta\omega_0}{\omega_0}\right|_{rel}(T) = \frac{\omega_0^2 P_0 \overline{\gamma}^2 I}{\rho e w c_f^4}\mathcal{R}(T) = C\mathcal{R}(T), \tag{6.45}$$

where $\mathcal{R}(T)$ is defined analogously with $\mathcal{I}(T)$, as the averaging over all TLS susceptibilities' real parts:

$$\mathcal{R}(T) = \int_{u_{min}}^{\infty} \mathrm{d}u \int_0^1 \mathrm{d}v \frac{v^2}{1-v^2}\mathrm{sech}^2\left(\frac{u}{2}\right)\frac{1}{1+\omega^2\tau_{rel}^2(u,v)}. \tag{6.46}$$

Phonon-driven TLS relaxation rate in a nanostring at low temperatures

We now turn to a derivation of the TLS relaxation rate τ_{rel}^{-1}. To do so we must make reasonable assumptions on the bath to which an out-of-equilibrium TLS relaxes energy. First we investigate phonon-driven relaxation: its role is rather well known [37, 25, 149], and in our case the metallic layer can be made superconducting at very low temperature, suppressing the electron bath. However, in our case, dimensionality plays a crucial role: indeed most studies consider bulk phonon modes, that are irrelevant in the case of a truly 1D beam [43] at low temperatures. The energies of the two first transverse-polarized bulk modes are of the order $\hbar c_t\pi/e$ and $\hbar c_t\pi/w$ where $c_t \sim \sqrt{E/\rho}$ is the transverse sound speed and E is the elastic Young's modulus. For

temperatures below 1 K such modes' thermal populations are vanishingly small, and thus these modes do not exchange energy with TLS. This is where dimensionality reduction comes into play, as it amounts to saying that the dominant phonon wavelength $hc_t/(2.82k_BT)$ of the bulk equilibrium phonons is bigger than transverse dimensions. Only the longitudinal and torsional polarizations survive, and new families of modes emerge, that are solutions of the 1D Euler-Bernoulli equation (2.2) [43]: our usual flexural modes. It means that we have to consider four families of modes: one bulk longitudinal with sound speed $c_l = \sqrt{E/\rho}$, one torsional with $c_r = \sqrt{E/[2(1+\nu)]}$ and two flexural, with $c_f = \sqrt{\sigma_0/\rho}$ in the string limit. These four families of modes are all 1D channels into which phonons in thermal equilibrium propagate.

A TLS can relax from the high to the low energy state by emitting a phonon, with a rate $\tau_{e\to g}^{-1}$, or go from low to high energy by absorbing one, with a rate $\tau_{g\to e}^{-1}$. Populations p_e, p_g for the two states $|g\rangle, |e\rangle$ follow standard rate equations in the limit of weak perturbation from equilibrium:

$$\begin{cases} \dot{p}_g &= -\tau_{g\to e}^{-1} p_g + \tau_{e\to g}^{-1} p_e, \\ \\ \dot{p}_e &= -\tau_{e\to g}^{-1} p_e + \tau_{g\to e}^{-1} p_g, \end{cases} \tag{6.47}$$

with $p_e + p_g = 1$. The total rate τ_{rel}^{-1} at which the TLS polarization $p = p_e - p_g$ reaches equilibrium is the sum of both processes rates: $\tau_{rel}^{-1} = \tau_{e\to g}^{-1} + \tau_{g\to e}^{-1}$. Since the equilibrium polarization writes $p_0 = \tanh[\varepsilon/(2k_BT)]$, we have by solving the system (6.47) at equilibrium the detailed balance between the two rates (due to the possibility of spontaneous emission of a phonon), leading to: $\tau_{rel}^{-1} = \tau_{e\to g}^{-1}(1 + e^{-\varepsilon/(k_BT)})$. Thus, we only have to derive the emission rate. Initially, phonon populations are in thermal equilibrium at temperature T. Therefore, each mode $\omega_{\mathbf{k},s}$ (s corresponds to a given family: torsion, longitudinal or one flexural) has a population determined by the Bose factor $n_{k,s} = \left(\exp\left(\frac{\hbar\omega_{k,s}}{k_BT}\right) - 1\right)^{-1}$, and Fermi's Golden rule associated to an emission process writes:

$$\tau_{e\to g}^{-1} = \sum_{k,s} \frac{2\pi}{\hbar} \left| \left\langle g, n_{k,s}+1 \left| \widehat{\mathcal{H}}_{int}^{ph,\varepsilon} \right| e, n_{k,s} \right\rangle \right|^2 \delta\left(\varepsilon - \hbar\omega_{k,s}\right). \tag{6.48}$$

From reference books [155, 43], one can write the longitudinal strain field due to propagating phonons at thermal equilibrium in a simple second quantized form:

$$\overrightarrow{\widehat{\mathcal{E}}}_{k,l} = \sqrt{\frac{\hbar}{2\rho\mathcal{V}\omega_{k,l}}} \left(\widehat{a}_{-k,l}^{\dagger} + \widehat{a}_{k,l}\right) ik_l(-\nu, -\nu, 1, 0, 0, 0), \tag{6.49}$$

where $\mathcal{V}$ is the NEMS volume. The $\widehat{a}_{k,l}^{(\dagger)}$ operator is the annihilation (creation) operator for a phonon in the mode k_l, such that $n_{k,l} = \langle \hat{n}_{k,l} \rangle \equiv \langle \hat{a}_{k,l}^{\dagger} \hat{a}_{k,l} \rangle$. From the definitions of the strain operator (6.49) and Pauli matrices, the squared matrix element in (6.48)

can be evaluated:

$$\left|\left\langle g, n_{k,l}+1 \left| \widehat{\mathcal{H}}_{int}^{ph,\varepsilon} \right| e, n_{k,l} \right\rangle\right|^2 = \frac{\hbar k_l^2}{2\rho\mathcal{V}\omega_{k,l}} \frac{\overline{\gamma}^2\Delta_0^2}{\varepsilon^2}(n_{k,l}+1). \tag{6.50}$$

Here we have assumed that $\overline{\gamma}$ was the parameter introduced above, which was then taking into account the shear strain component. However, this shear component has a negligible contribution if we consider TLS: it is unlikely to be large, as strain is directed mainly towards z. Thus we neglect it, as well as torsional modes which emerge from shear. Going to the continuum limit for phonon modes, one needs to introduce the phononic density of states (DOS), $g(\hbar\omega_{k,l})$. Since phonon modes considered are those who match the TLS energy splitting by energy conservation, i.e. $\omega_{k,l} = \varepsilon/\hbar$, the TLS relaxation rate is easily calculated:

$$\tau_{rel}^{-1}(\varepsilon, \Delta_0) = \frac{\pi\Delta_0^2\overline{\gamma}^2 g(\varepsilon)}{\hbar^2\rho\mathcal{V}\varepsilon c_l^2} \coth\left(\frac{\varepsilon}{2k_BT}\right), \tag{6.51}$$

where we have used $\omega_{k,l} = c_l k_l$. Thus, in a similar fashion to phononic specific heat, the phonon-driven relaxation rate of two-level systems is **proportional to the phonon DOS**, which becomes crucial when the system studied has small characteristic dimensions. In addition, the quadratic dependence on the tunneling amplitude highlights the genuine role played by quantum tunneling of the atom in the process.

As we said earlier, the dominant phonon wavelength is roughly comparable with the structure's cross-dimensions in the $0.1-1$ K range. In this situation, confinement imposes a lower energy cutoff on the available phonon states, and only the longitudinal polarization survives. For 1D phonons in the pure linear dispersion relation case, the Debye DOS is constant [155]: $g_{1\mathrm{D}}(\varepsilon) = l/(\pi c)$, and therefore the TLS relaxation rate $\tau_{rel}^{-1} \propto \Delta_0^2/\varepsilon$ instead of $\Delta_0^2\varepsilon$ in the case of 3D phonons. In reduced units:

$$\tau_{rel}^{-1}(u, v, T) = \frac{\overline{\gamma}^2 k_B T}{\hbar^2\rho e w c_l^3}(1-v^2)u\coth\left(\frac{u}{2}\right). \tag{6.52}$$

In contrast to bulk structures where $\tau_{rel}^{-1} \propto T^3$, we obtain a relaxation rate that is linear in temperature, as a direct consequence of dimensionality reduction. Note also that the dependence in (u, v) is quite different. Thus, in one dimension, we can expect that the TLS contributing the most to the response are not the same as in 3D. A 2D plot of TLS contributions is shown in Fig. 6.13: we plot the real and imaginary part magnitudes of the TLS susceptibility normalized to the prefactor $\frac{\vec{\gamma}\cdot\vec{\mathcal{E}_0}}{2k_BT}$, as a function of the TLS parameters in reduced units, at 10 K (i.e. $\omega\tau_{rel} \gg 1$) and 0.1 K (i.e. $\omega\tau_{rel} \ll 1$).

As expected, the contribution of large tunneling amplitude TLS is almost inexistant at high temperatures: the TLS who dominate are those with $\Delta \sim \varepsilon$, simply because the

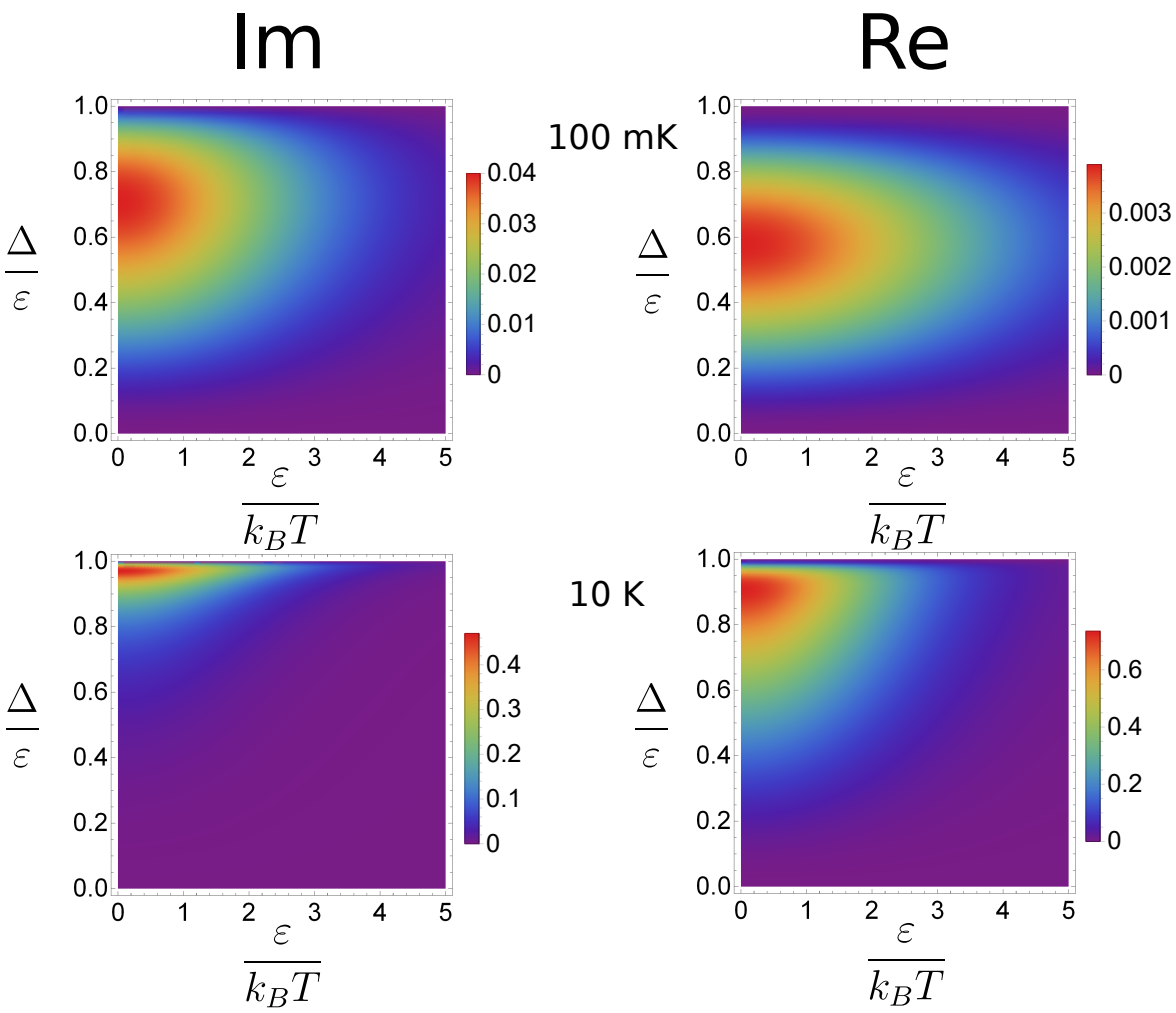

Figure 6.13: magnitude of the real and imaginary part of a TLS susceptibility normalized to $\gamma \cdot \mathcal{E}/(2k_BT)$, as a function of the reduced parameters $u = E/(k_BT)$ and $v = \Delta/\varepsilon$, for two temperatures representative of the two limit behaviours fixed by $\omega\tau_{rel}$.

TLS relaxation to the bath, which destroys the TLS coherence, is too fast compared to the drive to favor TLS with large tunneling amplitudes. At low temperatures, roughly $T < 1$ K, TLS with significant tunneling $\Delta_0 \sim 0.7\,\varepsilon$ dominate the response. Again, this is expected, since this time strain modulation prevents TLS to relax to the bath as it is faster than relaxation processes, thus protecting the TLS quantum coherence. However, we see also that low energy TLS $\varepsilon < k_BT$ are dominant in the relaxational response, in stark contrast to structures in the 3D phonon limit where dominant TLS are those whose energy is comparable to k_BT [156].

Now that we have the explicit TLS relaxation rate 6.52, we can calculate analytically the damping rate of the NEMS (6.39) in the limit $\omega\tau_{rel} \gg 1$:

$$\Gamma_{rel}(T) \underset{\omega\tau_{rel}\gg 1}{=} \frac{\pi^2\overline{\gamma}^2 C k_B T}{3\hbar^2 \rho e w c_l^3}. \tag{6.53}$$

We have not considered the contribution of flexural modes in this model. With the same reasoning, however, and adapting the strain field expression to flexural modes [38], a suppelementary ε^2 dependence appears in the relaxation rate (6.51), and thus one is left with a T^3 dependence which is masked by the linear dependence (6.53) below 1 K, so we discard it: TLS relaxation to these modes is too slow compared to relaxation to longitudinal modes. Furthermore, the macroscopic mode which is addressed (flexure) couples mostly through the strain field along the z direction. It is rather reasonable to imagine that the family of TLS sensitive to these deformations is not reacting much to shear. We can thus assume $\gamma_s \approx 0$ and discard the torsional family of phononic modes in our discussion (which produce only shear [43]).

Meanwhile, the frequency shift is suppressed for $T \ll 1$ K, and exhibits a logarithmic dependence for $T \gtrsim 1$ K:

$$\begin{aligned} \left.\frac{\delta\omega_0}{\omega_0}\right|_{rel}(T) &= 0 && \text{for} \quad \omega\tau_{rel} \gg 1, \\ &= -C \ln\left(\frac{T}{T_0}\right) && \text{for} \quad \omega\tau_{rel} \ll 1, \end{aligned} \tag{6.54}$$

with T_0 a reference temperature in the limit $\omega\tau_{rel} \ll 1$, that is, typically above 1 K, and $\omega_0 \equiv \omega_0(T_0)$ the corresponding reference frequency.

6.3.6 Resonant TLS-phonon interaction

Assuming that TLS are numerous enough to feature a continuous distribution, it follows that a collection of TLS have a splitting that matches the energy of a phonon from the excited mode at frequency ω **close to** ω_0 ($\varepsilon = \hbar\omega$), and thus resonant scattering of phonons by TLS has to be considered. The description of the resonant process is more straightforward than the relaxational one: the applied phonons are directly scattered by TLS at equilibrium through resonant absorption and emission, and we did not consider any effect of dimensional confinement on the distribution of TLS as soon as it is taken continuous. The number of phonons n_{ph} scattered by the whole ensemble of TLS per unit volume evolves as:

$$\dot{n}_{ph,V}(\omega) = -\int_{\varepsilon_{min}}^{\infty}\int_{\Delta_{0,min}}^{\varepsilon} \left[p_e\tau_{em}^{-1} - p_g\tau_{abs}^{-1}\right] \delta(\varepsilon - \hbar\omega) P(\varepsilon, \Delta_0) \mathrm{d}\varepsilon \mathrm{d}\Delta_0. \tag{6.55}$$

The absorption and emission rates $\tau_{abs}^{-1}, \tau_{em}^{-1}$ are again calculated with Fermi's Golden

rule, see Eq. (6.50), except this time we sum over TLS states instead of phonon ones, and the phonon number is not the thermal equilibrium one but the number of applied phonons. In addition, we have to consider here phonons from the excited flexural mode instead of the longitudinal ones. The strain field amplitude for the excited mode, in a second quantized fashion, writes [38]:

$$\overrightarrow{\overrightarrow{\mathcal{E}}}_0 = \sqrt{\frac{\hbar}{2m\omega_0}}\left(\widehat{a}^\dagger + \widehat{a}\right) x_t \frac{\partial^2 \Psi(z)}{\partial z^2}(\nu, \nu, -1, 0, 0, \nu). \tag{6.56}$$

Knowing the expression of the strain field, we can apply Fermi's Golden Rule to obtain τ_{em} and τ_{abs}. In the end after integration over the volume we have the following evolution for the phonon number:

$$\dot{n}_{ph} = -\int_{\varepsilon_{min}}^{\infty}\int_{\Delta_{0,min}}^{\varepsilon} \frac{\pi\omega^3\overline{\gamma}^2 I}{\rho e w c_f^4}(n_{ph}p_0 - p_e)\left(\frac{\Delta_0}{\varepsilon}\right)^2 \delta(\varepsilon - \hbar\omega)P(\varepsilon, \Delta_0)\mathrm{d}\varepsilon\mathrm{d}\Delta_0. \tag{6.57}$$

The solution to this equation yields a decay rate that writes:

$$\tau_{res}^{-1} = \int_{\varepsilon_{min}}^{\infty}\int_{\Delta_{0,min}}^{\varepsilon} \frac{\pi\omega^3\overline{\gamma}^2 I}{\rho e w c_f^4} p_0 \left(\frac{\Delta_0}{\varepsilon}\right)^2 \delta(\varepsilon - \hbar\omega)P(\varepsilon, \Delta_0)\mathrm{d}\varepsilon\mathrm{d}\Delta_0. \tag{6.58}$$

As pointed out earlier, the equilibrium TLS polarization is $p_0 = \tanh\left(\frac{\varepsilon}{2k_BT}\right)$. Integrating over the tunneling energies is straightforward and can be taken easily in the $\Delta_{0,min} \to 0$ limit. That also permits to extend the other integral to $\varepsilon_{min} \to 0$, which vanishes with the Dirac function that imposes $\varepsilon = \hbar\omega$. In the end, the damping rate is directly the phonon relaxation time:

$$\tau_{res}^{-1} = \pi\omega C \tanh\left(\frac{\hbar\omega}{2k_BT}\right). \tag{6.59}$$

In the limit where $\hbar\omega \ll k_BT$ it is negligible. Yet the change in the sound speed (the instantaneous modulus) is obtained through the Kramers-Kroenig relation [149]:

$$\delta c_f = \frac{c_f}{\pi}\int_0^{+\infty} \frac{\tau_{res}^{-1}(\omega')}{\omega^2 - \omega'^2}\mathrm{d}\omega', \tag{6.60}$$

Since there is an integration over all frequencies, the change in the sound speed is not necessarily negligible. Finally, the frequency shift (i.e. the change in the sound speed) relative to a reference frequency at an arbitrary temperature T_0, for temperatures such that $k_BT \gg \hbar\omega$, writes:

$$\left.\frac{\delta\omega_0}{\omega_0}\right|_{res}(T) = C\ln\left(\frac{T}{T_0}\right), \tag{6.61}$$

with again T_0 the reference temperature. Interestingly, the resonant and relaxational contribution to the frequency shift cancel each other above 1 K, leading to a zero net contribution. At very low temperatures however, the resonant contribution should be the only one left, and its observation a clear signature of a TLS-like behaviour.

Note that the C constant appears as a single fit parameter for the two different processes: as a slope for the frequency shift and the plateau value of the damping. Therefore the values found should be reasonably similar to confirm the theory. At the same time, the damping rate on the NEMS at low temperatures, Eq. (6.53) involves C, known macroscopic mechanical parameters and the coupling strength $\overline{\gamma}$. By fitting damping and shift in the different regimes, it is thus possible in fine to extract the density of TLS P_0 and the effective coupling strength $\overline{\gamma}$. This is what we shall discuss now on the basis of our experiments.

6.4 Results and discussion

6.4.1 Measurement protocol

The experimental procedure is simple. For a given temperature T, we measure the resonance frequency and mechanical damping using the magnetomotive technique, and subtract first the capacitive and resistive loading contributions (see Chapter 2 Section 2.6.3). A few precautions need to be taken: firstly, we measured in both normal and superconducting states of the metallic layer by tuning the magnetic field (see Fig. 6.14), searching for signatures of normal-state electrons contribution to the damping, following Ref. [28]. The magnetic field is parallel to the thin metallic film, leading to high enough critical applied magnetic fields so we can safely investigate the superconducting regime for temperatures below 1 K. The critical temperature of the Al thin film is found to be $T_c = 1.4 \pm 0.05$ K, typical of thin films whose critical temperature is usually higher than for bulk Al [157] where it is 1.2 K [44]. Incidentally, the temperature was monitored by two thermometers anchored to the mixing chamber plate of the cryostat with a regulation loop so as to ensure that our measurements were made at a stable temperature.

In the superconducting state, a damping rate non-linear in the displacement amplitude is observed, as reported in Ref. [28]. We do not focus on this feature here, which might arise from a departure from the small strain perturbation limit used in our modelling and calls for further investigations. Thus, we measure a resonance with a decreasing driving force, and in case the non-linear dependence is significant, we extrapolate the behaviour at zero force. In particular, additional non-linearities distorting the resonance line come into play below 100 mK, that might originate from vortices unpinned in the metallic layer (thin film Aluminum is in practice a type-II superconductor) [158]. They are rather well captured by a phenomenological Duffing-

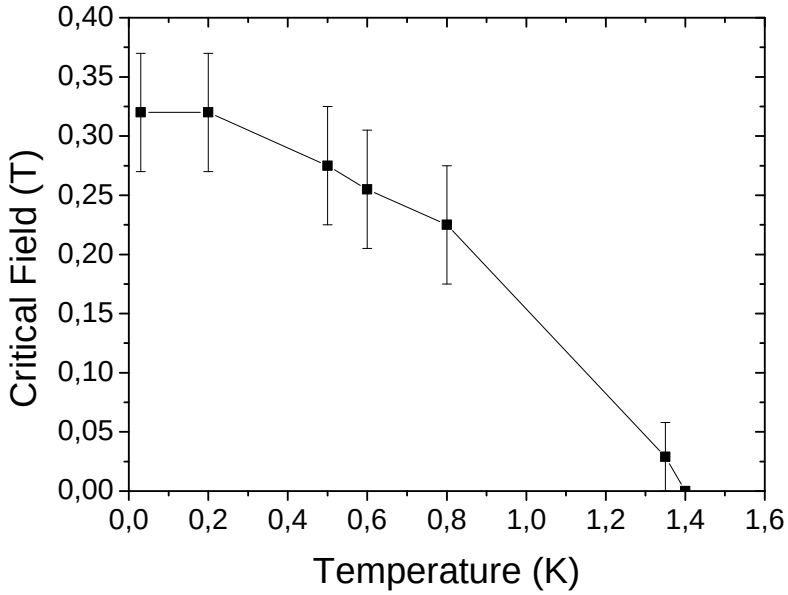

Figure 6.14: average critical field as a function of temperature. The intermediate region between superconducting and normal state due to the type II nature of the thin film superconductor is not shown, but it explains the rather large error bars. The critical temperature is evaluated at $T_c = 1.4 \pm 0.1$ K.

like non-linearity, explained in greater detail in Ref. [28]. These non-linearities are not addressed here. We simply measure the response down to the lowest force possible to obtain a reliable extrapolation, using our calibrations to convert the resonance amplitude to a displacement and thus to a damping rate through $x_{max} = \frac{F_0}{m\omega_0 \Gamma}$. We use the 15 µm beam because its cross-over temperature between the plateau regime at high temperatures and the power law one at low temperatures is higher than for, say, the 250 µm device used for frequency noise measurements. Thus, the investigation range for TLS behaviour is larger in temperature.

6.4.2 Results for the damping

With these precautions we can reach a resolution of 10 % on the extrapolated NEMS damping rate and frequency shifts in the superconducting state. The result for the damping rate is shown in Fig. 6.15, for both normal and superconducting state, down to 30 mK. Below this temperature, the signal is not clear enough to obtain reliable information.

At high temperatures ($T \gtrsim 2$ K) the damping rate exhibits a small linear dependence, that was measured already for all our devices and is attributed to friction at grain boundaries. The slope is very small (~ 3 %), starting from a constant value

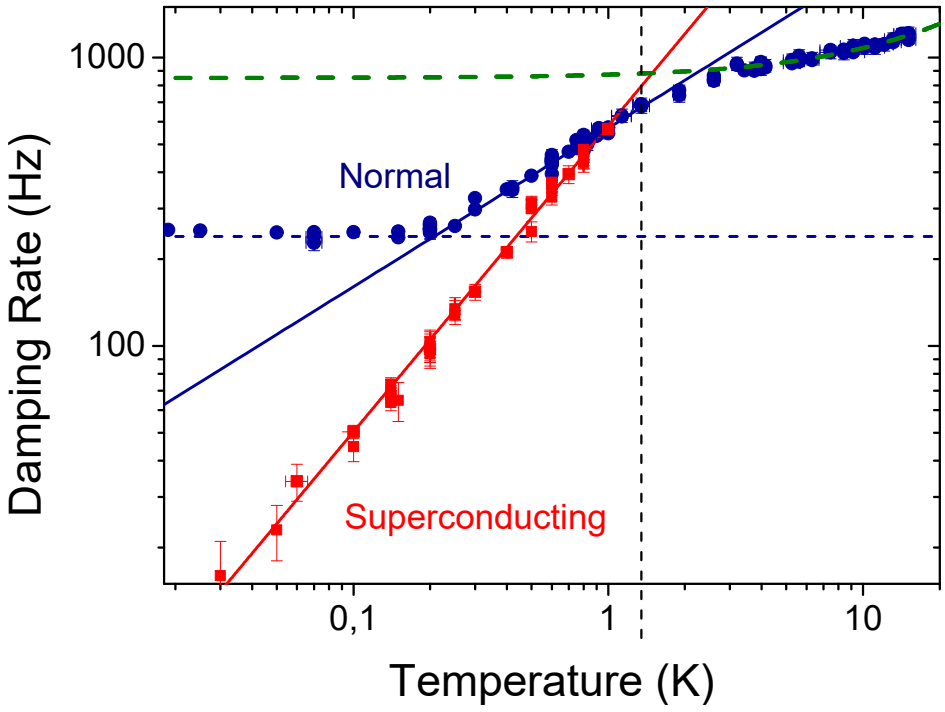

Figure 6.15: damping rate as a function of the cryostat base temperature for a 15 µm long device. The red dots are data taken in the superconducting state (S) and extrapolated at zero magnetic field, while the blue dots are obtained in the normal state (N), with the loading contribution removed. Solid lines are power law fits, yielding an exponent 1.06 in the superconducting state (red line) and 0.55 in the normal state (blue line). The dashed vertical line indicates the critical temperature of the aluminum layer $T_c = 1.4$ K, while the green dashed line is the high-temperature dependence already discussed in Chapter 2 section 2.7. In the normal state, a saturation is seen at the lowest temperatures (dashed horizontal blue line).

around 3 K at 850 ± 25 Hz which we think is the plateau value (6.53) due to the contribution from all TLS relaxing faster to the environment than the strain variation: as temperature is increased, their interaction with the environment is stronger so they relax faster. Below 2 K, the damping rate decreases rather quickly as the NEMS is cooled down. Below $T_c = 1.4$ K and down to about $T \approx 800$ mK, it follows a rather weak power law $\Gamma \propto T^{0.5\pm0.05}$ for both normal and superconducting states, i.e. a sublinear dependence that is qualitatively close to results previously obtained in the literature for NEMS at least partially metallic [151, 27]. Note, however, that these results were obtained with unstressed devices, which might limit our comparison as far as relaxation to phonons is concerned: indeed, it is argued in Ref. [159] that flexural modes with quadratic dispersion relations instead of linear (our case, because of high in-built stress) dominate over the other modes in the TLS relaxation, which ultimately leads to a $T^{1/2}$ damping rate.

Nevertheless, below 800 mK, the damping rate in the superconducting state departs from its normal state counterpart, following instead a linear ($\Gamma \propto T^{1.06\pm0.1}$) law down to 30 mK. Meanwhile the normal state damping follows the same law as above, down to 200 mK where it saturates around 250 Hz. The damping in the superconducting state is rather close to our expectations: its temperature dependence compares well qualitatively with the expression (6.39) derived above, as well as with the results obtained on a similar sample (dimension-wise), made of superconducting Aluminum in Ref. [160]. Note that we do not reproduce the $T^{3/2}$ law reported in Ref. [28] for a goalpost cantilever structure: if we allow ourselves to speculate a little, such a feature might owe to the goalpost peculiar geometry and modal decomposition [161], combined with the fact that according to Ref. [159] flexural modes with quadratic dispersion relations (as in the goalpost cantilever or unstressed beam cases) should dominate the phonon-driven relaxation of TLS, leading to non-integer power laws of temperatures.

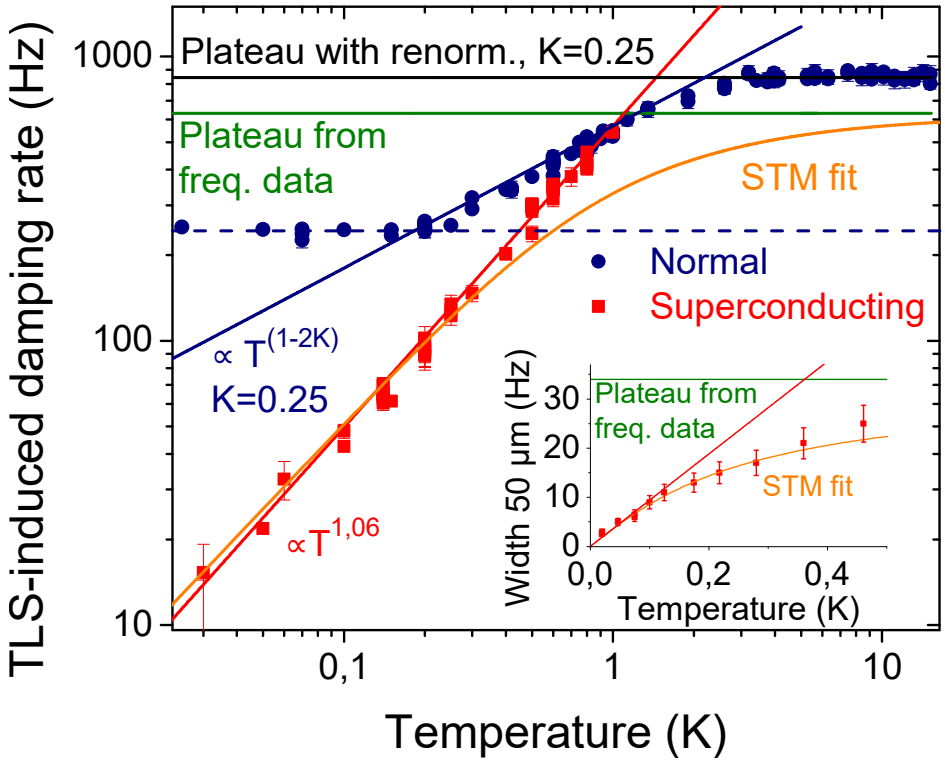

Figure 6.16: damping rate as a function of the cryostat base temperature with the small linear slope subtracted, with the same convention for the dots as in Fig. 6.15. Added solid lines are various fits corresponding to different scenarios detailed in the text. Inset: same data for the 50 µm device embedded in a microwave cavity.

One can remove the tiny slope at high temperature so as to leave only what is thought to be the damping due to TLS relaxing. The result is shown in Fig. 6.16. If we take as a given the plateau value predicted by the STM at 625 Hz, obtained

from frequency shift measurements (see Fig. 6.18 in the next section, $C = 2.3 \times 10^{-5}$ should be the same for the plateau and the frequency shift below 1 K), we observe a discrepancy between the STM model prediction (yellow curve in Fig. 6.16) and the measured plateau value at 850 Hz, of about 25 %. One can argue that the plateau is measured for temperatures at which the aluminum layer cannot be superconducting, and that a contribution from electrons might renormalize the expected plateau value. This possibility is discussed later. We fit the data to the expression (6.39) with the 1D phonon-driven relaxation rate (6.52) with a coupling strength $\overline{\gamma} = 10$ eV and a TLS density $P_0 = 1.9 \times 10^{44}$ J^{-1}.m^{-3}, thus assuming that the plateau value that truly counts with respect to our modelling is the one in agreement with the slope of the frequency shift, while the measured value depends on electron-mediated mechanisms (see our discussion in the next section).

A comparison can be made with a 50 µm NEMS mounted for microwave optomechanical experiments and measured with our collaborators Xin Zhou, Rasul Gazizulin and Dylan Cattiaux. Except for its length and its read-out system (a superconducting microwave LC circuit capacitively coupled to the NEMS thermomechanical motion [162]), its mechanical characteristics are identical to the 15 µm device. Due to the experiment configuration, it was not possible to measure the device at higher temperatures than 500 mK, as quasiparticles start to alter the microwave cavity functioning above this temperature. For the same reason, we cannot measure the damping rate in the normal state because a magnetic field would also destroy the cavity superconductivity which is necessary. Thus, we only have the data in the superconducting regime in the slow TLS limit, where it initially follows the linear slope but rather quickly curves: if we take as a plateau value the constant extracted from frequency measurements (see Fig. 6.18 inset in the following section), however, we see that this is perfectly consistent with the tunneling model if we take roughly the same strain-TLS coupling constant as for the 15 µm, $\overline{\gamma} = 8.5$ eV but increase the density of TLS by almost one order of magnitude $P_0 = 1.2 \times 10^{45}$ J^{-1}.m^{-3}. Considering the discrepancy usually reported on this parameter, which spreads over a couple of orders of magnitude, this seems acceptable: the two beams have not been realized at the same time, and did not undergo the same process. The 50 µm higher density of TLS might as well be explained by all the additional steps that were required to fabricate an embedded sample. Besides, it might be that with submicronic structures we truly reach the regime where the discrete nature of the TLS distribution come into play: in that case, it makes a description in terms of P_0 rather inaccurate, as there is not enough volume to really consider a significant number of TLS so as to form a continuous distribution. Usual densities reported for $P_0 \sim 10^{44}$ J^{-1}.m^{-3} are in the $10^{19} - 10^{20}$ m^{-3} range, [151, 163], which leads to an estimate of the number of TLS as small as $\sim 10 - 100$ in our beams (there is only roughly a factor of 3 in length between our two beams). Such an estimate poses a limitation to really quantitative modelling, as this number is likely to vary a lot in relative units, depending on the materials and the fabrication process.

In 1D, the cross-over from fast to slow TLS (relative to the drive frequency) happens to be rather smooth, which explains why the data remain still a factor of 2 below the predicted plateau. Despite this, they are well captured by the fit, and deep enough in the superconducting regime so we do not see any quasiparticle effect that might lead to a disagreement with the model as opposed to the case of the 15 µm beam.

The discrepancy between normal and superconducting state damping, on the other hand, is qualitatively consistent with previous measurements reported in Ref. [28]. In addition, we report a similar power law as in this work and that of Refs. [151, 27], where measurements on metallic beams were made in the normal state. One notable exception is the work of Ref. [26], where no sublinear dependence was observed in the damping, falling linearly even in presence of normal-state electrons. However, the authors raised the possibility that kinks on dislocations were more likely candidates than TLS in their polycrystalline materials, leading to different relaxation mechanisms. This exception left aside, the similarity between several measurements in rather different conditions (different metals, partially or fully metallic beam, bending and string limit) but all having in common normal-state electrons, added to the comparison with the superconducting state in our case, points towards an electron-assisted mechanism rather than what Ref. [159] proposes, i.e. a pure phononic relaxation leading to a sublinear temperature dependence. This is further supported by the fact that no difference between the two states is observed above 800 mK: it seems natural insofar as in the superconducting regime, the fraction of electronic quasi-particles becomes dominant for temperatures above $T_c/2$ [164]. Electron-driven mechanisms are discussed later in this section.

The saturation observed in the normal state at 200 mK and below is not specific to our measurements: it has been measured also in Refs. [151, 27, 28]. However, in the case of Ref. [27], this saturation occurs at lower temperatures, around 30 mK. One should notice that in this work care was taken to filter both injection and detection lines, which is not the case here or in Refs. [151, 28]. Thus, a possible explanation is simple thermal decoupling from the cryostat temperature due to electromagnetic radiation carried out by unfiltered injection and detection lines, which heats up electrons in the metallic layer. Since at such temperatures phonons and electrons are still well coupled, it means that the environment temperature, whether it is phonons or electrons for the TLS, remains at 200 mK and progressively gets decoupled from base temperature as the latter is lowered.

6.4.3 Results for the frequency shift

The resonance frequency is also systematically measured as a function of temperature, both in normal and superconducting state for the 15 µm device. Again, all known extra-contributions (Duffing-type non-linearities, magnetomotive loading) were removed. The result is shown in Fig. 6.17. Above 1 K, the resonance shifts downwards

quickly, as already measured for all our samples (see Fig. 2.18). We fit the data to our usual $aT + bT^3$ law (see Chapter 2 section 2.7): in this limit, the frequency shift seems only to originate from the interface mismatch between Al and SiN generating differential stress. The fact that no other contribution is observed above 1 K is consistent with our modelling, which predicts that the resonant (6.61) and the relaxational contribution (6.45) of the STM should cancel each other in this limit.

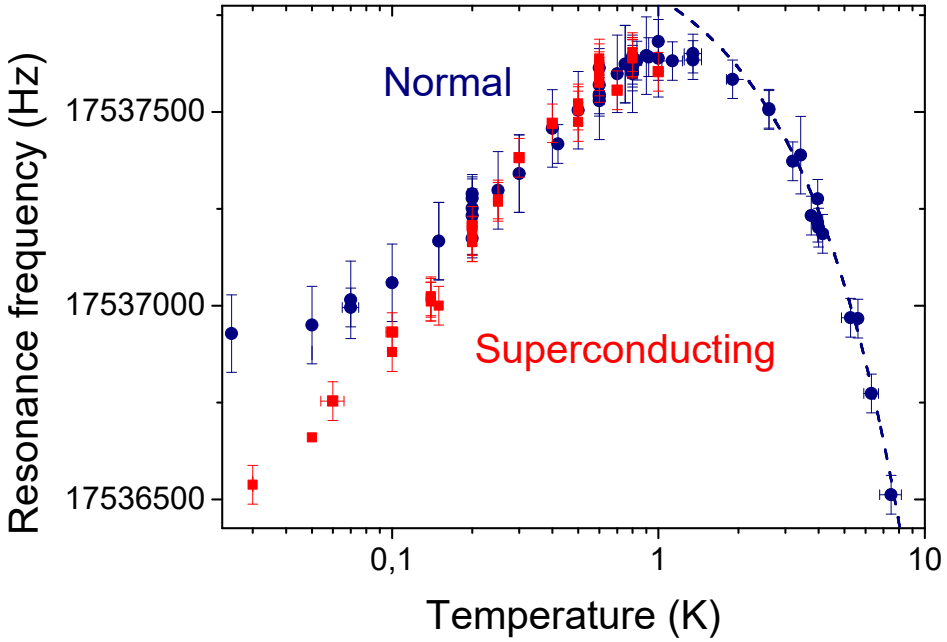

Figure 6.17: resonance frequency as a function of temperature for the 15 µm device, with the same color conventions as in Fig. 6.15. The dashed line is a fit of the type $aT + bT^3$.

Below 1 K, however, we observe the usual logarithmic dependence. Note that this behaviour is rather weak and is not directly observable in the superconducting state because of non-linear features [28], which explains the rather large error bars. From 1 K down to 200 mK, in contrast with damping data, there is no discrepancy between the normal and superconducting states, as observed in Ref. [28]. This seems reasonable, as the dominant process, i.e. resonant, is different in nature from the relaxational one which dominates the damping: in the resonant interaction picture, the applied phonons are directly scattered by TLS, without any intervention of the electrons, and thus the frequency shift should not depend on the electronic state since the relaxational interaction contribution (6.54) is essentially zero in this temperature range. Below 200 mK the normal state shift departs from the superconducting one. However, the deviation is much "softer" than the kink observed when saturation occurs for the damping data. It indicates that the mechanism behind the observed saturation might be a true physical effect, and not a simple thermal decoupling. This calls for further work with proper shielding from electromagnetic radiation, to decide between

a spurious effect due to thermal decoupling from the cryostat temperature or some additional mechanism yet unknown.

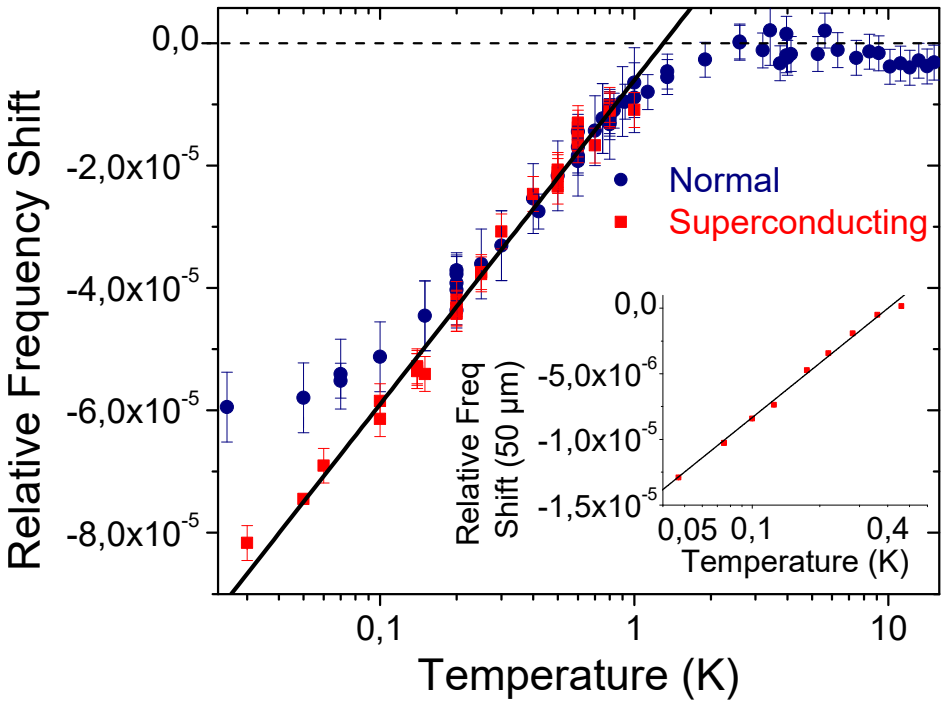

Figure 6.18: relative frequency shift $\delta\omega/\omega_0$ as a function of temperature, with the differential stress contribution (see Fig. 6.17) removed. The black solid line is the application of Eq. (6.54), i.e. a logarithmic fit yielding a slope $C = 2.3 \pm 0.3 \times 10^{-5}$. Inset: same procedure applied to the 50 µm long NEMS embedded in a microwave cavity. The fit slope is $C = 0.6 \pm 0.1 \times 10^{-5}$.

The fit to the data using Eq. (6.61) for the logarithmic slope yields a parameter $C = 2.3 \pm 0.3 \times 10^{-5}$. This is a little low compared to the usually expected glassy range plateau, which situates it more in the $10^{-3} - 10^{-4}$ range. However, with the aspect ratio renormalisation of C developed in our modelling, it makes more sense, and compares well with the values obtained for nanomechanical resonators in Refs. [27, 28]. It leads through Eq. (6.41) to a comparative bulk C constant in the 10^{-4} range, which is very reasonable with respect to the hypothesis of the universality of glasses. For the 50 µm long NEMS, it is also reasonable, as it leads through renormalization to a corresponding $C_{bulk} \sim 10^{-3}$, still well in the glassy range. For a TLS density $P_0 \sim 10^{44}$ J^{-1}.m^{-3} in accordance with literature [156], we assume that the TLS-strain coupling constant $\overline{\gamma}$ is in the 10 eV range, that is, one order of magnitude higher than usually reported constants. Note that such a high value has been recently reported for GaAs optomechanical structures [163].

6.4.4 Discussion on the contribution of normal state electrons

Even though the role of normal state electrons is qualitatively evidenced, the microscopic mechanism remains elusive. One first striking fact is that this effect is only visible in such manner (discrepancy between normal and superconducting state + sublinear in normal state) for sub-micronic devices: experiments performed on micron-size structures [165] and macroscopic vibrating wires [166] did not reveal such a difference. In Ref. [167], a discrepancy between normal state and superconducting frequency shifts was reported for a vibrating Al reed, though nothing could be concluded on the influence over the damping due to the presence of large eddy current damping.

The question of the interplay between electrons and two level systems in metallic glasses has attracted a consequent number of studies ever since the beginning of the Standard Tunneling Model as a realistic theory to explain low temperature properties of amorphous solids. Notably, sound attenuation experiments [153] have established that for bulk metallic glasses at low temperature, the temperature dependence of the TLS relaxation rate was much weaker than that observed for the same experiments in dielectric materials where they were explained by the usual TLS-phonon coupling. However, this discrepancy is not expected in our experiments, as the NEMS cross dimensions, below 1 K, are smaller than the dominant phonon wavelength, thus leading to much weaker dependences in T of the TLS relaxation rate (see section above). Besides, the Al film structure is more polycrystalline than amorphous, though it is claimed in Ref. [168] that it is irrelevant. We can assume that our measurements in the superconducting state of the metallic layer below $T_c/2$ give us access to a pure phononic contribution to the TLS relaxation, as the Cooper pair condensate is not scattered by TLS [169] and the quasiparticles density is small. Note that in principle, electron-driven relaxation is irrelevant at high temperatures since the damping does not depend anymore on the TLS relaxation times. However, it is impossible, with our data, to find a quantitative agreement between the slope of the frequency shift and the plateau value to more than 25 % (see Fig. 6.16). One can argue that in the plateau region, we cannot have access to a pure phononic contribution as the layer is not superconducting, which means that the role of electrons might extend to more than a simple change in the TLS relaxation rate.

A simple microscopic picture can describe the basic electron-driven relaxation of TLS: while tunneling, a TLS changes the local atomic configuration, which causes a local variation of the Coulomb atomic potential that scatters conduction electrons: this can be seen as scattering of the electrons by TLS mediated by virtual phonons, resulting in the following effective Hamiltonian in the position basis, which takes into account the electron spin s:

$$\widehat{\mathcal{H}}_{int}^{el,p} = \sum_{\mathbf{k},\mathbf{q},s} \left(V_{\mathbf{k},\mathbf{q}}^{z} \widehat{\sigma}_z + V_{\mathbf{k},\mathbf{q}}^{x} \widehat{\sigma}_x \right) \widehat{c}_{\mathbf{k},s}^{\dagger} \widehat{c}_{\mathbf{q},s}, \tag{6.62}$$

where we have introduced fermionic creation/annihilation operators $\widehat{c}^{(\dagger)}_{\mathbf{k},s}$. Note that this interaction conserves the electron spin, ruling out at first order mechanisms of magnetic origin to explain our observations. Considering only conduction electrons in a narrow band on the surface of the Fermi sea, since the TLS have energies $\ll \varepsilon_F$, we can approximate $V^{x,z}_{\mathbf{k},\mathbf{q}} \approx V^{x,z}$. Since the Fermi wavelength $\sim 1-10$ nm is smaller than the aluminium layer cross-dimensions, the electronic density of states n is assumed to be 3D. As our working temperature is much lower than the Fermi temperature $T_F \sim 10^5$ K for aluminium, we assume that the electronic DOS n_e is slowly varying in the vicinity of the Fermi-Dirac distribution. In other words, $n_e(\varepsilon) \approx n_e(\varepsilon_F) \propto \sqrt{\varepsilon_F}$. Therefore, the wavelengths at stake are this time a few Å at most, so at first glance there is no reason to neglect electron-assisted tunneling, i.e. the $\widehat{\sigma}_x$ term in the coupling Hamiltonian (6.62). Note that in principle, the tunneling amplitude is due to the two-well wavefunctions overlap, which is by definition small: thus, we do not expect electron-assisted tunneling to play a significant role in the TLS relaxation to electrons but keep it in the calculation of the TLS-electron bath relaxation rate.

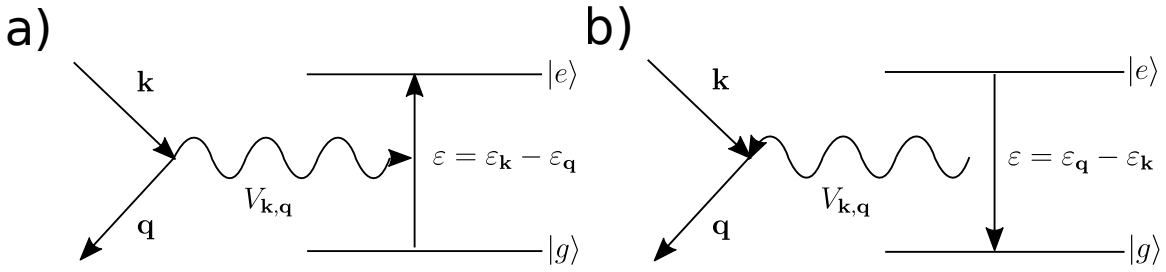

Figure 6.19: diagrams of the first order processes leading to electron-TLS energy exchange as calculated in Eq. (6.63).

Using again lowest order perturbation theory, Fermi's Golden Rule provides a relaxation rate for weak electron-TLS coupling, accounting for processes depicted in Fig. 6.19:

$$\tau_{el}^{-1}(\varepsilon) = \frac{2\pi}{\hbar} \sum_{\mathbf{k},\mathbf{q},s} \left[\left| \left\langle e, N_{\mathbf{q},s}+1, N_{\mathbf{k},s}-1 \left| \widehat{\mathcal{H}}^{el,\varepsilon}_{int} \right| g, N_{\mathbf{q},s}, N_{\mathbf{k},s} \right\rangle \right|^2 \delta\left(\varepsilon - \varepsilon_{\mathbf{k}} + \varepsilon_{\mathbf{q}}\right) \right.$$
$$\left. + \left| \left\langle g, N_{\mathbf{q},s}+1, N_{\mathbf{k},s}-1 \left| \widehat{\mathcal{H}}^{el,\varepsilon}_{int} \right| e, N_{\mathbf{q},s}, N_{\mathbf{k},s} \right\rangle \right|^2 \delta\left(\varepsilon - \varepsilon_{\mathbf{q}} + \varepsilon_{\mathbf{k}}\right) \right], \quad (6.63)$$

where $\widehat{\mathcal{H}}^{el,\varepsilon}_{int}$ is the interaction Hamiltonian with the fermionic bath re-written in the energy eigenbasis and $|N_{\mathbf{k},s}\rangle$ refers to the number of electrons in a state $|\mathbf{k},s\rangle$ in Fock space. Because of fermionic rules of occupation, for an electron of spin s going from state $|\mathbf{k},s\rangle$ to state $|\mathbf{q},s\rangle$ by TLS scattering there must be initially one

electron in $|\mathbf{k}, s\rangle$ and zero in $|\mathbf{q}, s\rangle$. Assuming conduction electrons are thermalized at a temperature T, this appears by introducing the Fermi-Dirac distribution $f(\varepsilon_\mathbf{k}) = 1/\left[1 + \exp\left(\frac{\varepsilon_\mathbf{k} - \varepsilon_F}{k_B T}\right)\right]$. Summing over all possible initial (final) states $|\mathbf{k}, s\rangle$ ($|\mathbf{q}, s\rangle$) allowed by energy conservation and taking into account spin degeneracy, we obtain:

$$\tau_{el}^{-1}(\varepsilon) = \frac{4\pi n_e^2(\varepsilon_F)\mathcal{V}^2}{\hbar}\left[(\Delta_0/\varepsilon)^2|V^z|^2 + \left(1 - (\Delta_0/\varepsilon)^2\right)|V^x|^2\right] \times \left[h(\varepsilon) + h(-\varepsilon)\right], \quad (6.64)$$

where $h(\varepsilon)$ is an overlap integral of Fermi-Dirac distributions obtained by summing over all final electron states of energies $\varepsilon_\mathbf{q} = \varepsilon_\mathbf{k} - \varepsilon$ (or $\varepsilon_\mathbf{k} + \varepsilon$ if energy is yielded by the TLS rather than absorbed):

$$h(\pm\varepsilon) = \int_0^{+\infty} f(\varepsilon_\mathbf{k})\left[1 - f(\varepsilon_\mathbf{k} \pm \varepsilon)\right] \mathrm{d}\varepsilon_\mathbf{k}. \quad (6.65)$$

This integral is analytic, and in the limit $\varepsilon_F \gg k_B T$, the electron relaxation rate yields:

$$\tau_{el}^{-1}(\varepsilon) = \frac{4\pi n_e^2(\varepsilon_F)\mathcal{V}^2}{\hbar}\left[(\Delta_0^2/\varepsilon)|V^z|^2 + \left(\varepsilon - (\Delta_0^2/\varepsilon)\right)|V^x|^2\right] \coth\left(\frac{\varepsilon}{2k_B T}\right). \quad (6.66)$$

This result is rather disappointing: writing τ_{el}^{-1} in reduced units makes a linear dependence in temperature appear, which is no different from phonon-driven relaxation. Therefore, it is not enough to explain our $T^{1/2}$ dependence.

However, this is only true if we sum over the usual distribution of TLS energies. It might as well be that the collection of TLS that effectively contribute to the electron-TLS interaction is not the usual distribution. Theoretical attempts have been made to explain anomalous sound attenuation in metallic glasses [170], which invoke a renormalisation of the TLS distribution due to second-order perturbation contributions in the electron-TLS interaction, which appear to be strong in most experiments. The argument, developed by Kondo [171], is that the second order term of the electron-TLS interaction depends logarithmically on the ratio between the conduction bandwidth and thermal energy $k_B T$. Therefore, at low temperature (analogous to temperatures below a Kondo temperature for resistivity), there is no reason to neglect this second-order term, leading to qualitative features in stark contrast with what we obtained through Eq. (6.66). In Ref. [170], a calculation based on dissipative tunneling theory [172] leads the authors to propose the following explanation: the strong coupling of a TLS to the fermionic bath leads to a renormalisation of the tunneling amplitudes $\Delta_0 \to \Delta_r = \Delta_0(\Delta_0/D)^{K/(1-K)}$, where D is a high-energy cut-off and $K \propto n_e(\varepsilon_F)|V^z|^2$ is a normalized electron-TLS coupling strength. This renormalization affects substantially low-energy TLS, whose energy lies within the electron conduction band. In the end the TLS relaxation time, and thus the damping scales as:

$$\begin{aligned} \Gamma_{rel} &\propto T^{1-2K} && \text{for} \quad \omega\tau_{rel} \gg 1, \\ &= \frac{\pi C \omega}{2(1-K)} && \text{for} \quad \omega\tau_{rel} \ll 1, \end{aligned} \tag{6.67}$$

This is valid in the incoherent tunneling regime, that is, as long as $Kk_BT/\Delta_r \gg 1$, which is always true in our case. Thus, the strong interaction between electrons and TLS would not only renormalize the low-temperature damping rate, but it would also affect the plateau value (see the data and the black horizontal solid line in Fig. 6.16). The K constant is left as a free parameter, and we find out that both the plateau and the damping rate in the normal state are well captured for $K = 0.25$, as shown in Fig. 6.16. This is consistent with the fact that the normal state and superconducting state give equal damping rates above 800 mK, because the distribution of TLS is renormalized the same way independently of the relaxation channel. Indeed, above $T_c/2$ the quasiparticles density is significant enough to ensure that the distribution is renormalized by the strong electron-TLS coupling. Then it leads also to a renormalized damping rate for TLS-phonon coupling since it involves a sum over the TLS distribution. In that case it would explain why such a discrepancy is observed only for low dimensional structures: we have seen in section 6.3.5 that if the phonon bath is reduced to one dimension, the TLS that are most affected by energy relaxation to the bath are the low energy ones $\varepsilon \ll k_BT$, that is, the ones more likely to be affected by a strong coupling to electrons. In short, the mechanism we propose is not directly electron-driven relaxation; it is rather the relaxation to phonons of TLS with a distribution renormalized by the TLS interaction with electrons, which somehow screen the TLS seen by the phonon bath, in analogy with conduction electrons spins screening the spin of a magnetic impurity in the Kondo problem. Note that discrepancies in the K constant, which is material-dependent, might explain the variety of sublinear laws observed in the literature, between 0.3 and 0.7 [151, 27, 28].

6.4.5 Discussion on the TLS location

While the modelling seems robust, and the results reveal many signatures of a TLS-like behaviour, the coupling strength extracted is not very satisfying. Besides, our calculation assumed for simplicity that TLS were uniformly distributed spatially in the beam. This last assumption, for our actual beams, might well be wrong, because of the beam's bilayer nature: while a TLS model seems licit if we address the dissipation arising from the SiN amorphous layer, it is more difficult to justify in the metallic layer because of the latter's polycrystalline structure. Yet, the discrepancy we observe between normal state and superconducting damping clearly favours TLS present in the metallic layer, as the nitride is electrically insulating. In Ref. [152] it is argued that

TLS-like behaviour might still emerge in a crystal, though the excitations would be very narrowly distributed in energy around zero due to the long-range order present in a crystal. This so-called Phillips model leads to a linear temperature dependence of the TLS relaxation rate with a logarithmic relative change in frequency, which would be in agreement with our measurements and the results of Ref. [160] where the beam was metallized. However, this is inconsistent with the observation of Ref. [28] where both the metallic layer and the insulating one were crystalline, with the same deposition method as the present work, and where a damping $\propto T^{3/2}$ was observed.

In the end, a reasonable assumption would be that TLS be located in the oxide Al_2O_3 layer that inevitably grows after a few minutes on the aluminum layer [173]. As this occurs essentially on the surface, the TLS that form in this oxide matrix couple much more to the strain field, which is larger on the surface (that is, the furthest from the neutral axis) according to Eq. (6.34). Besides, the surface TLS can show rather different natures than their bulk counterpart: they can be e.g. nanovoids due to the deposition process. Such a difference might explain the difference in coupling strength. As our modelling shows, the low-dimensional character of the beams makes them much more sensitive to the surface contribution, while the volume contribution is smeared out: this is somewhat the spirit of the renormalisation on C presented in Eq. 6.41: if the structure was truly bulky, the C constant would not likely lie in the 10^{-5} range. This is because the volume contribution would dominate over the surface one, since the strain field would gradually be reduced to the bulk modes, leading to enhanced couplings to bulk TLS rather than surface ones and reducing to the usual plateau constant of glasses. Note that the oxide layer explanation also reconciles qualitatively our measurements in the superconducting state with those obtained in Ref. [28], as it is certain that the same oxide was present. It is also consistent with the electronic relaxation scenario, as the oxide layer is only a few atomic layers thick above the conducting aluminum layer, and maybe not uniform.

6.4.6 Link to frequency noise

The last part of this chapter shows our experimental attempt to demonstrate the link between TLS features in the nanomechanical damping and the frequency noise of nanomechanical structures at low temperatures. Using the technique described earlier in this Chapter to measure frequency noise, by systematically counting bifurcation events on the lower branch in order to be sensitive only to actual frequency noise, we measure the frequency fluctuations of our device in an unprecedented way, separating normal state data from superconducting ones. The spectrum for this sample scales as $1/\omega^{1.2}$ regardless of the electronic layer state. The result for the frequency noise magnitude, plotted in terms of Allan deviation to bypass non-stationary contributions (see the first section of this Chapter), is shown in Fig. 6.20, along with damping fluctuations measurements that also reveal a discrepancy (see Fig. 6.20 inset).

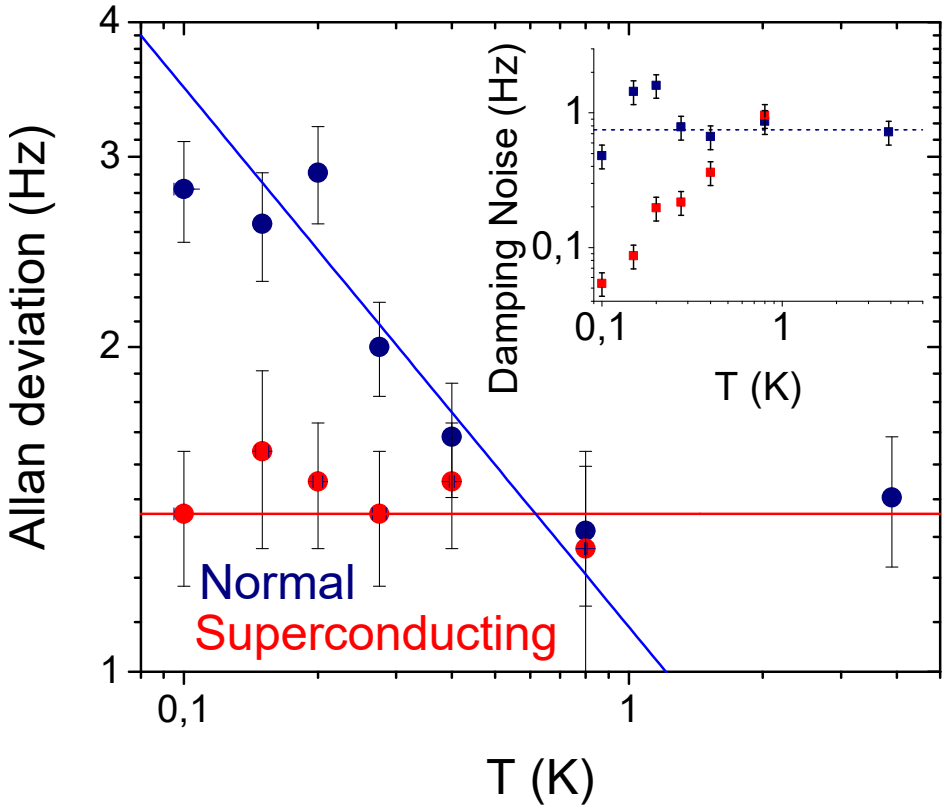

Figure 6.20: Allan deviation of the frequency noise for the 15 µm device in the superconducting (red squares) and normal state (blue dots). The red solid line is a constant value set at 1.45 Hz. The blue solid line is a fit function $1.1/\sqrt{T}$. Inset: damping noise measured with our technique. The blue dashed line is a guide for the eyes.

Once again, a clear discrepancy is visible between the frequency noise in the normal state and in the superconducting one, appearing again around $T \approx 700 - 800$ mK. Besides, the frequency noise saturates in the superconducting state while spectacularly increasing when we go down to 100 mK as $T^{-1/2}$ when the metallic layer is normal. Below 100 mK data are not shown: in the superconducting state, the additional nonlinearity pollutes the signal, while in the normal state, the current required to be strongly bistable heats too much the device. One fact is particularly striking: the solid lines used as fits are mere tentatives, and if we take the measured damping rates and their fits for both normal and superconducting state as a given, the law used to fit the frequency noise data simply scales as Γ/T for both regimes, without any adjustment. We thus strongly believe that the observed excess frequency noise in the normal state has the same microscopic origin as the normal state damping.

Qualitatively, one can explain frequency fluctuations due to tunneling TLS: the latter are in equilibrium with a phonon bath, and these phonons are atomic displacements, thus causing strain field fluctuations, translated as TLS polarization fluctua-

tions by the TLS susceptibility (6.30), and this noise causes in turn fluctuations in the stored stress of the mechanical mode, that is, in its resonance frequency. Through the fluctuation-dissipation relation (3.3), the spectrum of polarization fluctuations of a TLS is directly linked to the imaginary part of the TLS susceptibility, that is responsible for the NEMS damping. We measure very low frequency fluctuations in the mHz − Hz range, that is, frequencies that are well within the regime $\omega\tau_{rel} \ll 1$. In this limit the imaginary part of the TLS susceptibility is a constant, as seen through Eq. (6.40). It results through the fluctuation-dissipation theorem in a spectrum of polarization fluctuations, and thus, frequency fluctuations, scaling as $1/\omega$ in the low frequency range.

6.5 Conclusion and prospects

Summary of the results

We have presented a technique adapted from Ref. [12] based on the bifurcation phenomenon for a NEMS in the bistable regime in order to measure frequency noise with an arbitrary precision. We have used it to extract Allan deviations that are reliable estimates of the frequency noise magnitude, and found out it was quadratically dependent on the motion amplitude, for two very different samples. This can be explained by the properties of the bifurcation points: on the high amplitude branch bifurcation, we believe that fluctuations of the damping rate are amplified, masking the true frequency noise. Operating on the low amplitude branch, we are insensitive to these damping fluctuations, thus truly measuring the frequency noise. We have then used it to measure the temperature dependence of the frequency noise from 1 K to 25 K, which is linear with an offset. The results are consistent with the ongoing literature on nanomechanical frequency noise at low temperatures. It agrees qualitatively with a model of thermally switching two-level-systems, which predicts a linear temperature dependence [104, 147]. To investigate further this possibility, we have measured the NEMS damping from 30 mK to 20 K, where two-level systems that tunnel quantum mechanically instead of thermally switching are thought to be a dominant source of nanomechanical damping. We have derived a semi-quantitative model that takes into account the dimensionality of the beam, the role of internal stress as well as its modal decomposition, showing that the usual 3D model (with respect to phonons) of tunneling TLS is not accurate when describing the interaction of a truly highly pre-stressed nanomechanical beam at low temperatures with its constitutive TLS. Our measurements of damping rate and frequency shift are rather well explained by this model when the metallic layer is superconducting. In particular, the shift at low temperatures is undoubtedly logarithmic, providing a strong signature of the role of TLS. The results are compared with another device of similar characteristics except for its length, yielding again a rather good agreement with our model. However, the model

fails to explain the damping observed in the normal state that is similar to that in Ref. [28], even with the standard electron-driven relaxation model of TLS. A qualitative argument which invokes second-order processes in the electron-TLS interaction, leading to renormalized TLS distributions and relaxation rates, might explain our findings, even though more theoretical work is required to get deeper into quantitative considerations. We finally use the technique developed to measure frequency noise in the superconducting and normal state regimes of the metallic layer: again, a discrepancy is observed between the two, starting from 800 mK where the fraction of quasiparticles in the superconducting regime begins to significantly decrease towards low temperatures. Tentative fits show that the magnitude of the frequency noise scales as Γ/T for both superconducting and normal state regimes. Thus we believe it is a good evidence of the role of tunneling TLS in the internal frequency noise of NEMS at low temperature. It makes the link with what is observed at higher temperatures up to 30 K and more in Ref. [146], where TLS that thermally switch between states instead of tunneling are thought to be the dominant contribution.

Prospects

The large dependence of the Standard Tunneling Model on materials-dependent properties makes it uneasy to study in a fully quantitative way. However, to elude the major problem of renormalization, our setup might be adapted so the NEMS is controlled capacitively [63], with no need for a metallic layer otherwise mandatory for magnetomotive measurements. This would be convenient for another reason: indeed, an issue that remains unsolved beyond educated guesses is the location of TLS. While we know that surface TLS are more involved due to larger stress at the surface of the beam, it is not clear whether these TLS are more in the metal (oxidized) surface or the nitride one. Pure silicon nitride is expected to give high Q factors [39], and we do not measure so high values, which makes us think, complementarily to [50, 56], that the TLS that contribute the most are hosted in the metallic layer. Measurements on bare SiN samples might help to clarify the discussion. Note that the problem is not specific to silicon nitride, and that experimentally, the best way to address it is to painfully acquire statistics on the low-temperature damping properties of uniform beams made of different materials. If the results were strikingly different, it would then pose the very interesting question of the reality of TLS found in metallized beams, which are not supposed to exist in a polycrystal in their usual form [26] and with their usually assumed distribution [152].

Besides, the question of renormalization by normal state electrons is still bound to qualitative considerations only, and clearly requires some theoretical input, in link with Kondo physics. In particular, it is interesting to clarify the role of dimensionality in the renormalization procedure, as it seems that this discrepancy was observed only for resonators with submicronic cross-dimensions. Note that this model does not explain

the saturation observed at 200 mK in the normal state, which cannot yet be explained for certain with thermal decoupling. Other models of electron-mediated interactions could be considered. It might be for instance that the electrons in the normal state introduce correlations between TLS that are confined in the nano-string, in analogy with the RKKY interaction. More experiments are thus clearly required. Besides, most experiments at low temperatures are easily performed at 4 K, where not all BCS superconductors are below their critical temperature. Thus, understanding the interplay between electrons, phonons and TLS is also of practical interest.

6.6 Résumé en français

Dans ce chapitre nous mesurons la dissipation intrinsèque du NEMS jusqu'à 30 milliKelvin. Nous mettons en évidence le rôle des excitations de basse énergie couplées à la déformation du NEMS dans la relaxation d'énergie mécanique. Ces excitations, permises par la structure désordonnée des matériaux constitutifs du NEMS, sont modélisés comme des atomes se déplaçant par effet tunnel entre deux positions équivalentes du réseau atomique (TLS). Nous obtenons également le bruit en fréquence intrinsèque en développant une nouvelle technique de mesure utilisant la non-linéarité du NEMS. L'étude poussée nous permet de lier phénoménologiquement les deux observations.

Chapter 7

General Conclusion

Contents

7.1 Main achievements

This thesis was concerned with behaviours in nano-mechanical systems that arise from fluctuations or disorder and their interplay with non-linearities. On the purely macroscopic aspects, we have demonstrated an example of spectral diffusion that is non-trivial, arising from the presence of both Brownian motion and non-linearities: its observable effects are more or less important depending on whether the noise correlations are kept slow or not. We have showed the limitations it can put on sensing applications through the derivation of a fundamental limit to frequency resolution. We have demonstrated that additional complexity arises from the application of a strong driving, with Brownian motion of the driven motion that becomes squeezed and slowed down. In complement, we have performed time and frequency resolved measurements at the mechanical resonance with a similar but externally created frequency noise to model the difference between damping and decoherence in a framework inspired by NMR.

Concerning microscopic aspects, we have demonstrated, when the NEMS is surrounded by a rarefied gas, the existence of a boundary (Knudsen) layer near the sample wall, spread over a distance comparable with the atoms mean free path. We have shown that it is the result of a deviation to the well-known Maxwell-Boltzmann equilibrium distribution in the bulk, due to diffusive scattering of gas particles at the sample wall. This deviation is shown to lead to a rarefaction of the gas near the wall, which results in a renormalized, reduced damping of the NEMS (up to almost a factor of 10), validating its use as a non-invasive probe for a medium in confined geometries and paving the way towards studies of the intimate behaviour of quantum fluids. Finally, we have developed a new technique of measuring intrinsic frequency noise which relies on the bifurcation phenomenon (made possible through the Duffing

non-linearity). We applied it to the characterization of our nitride beams, and discussed the results in the framework of the Two-Level Systems model also invoked to explain low-temperature mechanical damping. The latter was measured so as to assess the validity of the Standard Tunneling Model at low temperatures. We found additional evidence of the role of stress, structure dimensionality, and of the electron bath in TLS mediated dissipation, and extended these measurements to frequency noise. A qualitative explanation involving renormalisation of the TLS distribution seen by the phonon bath was proposed.

7.2 Outlook

These results are performed in a purely **classical** fashion: neither is the system quantum, nor is its measurement apparatus, unlike e.g. in hybrid opto- and electromechanical systems [18, 174, 175]. We currently work on a more demanding experiment that aims at cooling down to the quantum regime a high frequency nanomechanical beam coupled to a quantum-limited superconducting microwave cavity. While this has been achieved already for almost a decade [18, 19], it has never been performed for a MHz range NEMS having a good Q factor, without active cooling. Here we intend to benefit from ultra-low temperature techniques to cool down the sample, by using nuclear adiabatic demagnetization [44] of a copper stage to which the sample is thermally anchored. At the lowest temperatures, such that $\hbar\omega_m \sim k_B T$, quantum effects start to play a role in the dynamics of the resonator: the thermal occupation becomes vanishingly small as temperature is lowered, and only the mode's quantum fluctuations remain. In this limit the classical treatment exposed in the above sections fails to describe the behaviour of the resonator. The macroscopic collective variable that is used to describe its dynamics is that of a true **quantum harmonic oscillator**. It represents an exciting endeavour insofar as almost nothing is known, beyond speculation, on macroscopic quantum coherence for a mechanical degree of freedom. It will require further developments allowing the coupling of the resonator to e.g. a quantum bit, in order to generate entanglement and witness decoherence of quantum states of motion [20].

Even though the results are not reported in this manuscript, a microwave optomechanical setup embedding a 50 µm long NEMS resonating at 4 MHz has been designed in our team. It has been cooled down passively and operated successfully down to 10 mK. Results already obtained in the field, such as the use of dynamical back-action of the micro-wave field on the nanomechanical beam to cool down or heat up the mechanical mode [162], or the opto-mechanically induced transparency observed for optomechanical systems [176], have been reproduced. Besides, the data in dissipation and frequency shift, that are interpreted in the framework exposed in Chapter 6, are very convincing proofs that the NEMS thermalizes to the dilution base

temperature, which make this device a good example of **phononic thermometer** when its coating is superconducting. It bypasses saturation problems encountered with electronics-based thermometers [60], where electron-phonon decoupling is a crucial bottleneck. Nuclear demagnetization has been performed with a base temperature of 700 μK reached. While the results are encouraging, the analysis is more involved, which is why no colder attempt has been made on this setup. In particular, the NEMS thermal decoupling is a highly non-trivial problem in the $1-10$ mK temperature range, and nothing is really known about the thermalization of a NEMS below 1 mK. Our fabrication process make 50 MHz NEMS attainable, so it is vital that the NEMS thermalize around 1 mK at least in order to reach the quantum regime of the mechanical resonator.

Appendix A

Scientific output

Publications

1. M. Defoort, K. J. Lulla, T. Crozes, O. Maillet, O. Bourgeois, and E. Collin. Slippage and Boundary Layer Probed in an Almost Ideal Gas by a Nanomechanical Oscillator. *Phys. Rev. Lett.*, 113(13):136101, September 2014.

2. O. Maillet, F. Vavrek, A. D. Fefferman, O. Bourgeois, and E. Collin. Classical decoherence in a nanomechanical resonator. *New J. Phys.*, 18(7):073022, 2016.

3. Olivier Maillet, Xin Zhou, Rasul Gazizulin, Ana Maldonado Cid, Martial Defoort, Olivier Bourgeois, and Eddy Collin. Nonlinear frequency transduction of nanomechanical Brownian motion. *Phys. Rev. B*, 96(16):165434, October 2017.

4. R. R. Gazizulin, O. Maillet, X. Zhou, A. Maldonado Cid, O. Bourgeois, and E. Collin. Surface-Induced Near-Field Scaling in the Knudsen Layer of a Rarefied Gas. *Phys. Rev. Lett.*, 120(3):036802, January 2018.

5. O. Maillet, X. Zhou, R. Gazizulin, J. M. Parpia, O. Bourgeois, A. Fefferman, and E. Collin. Measuring frequency fluctuations in non-linear nano-mechanical resonators. accepted in *ACS Nano*, June 2018.

6. A. Guénault, A. Guthrie, R. P. Haley, A. Jennings, S. Kafanov, Yu. A. Pashkin, G. R. Pickett, M. Poole, R. Schanen, V. Tsepelin, E. Collin, O. Maillet, and R. Gazizulin. Probing Superfluid ^{4}He using Nanobeams at mK Temperatures. In preparation, June 2018.

7. O. Maillet, R. Gazizulin, X. Zhou, J. M. Parpia, O. Bourgeois, A. Fefferman, and E. Collin. Nanomechanical damping and frequency noise due to strong TLS-electron interaction in a 1D phononic channel. In preparation, June 2018.

Oral communications (only when speaker)

1. Classical Decoherence in a Nanomechanical Resonator. *APS March Meeting*, Baltimore, USA, March 2016.

2. Interplay between fluctuations and non-linearities in nanomechanical resonators. *Journées de la Matière Condensée*, Bordeaux, France, August 2016.

3. Fluctuations, non-linear dynamics, and their interplay in nanomechanical resonators. *Séminaire MBCT de l'Institut Néel*, Grenoble, France, November 2016.

4. Probing gaseous matter in confined geometries with nano-mechanical resonators. *Rencontres des Jeunes Physiciens*, Grenoble, France, April 2017.

5. Non-linear frequency transduction of nano-mechanical Brownian motion. *Mesoscopic Physics and Quantum Coherence*, Espoo, Finland, August 2017.

6. Investigating non-linear decoherence in nano-mechanical resonators at low temperatures. *28th International Conference on Low Temperature Physics*, Gothenburg, Sweden, August 2017.

Bibliography

[1] LIGO Scientific Collaboration and Virgo Collaboration. Observation of Gravitational Waves from a Binary Black Hole Merger. *Phys. Rev. Lett.*, 116(6):061102, February 2016. (Cited on page 1.)

[2] R. Adam, B. Comis, J. F. Macías-Pérez, A. Adane, P. Ade, P. André, A. Beelen, B. Belier, A. Benoît, A. Bideaud, N. Billot, N. Boudou, O. Bourrion, M. Calvo, A. Catalano, G. Coiffard, A. D'Addabbo, F.-X. Désert, S. Doyle, J. Goupy, C. Kramer, S. Leclercq, J. Martino, P. Mauskopf, F. Mayet, A. Monfardini, F. Pajot, E. Pascale, L. Perotto, E. Pointecouteau, N. Ponthieu, V. Revéret, L. Rodriguez, G. Savini, K. Schuster, A. Sievers, C. Tucker, and R. Zylka. First observation of the thermal Sunyaev-Zel'dovich effect with kinetic inductance detectors. *A&A*, 569:A66, September 2014. (Cited on page 1.)

[3] P. F. Cohadon, A. Heidmann, and M. Pinard. Cooling of a Mirror by Radiation Pressure. *Phys. Rev. Lett.*, 83(16):3174–3177, October 1999. (Cited on pages 1 and 2.)

[4] Y. Hadjar, P. F. Cohadon, C. G. Aminoff, M. Pinard, and A. Heidmann. High-sensitivity optical measurement of mechanical Brownian motion. *Europhys. Lett.*, 47(5):545–551, September 1999. (Cited on pages 1, 30 and 85.)

[5] H. B. Chan, V. A. Aksyuk, R. N. Kleiman, D. J. Bishop, and Federico Capasso. Quantum Mechanical Actuation of Microelectromechanical Systems by the Casimir Force. *Science*, 291(5510):1941–1944, March 2001. (Cited on page 1.)

[6] J. Chiaverini, S. J. Smullin, A. A. Geraci, D. M. Weld, and A. Kapitulnik. New Experimental Constraints on Non-Newtonian Forces below 100 μm. *Phys. Rev. Lett.*, 90(15):151101, April 2003. (Cited on page 1.)

[7] A. N. Cleland and M. L. Roukes. Fabrication of high frequency nanometer scale mechanical resonators from bulk Si crystals. *Appl. Phys. Lett.*, 69(18):2653–2655, October 1996. (Cited on page 1.)

[8] A. N. Cleland and M. L. Roukes. A nanometre-scale mechanical electrometer. *Nature*, 392(6672):160, March 1998. (Cited on page 1.)

[9] A. Eichler, J. Moser, J. Chaste, M. Zdrojek, I. Wilson-Rae, and A. Bachtold. Nonlinear damping in mechanical resonators made from carbon nanotubes and graphene. *Nature Nanotechnology*, 6(6):339, June 2011. (Cited on pages 2, 108 and 131.)

[10] J. Chaste, A. Eichler, J. Moser, G. Ceballos, R. Rurali, and A. Bachtold. A nanomechanical mass sensor with yoctogram resolution. *Nature Nanotechnology*, 7(5):301, May 2012. (Cited on pages 2, 3 and 62.)

[11] Ron Lifshitz and M. L. Roukes. Thermoelastic damping in micro- and nanomechanical systems. *Phys. Rev. B*, 61(8):5600–5609, February 2000. (Cited on pages 2, 35, 136 and 187.)

[12] J. S. Aldridge and A. N. Cleland. Noise-Enabled Precision Measurements of a Duffing Nanomechanical Resonator. *Phys. Rev. Lett.*, 94(15):156403, 2005. (Cited on pages 2, 49, 172 and 218.)

[13] I. Kozinsky, H. W. Ch. Postma, O. Kogan, A. Husain, and M. L. Roukes. Basins of Attraction of a Nonlinear Nanomechanical Resonator. *Phys. Rev. Lett.*, 99(20):207201, November 2007. (Cited on pages 2 and 49.)

[14] Jan Gieseler, Lukas Novotny, and Romain Quidant. Thermal nonlinearities in a nanomechanical oscillator. *Nature Physics*, 9(12):806, December 2013. (Cited on pages 2, 5, 62, 70, 91 and 103.)

[15] Yaxing Zhang, J. Moser, J. Güttinger, A. Bachtold, and M. I. Dykman. Interplay of Driving and Frequency Noise in the Spectra of Vibrational Systems. *Phys. Rev. Lett.*, 113(25):255502, December 2014. (Cited on pages 2, 62, 103 and 108.)

[16] O. Arcizet, P.-F. Cohadon, T. Briant, M. Pinard, and A. Heidmann. Radiation-pressure cooling and optomechanical instability of a micromirror. *Nature*, 444(7115):71, November 2006. (Cited on page 2.)

[17] Markus Aspelmeyer, Tobias J. Kippenberg, and Florian Marquardt. Cavity optomechanics. *Rev. Mod. Phys.*, 86(4):1391–1452, December 2014. (Cited on page 2.)

[18] A. D. O'Connell, M. Hofheinz, M. Ansmann, Radoslaw C. Bialczak, M. Lenander, Erik Lucero, M. Neeley, D. Sank, H. Wang, M. Weides, J. Wenner, John M. Martinis, and A. N. Cleland. Quantum ground state and single-phonon control of a mechanical resonator. *Nature*, 464(7289):697–703, April 2010. (Cited on pages 2, 3, 56 and 222.)

[19] J. D. Teufel, T. Donner, Dale Li, J. W. Harlow, M. S. Allman, K. Cicak, A. J. Sirois, J. D. Whittaker, K. W. Lehnert, and R. W. Simmonds. Sideband cooling of micromechanical motion to the quantum ground state. *Nature*, 475(7356):359, July 2011. (Cited on pages 2, 3, 56 and 222.)

[20] A. D. Armour, M. P. Blencowe, and K. C. Schwab. Entanglement and Decoherence of a Micromechanical Resonator via Coupling to a Cooper-Pair Box. *Phys. Rev. Lett.*, 88(14):148301, March 2002. (Cited on pages 2, 136 and 222.)

[21] Mika A. Sillanpää, Raphaël Khan, Tero T. Heikkilä, and Pertti J. Hakonen. Macroscopic quantum tunneling in nanoelectromechanical systems. *Phys. Rev. B*, 84(19):195433, November 2011. (Cited on page 2.)

[22] Erich Joos, H. Dieter Zeh, Claus Kiefer, Domenico Giulini, Joachim Kupsch, Domenico J. W. Giulini, and Ion-Olimpiu Stamatescu. *Decoherence and the Appearance of a Classical World in Quantum Theory.* Springer-Verlag Berlin and Heidelberg GmbH & Co. K, Berlin ; New York, 2nd ed. 2003 edition, 2003. (Cited on page 2.)

[23] Thomas Faust, Johannes Rieger, Maximilian J. Seitner, Peter Krenn, Jörg P. Kotthaus, and Eva M. Weig. Nonadiabatic Dynamics of Two Strongly Coupled Nanomechanical Resonator Modes. *Phys. Rev. Lett.*, 109(3):037205, 2012. (Cited on pages 2 and 56.)

[24] T. Faust, J. Rieger, M. J. Seitner, J. P. Kotthaus, and E. M. Weig. Coherent control of a classical nanomechanical two-level system. *Nature Physics*, 9(8):485, 2013. (Cited on pages 2, 3, 44, 56 and 126.)

[25] P. W. Anderson, B. I. Halperin, and C. M. Varma. Anomalous low-temperature thermal properties of glasses and spin glasses. *The Philosophical Magazine: A Journal of Theoretical Experimental and Applied Physics*, 25(1):1–9, January 1972. (Cited on pages 4, 5, 187, 192 and 198.)

[26] F. Hoehne, Yu. A. Pashkin, O. Astafiev, L. Faoro, L. B. Ioffe, Y. Nakamura, and J. S. Tsai. Damping in high-frequency metallic nanomechanical resonators. *Phys. Rev. B*, 81(18):184112, May 2010. (Cited on pages 4, 188, 189, 209 and 219.)

[27] A. Venkatesan, K. J. Lulla, M. J. Patton, A. D. Armour, C. J. Mellor, and J. R. Owers-Bradley. Dissipation due to tunneling two-level systems in gold nanomechanical resonators. *Phys. Rev. B*, 81(7):073410, February 2010. (Cited on pages 4, 188, 206, 209, 211 and 215.)

[28] K. J. Lulla, M. Defoort, C. Blanc, O. Bourgeois, and E. Collin. Evidence for the Role of Normal-State Electrons in Nanoelectromechanical Damping Mechanisms at Very Low Temperatures. *Phys. Rev. Lett.*, 110(17):177206, April 2013. (Cited on pages 4, 136, 188, 189, 204, 205, 207, 209, 210, 211, 215, 216 and 219.)

[29] Ron Lifshitz and M. C. Cross. Nonlinear Dynamics of Nanomechanical and Micromechanical Resonators. In Heinz Georg Schuster, editor, *Reviews of Non-*

linear Dynamics and Complexity, pages 1–52. Wiley-VCH Verlag GmbH & Co. KGaA, 2008. (Cited on pages 4, 47 and 55.)

[30] A. Vinante. Thermal frequency noise in micromechanical resonators due to nonlinear mode coupling. *Phys. Rev. B*, 90(2):024308, July 2014. (Cited on pages 5, 62 and 80.)

[31] Yaxing Zhang and M. I. Dykman. Spectral effects of dispersive mode coupling in driven mesoscopic systems. *Phys. Rev. B*, 92(16):165419, October 2015. (Cited on pages 5, 62, 72, 75, 83, 103 and 104.)

[32] A. Eichler, J. Moser, M. I. Dykman, and A. Bachtold. Symmetry breaking in a mechanical resonator made from a carbon nanotube. *Nature Communications*, 4:2843, November 2013. (Cited on pages 5, 62, 93 and 105.)

[33] Olivier Maillet, Xin Zhou, Rasul Gazizulin, Ana Maldonado Cid, Martial Defoort, Olivier Bourgeois, and Eddy Collin. Nonlinear frequency transduction of nanomechanical Brownian motion. *Phys. Rev. B*, 96(16):165434, October 2017. (Cited on pages 5, 93, 105 and 179.)

[34] O. Maillet, F. Vavrek, A. D. Fefferman, O. Bourgeois, and E. Collin. Classical decoherence in a nanomechanical resonator. *New J. Phys.*, 18(7):073022, 2016. (Cited on pages 5, 132 and 185.)

[35] M. Defoort, K. J. Lulla, T. Crozes, O. Maillet, O. Bourgeois, and E. Collin. Slippage and Boundary Layer Probed in an Almost Ideal Gas by a Nanomechanical Oscillator. *Phys. Rev. Lett.*, 113(13):136101, September 2014. (Cited on pages 5, 142, 147, 148, 149 and 168.)

[36] R. R. Gazizulin, O. Maillet, X. Zhou, A. Maldonado Cid, O. Bourgeois, and E. Collin. Surface-Induced Near-Field Scaling in the Knudsen Layer of a Rarefied Gas. *Phys. Rev. Lett.*, 120(3):036802, January 2018. (Cited on pages 5, 152, 164, 172 and 187.)

[37] W. A. Phillips. Tunneling states in amorphous solids. *J Low Temp Phys*, 7(3-4):351–360, May 1972. (Cited on pages 5, 187 and 198.)

[38] Laura G. Remus, Miles P. Blencowe, and Yukihiro Tanaka. Damping and decoherence of a nanomechanical resonator due to a few two-level systems. *Phys. Rev. B*, 80(17):174103, November 2009. (Cited on pages 6, 188, 193, 202 and 203.)

[39] Quirin P. Unterreithmeier, Thomas Faust, and Jörg P. Kotthaus. Damping of Nanomechanical Resonators. *Phys. Rev. Lett.*, 105(2):027205, July 2010. (Cited on pages 6, 35, 93, 182, 196 and 219.)

[40] O. Maillet, X. Zhou, R. Gazizulin, J. M. Parpia, O. Bourgeois, A. Fefferman, and E. Collin. Measuring frequency fluctuations in non-linear nano-mechanical resonators. *Submitted for publication*, February 2018. (Cited on pages 6 and 180.)

[41] E. Collin, M. Defoort, K. Lulla, T. Moutonet, J.-S. Heron, O. Bourgeois, Yu. M. Bunkov, and H. Godfrin. In-situ comprehensive calibration of a tri-port nano-electro-mechanical device. *Review of Scientific Instruments*, 83(4):045005, April 2012. (Cited on pages 8, 34, 37 and 39.)

[42] Martial Defoort. *Non-linear dynamics in nano-electromechanical systems at low temperatures*. Grenoble, December 2014. (Cited on pages 8, 93, 94, 173, 185 and 186.)

[43] Andrew N. Cleland. *Foundations of Nanomechanics*. Springer, Berlin, 2003 edition edition, November 2002. (Cited on pages 13, 19, 21, 46, 47, 172, 187, 192, 195, 198, 199 and 202.)

[44] Frank Pobell. *Matter and Methods at Low Temperatures*. Springer-Verlag Berlin and Heidelberg GmbH & Co. K, Berlin, 3 edition, February 2007. (Cited on pages 15, 16, 155, 158, 167, 204 and 222.)

[45] Olli V. Lounasmaa. *Experimental principles and methods below 1K*. 1974. (Cited on page 15.)

[46] Valérie Goudon. *Magnétisme nucléaire de l'^{3}He liquide : nouvelle détermination du paramètre de Landau F_0^a*. Université Joseph Fourier (Grenoble), January 2006. (Cited on page 18.)

[47] C. P. Lusher, Junyun Li, V. A. Maidanov, M. E. Digby, H. Dyball, A. Casey, J. Nyéki, V. V. Dmitriev, B. P. Cowan, and J Saunders. Current sensing noise thermometry using a low T_c DC SQUID preamplifier. *Meas. Sci. Technol.*, 12(1):1, 2001. (Cited on page 19.)

[48] S. Timoshenko. *Theory of Elasticity*. McGraw-Hill Publishing Company, Auckland, 3rd edition edition, October 1970. (Cited on page 19.)

[49] Kunal Lulla. *Dissipation and nonlinear effects in nanomechanical resonators at low temperatures*. April 2011. (Cited on pages 22 and 188.)

[50] E. Collin, J. Kofler, S. Lakhloufi, S. Pairis, Yu. M. Bunkov, and H. Godfrin. Metallic coatings of microelectromechanical structures at low temperatures: Stress, elasticity, and nonlinear dissipation. *Journal of Applied Physics*, 107(11):114905, June 2010. (Cited on pages 23, 34, 182 and 219.)

[51] A. M. Guénault, V. Keith, C. J. Kennedy, S. G. Mussett, and G. R. Pickett. The mechanical behavior of a vibrating wire in superfluid ^{3}He-B in the ballistic limit. *J Low Temp Phys*, 62(5-6):511–523, March 1986. (Cited on pages 27, 136 and 167.)

[52] C. Bäuerle, Yu. M. Bunkov, S. N. Fisher, and H. Godfrin. Temperature scale and heat capacity of superfluid ^{3}He in the 100 μK range. *Phys. Rev. B*, 57(22):14381–14386, June 1998. (Cited on page 27.)

[53] A. N. Cleland and M. L. Roukes. External control of dissipation in a nanometer-scale radiofrequency mechanical resonator. *Sensors and Actuators A: Physical*, 72(3):256–261, February 1999. (Cited on pages 27, 31 and 172.)

[54] Laure Mercier de Lépinay, Benjamin Pigeau, Benjamin Besga, Pascal Vincent, Philippe Poncharal, and Olivier Arcizet. A universal and ultrasensitive vectorial nanomechanical sensor for imaging 2d force fields. *Nature Nanotechnology*, 12(2):156, February 2017. (Cited on page 30.)

[55] A. Olkhovets, S. Evoy, D. W. Carr, J. M. Parpia, and H. G. Craighead. Actuation and internal friction of torsional nanomechanical silicon resonators. *Journal of Vacuum Science & Technology B: Microelectronics and Nanometer Structures Processing, Measurement, and Phenomena*, 18(6):3549–3551, November 2000. (Cited on pages 34 and 182.)

[56] Maximilian J. Seitner, Katrin Gajo, and Eva M. Weig. Damping of metallized bilayer nanomechanical resonators at room temperature. *Appl. Phys. Lett.*, 105(21):213101, November 2014. (Cited on pages 34, 182 and 219.)

[57] M. Defoort, K. J. Lulla, C. Blanc, H. Ftouni, O. Bourgeois, and E. Collin. Stressed Silicon Nitride Nanomechanical Resonators at Helium Temperatures. *J Low Temp Phys*, 171(5-6):731–736, June 2013. (Cited on page 35.)

[58] I. Wilson-Rae. Intrinsic dissipation in nanomechanical resonators due to phonon tunneling. *Phys. Rev. B*, 77(24):245418, June 2008. (Cited on pages 35, 136 and 187.)

[59] Adib Tavakoli, Christophe Blanc, Hossein Ftouni, Kunal J. Lulla, Andrew D. Fefferman, Eddy Collin, and Olivier Bourgeois. Universality of thermal transport in amorphous nanowires at low temperatures. *Phys. Rev. B*, 95(16):165411, April 2017. (Cited on page 36.)

[60] M. Meschke, J. P. Pekola, F. Gay, R. E. Rapp, and H. Godfrin. Electron Thermalization in Metallic Islands Probed by Coulomb Blockade Thermometry. *Journal of Low Temperature Physics*, 134(5-6):1119–1143, March 2004. (Cited on pages 39 and 223.)

[61] M. Defoort, K. J. Lulla, C. Blanc, O. Bourgeois, E. Collin, and A. D. Armour. Modal "self-coupling" as a sensitive probe for nanomechanical detection. *Appl. Phys. Lett.*, 103(1):013104, July 2013. (Cited on page 42.)

[62] I. Kozinsky, H. W. Ch. Postma, I. Bargatin, and M. L. Roukes. Tuning nonlinearity, dynamic range, and frequency of nanomechanical resonators. *Appl. Phys. Lett.*, 88(25):253101, June 2006. (Cited on pages 44 and 45.)

[63] Quirin P. Unterreithmeier, Eva M. Weig, and Jörg P. Kotthaus. Universal transduction scheme for nanomechanical systems based on dielectric forces. *Nature*, 458(7241):1001–1004, April 2009. (Cited on pages 44, 56 and 219.)

[64] E. Collin, T. Moutonet, J.-S. Heron, O. Bourgeois, Yu. M. Bunkov, and H. Godfrin. Nonlinear parametric amplification in a triport nanoelectromechanical device. *Phys. Rev. B*, 84(5):054108, August 2011. (Cited on pages 44, 45, 54 and 55.)

[65] E. Collin, T. Moutonet, J.-S. Heron, O. Bourgeois, Yu M. Bunkov, and H. Godfrin. A Tunable Hybrid Electro-magnetomotive NEMS Device for Low Temperature Physics. *J Low Temp Phys*, 162(5-6):653–660, March 2011. (Cited on page 45.)

[66] Ali H. Nayfeh and Dean T. Mook. *Nonlinear Oscillations*. Wiley VCH, New York, 2nd revised edition edition, March 1995. (Cited on page 47.)

[67] M. H. Matheny, L. G. Villanueva, R. B. Karabalin, J. E. Sader, and M. L. Roukes. Nonlinear Mode-Coupling in Nanomechanical Systems. *Nano Lett.*, 13(4):1622–1626, 2013. (Cited on pages 47 and 52.)

[68] L. G. Villanueva, R. B. Karabalin, M. H. Matheny, D. Chi, J. E. Sader, and M. L. Roukes. Nonlinearity in nanomechanical cantilevers. *Phys. Rev. B*, 87(2):024304, January 2013. (Cited on page 47.)

[69] E. Collin, Yu. M. Bunkov, and H. Godfrin. Addressing geometric nonlinearities with cantilever microelectromechanical systems: Beyond the Duffing model. *Phys. Rev. B*, 82(23):235416, December 2010. (Cited on pages 47, 123 and 125.)

[70] L. D. Landau and E. M. Lifshitz. *Mechanics, Third Edition: Volume 1*. Butterworth-Heinemann, Amsterdam u.a, 3 edition edition, January 1976. (Cited on page 48.)

[71] M. Defoort, V. Puller, O. Bourgeois, F. Pistolesi, and E. Collin. Scaling laws for the bifurcation escape rate in a nanomechanical resonator. *Phys. Rev. E*, 92(5):050903, November 2015. (Cited on pages 49 and 98.)

[72] H. J. R. Westra, M. Poot, H. S. J. van der Zant, and W. J. Venstra. Nonlinear Modal Interactions in Clamped-Clamped Mechanical Resonators. *Phys. Rev. Lett.*, 105(11):117205, September 2010. (Cited on page 52.)

[73] K. J. Lulla, R. B. Cousins, A. Venkatesan, M. J. Patton, A. D. Armour, C. J. Mellor, and J. R. Owers-Bradley. Nonlinear modal coupling in a high-stress doubly-clamped nanomechanical resonator. *New J. Phys.*, 14(11):113040, 2012. (Cited on page 52.)

[74] M. S. Hanay, S. Kelber, A. K. Naik, D. Chi, S. Hentz, E. C. Bullard, E. Colinet, L. Duraffourg, and M. L. Roukes. Single-protein nanomechanical mass spectrometry in real time. *Nature Nanotechnology*, 7(9):602, September 2012. (Cited on page 62.)

[75] Ben H. Schneider, Vibhor Singh, Warner J. Venstra, Harold B. Meerwaldt, and Gary A. Steele. Observation of decoherence in a carbon nanotube mechanical resonator. *Nature Communications*, 5:5819, December 2014. (Cited on pages 62, 108 and 131.)

[76] Arthur W. Barnard, Vera Sazonova, Arend M. van der Zande, and Paul L. McEuen. Fluctuation broadening in carbon nanotube resonators. *PNAS*, 109(47):19093–19096, November 2012. (Cited on pages 62, 93 and 94.)

[77] Tengfei Miao, Sinchul Yeom, Peng Wang, Brian Standley, and Marc Bockrath. Graphene Nanoelectromechanical Systems as Stochastic-Frequency Oscillators. *Nano Lett.*, 14(6):2982–2987, June 2014. (Cited on pages 62 and 108.)

[78] Marc Sansa, Eric Sage, Elizabeth C. Bullard, Marc Gély, Thomas Alava, Eric Colinet, Akshay K. Naik, Luis Guillermo Villanueva, Laurent Duraffourg, Michael L. Roukes, Guillaume Jourdan, and Sébastien Hentz. Frequency fluctuations in silicon nanoresonators. *Nature Nanotechnology*, 11(6):552, June 2016. (Cited on pages 62 and 186.)

[79] M. I. Dykman, M. Khasin, J. Portman, and S. W. Shaw. Spectrum of an Oscillator with Jumping Frequency and the Interference of Partial Susceptibilities. *Phys. Rev. Lett.*, 105(23):230601, December 2010. (Cited on pages 62 and 76.)

[80] J. Atalaya, A. Isacsson, and M. I. Dykman. Diffusion-Induced Bistability of Driven Nanomechanical Resonators. *Phys. Rev. Lett.*, 106(22):227202, May 2011. (Cited on page 62.)

[81] F. Sun, J. Zou, Z. A. Maizelis, and H. B. Chan. Telegraph frequency noise in electromechanical resonators. *Phys. Rev. B*, 91(17):174102, May 2015. (Cited on pages 62, 71 and 103.)

[82] M. I. Dykman and M. A. Krivoglaz. Theory of fluctuational transitions between stable states of a nonlinear oscillator. *ZhETF*, 77(1):60–73, July 1979. (Cited on pages 63, 94, 102 and 183.)

[83] Herbert B. Callen and Theodore A. Welton. Irreversibility and Generalized Noise. *Phys. Rev.*, 83(1):34–40, July 1951. (Cited on page 64.)

[84] R. Kubo. The fluctuation-dissipation theorem. *Rep. Prog. Phys.*, 29(1):255, 1966. (Cited on page 64.)

[85] Thomas K. Caughey. Derivation and Application of the Fokker-Planck Equation to Discrete Nonlinear Dynamic Systems Subjected to White Random Excitation. *Journal of the Acoustical Society of America*, 35(11):1683–1692, November 1963. (Cited on page 69.)

[86] Charles P. Slichter. *Principles of Magnetic Resonance*. Springer, Berlin ; New York, 3rd enlarged and updated ed. 1990. corr. 3rd printing 1996 edition edition, March 1996. (Cited on pages 70, 72 and 108.)

[87] A. Berthelot, I. Favero, G. Cassabois, C. Voisin, C. Delalande, Ph Roussignol, R. Ferreira, and J. M. Gérard. Unconventional motional narrowing in the optical spectrum of a semiconductor quantum dot. *Nature Physics*, 2(11):759, November 2006. (Cited on page 72.)

[88] D. Cadeddu, F. R. Braakman, G. Tütüncüoglu, F. Matteini, D. Rüffer, A. Fontcuberta i Morral, and M. Poggio. Time-Resolved Nonlinear Coupling between Orthogonal Flexural Modes of a Pristine GaAs Nanowire. *Nano Lett.*, 16(2):926–931, February 2016. (Cited on page 92.)

[89] A. Suhel, B. D. Hauer, T. S. Biswas, K. S. D. Beach, and J. P. Davis. Dissipation mechanisms in thermomechanically driven silicon nitride nanostrings. *Appl. Phys. Lett.*, 100(17):173111, April 2012. (Cited on page 93.)

[90] L. D. Landau and E. M. Lifshitz. *Statistical Physics, Third Edition, Part 1: Volume 5*. Butterworth-Heinemann, Amsterdam u.a, 3 edition edition, January 1980. (Cited on page 96.)

[91] R. Almog, S. Zaitsev, O. Shtempluck, and E. Buks. Noise Squeezing in a Nanomechanical Duffing Resonator. *Phys. Rev. Lett.*, 98(7):078103, February 2007. (Cited on page 102.)

[92] D. Rugar and P. Grütter. Mechanical parametric amplification and thermomechanical noise squeezing. *Phys. Rev. Lett.*, 67(6):699–702, August 1991. (Cited on page 102.)

[93] S. Reynaud, C. Fabre, E. Giacobino, and A. Heidmann. Photon noise reduction by passive optical bistable systems. *Phys. Rev. A*, 40(3):1440–1446, August 1989. (Cited on page 102.)

[94] C. Fabre, M. Pinard, S. Bourzeix, A. Heidmann, E. Giacobino, and S. Reynaud. Quantum-noise reduction using a cavity with a movable mirror. *Phys. Rev. A*, 49(2):1337–1343, February 1994. (Cited on page 102.)

[95] F. Sun, X. Dong, J. Zou, M. I. Dykman, and H. B. Chan. Correlated anomalous phase diffusion of coupled phononic modes in a sideband-driven resonator. *Nature Communications*, 7:12694, August 2016. (Cited on page 104.)

[96] Itamar Katz, Alex Retzker, Raphael Straub, and Ron Lifshitz. Signatures for a Classical to Quantum Transition of a Driven Nonlinear Nanomechanical Resonator. *Phys. Rev. Lett.*, 99(4):040404, July 2007. (Cited on page 104.)

[97] T. Rentrop, A. Trautmann, F. A. Olivares, F. Jendrzejewski, A. Komnik, and M. K. Oberthaler. Observation of the Phononic Lamb Shift with a Synthetic Vacuum. *Phys. Rev. X*, 6(4):041041, November 2016. (Cited on page 104.)

[98] J. Moser, J. Güttinger, A. Eichler, M. J. Esplandiu, D. E. Liu, M. I. Dykman, and A. Bachtold. Ultrasensitive force detection with a nanotube mechanical resonator. *Nature Nanotechnology*, 8(7):493, July 2013. (Cited on page 108.)

[99] Johannes Güttinger, Adrien Noury, Peter Weber, Axel Martin Eriksson, Camille Lagoin, Joel Moser, Christopher Eichler, Andreas Wallraff, Andreas Isacsson, and Adrian Bachtold. Energy-dependent path of dissipation in nanomechanical resonators. *Nature Nanotechnology*, 12(7):631, July 2017. (Cited on page 108.)

[100] R. van Leeuwen, A. Castellanos-Gomez, G. A. Steele, H. S. J. van der Zant, and W. J. Venstra. Time-domain response of atomically thin MoS2 nanomechanical resonators. *Appl. Phys. Lett.*, 105(4):041911, July 2014. (Cited on page 108.)

[101] Anthony E. Siegman. *Lasers*. University Science Books,U.S., Mill Valley, California, new edition edition, 1986. (Cited on page 119.)

[102] G. Ithier, E. Collin, P. Joyez, P. J. Meeson, D. Vion, D. Esteve, F. Chiarello, A. Shnirman, Y. Makhlin, J. Schriefl, and G. Schön. Decoherence in a superconducting quantum bit circuit. *Phys. Rev. B*, 72(13):134519, October 2005. (Cited on page 128.)

[103] Z. A. Maizelis, M. L. Roukes, and M. I. Dykman. Detecting and characterizing frequency fluctuations of vibrational modes. *Phys. Rev. B*, 84(14):144301, October 2011. (Cited on page 130.)

[104] A. N. Cleland and M. L. Roukes. Noise processes in nanomechanical resonators. *Journal of Applied Physics*, 92(5):2758–2769, August 2002. (Cited on pages 136, 178, 181, 187 and 218.)

[105] C. Lissandrello, V. Yakhot, and K. L. Ekinci. Crossover from Hydrodynamics to the Kinetic Regime in Confined Nanoflows. *Phys. Rev. Lett.*, 108(8):084501, February 2012. (Cited on pages 136 and 167.)

[106] V. Kara, V. Yakhot, and K. L. Ekinci. Generalized Knudsen Number for Unsteady Fluid Flow. *Phys. Rev. Lett.*, 118(7):074505, February 2017. (Cited on pages 136, 145 and 167.)

[107] Javier Tamayo, Priscila M. Kosaka, José J. Ruz, Álvaro San Paulo, and Montserrat Calleja. Biosensors based on nanomechanical systems. *Chem. Soc. Rev.*, 42(3):1287–1311, January 2013. (Cited on page 136.)

[108] V. D. Arp, R. D. McCarty, and Daniel G. Friend. Thermophysical Properties of Helium-4 from 0.8 to 1500 K with Pressures to 2000 MPa. *Technical Note (NIST TN) - 1334*, February 1998. (Cited on pages 136 and 137.)

[109] V. G. Chernyak, B. T. Porodnov, and P. E. Suetin. Application of the variation method to the problem of thermomolecular pressure difference in a cylindrical channel. *Journal of Engineering Physics*, 26(3):309–312, March 1974. (Cited on page 138.)

[110] John Elie Sader. Frequency response of cantilever beams immersed in viscous fluids with applications to the atomic force microscope. *Journal of Applied Physics*, 84(1):64–76, June 1998. (Cited on pages 140 and 141.)

[111] G. G. Stokes. On the Composition and Resolution of Streams of Polarized Light from different Sources. *Transactions of the Cambridge Philosophical Society*, 9:399, 1851. (Cited on page 141.)

[112] Eddy Collin, Laure Filleau, Thierry Fournier, Yuriy M. Bunkov, and Henri Godfrin. Silicon Vibrating Wires at Low Temperatures. *J Low Temp Phys*, 150(5-6):739–790, March 2008. (Cited on pages 141 and 142.)

[113] Philip M. Morse and K. Uno Ingard. *Theoretical Acoustics*. Princeton University Press, Princeton, NJ, 1992. (Cited on page 142.)

[114] L. D. Landau and E. M. Lifshitz. *Fluid Mechanics, Second Edition: Volume 6*. Butterworth-Heinemann, Amsterdam u.a, 2 edition edition, January 1987. (Cited on page 142.)

[115] Charles R. Lilley and John E. Sader. Velocity profile in the Knudsen layer according to the Boltzmann equation. *Proceedings of the Royal Society of London A: Mathematical, Physical and Engineering Sciences*, 464(2096):2015–2035, August 2008. (Cited on page 143.)

[116] D. C. Carless, H. E. Hall, and J. R. Hook. Vibrating wire measurements in liquid ^{3}He II. The superfluid B phase. *J Low Temp Phys*, 50(5-6):605–633, March 1983. (Cited on page 143.)

[117] R. M. Bowley and J. R. Owers-Bradley. Slip Corrections for Vibrating Wire Resonators. *Journal of Low Temperature Physics*, 136(1-2):15–38, July 2004. (Cited on page 143.)

[118] J. M. Ziman. *Electrons and Phonons: The Theory of Transport Phenomena in Solids*. Oxford Classic Texts in the Physical Sciences. Oxford University Press, Oxford, New York, February 2001. (Cited on page 143.)

[119] M. Sinvani, M. W. Cole, and D. L. Goodstein. Sticking Probability of ^{4}He on Solid Surfaces at Low Temperature. *Phys. Rev. Lett.*, 51(3):188–191, July 1983. (Cited on page 143.)

[120] P. Taborek and L. J. Senator. Helium on graphite: Low-temperature desorption kinetics and sticking coefficient. *Phys. Rev. Lett.*, 56(6):628–631, February 1986. (Cited on page 143.)

[121] H. Højgaard Jensen, H. Smith, P. Wölfle, K. Nagai, and T. Maack Bisgaard. Boundary effects in fluid flow. Application to quantum liquids. *J Low Temp Phys*, 41(5-6):473–519, December 1980. (Cited on page 143.)

[122] Jason K. Holt, Hyung Gyu Park, Yinmin Wang, Michael Stadermann, Alexander B. Artyukhin, Costas P. Grigoropoulos, Aleksandr Noy, and Olgica Bakajin. Fast Mass Transport Through Sub-2-Nanometer Carbon Nanotubes. *Science*, 312(5776):1034–1037, May 2006. (Cited on page 144.)

[123] Alessandro Siria, Philippe Poncharal, Anne-Laure Biance, Rémy Fulcrand, Xavier Blase, Stephen T. Purcell, and Lydéric Bocquet. Giant osmotic energy conversion measured in a single transmembrane boron nitride nanotube. *Nature*, 494(7438):455, February 2013. (Cited on page 144.)

[124] Elizabeth C. Bullard, Jianchang Li, Charles R. Lilley, Paul Mulvaney, Michael L. Roukes, and John E. Sader. Dynamic Similarity of Oscillatory Flows Induced by Nanomechanical Resonators. *Phys. Rev. Lett.*, 112(1):015501, January 2014. (Cited on pages 145 and 167.)

[125] Gordon Neil Patterson. *Molecular flow of gases*. Chapman & Hall, 1956. (Cited on pages 147, 160 and 162.)

[126] Kyoji Yamamoto and Kazuyuki Sera. Flow of a rarefied gas past a circular cylinder. *The Physics of Fluids*, 28(5):1286–1293, May 1985. (Cited on pages 148 and 150.)

[127] Charles R. Lilley and John E. Sader. Velocity gradient singularity and structure of the velocity profile in the Knudsen layer according to the Boltzmann equation. *Phys. Rev. E*, 76(2):026315, August 2007. (Cited on page 151.)

[128] G. J. Goellner, J. G. Daunt, and E. Lerner. Helium adsorption on exfoliated graphite. *J Low Temp Phys*, 21(3-4):347–358, November 1975. (Cited on page 155.)

[129] H. Godfrin and R. E. Rapp. Two-dimensional nuclear magnets. *Advances in Physics*, 44(2):113–186, January 1995. (Cited on page 155.)

[130] Nick D. Hutson and Ralph T. Yang. Theoretical basis for the Dubinin-Radushkevitch (D-R) adsorption isotherm equation. *Adsorption*, 3(3):189–195, September 1997. (Cited on pages 155 and 156.)

[131] W. Rudzinski and D. H. Everett. *Adsorption of Gases on Heterogeneous Surfaces*. Academic Press, London, January 1992. (Cited on page 155.)

[132] G. F. Cerofolini and R. M. Fondi. Electron emission from heterogeneous metal surfaces. *phys. stat. sol. (a)*, 7(1):103–111, September 1971. (Cited on page 156.)

[133] J. G. Dash. *Films on Solid Surfaces: The Physics and Chemistry of Physical Adsorption*. Academic Press, January 1975. (Cited on page 157.)

[134] Carlo Cercignani. *Mathematical Methods in Kinetic Theory*. Springer, 1969 edition edition, January 2014. (Cited on pages 159 and 162.)

[135] Sydney Chapman, T. G. Cowling, and C. Cercignani. *The Mathematical Theory of Non-uniform Gases: An Account of the Kinetic Theory of Viscosity, Thermal Conduction and Diffusion in Gases*. Cambridge University Press, Cambridge ; New York, 3^{rd} edition, January 1991. (Cited on page 160.)

[136] V. Kara, Y.-I. Sohn, H. Atikian, V. Yakhot, M. Lončar, and K. L. Ekinci. Nanofluidics of Single-Crystal Diamond Nanomechanical Resonators. *Nano Lett.*, 15(12):8070–8076, December 2015. (Cited on pages 165 and 167.)

[137] A. Tavernarakis, J. Chaste, A. Eichler, G. Ceballos, M. C. Gordillo, J. Boronat, and A. Bachtold. Atomic Monolayer Deposition on the Surface of Nanotube

Mechanical Resonators. *Phys. Rev. Lett.*, 112(19):196103, May 2014. (Cited on page 167.)

[138] G. I. Harris, D. L. McAuslan, E. Sheridan, Y. Sachkou, C. Baker, and W. P. Bowen. Laser cooling and control of excitations in superfluid helium. *Nature Physics*, 12(8):788, August 2016. (Cited on page 167.)

[139] E. Gil-Santos, C. Baker, D. T. Nguyen, W. Hease, C. Gomez, A. Lemaître, S. Ducci, G. Leo, and I. Favero. High-frequency nano-optomechanical disk resonators in liquids. *Nature Nanotechnology*, 10(9):810, September 2015. (Cited on page 167.)

[140] D. I. Bradley, R. George, A. M. Guénault, R. P. Haley, S. Kafanov, M. T. Noble, Yu A. Pashkin, G. R. Pickett, M. Poole, J. R. Prance, M. Sarsby, R. Schanen, V. Tsepelin, T. Wilcox, and D. E. Zmeev. Operating Nanobeams in a Quantum Fluid. *Scientific Reports*, 7(1):4876, July 2017. (Cited on page 167.)

[141] A. Guénault, A. Guthrie, R. P. Haley, A. Jennings, S. Kafanov, Yu. A. Pashkin, G. R. Pickett, M. Poole, R. Schanen, V. Tsepelin, E. Collin, O. Maillet, and R. Gazizulin. Probing Superfluid ^{4}He using Nanobeams at mK Temperatures. *In preparation*, February 2018. (Cited on page 167.)

[142] Dieter Vollhardt and Peter Wolfle. *The Superfluid Phases of Helium 3*. Dover Publications, Mineola, New York, reprint edition edition, October 2013. (Cited on page 167.)

[143] M. Defoort, S. Dufresnes, S. L. Ahlstrom, D. I. Bradley, R. P. Haley, A. M. Guénault, E. A. Guise, G. R. Pickett, M. Poole, A. J. Woods, V. Tsepelin, S. N. Fisher, H. Godfrin, and E. Collin. Probing Bogoliubov Quasiparticles in Superfluid ^{3}He with a 'Vibrating-Wire Like' MEMS Device. *J Low Temp Phys*, 183(3-4):284–291, May 2016. (Cited on page 167.)

[144] Hao Wu and J. A. Sauls. Majorana excitations, spin and mass currents on the surface of topological superfluid ^{3}He-B. *Phys. Rev. B*, 88(18):184506, November 2013. (Cited on page 167.)

[145] K. L. Ekinci and M. L. Roukes. Nanoelectromechanical systems. *Review of Scientific Instruments*, 76(6):061101, May 2005. (Cited on page 172.)

[146] King Y. Fong, Wolfram H. P. Pernice, and Hong X. Tang. Frequency and phase noise of ultrahigh q silicon nitride nanomechanical resonators. *Phys. Rev. B*, 85(16):161410, April 2012. (Cited on pages 181, 182, 186, 187 and 219.)

[147] P. Dutta and P. M. Horn. Low-frequency fluctuations in solids: $1/f$ noise. *Rev. Mod. Phys.*, 53(3):497–516, July 1981. (Cited on pages 187 and 218.)

[148] R. C. Zeller and R. O. Pohl. Thermal Conductivity and Specific Heat of Noncrystalline Solids. *Phys. Rev. B*, 4(6):2029–2041, September 1971. (Cited on page 187.)

[149] W. A. Phillips. Two-level states in glasses. *Rep. Prog. Phys.*, 50(12):1657, 1987. (Cited on pages 188, 193, 198 and 203.)

[150] Thomas Faust, Johannes Rieger, Maximilian J. Seitner, Jörg P. Kotthaus, and Eva M. Weig. Signatures of two-level defects in the temperature-dependent damping of nanomechanical silicon nitride resonators. *Phys. Rev. B*, 89(10):100102, March 2014. (Cited on page 188.)

[151] Guiti Zolfagharkhani, Alexei Gaidarzhy, Seung-Bo Shim, Robert L. Badzey, and Pritiraj Mohanty. Quantum friction in nanomechanical oscillators at millikelvin temperatures. *Phys. Rev. B*, 72(22):224101, December 2005. (Cited on pages 188, 206, 208, 209 and 215.)

[152] W. A. Phillips. Comment on "Two-Level Systems Observed in the Mechanical Properties of Single-Crystal Silicon at Low Temperatures". *Phys. Rev. Lett.*, 61(22):2632–2632, November 1988. (Cited on pages 189, 215 and 219.)

[153] S. Hunklinger and A. K. Raychaudhuri. Chapter 3: Thermal and Elastic Anomalies in Glasses at Low Temperatures. In D. F. Brewer, editor, *Progress in Low Temperature Physics*, volume 9, pages 265–344. Elsevier, January 1986. DOI: 10.1016/S0079-6417(08)60015-3. (Cited on pages 192, 197 and 212.)

[154] Clarence M. Zener and Sidney Siegel. Elasticity and Anelasticity of Metals. *J. Phys. Chem.*, 53(9):1468–1468, September 1949. (Cited on page 193.)

[155] Neil W. Ashcroft and N. Mermin. *Solid State Physics*. Brooks/Cole, South Melbourne, January 1976. (Cited on pages 199 and 200.)

[156] Andrew Fefferman. The Low Temperature Acoustic Properties Of Amorphous Silica And Polycrystalline Aluminum. October 2009. (Cited on pages 201 and 211.)

[157] P. Townsend, S. Gregory, and R. G. Taylor. Superconducting Behavior of Thin Films and Small Particles of Aluminum. *Phys. Rev. B*, 5(1):54–66, January 1972. (Cited on page 204.)

[158] E. H. Brandt, P. Esquinazi, H. Neckel, and G. Weiss. Drastic increases of frequency and damping of a superconducting vibrating reed in a longitudinal magnetic field. *Phys. Rev. Lett.*, 56(1):89–92, January 1986. (Cited on page 204.)

[159] C. Seoánez, F. Guinea, and A. H. Castro Neto. Surface dissipation in nanoelectromechanical systems: Unified description with the standard tunneling model and effects of metallic electrodes. *Phys. Rev. B*, 77(12):125107, March 2008. (Cited on pages 206, 207 and 209.)

[160] Jaakko Sulkko, Mika A. Sillanpää, Pasi Häkkinen, Lorenz Lechner, Meri Helle, Andrew Fefferman, Jeevak Parpia, and Pertti J. Hakonen. Strong Gate Coupling of High-Q Nanomechanical Resonators. *Nano Lett.*, 10(12):4884–4889, December 2010. (Cited on pages 207 and 216.)

[161] E. Collin, M. Defoort, K. J. Lulla, J. Guidi, S. Dufresnes, and H. Godfrin. Modal Decomposition in Goalpost Micro/Nano Electro-Mechanical Devices. *J Low Temp Phys*, 175(1-2):442–448, April 2014. (Cited on page 207.)

[162] J. D. Teufel, J. W. Harlow, C. A. Regal, and K. W. Lehnert. Dynamical Backaction of Microwave Fields on a Nanomechanical Oscillator. *Phys. Rev. Lett.*, 101(19):197203, November 2008. (Cited on pages 208 and 222.)

[163] Mehdi Hamoumi, Pierre Etienne Allain, William Hease, Laurence Morgenroth, Bruno Gérard, Aristide Lemaître, Giuseppe Leo, and Ivan Favero. Microscopic nanomechanical dissipation in gallium arsenide resonators. *arXiv:1801.09078 [cond-mat]*, January 2018. arXiv: 1801.09078. (Cited on pages 208 and 211.)

[164] Michael Tinkham. *Introduction to Superconductivity*. Dover Publications Inc., Mineola, NY, 2nd revised edition edition, 2004. (Cited on page 209.)

[165] A. D. Fefferman, R. O. Pohl, and J. M. Parpia. Elastic properties of polycrystalline Al and Ag films down to 6 mK. *Phys. Rev. B*, 82(6):064302, August 2010. (Cited on page 212.)

[166] R. König, P. Esquinazi, and B. Neppert. Tunneling systems in polycrystalline metals: Absence of electron-assisted relaxation. *Phys. Rev. B*, 51(17):11424–11432, May 1995. (Cited on page 212.)

[167] J. Haust, M. Burst, R. Haueisen, and G. Weiss. Low Temperature Acoustic Properties of Poly-Crystalline Aluminium. *Journal of Low Temperature Physics*, 137(3-4):523–533, November 2004. (Cited on page 212.)

[168] P. Esquinazi, R. König, and F. Pobell. Acoustic properties of amorphous SiO2 and PdSiCu, and of crystalline Ag, NbTi and Ta at very low temperatures. *Z. Physik B - Condensed Matter*, 87(3):305–321, October 1992. (Cited on page 212.)

[169] J. L. Black and P. Fulde. Influence of the Superconducting State upon the Low-Temperature Properties of Metallic Glasses. *Phys. Rev. Lett.*, 43(6):453–456, August 1979. (Cited on page 212.)

[170] S. N. Coppersmith and Brage Golding. Low-temperature acoustic properties of metallic glasses. *Phys. Rev. B*, 47(9):4922–4936, March 1993. (Cited on page 214.)

[171] J. Kondo. Two-Level Systems in Metals. In *Fermi Surface Effects*, Springer Series in Solid-State Sciences, pages 1–39. Springer, Berlin, Heidelberg, 1988. DOI: 10.1007/978-3-642-83425-7_1. (Cited on page 214.)

[172] A. J. Leggett, S. Chakravarty, A. T. Dorsey, Matthew P. A. Fisher, Anupam Garg, and W. Zwerger. Dynamics of the dissipative two-state system. *Rev. Mod. Phys.*, 59(1):1–85, January 1987. (Cited on page 214.)

[173] L. P. H. Jeurgens, W. G. Sloof, F. D. Tichelaar, and E. J. Mittemeijer. Growth kinetics and mechanisms of aluminum-oxide films formed by thermal oxidation of aluminum. *Journal of Applied Physics*, 92(3):1649–1656, July 2002. (Cited on page 216.)

[174] O. Arcizet, V. Jacques, A. Siria, P. Poncharal, P. Vincent, and S. Seidelin. A single nitrogen-vacancy defect coupled to a nanomechanical oscillator. *Nature Physics*, 7(11):879, November 2011. (Cited on page 222.)

[175] I. Yeo, P.-L. de Assis, A. Gloppe, E. Dupont-Ferrier, P. Verlot, N. S. Malik, E. Dupuy, J. Claudon, J.-M. Gérard, A. Auffèves, G. Nogues, S. Seidelin, J.-Ph Poizat, O. Arcizet, and M. Richard. Strain-mediated coupling in a quantum dot–mechanical oscillator hybrid system. *Nature Nanotechnology*, 9(2):106, February 2014. (Cited on page 222.)

[176] Stefan Weis, Rémi Rivière, Samuel Deléglise, Emanuel Gavartin, Olivier Arcizet, Albert Schliesser, and Tobias J. Kippenberg. Optomechanically Induced Transparency. *Science*, 330(6010):1520–1523, December 2010. (Cited on page 222.)